

UC Berkeley

UC Berkeley Electronic Theses and Dissertations

Title

Reticular Chemistry of Mesoscopic Constructs, Glasses and Weaving Materials

Permalink

<https://escholarship.org/uc/item/5x5526zn>

Author

Zhao, Yingbo

Publication Date

2017

Peer reviewed|Thesis/dissertation

Reticular Chemistry of Mesoscopic Constructs, Glasses
and Weaving Materials

by
Yingbo Zhao

A dissertation submitted in partial satisfaction of the
requirements for the degree of

Doctor of Philosophy

in

Chemistry

in the

Graduate Division

of the

University of California, Berkeley

Committee in charge:

Professor Omar M. Yaghi, Chair
Professor Peidong Yang
Professor Christopher J. Chang
Professor Alex Zettl

Summer 2017

Reticular Chemistry of Mesoscopic Constructs, Glasses
and Weaving Materials

© Copyright 2017

by

Yingbo Zhao

Abstract

Reticular Chemistry of Mesoscopic Constructs, Glasses
and Weaving Materials

by

Yingbo Zhao

Doctor of Philosophy in Chemistry

University of California, Berkeley

Professor Omar M. Yaghi, Chair

The subject of this dissertation focuses on the development of reticular chemistry, where molecular building blocks are linked into extended frameworks using strong bonds, in the context of materials chemistry. Specifically, the work herein advances the frontier of reticular chemistry in three aspects: (a) bringing metal-organic frameworks (MOFs) and covalent organic frameworks (COFs), the products of reticular chemistry, into nanometer size regime and integrating them into mesoscopic constructs; (b) developing reticular chemistry beyond crystalline materials and synthesizing glassy form of MOFs; (c) Designing woven frameworks where interlacing molecular threads form crystalline three-dimensional frameworks.

Chapter 1 introduces the principles and main discoveries of reticular chemistry under the scheme of covalent bond beyond molecules. By linking molecular building blocks into well-defined extended structures through strong covalent bonds, reticular chemistry has essentially brought covalent chemistry beyond discrete molecules and led to the discovery of numerous MOFs and COFs with diverse structures, different functional groups and vast surface areas. The chapters hereafter explore the synthesis and fabrication of MOFs and COFs as nanosized, glassy and woven materials.

Chapter 2 describes the fabrication of mesoscopic constructs of MOFs and inorganic nanocrystals, where thickness controlled and oriented $\text{Al}_2(\text{OH})_2\text{TCPP}$ MOF [TCPP = 4,4,4,4''-(porphyrin-5,10,15,20-tetrayl)-tetrabenzoate] enclosures are uniformly grown on inorganic nanostructures with pristine interface. The fabrication process involves atomic layered deposition of alumina on inorganic substrates (*i.e.* silver nanocrystals) and reacting them with TCPP linkers to nucleate MOF. By growing $\text{Al}_2(\text{OH})_2\text{TCPP}$ MOF enclosure on silver nanocrystals, surface enhanced Raman spectroscopy can be employed to study the metalation process of the porphyrin units in the MOF.

Chapter 3 generalizes the fabrication methodology of $\text{Al}_2(\text{OH})_2\text{TCCP}$ MOF enclosures to prepare thickness controlled cobalt metalated $\text{Al}_2(\text{OH})_2\text{TCCP-Co}$ MOF thin films and studied their performance as catalysts for electrochemical CO_2 reduction. For $\text{Al}_2(\text{OH})_2\text{TCCP-Co}$ MOF of 50 nm thickness on carbon disk, 76% faradic efficiency for CO can be achieved at -0.7 V vs. RHE in aqueous media with a turn over frequency of 200 h^{-1} (per cobalt atom). The catalyst was found to be stable for at least seven hours. This study demonstrates that insulating MOFs can be active electrocatalyst when fabricated into thin films with thickness of tens of nanometers.

Chapter 4 expands reticular chemistry into glassy materials by developing the synthesis of porous MOF glasses, which consist of titanium-oxo clusters linked with bisphenol linkers. By employing *m*-cresol as a solvent-modulator, monolithic and transparent MOF glasses can be formed by evaporating viscous *m*-cresol solutions of the molecular building blocks. In this process, the glass transition temperature of this solution increases exponentially with decreasing amount of *m*-cresol until the vitrification of the glass. After removing *m*-cresol from the pores, the internal surface of MOF glasses can be accessible to gas molecules and display surface area of around $300 \text{ m}^2/\text{g}$.

Chapter 5 turns to COFs and presents the synthesis of woven frameworks COF-505 and COF-112. In the synthetic design, aldehyde (amine) functionalized derivative of tetra-topic metal complexes [copper *bis*-phenanthroline for COF-505 and cobalt bis(diiminopyridine) for COF-112] are used as the tetrahedral building block, where the position of the aldehyde (amine) groups approximates a tetrahedral geometry. The tetrahedral building block is linked with a linear amine (aldehyde) to give a three-dimensional framework with diamond topology. The fact that the phenanthroline/diiminopyridine units are oriented in a mutually interlacing fashion ensures that the threads produced from linking them are entirely independent, with the metal ions serving as templates (points-of-registry) to bring those threads together in a precise manner at well-defined intervals. For COF-505, the copper(I) ions can be removed and inserted reversibly and tune the Young's modulus of the material.

The dissertation concludes in chapter 6, which brings COFs into nanometer size regime and paves the way for the integration of COFs into mesoscopic constructs. In this chapter, a new synthetic approach employing Boc-protected amine building blocks is developed to homogenize the growth of imine COFs (LZU-1, TFPB-PDA COF and Por-COF) to produce monodisperse nanocrystals and oriented thin films. The synthetic approach avoids the formation of polyimine precipitate in the early stage of conventional imine COF crystallization process and allows crystalline COF particles to nucleate directly from clear solutions. This feature enables the imine COF growth to be tuned by modulators [*i.e.* poly(vinylpyrrolidone)] to give colloiddally stable nanocrystals and manipulated by selective secondary nucleation to give uniform thin films.

To my parents

Table of Contents

List of Figures	v
List of Tables and Schemes	viii
Acknowledgement	ix
Vita.....	xi
Chapter 1. Introduction to Reticular Chemistry: Covalent Bond Beyond Molecules	1
Section 1.1 Metal-organic Frameworks and Covalent Organic Frameworks	1
Section 1.2 Covalently Linking Molecules into Extended Structures	1
Section 1.3 Strategies for Addressing the ‘Crystallization Problem’	2
Section 1.4 Design of Porosity and Access to Encompassed 3D Space	3
Section 1.5 Addressable Reticular Molecules.....	7
Section 1.6 Covalent Chemistry Within Frameworks.....	8
Section 1.7 Multivariate Covalent Chemistry	11
Section 1.8 Reference	14
Chapter 2. Mesoscopic Constructs of Metal-Organic Frameworks on Silver Nanocrystals	22
Section 2.1 Introduction	22
Section 2.2 Experimental Section	23
Section 2.2.1 Methods and Materials	23
Section 2.2.2 Synthesis of $\text{Al}_2(\text{OH})_2(\text{TCPP})$ MOFs and O_h -nano-Ag@MOF Mesoscopic Constructs	25
Section 2.3 Results and Discussion.....	25
Section 2.3.1 Fabrication of O_h -nano-Ag@MOF Mesoscopic Constructs	25
Section 2.3.2 Determination of the Orientation of MOF Enclosure.....	31
Section 2.3.3 Tracking Post-synthetic Metalation of $\text{Al}_2(\text{OH})_2(\text{TCPP})$ MOF Enclosure on O_h -nano-Ag@MOF by SERS	36
Section 2.3.4 Mapping of Metalated Linker Distribution in MOF Enclosure by SERS	40
Section 2.4 Conclusion.....	44
Section 2.5 References	45
Section 2.6 Appendix	46
Section 2.6.1 Synthesis of $\text{H}_4\text{TCPP-Co}$	46

Section 2.6.2 XRD Patterns of $\text{Al}_2(\text{OH})_2\text{TCPP}$ and $\text{Al}_2(\text{OH})_2\text{TCPP-Co}$	47
Section 2.6.3 Morphological Control of $\text{Al}_2(\text{OH})_2\text{TCPP}$ MOF Enclosure by Solvent	48
Section 2.6.4 Removal of PVP on Silver Nanocrystals.....	49
Section 2.6.5 Fabrication of $\text{Al}_2(\text{OH})_2(\text{TCPP})$ MOF on Other Substrates	50
Section 2.6.6 Fabrication of Other MOFs on Silver Nanocrystals	53
Chapter 3. Application of MOF Thin Film in Electrochemical CO_2 Reduction.....	55
Section 3.1 Introduction	55
Section 3.2 Experimental Section	56
Section 3.2.1 Methods and Materials	56
Section 3.3 Results and Discussion.....	59
Section 3.3.1 Catalytic Activity Screening of $\text{Al}_2(\text{OH})_2\text{TCPP-M}'$ MOFs.....	59
Section 3.3.2 Catalytic Performance of $\text{Al}_2(\text{OH})_2\text{TCPP-Co}$ MOF Thin Films	60
Section 3.3.3 Oxidation State Study of $\text{Al}_2(\text{OH})_2\text{TCPP-Co}$ Catalyst.....	63
Section 3.4 Conclusion.....	64
Section 3.5 References	64
Section 3.6 Appendix	69
Chapter 4. Synthesis of Glassy Metal-organic Frameworks.....	73
Section 4.1 Introduction	73
Section 4.2 Experimental Section	75
Section 4.2.1 Methods and Materials	75
Section 4.2.2 Synthesis and Activation of MOF Glasses	75
Section 4.2.3 EXAFS Study of Ti-BPA Glass	77
Section 4.3 Result and Discussion	78
Section 4.3.1 Chemical Composition and Building Blocks Analysis of MOF Glasses	78
Section 4.3.2 Structural and Porosity Characterization of Ti-BPP and Ti-BPA Glass	85
Section 4.3.3 Glass Transition in MOF Glasses	86
Section 4.4 Conclusion.....	88
Section 4.5 Reference.....	88
Section 4.6 Appendix	90

Chapter 5. Reticular Design of Woven Frameworks	92
Section 5.1 Introduction	92
Section 5.2 Experimental Section	93
Section 5.2.1 Methods and Materials	93
Section 5.2.3 Synthesis and Characterization of COF-505	95
Section 5.2.3 Synthesis and Characterization of COF-112	97
Section 5.3 Result and Discussion	100
Section 5.4 Conclusion.....	116
Section 5.5 Reference.....	117
Section 5.6 Appendix	119
Chapter 6. Synthesis of Covalent Organic Frameworks as Monodisperse Nanocrystals and Oriented Thin Films	129
Section 6.1 Introduction	129
Section 6.2 Experimental Section	130
Section 6.2.1 Methods and Materials	130
Section 6.2.2 Synthesis of COF Nanocrystals and Thin Films	130
Section 6.3 Result and Discussion	132
Section 6.3.1 Synthesis and Characterization of Monodisperse Nanocrystals	132
Section 6.3.2 Synthesis and Characterization of Oriented Thin Films.....	140
Section 6.4 Conclusion.....	143
Section 6.5 Reference.....	143
Section 6.6 Appendix	145

List of Figures

Chapter 1

Figure 1.1	Crystallization challenge to form extended structures.	2
Figure 1.2	Covalent linkages employed in the synthesis of MOFs and COFs	4
Figure 1.3	Examples of highly porous MOFs.....	6
Figure 1.4	Symmetry-independent adsorption sites in MOF-5.	7
Figure 1.5	Covalent chemistry employed to modify MOF crystals as discrete molecules.....	10
Figure 1.6	A conceptual example of precisely designed interiors of MOFs to carry out complex catalytic reactions.....	12
Figure 1.7	Scenarios of linker apportionment in MTV-MOF materials.....	13

Chapter 2

Figure 2.1	Reticular construction of $\text{Al}_2(\text{OH})_2\text{TCPP}$ MOF.....	23
Figure 2.2	SEM images of silver nanocrystals after 30 cycles ALD	26
Figure 2.3	The fabrication of MOF enclosure on silver nanocrystals.	27
Figure 2.4	The SEM and TEM images of the O_h -nano- $\text{Ag} \subset \text{MOF}$ particles.	27
Figure 2.5	The SEM images of the silver nanocrystals at different stage of the fabrication..	28
Figure 2.6	Thickness control of MOF enclosures.....	29
Figure 2.7	The 1-D profiles of GIWAXS pattern of the $\text{Al}_2(\text{OH})_2(\text{TCPP})$ MOF enclosures.	30
Figure 2.8	Crystal structure of $\text{Al}_2(\text{OH})_2(\text{TCPP})$ viewed along different axes.....	31
Figure 2.9	TEM image showing the overall orientation of the O_h -nano- $\text{Ag} \subset \text{MOF}$	32
Figure 2.10	High-resolution TEM image of the MOF crystalline domains on silver nanocrystal and its FFT image.	32
Figure 2.11	The structure model of the interface in O_h -nano- $\text{Ag} \subset \text{MOF}$	33
Figure 2.12	Two-dimensional lattice fringes observed for O_h -nano- $\text{Ag} \subset \text{MOF}$	33
Figure 2.13	Summary of MOF orientation on silver nanocrystals	34
Figure 2.14	High-resolution SEM images of the O_h -nano- $\text{Ag} \subset \text{MOF}$	34
Figure 2.15	The GIWAXS pattern and SEM image of MOF grown on silicon substrate.....	35
Figure 2.16	Characterization of metalated $\text{Al}_2(\text{OH})_2(\text{TCPP})$ MOF enclosures.....	36
Figure 2.17	Raman spectra of O_h -nano- $\text{Ag} \subset \text{MOF}$ and the assignment of the main peaks.	37
Figure 2.18	SERS spectra of the all-metalated MOF and model compounds.	38

Figure 2.19	SERS spectra of the un-metalated MOF and model compounds.	38
Figure 2.20	SERS spectra of the MOF enclosure after different metalation times.	39
Figure 2.21	Illustration of vibrational modes of the H ₄ TCPP molecule.....	39
Figure 2.22	The SEM image and XRD of fully metalated MOF enclosure.	40
Figure 2.23	The SEM image and XRD of multivariate metalated MOF on silver.	41
Figure 2.24	Characterization of MTV MOF enclosure	41
Figure 2.25	Monolayer of closed packed O _h -nano-Ag⊂MOF mapped by SERS	42
Figure 2.26	SERS spectra of metalated, unmetalated, and multivariate O _h -nano-Ag⊂MOF. .	43
Figure 2.27	SERS enhancement for single particles and clusters of O _h -nano-Ag⊂MOF.	43

Chapter 3

Figure 3.1	MOF catalyst allows for modulation of metal centers, molecular linkers, and functional groups at the molecular level	55
Figure 3.2	Catalytic performance screening of Al ₂ (OH) ₂ TCPP-M series of MOFs.....	60
Figure 3.3	Electrochemical CO ₂ reduction catalyzed by Al ₂ (OH) ₂ TCPP-Co MOF.....	61
Figure 3.4	Stability of the Al ₂ (OH) ₂ TCPP-Co MOF catalyst.....	62
Figure 3.5	In situ spectroelectrochemical analysis of Al ₂ (OH) ₂ TCPP-Co MOF	63

Chapter 4

Figure 4.1	MOF glasses consist of Ti-oxo clusters linked up with bisphenol linkers.....	79
Figure 4.2	Digested NMR spectrum of activated Ti-BPP glass	83
Figure 4.3	Digested NMR spectrum of activated Ti-BPA glass.....	83
Figure 4.4	IR spectrum of activated Ti-BPP glass.....	84
Figure 4.5	IR spectrum of activated Ti-BPA glass	84
Figure 4.6	Structural characterization of the MOF glasses.....	85
Figure 4.7	N ₂ adsorption isotherms of MOFs glasses.....	86
Figure 4.8	Glass transition temperature of Ti-BPA solution.	87

Chapter 5

Figure 5.1	Crystal structure of Cu(PBD) ₂	96
Figure 5.2	Strategy for the design of weaving structures from organic threads	101
Figure 5.3	Morphology of COF-505 studied by SEM.....	102

Figure 5.4	Structural determination of COF-505.....	103
Figure 5.5	The woven structure of COF-505.....	105
Figure 5.6	PXRD patterns of as-synthesized, demetalated and remetalated COF-505	106
Figure 5.7	AFM study of the as-synthesized and demetalated COF-505.....	107
Figure 5.8.	Weaving molecular threads into frameworks of various topologies	108
Figure 5.9	SEM images of COF-112 crystallites synthesized in the metal-complex route..	111
Figure 5.10	Infrared spectrum of COF-112 and its starting material.	113
Figure 5.11	Infrared spectrum of COF-112 and $\text{Co}(\text{NH}_2\text{-DIP})_2(\text{BF}_4)_2$	113
Figure 5.12	Structural determination of COF-112.....	114
Figure 5.13	The woven structure of COF-112.....	116

Chapter 6

Figure 6.1	SEM and size distribution of LZU-1 nanocrystals.	133
Figure 6.2	XRD and TEM study of LZU-1 nanocrystals.	134
Figure 6.4	Poly-dispersed LZU-1 nanocrystals result from unoptimized conditions.....	136
Figure 6.5	N_2 uptake of 245 nm LZU-1 nanocrystals.....	137
Figure 6.6	SEM images and PXRD of Por-COF and TFPB-PDA-COF nanocrystals.	138
Figure 6.7	Mixed matrix membrane of LZU-1 nanocrystals.	139
Figure 6.8	SEM image of LZU-1 thin film.....	140
Figure 6.9	The uniformity, orientation, and crystallinity of LZU-1 COF thin film.	141
Figure 6.10	Gas adsorption triggered color change in LZU-1 thin film.....	142

List of Tables and Schemes

Chapter 4

Table 4.1	Various bisphenol struts used in glassy MOF synthesis.....	74
Table 4.2	Multiple-shell EXAFS fitting results for fits to the Ti-BPA MOF.....	80
Table 4.3	First-shell EXAFS fitting results for fits to the Ti-BPA MOF.	81

Chapter 5

Scheme 5.1	Illustrations of weaving and entanglement.....	93
Scheme 5.2	Synthetic routes to crystalline woven COF-112.	110
Scheme 5.3	Dynamic nature of $\text{Co}(\text{NH}_2\text{-DIP})_2(\text{BF}_4)_2$ in imine COF synthesis	112

Chapter 6

Scheme 6.1	Aldehyde building blocks of the Por-COF and TFPB-PDA COF.	137
------------	--	-----

Acknowledgement

It was twenty days before my nineteenth birthday when I arrived at Berkeley to start my Ph.D. study in chemistry. With eagerness to conduct my own research but very little knowledge or experience in material chemistry, I was fascinated by every group I visited. I was assigned a temporary desk in the Yaghi group, who just moved to Berkeley from UCLA and not even had a group website link in the department of chemistry at the time. Deeply intrigued by his speech on the chemistry of MOF and encouraged by his welcoming and energetic group, I joined the group on mid-September 2012, which I later realized is the most fortunate decision I made in my Ph.D. period. Throughout my graduate study, Prof. Yaghi has been extraordinarily supportive, inspiring, encouraging and understanding, and his office is the most memorable place for me in Berkeley where he encouraged me after frustrating experiment, discussed with me how to strengthen my project and taught me how to write a good paper. He is a remarkable person that is determined and uncompromising on his scientific standard but at same time forgiving and open minded to his students, and he can see strength in me that I don't realize. He is enormously hardworking, honorable, resourceful and caring and helped me to develop my projects based on my research interests regardless of whether it fit his perspective of the field. His mentorship and support, both direct and indirect, has fundamentally shaped my perspective of research and I would not be who I am without him.

I am also deeply grateful to Prof. Peidong Yang, who is, in the first place, the postdoctoral adviser of my undergraduate research mentor Prof. Aidi Zhao in University of Science and Technology of China. It was in Prof. Zhao's group when I developed my earliest interest in chemical research and his mental strength, enthusiasm and persistence passed down from Prof. Yang has deeply influenced me. In my Ph.D. study, I collaborated extensively with Prof. Peidong Yang's group on the fabrication of mesoscopic constructs and electrocatalysts of MOFs. I learnt much of my knowledge in nanoscience from him, and his hands-on and effective mentoring throughout these projects greatly accelerated my intellectual growth. He initiated the SIP fellowship program through which I was funded and he was also my qualifying exam committee member. I am equally thankful to Prof. Delia Milliron, who was a staff scientist in the Molecular Foundry in LBNL when I joined the Yaghi lab. I worked with her for almost a year on synthesizing MOF nanocrystals and she patiently taught me everything about nanocrystals, from theory to experimental details, from synthesis procedures to various characterization techniques. I would also want to express my gratitude to Prof. Osamu Terasaki, who I spent two months with in Stockholm University in 2013 and has been my long-term collaborator and mentor in electron microscopy since then. His keen interest in science, high standard and perfection in research made him a role model for me. He is also an extraordinarily fun person at his seventies, and we had many good times together outside the lab. Prof. Austen Angell in Arizona State University is another great collaborator and mentor of me. He brought me into the field of glassy materials and set a great example for me as a physical chemist. I would also like to thank Prof. Christopher J. Chang for collaboration in electrochemical CO₂ reduction and being my qualifying exam committee, Prof. Jefferey Long for being my qualifying exam committee chair and Prof. Alex Zettl for being my qualifying exam outside committee.

It would not be possible for me to carry out the research projects presented herein without the help of all my collaborators: Dr. Chenhui Zhu in the Advanced Light Source, Dr. Zheng Liu in AIST, Dr. Yanhang Ma in Stockholm University, Dr. Felipe Gandara who is a former member of

the Yaghi group, Dr. Wei Bao in the Molecular Foundry, Dr. Nickolay Kornienko, Dr. Nigel Becknell, Dr. Chen Chen, Dr. Tsung-Rong Kuo, and Dr. Chris Kley in the Yang group, Dr. Dillon Miles and Dr. Souvagya Biswas in the Toste group, and Dr. Xingchen Ye in the Alivisatos group. I am also grateful for the very helpful discussion and morale support from Dr. Yi Liu, Dr. Brett Helm and Dr. David Britt in the Molecular Foundry and Dr. Qian Chen in the Alivisatos group.

In my graduate study, the Yaghi lab members have always stood behind me. Dr. Hexiang Deng and Dr. Yuebiao Zhang were my early mentor in MOF chemistry, Dr. Mitsuharu Suzuki guided me on organic chemistry. Dr. Kyungmin Choi was the only person in the lab working on nanosized MOF in my early days in the lab and we had many helpful discussions and collaborations. Mr. Christian Diercks is an incredibly nice and fun person and we collaborated on several COF projects. Ms. Yuzhong Liu and Dr. Xixi Sun contributed tremendous work on the development of weaving materials and we also had many good times outside the lab. Ms. Lei Guo and Mr. Lyu Hao have been very hardworking and collaborated with me on the weaving materials and nanosized COF project. Mr. Jingjing Yang and Dr. Christopher A. Trickett always helped me when I had a single crystal to measure. Ms. Noelle Catarineu and Dr. Juncong Jiang are in the same year as me and we had faced all the challenges side-by-side. Along the way I learned from every single member of the Yaghi lab and benefit a lot from the open, hard-working and encouraging lab culture.

I owe my greatest gratitude to my parents, who raised me up and always encourage me to pursue my genuine interest and stay curious to the world. Their persistent and hardworking in their own career and research despite all the difficulties have profoundly influenced me and their love and understanding always give me courage to face the challenges of life. Meeting Chenlu is the greatest fortune and blessing in my graduate school, and it is her that made Berkeley another home for me. She provided the warmest supported for me and has become an inseparable part of my life. I am thankful to everything my family is and continues to be.

Vita

August 1993	Born, Shenyang, Liaoning, China
2012	B.S., Chemistry University of Science and Technology of China Hefei, Anhui, China
2014	Ph.D. Candidate, Chemistry University of California, Berkeley Berkeley, California
2012-2017	Graduate Student Instructor and Researcher University of California, Berkeley Berkeley, California

PUBLICATIONS

Kornienko, N., Zhao, Y., Kley, C. S., Zhu, C., Kim, D., Lin, S., Chang, C. J., Yaghi, O. M. & Yang, P. Metal–Organic Frameworks for Electrocatalytic Reduction of Carbon Dioxide. *J. Am. Chem. Soc.* **2015**, 137, 14129-14135.

Zhao, Y., Kornienko, N., Liu, Z., Zhu, C., Asahina, S., Kuo, T.-R., Bao, W., Xie, C., Hexemer, A., Terasaki, O., Yang, P. & Yaghi, O. M. Mesoscopic Constructs of Ordered and Oriented Metal–Organic Frameworks on Plasmonic Silver Nanocrystals. *J. Am. Chem. Soc.* **2015**, 137, 2199-2202.

Jiang, J., Zhao, Y. & Yaghi, O. M. Covalent Chemistry beyond Molecules. *J. Am. Chem. Soc.* **2016**, 138, 3255-3265.

Zhao, Y., Lee, S-Y., Becknell, N., Yaghi, O. M., & Angell, C.A., Nanoporous transparent MOF glasses with accessible internal surface. *J. Am. Chem. Soc.* **2016**, 138, 10818-10821.

Liu, Y., Ma, Y., Zhao, Y., Sun, X., Gándara, F., Furukawa, H., Liu, Z., Zhu, H., Zhu, C., Suenaga, K., Oleynikov, P., Alshammari, A. S., Zhang, X., Terasaki, O. & Yaghi, O. M. Weaving of organic threads into a crystalline covalent organic framework. *Science* **2016**, 351, 365-369.

Chapter 1. Introduction to Reticular Chemistry: Covalent Bond Beyond Molecules

Section 1.1 Metal-organic Frameworks and Covalent Organic Frameworks

The covalent chemistry of organic and inorganic molecules has long been the practice of chemists and at the heart of many important advances in science. The building-up and modification of organic molecules by covalent bonds to make pharmaceuticals, chemicals, and polymers have fundamentally changed our way of life. Similarly, covalent synthesis of inorganic complexes has led to useful catalysts capable of high activity and selectivity. The precision and versatility with which covalent chemistry on such molecules is practiced have not been translated to either the build-up of extended structures or their modification. This is until the invention of metal-organic frameworks (MOFs)¹⁻³ and covalent organic frameworks (COFs),⁴ where molecular building units are covalently linked to make porous crystals of extended structures. These structures can also be modified by covalent chemistry through post-synthetic modification (PSM) without losing their long-range order.⁵⁻⁷ In essence, MOF and COF chemistry has taken covalent chemistry beyond molecules to build up crystals of covalently linked extended structures, and to carry out reactions on such crystals as if they are discrete molecules. The ability to reticulate molecular building units into frameworks^{8,9} not only allows chemistry to be done in a precise manner on those units but also positions and confines them in a new chemical environment otherwise not possible in solution or in the molecular crystals of the unlinked constituents. Here, we highlight how this covalent chemistry practiced beyond molecules has led to: (a) linking of building units into covalent crystals by combining organic and inorganic constituents to make MOFs and organic units to make COFs, both as robust materials with ultrahigh porosity; (b) covalent chemistry done by performing PSMs on MOF crystals, which maintain their order throughout the process and therefore provide means of designing the interior of MOFs; (c) emergent behavior resulting from mixing of functionalities within the pores of MOFs that have specific spatial, metric, and compositional characteristics; and (d) MOFs with sequences of chemical functionality running along their pores that are apportioned and compartmentalized on the molecular and nano-levels to make mesoscopic constructs. (Reproduced with permission from *J. Am. Chem. Soc.* **2016**, 138, 3255. Copyright 2016 American Chemical Society.)

Section 1.2 Covalently Linking Molecules into Extended Structures

A covalent bond is a chemical bond made by sharing electrons between atoms.¹⁰ Organic synthesis of molecules takes full advantage of the directionality of covalent bonds to build-up elaborate chemical structures using step-by-step reactions as exemplified by the original synthesis of vitamin B₁₂.^{11,12}

In contrast, building-up a covalent extended structure is essentially a one-step synthesis leading to an insoluble product. Thus, the synthetic procedure has to be carefully designed to yield a well-defined material. If covalent chemistry beyond molecules is to be carried out with the same precision as that done for organic and inorganic molecules, the products have to be crystalline so that they are easily characterized. Furthermore, their crystallinity must be maintained even after

they have been subjected to PSMs. Both of these challenges have been addressed for MOFs and COFs.

The ‘crystallization problem’ encountered is usually magnified when linking molecular building units by increasingly stronger bonds (Figure 1.1).^{8,13-15} For example, it is relatively easy to make crystals in which weak interactions hold the molecules together such as van der Waals forces in dry ice and hydrogen bonding in ice, notwithstanding are some cases where lower symmetry and/or flexible molecules are difficult to organize as molecular crystals. Even crystals of metal-bipyridine type structures are easy to obtain because of the weak bonding between the metal and the neutral Lewis base linker (Figure 1.1). However, crystallizing extended structures in which metal to charged ligand bonds and non-metal to non-metal bonds are employed is relatively more difficult as the case previously experienced for MOFs and COFs (Figure 1.1). The success in the synthesis of MOF and COF materials as crystals (Figure 1.2), which are held together by strong bonds, vastly expands the realm of covalent chemistry to include extended and nanosized structures, as discussed below.^{2,4,16-24}

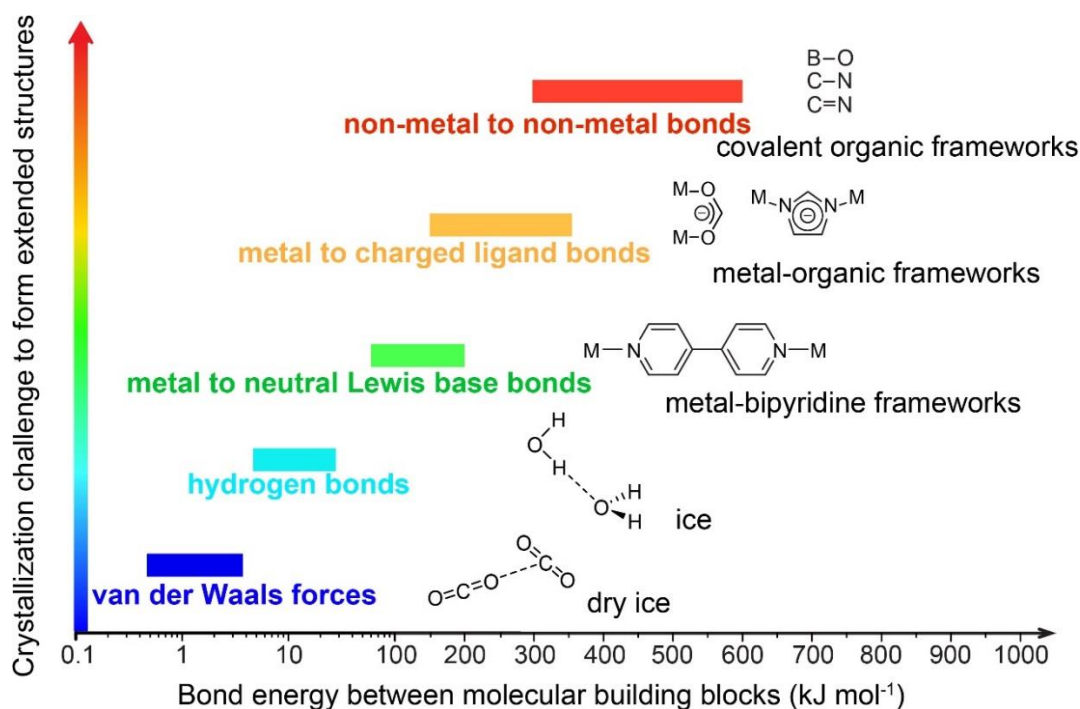


Figure 1.1 Crystallization challenge to form extended structures. Increasing bond energy of linkages between molecular building blocks leads to increased difficulty in obtaining their corresponding crystalline extended structures.

Section 1.3 Strategies for Addressing the ‘Crystallization Problem’

The crystallization process requires reversible bond formation to allow for self-correction of defects and avoid the formation of amorphous or poorly crystalline products. Elegant examples exist where crystalline covalent extended structures are constructed through single-crystal-to-single-crystal topochemical linking of organic building units by exposure to UV light.²⁵ This approach is not as widely deployed as that used for MOFs and COFs because it requires meticulous design of the molecular building blocks and their precise positioning in the crystal prior to carrying out the covalent bond linkage between adjacent molecules.

In MOF chemistry, the goal of obtaining crystalline solids has been realized largely by slowing down the formation of strong metal-oxygen covalent bonds [M-O bonds, M = Ti(IV), V(III), Cr(III), Mn(II), Fe(III), Co(II), Ni(II), Cu(II), Zn(II), Zr(IV), Ln(III), Al(III), and Mg(II)] between the inorganic and organic building units (termed secondary building units, SBUs) to a point permitting self-correction. Typically, the formation of a MOF requires deprotonation of the organic acid in order to make the metal-oxygen bonds. However, the rate at which this deprotonation process takes place is a critical factor in controlling the crystallization process of the MOF. The key development in making MOF crystals of metal-carboxyl bonds was the use of amide solvents such as *N,N*-dimethylformamide, *N,N*-dimethylacetamide, and *N*-methyl-2-pyrrolidone.^{1,3} Since these solvents are heated in the synthesis of MOFs, they function as sources for the slow release of basic amines,²⁶ which gradually deprotonate the organic acid and facilitate the formation of covalent bonds between the inorganic and organic SBUs.¹ Large MOF single crystals of millimeter sizes have been reported using these solvents.^{27,28} Needless to say, this basic procedure has been employed in the synthesis of the vast majority of MOFs.²⁹ Recently, other methods involving the use of water as a solvent,^{2,30} microwave irradiation,³¹ and mechanochemical procedures^{32,33} have been developed for MOFs.

It was also shown that highly crystalline MOFs of zirconium, aluminum, chromium and lanthanide can be obtained by adding modulators;³⁴⁻³⁷ these are usually monocarboxylic acids such as formic acid, acetic acid and benzoic acid. Addition of these modulators along with di- and multi-topic carboxylate linkers suppresses the hydrolysis of the metal ions to metal oxides due to their acidity, and slows down the crystal growth process to give the control needed for obtaining MOF crystals.

Different strategies are applied in COF chemistry to make crystalline covalent organic solids. Typically, this is achieved by reactions where stoichiometric quantities of a small molecular byproduct such as water are generated. In a closed system, such byproducts of the covalent bond formation are used to modulate the extent of equilibrium between the product and reactants according to Le Châtelier's principle. For example, water generated from the formation of boroxine anhydride in COF-102 and boronate ester in COF-108 is capable of hydrolyzing and modulating the reversibility of the covalent bonds (B-O and C-O bonds) formed in those COFs.³⁸ The extra space intentionally left in the closed reactor and the combination of hydrophilic and hydrophobic solvents allow the water formed to be partitioned between the reaction mixture and the headspace. In this way, the formation of the extended structure is driven by the equilibrium between water in the reaction mixture and the headspace. Catalysts, such as acetic acid and hydrochloric acid, which are effective in reversibly controlling reaction rates can be used to accelerate an otherwise slow covalent bond formation/cleavage as was illustrated in COFs linked by imine and hydrazone bonds.^{18,39-42} Efforts devoted to the crystallization of these extended structures have produced highly crystalline materials and made possible their structural characterization by diffraction techniques (powder and single crystal X-ray, neutron, and electron) and the study of their covalent reaction chemistry.

Section 1.4 Design of Porosity and Access to Encompassed 3D Space

Thus far, we have outlined how building-up covalent extended structures from molecular building units can lead to crystalline MOFs and COFs. The study of these solids by X-ray diffraction techniques revealed not only the strong linkages making up the backbone of the

frameworks, but also the space encompassed within them.¹ This space is filled with solvent and, in the case of charged frameworks, solvated counter ions, which have to be removed and desolvated in order to access the porosity of the material (this process is referred to as ‘activation’) and allow the development of covalent chemistry within the pores.

Early studies on metal-organic materials composed of metal to neutral Lewis base bonds (*e.g.* bipyridine and nitrile-type) reveal that these frameworks collapse when activated because of their frail architecture.⁸ In contrast, MOFs composed of strong covalent linkages such as metal-carboxyl bonds are robust upon removal of the guest solvent molecules, and therefore were shown to have permanent porosity by gas sorption isotherm measurements.

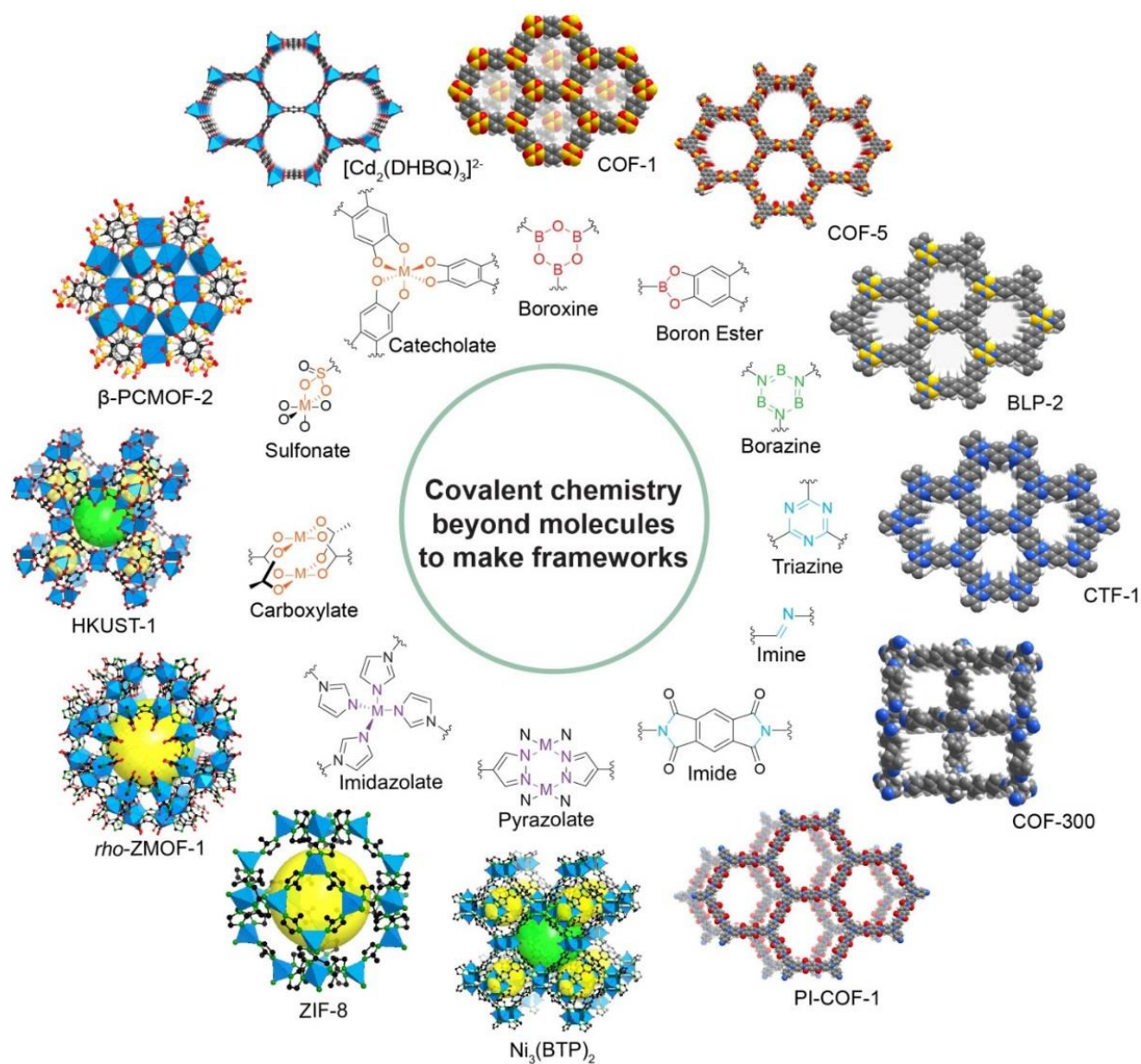


Figure 1.2 Covalent linkages (inner region) employed in the synthesis of MOFs and COFs (outer region).

Proof of permanent porosity was obtained as early as 1998 for MOFs¹ and 2005 for COFs,⁴ respectively. This has allowed comparisons to be made between these frameworks and the more traditional porous materials, such as zeolites and related inorganic microporous materials.

It is worth mentioning that activation of MOFs and COFs has been a subject of intense study because of their high porosity and the challenges associated with evacuating large amounts of solvent from the pores. The most reliable activation methods have involved: (a) ‘solvent-exchange’ where the as-synthesized material is immersed in a solvent of less polarity and lower boiling point than the one already in the pores, followed by frequent refreshing and evacuation of that solvent;⁴³ (b) ‘supercritical CO₂ drying’ where liquid CO₂ is used to exchange the solvent in the pores and the system’s temperature and pressure are elevated beyond the critical point of CO₂, followed by depressurization to leave behind vacuous pores. The latter method has been proven to be successful for a few cases in which the framework bears large pores but with small pore apertures, or has highly hydrophilic pores.^{44,45} Presently, these methods are used routinely, thus offering new opportunity for covalently designing the interior of the pores.

The permanent porosity of MOFs has led to unparalleled precision in: expanding the pores, designing the pore shape, and the covalent attachment of functional groups to the organic linkers and/or open metal sites within the backbone of MOFs. Thus, in the remainder of this section, we focus on the first two aspects, while the third is discussed in a separate section below. From this point on, we use MOFs as examples because their chemistry is illustrative and, in these respects, far more developed than COFs.

The precision with which covalent chemistry is used to stitch molecular building blocks into extended structures, referred to as reticular chemistry, has made available a diverse class of MOFs in which the pore shape and pore size can be varied nearly at will. For example, isoreticular expansion (expanding the metrics of the framework without changing its underlying topology) has yielded the most porous materials and the largest pore opening in crystals.⁴⁶⁻⁵¹ In the cubic HKUST-1 system, the most expanded member, MOF-399, [Cu₃(BBC)₂; BBC = 4,4',4''-(benzene-1,3,5-triyl-tris(benzene-4,1-diyl))tribenzoate] (Figure 1.3a), bears a pore of the same shape but 16 times larger in volume than that of the smallest member HKUST-1, [Cu₃(BTC)₂; BTC = benzene-1,3,5-tricarboxylate].⁴⁷ In the hexagonal MOF-74 system, [Mg₂(DOT); DOT = dioxidoterephthalate], the organic linker with one phenylene unit was expanded to have 11 phenylene units resulting in a pore aperture of 98 Å in diameter for the corresponding IRMOF-74-XI (Figure 1.3b).⁵¹ Modulation of the pore shape is achieved either by changing the combination of SBU geometry or by varying the linker length ratio. For example, linking the Zn₄O(-COO)₆ SBU with mixed dicarboxylates and tricarboxylates of different length ratios gives: (a) two types of cages (dodecahedral and tetrahedral cages of 2.5 nm × 3.0 nm and 0.5 nm × 0.5 nm in size) in DUT-6 [MOF-205, Zn₄O(NDC)(BTB)_{4/3}, NDC = naphthalene-2,6-dicarboxylate, BTB = benzene-1,3,5-tribenzoate] (Figure 1.3c);^{46,52} (b) 1.4 nm × 1.7 nm cages and 2.7 nm × 3.2 nm meso-scale 1D channels in UCMC-1, [Zn₄O(BDC)(BTB)_{4/3}; BDC = benzene-1,4-dicarboxylate] (Figure 1.3d);⁵³ and (c) three different types of cages (2.7 nm × 4.8 nm, 2.0 nm × 2.0 nm, and 0.6 nm × 0.6 nm) in MOF-210, {Zn₄O(BPDC)(BTE)_{4/3}; BPDC = biphenyl-4,4'-dicarboxylate, BTE = 4,4',4''-[benzene-1,3,5-triyl-tris(ethyne-2,1-diyl)]tribenzoate} (Figure 1.3e).⁴⁶

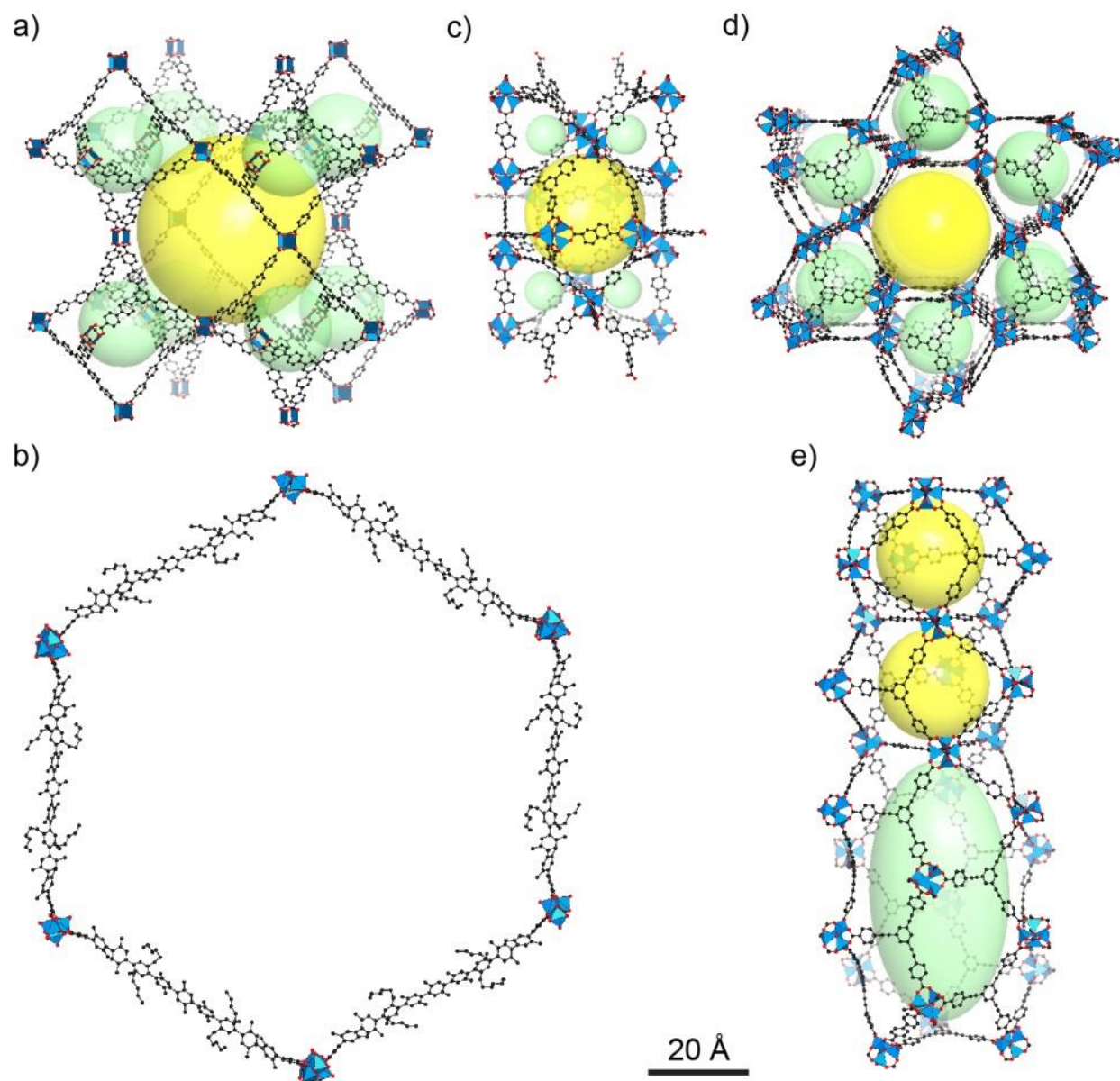


Figure 1.3 Examples of highly porous MOFs: (a) MOF-399, (b) IRMOF-74-XI, (c) DUT-6 (MOF-205), (d) UMCM-1, and (e) MOF-210. The pores are represented as green and yellow spheres. Atom labelling scheme: M (blue polyhedra, M = Zn, Cu, Mg), C (black), and O (red). All H atoms are omitted for clarity.

Section 1.5 Addressable Reticular Molecules

On a fundamental level, the ability to make MOF structures permanently porous has given access to molecules within the confines of an extended structure. From the forgoing discussion, this would not be possible without the covalent chemistry being developed beyond molecules. Indeed, all atoms [with the exception of a central atom which might reside within an inorganic SBU as the O in $\text{Zn}_4\text{O}(-\text{COO})_6$] that make up the inorganic and organic SBUs are accessible to incoming guests such as gases and organic molecules. This advantage is only possible because the SBUs are stitched through covalent chemistry and thus are suspended in 3D without being solvated as discrete molecules. Additionally, they do not suffer from being inaccessible in the solid state, as would be the case in a closely packed molecular crystal.

Access to each of the atoms in MOFs was revealed by an X-ray diffraction experiment conducted on single crystals of MOF-5 at 30 K.⁵⁴ Here, small doses of Ar or N_2 introduced into the already evacuated pores revealed accessible adsorption sites within the pores: the zinc oxide SBU (Figure 1.4a-c), the faces and the edges of the phenyl ring of the BDC linkers (Figure 1.4d-e). This study also served as a benchmark for identifying the origin of the ultrahigh surface areas found in MOFs. Subsequently, adsorption sites for gases, such as $\text{D}_2(\text{H}_2)$, CH_4 , CO_2 , and H_2O , and their behavior in MOFs were identified using a variety of techniques,⁵⁵⁻⁶¹ and their interaction strength assessed for a large variety of MOFs. Thus, suspending molecules in 3D space and having access to these molecules by covalently linking them into scaffolds is the best strategy for maximizing access to them as well as for increasing the number of adsorption sites. Other means of increasing adsorption sites involve having multiple interpenetrating frameworks in the crystal.^{62,63} It is important to give consideration to the size of substrate to be incorporated in the pores and the most efficient pore size needed from the division of space to maximize its interaction with the framework.

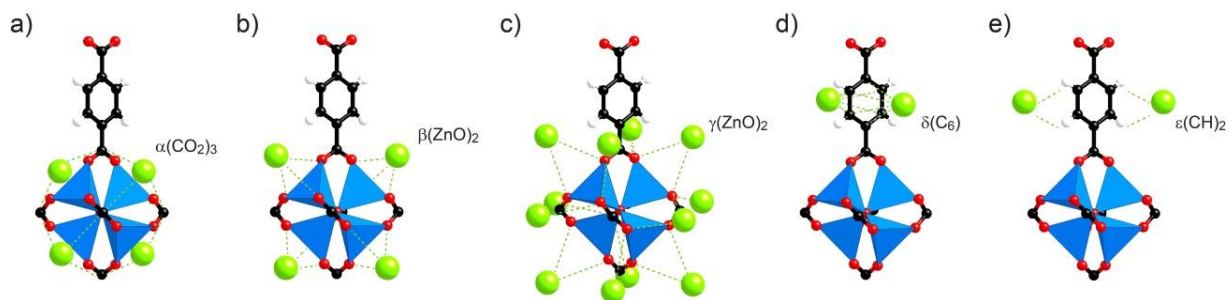


Figure 1.4 Symmetry-independent adsorption sites in MOF-5. These include (a to c) three sites primarily associated with the secondary building unit and those above the (d) face and (e) edges of the linker. The absorption sites are represented as green spheres. Atom labelling scheme: Zn (blue polyhedra), C (black), O (red), and H (white). Adapted with permission from ref 54. Copyright 2005 AAAS.

Metal containing SBUs are strong adsorption sites for gases, and can be stronger and more selective if they have open metal sites (also known as unsaturated coordination sites). In the field of molecular metal complexes, however, this chemistry requires steric hindrance around open metal sites rendering them inaccessible. The covalent chemistry of frameworks helps to address this problem by using strong covalent bonds to fix the metal atoms in a rigid structure and prevent their rearrangement, aggregation, and ligation to them when they are coordinatively unsaturated. This feature greatly facilitates the generation and accessibility of open metal sites in MOFs. In 2000, the first example of open metal sites in MOF was created in MOF-11, [Cu₂(ATC)]; ATC = adamantane-1,3,5,7-tetracarboxylate], and characterized by single crystal X-ray diffraction experiments.⁶⁴ Water molecules bound to copper atoms in Cu₂(H₂O)₂(-COO)₄ SBUs of the as-synthesized MOFs were readily removed upon heating at 120 °C to generate open coordination sites on four-coordinate coppers in Cu₂(-COO)₄ SBUs of the activated MOF-11. Since then open metal sites have been produced in MOFs and used for: (a) enhanced storage capacity of H₂, CH₄, CO₂, and NH₃,⁶⁵⁻⁶⁸ (b) improved CO₂/N₂ separation,⁶⁹ (c) molecular recognition,⁷⁰ and (d) Lewis acid catalysis.⁷¹⁻⁷³

Section 1.6 Covalent Chemistry Within Frameworks

Covalent chemistry could also be employed to modify MOF crystals as if they were discrete molecules, because the MOF building units retain the same underlying structure and essential chemical reactivity as their molecular counterparts. PSMs involve either organic reactions modifying the organic linkers of the MOF and/or covalent bonding of incoming ligands to open metal sites (Figure 1.5).⁷⁴⁻⁸³ These modifications are performed orthogonally to the MOF backbone structure. Such chemical reactions are carried out at precise locations within the crystal and the product remains atomically well defined (*i.e.* crystalline). The ability to carry out reactions on extended solids in this manner is possible because of the robustness of the MOF structure due to the strong covalent bonds making up the framework. Furthermore, this chemistry allows functional groups that are not compatible with the MOF synthesis to be incorporated, and for the design of a series of MOFs of different functionality using a single synthetic condition. Thus, PSM is a powerful tool to design complexity within MOFs.

PSMs performed on extended solids require reagents to diffuse throughout the crystal. Reactions involving insoluble heterogeneous reagents and catalysts or those producing insoluble byproducts present a challenge to PSMs of MOFs. The candidate reactions for PSM should also be chemically compatible with the MOF backbone. Increasingly, MOFs with unusual stability in aqueous and non-aqueous conditions are being used.^{5,84,85} More recently, MOFs stable in acidic and basic media have been reported.^{21,30,86} These developments provide plenty of opportunities for PSMs to be used in the development of covalent chemistry beyond molecules.

A typical example of PSMs using metal coordination is the metalation of MOF-253, [Al(OH)(BPYDC), BPYDC = 2,2-Bipyridine-5,5-dicarboxylate],^{79,87,88} where BPYDC molecules linked up with alumina rods are metalated with Cu(II), Ru(II) and Pd(II), rendering the MOF with unusual gas separation and catalytic properties [*e.g.* Cu(II) metalated MOF-253, Al(OH)(BPYDC)·0.97Cu(BF₄)₂, shows four-fold increase of selectivity in N₂/CO₂ separation].⁷⁹ Other examples include metalations, with first row transition metals, of the free-base porphyrin TCPP-H₂ in MOF-545, [Zr₆O₈(H₂O)₈(TCPP-H₂)₂, TCPP-H₂ = 4,4,4,4''-(porphyrin-5,10,15,20-tetrayl)-tetrabenzoate], and Al₂(OH)₂(TCPP-H₂).⁸⁹⁻⁹¹

Coordinating ligands such as amines and sulfates can bind to metal SBUs containing open metal sites.^{2,92-94} These PSMs are facile and have proved to be useful in introducing catalytically active sites and new gas adsorption sites. For example, MOF-808, $[\text{Zr}_6\text{O}_5(\text{OH})_3(\text{BTC})_2(\text{HCOO})_5(\text{H}_2\text{O})_2]$, can be treated with sulfuric acid to produce its sulfated analogue, MOF-808-2.5SO₄, $[\text{Zr}_6\text{O}_5(\text{OH})_3(\text{BTC})_2(\text{SO}_4)_{2.5}(\text{H}_2\text{O})_{2.5}]$, which shows superacidity.⁹³ The sulfate groups are covalently bound to the zirconium based SBUs in a spatially well-defined manner as confirmed by single crystal X-ray diffraction.

Modification on the organic linkers has been done using various organic reactions involving click chemistry, imine condensation, amide bond formation and functional group deprotection (Figure 1.5). For example, primary amines can be incorporated in IRMOF-74-III through post-synthetic deprotection.⁷⁶ The MOF constructed with linkers bearing *tert*-butyloxycarbonyl group protected amines was heated at 230 °C in a ternary mixture of solvents under microwave irradiation to deprotect and obtain primary amine groups covalently linked in the pores. These primary amine groups, which are incompatible with the MOF synthesis conditions, enable the MOF to selectively bind CO₂ in the presence of water.⁷⁶ Other examples are the PSMs carried out on IRMOF-3, $[\text{Zn}_4\text{O}(\text{BDC-NH}_2)_3]$, BDC-NH₂ = 2-aminobenzene-1,4-dicarboxylate], where the amino groups react with alkyl anhydride to form amide bond and introduce alkyl groups into the MOF.⁹⁵ It is shown that with increased length of the alkyl group, the IRMOF-3 becomes more hydrophobic and resilient to moisture.⁸³

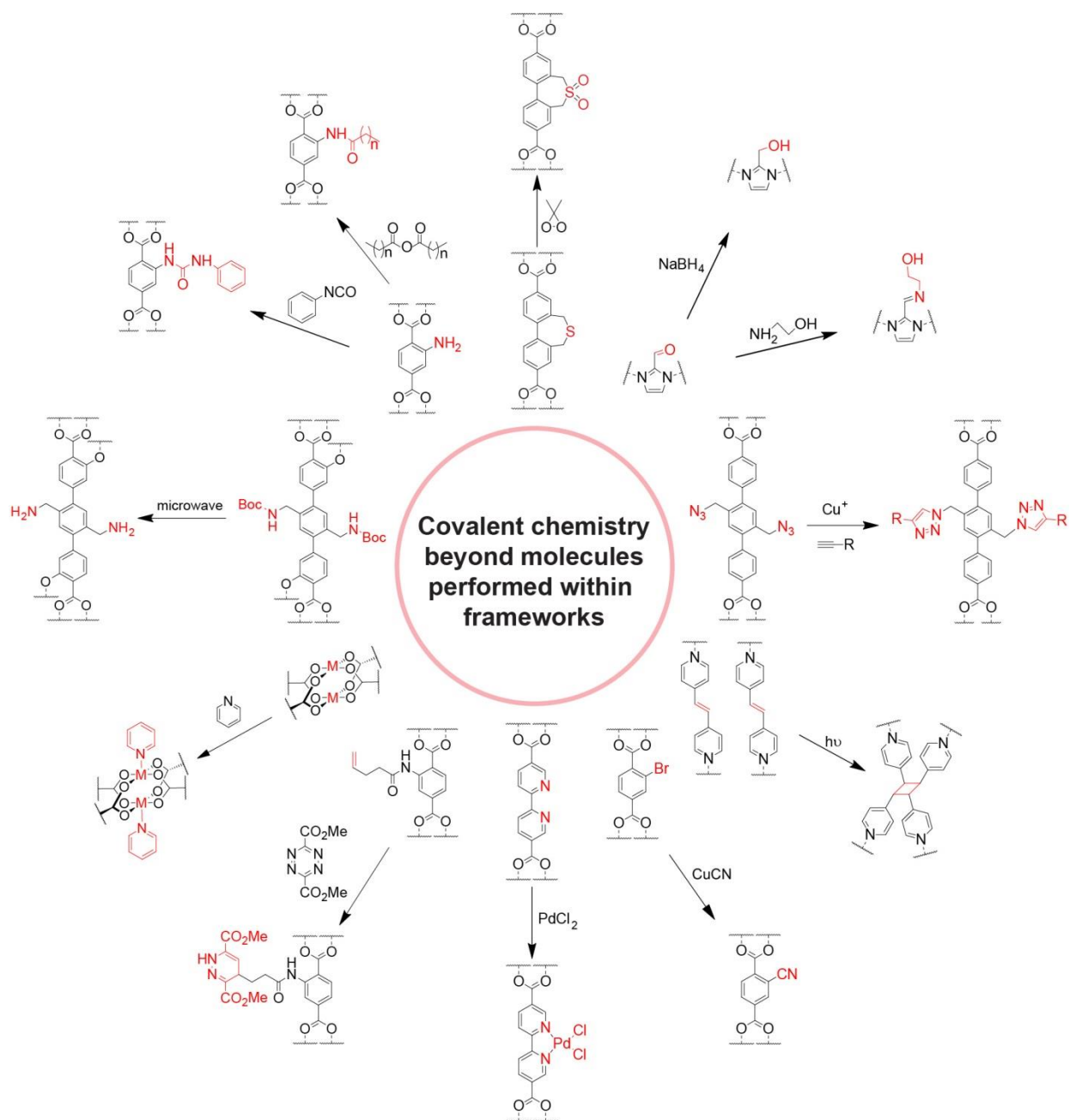


Figure 1.5 Covalent chemistry employed to modify MOF crystals as discrete molecules.¹⁰³

Metal binding sites,⁹⁶ carboxylic acids,⁹⁷ amines,⁷⁶ and triazoles^{81,98,99} have also been incorporated into the organic linkers of MOFs using similar PSMs. Bio-molecules such as amino acids have also been introduced into MOFs by multiple sequential reactions with full preservation of crystallinity. Aniline units in MIL-68-NH₂, [In(OH)(BDC-NH₂)], were coupled with protected proline and alanine using 4-dimethylaminopyridine/PyBroP[®] coupling reagent.¹⁰⁰ Upon deprotection, the free amino acid covalently attached to the organic linkers was obtained. These versatile multiple step covalent reactions on MOF crystals, just like the synthesis of vitamin B₁₂ referred to earlier, take full advantage of the directionality of covalent bonds while operating in 3D extended crystals.

Given the versatility of PSMs and the diversity of MOF structures, which can be modified without losing their crystallinity, we anticipate further growth of this approach to include precisely designed interiors of MOFs to carry out complex catalytic reactions. To illustrate this point, we use IRMOF-74-III as a platform for covalently dangling amino groups inside its 1.5 nm pores. A catalytic MOF can be made by covalently attaching a conventional organometallic catalyst inside the pore using imine condensation (Figure 1.6). Here, the MOF backbone may be considered as being analogous to the enzyme backbone ‘propping up’ the catalytic active site. The pores of the MOF help control the selection of substrates and products.^{101,102}

Section 1.7 Multivariate Covalent Chemistry

As covalent chemistry performed on discrete molecules may give mixtures of products, the same is true when such chemistry is performed on MOFs. However, the ‘reaction mixture’ resulting from PSMs remains as an integral and inseparable part of the MOF structure. Thus, such MOF crystals have both the functionalized and non-functionalized linkers in the backbone structure. In other words, the MOF interior and its multiple functionalities are of a multivariate nature (MTV-MOFs), where phase purity is preserved while incorporating multiple derivatives of linkers. For example, in the previous case of IRMOF-3 modified with alkyl anhydride, when the conversion of the amino group throughout the material is incomplete,⁹⁵ amino and amide groups coexist to make for mixed linkers in the make-up of the MOF crystal. Here, the amide and amino groups can only reside as attached units to the ordered arrangement of phenyl ring units of the linkers. However, the spatial distribution of the functional groups on the linkers is disordered because they all lie on the same crystallographic position. Thus, the question of how they are spatially arranged in the crystal is both a challenge and an opportunity.^{27,105} This can be best understood by conceptually considering the spatial arrangement of the functionalities in MTV-MOFs as a sequence of information which, in principle, is not very much unlike the sequence of nucleotide units in DNA molecules. In the MOF, these sequences are propagating in 3D and therefore are more complicated. The exciting opportunity is whether it is possible to characterize these functional group sequences and if indeed they could be designed to code for specific properties. A recent observation is encouraging: MTV-MOF-5, [Zn₄O(BDC-X)₃, BDC = benzene-1,4-dicarboxylate, and X=-NO₂, -(OC₃H₅)₂, and -(OC₇H₇)₂], was directly synthesized and shown to have 4 times better separation of CO₂ from CO compared to its best same-link counterpart.²⁷ Furthermore, it was intriguing to note that the whole performed significantly better than the sum of the parts.

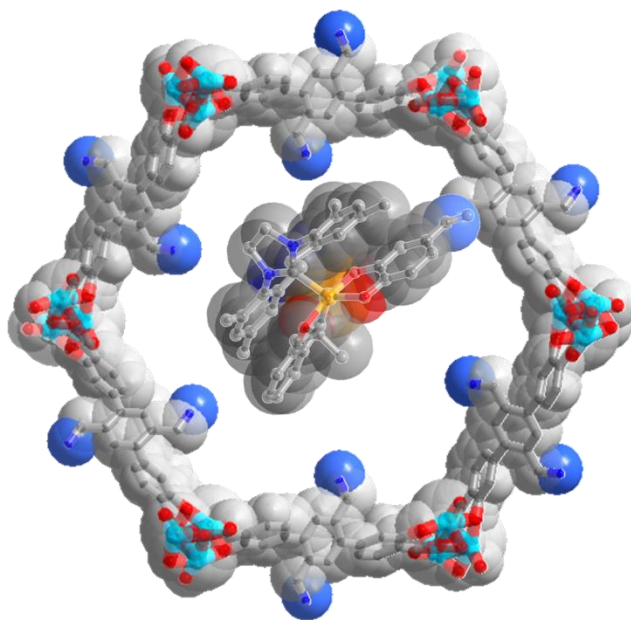


Figure 1.6. A conceptual example of precisely designed interiors of MOFs to carry out complex catalytic reactions. In this example, an organometallic complex is covalently linked in a MOF. A derivative of a ruthenium-based olefin metathesis catalyst, [1,3-bis-(2,4,6-trimethylphenyl)-2-imidazolidinylidene]catecholato(*o*-isopropoxyphenylmethylene) ruthenium,¹⁰⁴ is attached to a MOF (IRMOF-74-III) with 1D pore to produce a complex active site. Atom labelling scheme: Mg (light blue), C (grey), N (blue), O (red), Ru (orange). H atoms are omitted for clarity.

The question of characterizing the functional group sequences is a new one requiring development of physical techniques capable of deciphering them on the atomic level. However, a recent effort to determine the distribution of multiple functionalities in the MTV-MOF revealed that they are not always random. An indication of this was the observation that the ratio of the linkers used in the reaction is not the same as that actually incorporated into the product. This indicates biasing towards a specific linker or set of linkers. Indeed, it was shown by solid state NMR that mixed linkers are apportioned on the nanoscale throughout the crystal,^{105,106} Specifically, for the MTV-MOF-5 binary mixed linker systems: BDC-NO₂ and -(OC₇H₇)₂, BDC-NO₂ and -(CH₃)₂, and BDC-NH₂ and -(CH₃)₂, it was found that they are apportioned in an alternating, random and small clustering motif, respectively (Figure 1.7).¹⁰⁵

The MTV approach has also been effective in producing MOFs incorporating linkers into certain topologies not observed when only one kind of linker is used. In the case of MOF-177, [Zn₄O(BTB)₂], nitro group functionalized BTB (BTB-NO₂) linkers can be readily incorporated when mixed with BTB linkers, while the BTB-NO₂ linker itself, when used alone, does not form MOF-177.¹⁰⁷ In catalytic MOFs, the MTV concept has been used in the dilution of active sites, where ‘doping’ with an active linker into an otherwise inert framework has proved powerful in optimizing catalytic performance.¹⁰⁸

The MTV-MOF concept intellectually leads to further development of the compartmentalization of space within MOFs. Here, different compartments, which are linked and open to each other, can be functionalized differently so that they perform different functions; a likely scenario since in MTV-MOFs equivalent crystallographic positions can bear different functionalities. One can envision how this could produce multiple compartments spanning many

unit cells when the functionalities are apportioned in the crystal. We note that compartments of this kind are possibly intermingling and may very well be able to operate synergistically. This might be the reason for the unusual emergent properties observed for MTV-MOFs compared to the physical mixtures of same-linker MOFs.^{27,105}

The missing linker defects and their spatial arrangement in MOFs is another aspect of the MTV concept¹⁰⁹. It is common in zirconium MOFs especially UiO-66, $[\text{Zr}_6\text{O}_4(\text{OH})_4(\text{BDC})_6]$, that water or acetic acid instead of BDC is coordinating to the zirconium SBUs leading to defective frameworks with improved porosity.^{86,110,111} A more elaborate example involves the selective removal of half of the linkers and a quarter of the metal ions in $\text{Zn}_4\text{O}(\text{PyC})_3$ (PyC = 4-pyrazolecarboxylate) without losing the MOF crystallinity.¹¹² This process can be reversed with new metal ions and linkers to give new frameworks of the same topology, with preserved crystallinity and ordered distribution of linkers. Additionally, when functional mono-dentate molecules are incorporated, new functionalities arise without compromising the overall structural integrity and order.¹¹³ In addition to control of defects, a versatile aspect of this concept is the direct exchange of the linker and metal ions in MOFs. Here, a MOF is immersed in a solution containing different linkers or metal ions under mild condition to give a MOF that incorporates these components.^{49,114-117} This approach has enabled the incorporation of otherwise incompatible building units into MOFs and often affords MOFs of multivariate composition. In the case of UiO-66, Hf(IV) and Ti(IV) can be incorporated into the SBUs of a MOF by treating the crystals with the corresponding solution of the desired metal ion.¹¹⁴ All these mixed systems are intrinsically multivariate and subject to the same uncertainties associated with the question of spatial arrangement of functionality and metal atoms.

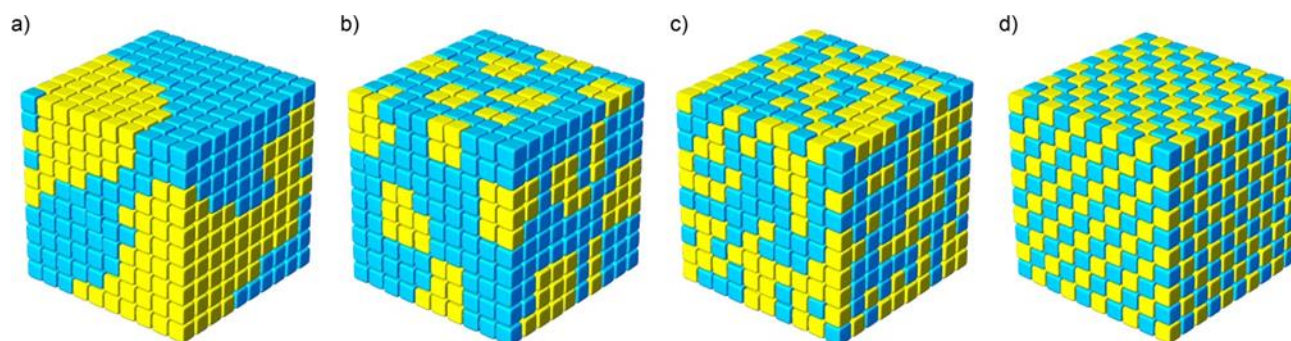


Figure 1.7 Scenarios of linker apportionment in MTV-MOF materials. (a) large clusters, (b) small clusters, (c) random, and (d) alternating.

Section 1.8 Reference

- (1) Li, H.; Eddaoudi, M.; Groy, T. L.; Yaghi, O. M. *J. Am. Chem. Soc.* **1998**, *120*, 8571-8572.
- (2) Chui, S. S.-Y.; Lo, S. M.-F.; Charmant, J. P. H.; Orpen, A. G.; Williams, I. D. *Science* **1999**, *283*, 1148-1150.
- (3) Li, H.; Eddaoudi, M.; O’Keeffe, M.; Yaghi, O. M. *Nature* **1999**, *402*, 276-279.
- (4) Côté, A. P.; Benin, A. I.; Ockwig, N. W.; O’Keeffe, M.; Yaghi, O. M. *Science* **2005**, *310*, 1166-1170.
- (5) Cohen, S. M. *Chem. Rev.* **2012**, *112*, 970-1000.
- (6) Evans, J. D.; Sumby, C. J.; Doonan, C. J. *Chem. Soc. Rev.* **2014**, *43*, 5933-5951.
- (7) Deria, P.; Mondloch, J. E.; Karagiari, O.; Bury, W.; Hupp, J. T.; Farha, O. K. *Chem. Soc. Rev.* **2014**, *43*, 5896-5912.
- (8) Yaghi, O. M.; O’Keeffe, M.; Ockwig, N. W.; Chae, H. K.; Eddaoudi, M.; Kim, J. *Nature* **2003**, *423*, 705-714.
- (9) Cook, T. R.; Zheng, Y.-R.; Stang, P. J. *Chem. Rev.* **2013**, *113*, 734-777.
- (10) Pauling, L. *The Nature of the Chemical Bond*, 2nd ed.; Cornell University Press: New York, **1940**; p. 7-10.
- (11) Woodward, R. B. *Pure Appl. Chem.* **1973**, *33*, 145-178.
- (12) Eschenmoser, A.; Wintner, C. E. *Science* **1977**, *196*, 1410-1420.
- (13) Atkins, P.; de Paula, J. *Physical Chemistry for the Life Sciences*, 2nd ed.; W. H. Freeman and Company: New York, **2011**; p. 435.
- (14) Rodgers, M. T.; Armentrout, P. B. *Mass Spectrom. Rev.* **2000**, *19*, 215-247.
- (15) Darwent, B. deB. *Bond Dissociation Energies in Simple Molecules*; National Bureau of Standards: Washington, DC, **1970**.
- (16) Jackson, K. T.; Reich, T. E.; El-Kaderi, H. M. *Chem. Commun.* **2012**, *48*, 8823-8825.
- (17) Kuhn, P.; Antonietti, M.; Thomas, A. *Angew. Chem. Int. Ed.* **2008**, *47*, 3450-3453.
- (18) Uribe-Romo, F. J.; Hunt, J. R.; Furukawa, H.; Klöck, C.; O’Keeffe, M.; Yaghi, O. M. *J. Am. Chem. Soc.* **2009**, *131*, 4570-4571.
- (19) Fang, Q.; Zhuang, Z.; Gu, S.; Kaspar, R. B.; Zheng, J.; Wang, J.; Qiu, S.; Yan, Y. *Nat. Commun.* **2014**, *5*, 4503.
- (20) Colombo, V.; Galli, S.; Choi, H. J.; Han, G. D.; Maspero, A.; Palmisano, G.; Masciocchi, N.; Long, J. R. *Chem. Sci.* **2011**, *2*, 1311-1319.
- (21) Park, K. S.; Ni, Z.; Côté, A. P.; Choi, J. Y.; Huang, R.; Uribe-Romo, F. J.; Chae, H. K.; O’Keeffe, M.; Yaghi, O. M. *Proc. Natl. Acad. Sci.* **2006**, *103*, 10186-10191.

- (22) Liu, Y.; Kravtsov, V. C.; Larsen, R.; Eddaoudi, M. *Chem. Commun.* **2006**, 1488-1490.
- (23) Hurd, J. A.; Vaidhyanathan, R.; Thangadurai, V.; Ratcliffe, C. I.; Moudrakovski, I. L.; Shimizu, G. K. H. *Nat. Chem.* **2009**, *1*, 705-710.
- (24) Abrahams, B. F.; Bond, A. M.; Le, T. H.; McCormick, L. J.; Nafady, A.; Robson, R.; Vo, N. *Chem. Commun.* **2012**, *48*, 11422-11424.
- (25) Lauher, J. W.; Fowler, F. W.; Goroff, N. S. *Acc. Chem. Res.* **2008**, *41*, 1215-1229.
- (26) Juillard, J. *Pure Appl. Chem.* **1977**, *49*, 885-892.
- (27) Deng, H.; Doonan, C. J.; Furukawa, H.; Ferreira, R. B.; Towne, J.; Knobler, C. B.; Wang, B.; Yaghi, O. M. *Science* **2010**, *327*, 846-850.
- (28) Li, L.; Sun, F.; Jia, J.; Borjigin, T.; Zhu, G. *CrystEngComm* **2013**, *15*, 4094-4098.
- (29) Stock, N.; Biswas, S. *Chem. Rev.* **2012**, *112*, 933-969.
- (30) Férey, G.; Drazniekes, C. M.; Serre, C.; Millange, F.; Dutour, J.; Surblé, S.; Margiolaki, I. *Science* **2005**, *309*, 2040-2042.
- (31) Jhung, S. H.; Lee, J. H.; Chang, J. S. *Bull. Korean Chem. Soc.* **2005**, *26*, 880-881.
- (32) Pichon, A.; Lazuen-Garay, A.; James, S. L. *CrystEngComm.* **2006**, *8*, 211-214.
- (33) Friščić, T. *J. Mater. Chem.* **2010**, *20*, 7599-7605.
- (34) Schaate, A.; Roy, P.; Godt, A.; Lippke, J.; Waltz, F.; Wiebcke, M.; Behrens, P. *Chem. Eur. J.* **2011**, *17*, 6643-6651.
- (35) Gándara, F.; Furukawa, H.; Lee, S.; Yaghi, O. M. *J. Am. Chem. Soc.* **2014**, *136*, 5271-5274.
- (36) Ren, J.; Musyoka, N. M.; Langmi, H. W.; Segakweng, T.; North, B. C.; Mathe, M.; Kang, X. *Int. J. Hydrogen Energy* **2014**, *39*, 12018-12023
- (37) Guo, H.; Zhu, Y.; Wang, S.; Su, S.; Zhou, L.; Zhang, H. *Chem. Mater.* **2012**, *24*, 444-450.
- (38) El-Kaderi, H. M.; Hunt, J. R.; Mendoza-Cortés, J. L.; Côté, A. P.; Taylor, R. E.; O'Keeffe, M.; Yaghi, O. M. *Science* **2007**, *316*, 268-272.
- (39) Dalapati, S.; Jin, S.; Gao, J.; Xu, Y.; Nagai, A.; Jiang, D. *J. Am. Chem. Soc.* **2013**, *135*, 17310-17313.
- (40) Uribe-Romo, F. J.; Doonan, C. J.; Furukawa, H.; Oisaki, K.; Yaghi, O. M. *J. Am. Chem. Soc.* **2011**, *133*, 11478-11481.
- (41) Nagai, A.; Chen, X.; Feng, X.; Ding, X.; Guo, Z.; Jiang, D. *Angew. Chem. Int. Ed.* **2013**, *52*, 3770-3774.
- (42) Deblase, C. R.; Silberstein, K. E.; Truong, T.-T.; Abruña, H. D.; Dichtel, W. R. *J. Am. Chem. Soc.* **2013**, *135*, 16821-16824.
- (43) Eddaoudi, M.; Kim, J.; Rosi, N.; Vodak, D.; Wachter, J.; O'Keeffe, M.; Yaghi, O. M. *Science* **2002**, *295*, 469-472.

- (44) Nelson, A. P.; Farha, O. K.; Mulfort, K. L.; Hupp, J. T. *J. Am. Chem. Soc.* **2008**, *131*, 458-460.
- (45) Farha, O. K.; Hupp, J. T. *Acc. Chem. Res.* **2010**, *43*, 1166-1175.
- (46) Furukawa, H.; Ko, N.; Go, Y. B.; Aratani, N.; Choi, S. B.; Choi, E.; Yazaydin, A. O.; Snurr, R. Q.; O’Keeffe, M.; Kim, J.; Yaghi, O. M. *Science* **2010**, *329*, 424-428.
- (47) Furukawa, H.; Go, Y. B.; Ko, N.; Park, Y. K.; Uribe-Romo, F. J.; Kim, J.; O’Keeffe, M.; Yaghi, O. M. *Inorg. Chem.* **2011**, *50*, 9147-9152.
- (48) Feng, D.; Liu, T.-F.; Su, J.; Bosch, M.; Wei, Z.; Wan, W.; Yuan, D.; Chen, Y.-P.; Wang, X.; Wang, K.; Lian, X.; Gu, Z.-Y.; Park, J.; Zou, X.; Zhou, H.-C. *Nat. Commun.* **2014**, *6*, 5979.
- (49) Li, T.; Kozlowski, M. T.; Doud, E. A.; Blakely, M. N.; Rosi, N. L. *J. Am. Chem. Soc.* **2013**, *135*, 11688-11691.
- (50) Farha, O. K.; Eryazici, I.; Jeong, N. C.; Hauser, B. G.; Wilmer, C. E.; Sarjeant, A. A.; Snurr, R. Q.; Nguyen, S. T.; Yazaydin, A. Ö.; Hupp, J. T. *J. Am. Chem. Soc.* **2014**, *134*, 15016-15021.
- (51) Deng, H.; Grunder, S.; Cordova, K. E.; Valente, C.; Furukawa, H.; Hmadeh, M.; Gándara, F.; Whalley, A. C.; Liu, Z.; Asahina, S.; Kazumori, H.; O’Keeffe, M.; Terasaki, O.; Stoddart, J. F.; Yaghi, O. M. *Science* **2012**, *336*, 1018-1023.
- (52) Klein, N.; Senkowska, I.; Gedrich, K.; Stoeck, U.; Henschel, A.; Mueller, U.; Kaskel, S. *Angew. Chem. Int. Ed.* **2009**, *48*, 9954-9957.
- (53) Koh, K.; Wong-Foy, A. G.; Matzger, A. J. *Angew. Chem. Int. Ed.* **2008**, *47*, 677-680.
- (54) Rowsell, J. L. C.; Spencer, E. C.; Eckert, J.; Howard, J. A. K.; Yaghi, O. M. *Science* **2005**, *309*, 1350-1354.
- (55) Carrington, E. J.; Vitórica-Yrezábal, I. J.; Brammer, L. *Acta Cryst.* **2014**, *B70*, 404-422.
- (56) Furukawa, H.; Gándara, F.; Zhang, Y.-B.; Jiang, J.; Queen, W. L.; Hudson, M. R.; Yaghi, O. M. *J. Am. Chem. Soc.* **2014**, *136*, 4369-4381.
- (57) Stallmach, F.; Gröger, S.; Künzel, V.; Kärger, J.; Yaghi, O. M.; Hesse, M.; Müller, U. *Angew. Chem. Int. Ed.* **2006**, *45*, 2123-2126.
- (58) Kong, X.; Scott, E.; Ding, W.; Mason, J. A.; Long, J. R.; Reimer, J. A. *J. Am. Chem. Soc.* **2012**, *134*, 14341-14344.
- (59) Lin, L.-C.; Kim, J.; Kong, X.; Scott, E.; McDonald, T. M.; Long, J. R.; Reimer, J. A.; Smit, B. *Angew. Chem. Int. Ed.* **2013**, *52*, 4410-4413.
- (60) McDonald, T. M.; Mason, J. A.; Kong, X.; Bloch, E. D.; Gygi, D.; Dani, A.; Crocellà, V.; Giordanino, F.; Odoh, S. O.; Drisdell, W. S.; Vlasisavljevich, B.; Dzubak, A.; Poloni, R.; Schnell, S. K.; Planas, N.; Lee, K.; Pascal, T.; Wan, L. F.; Prendergast, D.; Neaton, J. B.; Smit, B.; Kortright, J. B.; Gagliardi, L.; Bordiga, S.; Reimer, J. A.; Long, J. R. *Nature* **2015**, *519*, 303-308.
- (61) Cho, H. S.; Deng, H.; Miyasaka, K.; Dong, Z.; Cho, M.; Nelmark, A. V.; Kang, J. K.; Yaghi, O. M.; Terasaki, O. *Nature* **2015**, doi: 10.1038/nature15734.

- (62) Batten, S. R. *CrystEngComm* **2001**, *18*, 1-7.
- (63) Jiang, H.-L.; Makal, T. A.; Zhou, H.-C. *Coord. Chem. Rev.* **2013**, *257*, 2232-2249.
- (64) Chen, B.; Eddaoudi, M.; Reineke, T. M.; Kampf, J. W.; O’Keeffe, M.; Yaghi, O. M. *J. Am. Chem. Soc.* **2000**, *122*, 11559-11560.
- (65) Suh, M. P.; Park, H. J.; Prasad, T. K.; Lim, D.-W. *Chem Rev.* **2012**, *112*, 782-835.
- (66) He, Y.; Zhou, W.; Qian, G.; Chen, B. *Chem. Soc. Rev.* **2014**, *43*, 5657-5678.
- (67) Sumida, K.; Rogow, D. L.; Mason, J. A.; McDonald, T. M.; Bloch, E. D.; Herm, Z. R.; Bae, T.-H.; Long, J. R. *Chem. Rev.* **2012**, *112*, 724-781.
- (68) Decoste, J. B.; Peterson G. W. *Chem. Rev.* **2014**, *114*, 5695-5727.
- (69) Li, J.-R.; Sculley, J.; Zhou, H.-C. *Chem. Rev.* **2012**, *112*, 869-932.
- (70) Kreno, L. E.; Leong, K.; Farha, O. K.; Allendorf, M.; Van Duyne, R. P.; Hupp, J. T. *Chem. Rev.* **2011**, *112*, 1105-1125.
- (71) Gascon, J.; Corma, A.; Kapteijn, F.; Llabrés i Xamena, F. X. *ACS Catal.* **2014**, *4*, 361-378.
- (72) Liu, J.; Chen, L.; Cui, H.; Zhang, J.; Zhang, L.; Su, C.-Y. *Chem. Soc. Rev.* **2014**, *43*, 6011-6061.
- (73) Lee, J. Y.; Farha, O. K.; Roberts, J.; Scheidt, K. A.; Nguyen, S. T.; Hupp, J. T. *Chem. Soc. Rev.* **2009**, *38*, 1450-1459.
- (74) Burrows, A. D.; Frost, C. G.; Mahon, M. F.; Richardson, C. *Chem. Commun.* **2009**, 4218-4220.
- (75) Morris, W.; Doonan, C. J.; Furukawa, H.; Banerjee, R.; Yaghi, O. M. *J. Am. Chem. Soc.* **2008**, *130*, 12626-12627.
- (76) Fracaroli, A. M.; Furukawa, H.; Suzuki, M.; Dodd, M.; Okajima, S.; Gándara, F.; Reimer, J. A.; Yaghi, O. M. *J. Am. Chem. Soc.* **2014**, *136*, 8863-8866.
- (77) Mir, M. H.; Koh, L. L.; Tan, G. K.; Vittal, J. J. *Angew. Chem. Int. Ed.* **2010**, *49*, 390-393.
- (78) Kim, M.; Garibay, S. J.; Cohen, S. M. *Inorg. Chem.* **2011**, *50*, 729-731.
- (79) Bloch, E. D.; Britt, D.; Lee, C.; Doonan, C. J.; Uribe-Romo, F. J.; Furukawa, H.; Long, J. R.; Yaghi, O. M. *J. Am. Chem. Soc.* **2010**, *132*, 14382-14384.
- (80) Chen, C.; Allen, C. A.; Cohen, S. M. *Inorg. Chem.* **2011**, *50*, 10534-10536.
- (81) Goto, Y.; Sato, H.; Shinkai, S.; Sada, K. *J. Am. Chem. Soc.* **2008**, *130*, 14354-14355.
- (82) Dugan, E.; Wang, Z.; Okamura, M.; Medina, A.; Cohen, S. M. *Chem. Commun.* **2008**, 3366-3368.
- (83) Nguyen, J. G.; Cohen, S. M. *J. Am. Chem. Soc.* **2010**, *132*, 4560-4561.
- (84) Wang, Z.; Cohen, S. M. *Chem. Soc. Rev.* **2009**, *38*, 1315-1329.

- (85) Tanabe, K. K.; Cohen, S. M. *Chem. Soc. Rev.* **2011**, *40*, 498-519.
- (86) Cavka, J. H.; Jakobsen, S.; Olsbye, U.; Guillou, N.; Lamberti, C.; Bordiga, S.; Lillerud, K. P. *J. Am. Chem. Soc.* **2008**, *130*, 13850-13851.
- (87) Carson, F.; Agrawal, S.; Gustafsson, M.; Bartoszewicz, A.; Moraga, F.; Zou, X.; Martín-Matute, B. *Chem. Eur. J.* **2012**, *18*, 15337-15344.
- (88) Sun, D.; Gao, Y.; Fu, J.; Zeng, X.; Chen, Z.; Li, Z. *Chem. Commun.* **2015**, *51*, 2645-2648.
- (89) Morris, W.; Voloskiy, B.; Demir, S.; Gándara, F.; McGrier, P. L.; Furukawa, H.; Cascio, D.; Stoddart, J. F.; Yaghi, O. M. *Inorg. Chem.* **2012**, *51*, 6443-6445.
- (90) Zhao, Y.; Kornienko, N.; Liu, Z.; Zhu, C.; Asahina, S.; Kuo, T.-R.; Bao, W.; Xie, C.; Hexemer, A.; Terasaki, O.; Yang, P.; Yaghi, O. M. *J. Am. Chem. Soc.* **2015**, *137*, 2199-2202.
- (91) Fateeva, A.; Chater, P. A.; Ireland, C. P.; Tahir, A. A.; Khimyak, Y. Z.; Wiper, P. V.; Darwent, J. R.; Rosseinsky, M. J. *Angew. Chem. Int. Ed.* **2012**, *51*, 7440-7444.
- (92) Hwang, Y. K.; Hong, D.-Y.; Chang, J.-S.; Jhung, S. H.; Seo, Y.-K.; Kim, J.; Vimont, A.; Daturi, M.; Serre, C.; Férey, G. *Angew. Chem. Int. Ed.* **2008**, *47*, 4144-4148.
- (93) Jiang, J.; Gándara, F.; Zhang, Y.-B.; Na, K.; Yaghi, O. M.; Klemperer, W. G. *J. Am. Chem. Soc.* **2014**, *136*, 12844-12847.
- (94) Demessence, A.; D'Alessandro, D. M.; Foo, M. L.; Long, J. R. *J. Am. Chem. Soc.* **2009**, *131*, 8784-8786.
- (95) Garibay, S. J.; Wang, Z.; Tanabe, K. K.; Cohen, S. M. *Inorg. Chem.* **2009**, *48*, 7341-7349.
- (96) Doonan, C. J.; Morris, W.; Furukawa, H.; Yaghi, O. M. *J. Am. Chem. Soc.* **2009**, *131*, 9492-9493.
- (97) Garibay, S. J.; Wang, Z.; Cohen, S. M. *Inorg. Chem.* **2010**, *49*, 8086-8091.
- (98) Wang, Z.; Liu, J.; Arslan, H. K.; Grosjean, S.; Hagendorf, T.; Gliemann, H.; Bräse, S.; Wöll, C. *Langmuir* **2013**, *29*, 15958-15964.
- (99) Tuci, G.; Rossin, A.; Xu, X.; Ranocchiaro, M.; van Bokhoven, J. A.; Luconi, L.; Manet, I.; Melucci, M.; Giambastiani, G. *Chem. Mater.* **2013**, *25*, 2297-2308.
- (100) Canivet, J.; Aguado, S.; Bergeret, G.; Farrusseng, D. *Chem. Commun.* **2011**, *47*, 11650-11652.
- (101) Manna, K.; Zhang, T.; Greene, F. X.; Lin, W. *J. Am. Chem. Soc.* **2015**, *137*, 2665-2673.
- (102) Yang, D.; Odoh, S. O.; Wang, T. C.; Farha, O. K.; Hupp, J. T.; Cramer, C. J.; Gagliardi, L.; Gates, B. C. *J. Am. Chem. Soc.* **2015**, *137*, 7391-7396.
- (103) The reference of the PSMs in figure 5 are (start from the top PSM, going clockwise) 74-81, 2, 81-83.
- (104) Khan, R. K. M.; Torker, S.; Hoveyda, A. H. *J. Am. Chem. Soc.* **2014**, *136*, 14337-14340.

- (105) Kong, X.; Deng, H.; Yan, F.; Kim, J.; Swisher, J. A.; Smit, B.; Yaghi, O. M.; Reimer, J. A. *Science* **2013**, *341*, 882-885.
- (106) Baias, M.; Lesage, A.; Aguado, S.; Canivet, J.; Moizan-Basle, V.; Audebrand, N.; Farrusseng, D.; Emsley, L. *Angew. Chem. Int. Ed.* **2015**, *54*, 5971-5976.
- (107) Zhang, Y.-B.; Furukawa, H.; Ko, N.; Nie, W.; Park, H. J.; Okajima, S.; Cordova, K. E.; Deng, H.; Kim, J.; Yaghi, O. M. *J. Am. Chem. Soc.* **2015**, *137*, 2641-2650.
- (108) Manna, K.; Zhang, T.; Lin, W. *J. Am. Chem. Soc.* **2014**, *136*, 6566-6569.
- (109) Fang, Z.; Bueken, B.; De Vos, D. E.; Fischer, R. A. *Angew. Chem. Int. Ed.* **2015**, *54*, 7234-7254.
- (110) Trickett, C. A.; Gagnon, K. J.; Lee, S.; Gándara, F.; Bürgi, H.-B.; Yaghi, O. M. *Angew. Chem. Int. Ed.* **2015**, *54*, 11162-11167.
- (111) Wu, H.; Chua, Y. S.; Krungleviciute, V.; Tyagi, M.; Chen, P.; Yildirim, T.; Zhou, W. *J. Am. Chem. Soc.* **2013**, *135*, 10525-10532.
- (112) Tu, B.; Pang, Q.; Wu, D.; Song, Y.; Weng, L.; Li, Q. *J. Am. Chem. Soc.* **2014**, *136*, 14465-14471.
- (113) Fang, Z.; Dürholt, J. P.; Kauer, M.; Zhang, W.; Lochenie, C.; Jee, B.; Albada, B.; Metzler-Nolte, N.; Pöppel, A.; Weber, B.; Muhler, M.; Wang, Y.; Schmid, R.; Fischer, R. A. *J. Am. Chem. Soc.* **2014**, *136*, 9627-9636.
- (114) Kim, M.; Cahill, J. F.; Fei, H.; Prather, K. A.; Cohen, S. M. *J. Am. Chem. Soc.* **2012**, *134*, 18082-18088.
- (115) Brozek, C. K.; Michaelis, V. K.; Ong, T.-C.; Bellarosa, L.; López, N.; Griffin, R. G.; Dincă, M. *ACS Cent. Sci.* **2015**, *1*, 252-260.
- (116) Brozek, C. K.; Dincă, M. *J. Am. Chem. Soc.* **2013**, *135*, 12886-12891.
- (117) Brozek, C. K.; Dincă, M. *Chem. Soc. Rev.* **2014**, *43*, 5456-5467.
- (118) Pan, Y.; Heryadi, D.; Zhou, F.; Zhao, L.; Lestari, G.; Su, H.; Lai, Z. *CrystEngComm* **2011**, *13*, 6937-6940.
- (119) Valtchev, V.; Tosheva, L. *Chem. Rev.* **2013**, *113*, 6734-6760.
- (120) He, L.; Liu, Y.; Liu, J.; Xiong, Y.; Zheng, J.; Liu, Y.; Tang, Z. *Angew. Chem. Int. Ed.* **2013**, *52*, 3741-3745.
- (121) Khaletskaya, K.; Reboul, J.; Meilikhov, M.; Nakahama, M.; Diring, S.; Tsujimoto, M.; Isoda, S.; Kim, F.; Kamei, K.-i.; Fischer, R. A.; Kitagawa, S.; Furukawa, S. *J. Am. Chem. Soc.* **2013**, *135*, 10998-11005.
- (122) Na, K.; Choi, K. M.; Yaghi, O. M.; Somorjai, G. A. *Nano Lett.* **2014**, *14*, 5979-5983.
- (123) Zhao, M.; Deng, K.; He, L.; Liu, Y.; Li, G.; Zhao, H.; Tang, Z. *J. Am. Chem. Soc.* **2014**, *136*, 1738-1741.

- (124) Hu, P.; Zhuang, J.; Chou, L.-Y.; Lee, H. K.; Ling, X. Y.; Chuang, Y.-C.; Tsung, C.-K. *J. Am. Chem. Soc.* **2014**, *136*, 10561-10564.
- (125) Choi, K. M.; Na, K.; Somorjai, G. A.; Yaghi, O. M. *J. Am. Chem. Soc.* **2015**, *137*, 7810-7816.
- (126) Lu, G.; Li, S.; Guo, Z.; Farha, O. K.; Hauser, B. G.; Qi, X.; Wang, Y.; Wang, X.; Han, S.; Liu, X.; DuChene, J. S.; Zhang, H.; Zhang, Q.; Chen, X.; Ma, J.; Loo, S. C. J.; Wei, W. D.; Yang, Y.; Hupp, J. T.; Huo, F. *Nat. Chem.* **2012**, *4*, 310-316.
- (127) Huang, Y.; Zhang, Y.; Chen, X.; Wu, D.; Yi, Z.; Cao, R. *Chem. Commun.* **2014**, *50*, 10115-10117.
- (128) Chen, L.; Chen, H.; Luque, R.; Li, Y. *Chem. Sci.* **2014**, *5*, 3708-3714.
- (129) Guo, Z.; Xiao, C.; Maligal-Ganesh, R. V.; Zhou, L.; Goh, T. W.; Li, X.; Tesfagaber, D.; Thiel, A.; Huang, W. *ACS Catal.* **2014**, *4*, 1340-1348.
- (130) Huang, Y.; Lin, Z.; Cao, R. *Chem.-Eur. J.* **2011**, *17*, 12706-12712.
- (131) Jiang, H.-L.; Liu, B.; Akita, T.; Haruta, M.; Sakurai, H.; Xu, Q. *J. Am. Chem. Soc.* **2009**, *131*, 11302-11303.
- (132) Ke, F.; Zhu, J.; Qiu, L.-G.; Jiang, X. *Chem. Commun.* **2013**, *49*, 1267-1269.
- (133) Li, X.; Guo, Z.; Xiao, C.; Goh, T. W.; Tesfagaber, D.; Huang, W. *ACS Catal.* **2014**, *4*, 3490-3497.
- (134) Zhang, W.; Lu, G.; Cui, C.; Liu, Y.; Li, S.; Yan, W.; Xing, C.; Chi, Y. R.; Yang, Y.; Huo, F. *Adv. Mater.* **2014**, *26*, 4056-4060.
- (135) Kuo, C.-H.; Tang, Y.; Chou, L.-Y.; Sneed, B. T.; Brodsky, C. N.; Zhao, Z.; Tsung, C.-K. *J. Am. Chem. Soc.* **2012**, *134*, 14345-14348.
- (136) Deng, H.; Olson, M. A.; Stoddart, J. F.; Yaghi, O. M. *Nat. Chem.* **2010**, *2*, 439-443.
- (137) Li, Q.; Zhang, W.; Miljanić, O. Š.; Sue, C.-H.; Zhao, Y.-L.; Liu, L.; Knobler, C. B.; Stoddart, J. F.; Yaghi, O. M. *Science* **2009**, *325*, 855-859.
- (138) Park, S. S.; Hontz, E. R.; Sun, L.; Hendon, C. H.; Walsh, A.; Van Voorhis, T.; Dincă, M. *J. Am. Chem. Soc.* **2015**, *137*, 1774-1777.
- (139) Campbell, M. G.; Sheberla, D.; Liu, S. F.; Swager, T. M.; Dincă, M. *Angew. Chem. Int. Ed.* **2015**, *54*, 4349-4352.
- (140) Kung, C.-W.; Chang, T.-H.; Chou, L.-Y.; Hupp, J. T.; Farha, O. K.; Ho, K.-C. *Chem. Commun.* **2015**, *51*, 2414-2417.
- (141) Duhović, S.; Dincă, M. *Chem. Mater.* **2015**, *27*, 5487-5490.
- (142) Lin, S.; Diercks, C. S.; Zhang, Y.-B.; Kornienko, N.; Nichols, E. M.; Zhao, Y.; Paris, A. R.; Kim, D.; Yang, P.; Yaghi, O. M.; Chang, C. J. *Science* **2015**, *349*, 1208-1213.

(143) Choi, K. M.; Jeong, H. M.; Park, J. H.; Zhang, Y.-B.; Kang, J. K.; Yaghi, O. M. *ACS Nano* **2014**, *8*, 7451-7457.

(144) Jahan, M.; Bao, Q.; Loh, K. P. *J. Am. Chem. Soc.* **2012**, *134*, 6707-6713.

Chapter 2. Mesoscopic Constructs of Metal-Organic Frameworks on Silver Nanocrystals

Section 2.1 Introduction

Inorganic nanocrystals are important because they occupy a size regime intermediate between small molecules and extended structures. Their chemistry has been largely explored through surface functionalization. The fundamental problem is that it is difficult to control the spatial arrangement and order of the functional units and therefore the chemistry occurring at the interface between the inorganic nanocrystal and an incoming substrate. We believe that this ‘functionalization problem’ could be overcome by using metal-organic frameworks (MOFs) as well-defined units for which the spatial arrangement of functional organic and inorganic units, porosity, density and thickness can be precisely controlled. Addressing this problem requires a new synthetic approach to overcome four challenges: (a) a pristine interface between inorganic nanocrystals and MOFs that is free of surfactants and other surface ligands to take advantage of synergistic effects at the interface, (b) well-ordered and precisely oriented MOF enclosures around the inorganic nanocrystals to impart high degree of spatial control over the desired functional groups, (c) sufficiently thin MOF enclosures for facile diffusion and high resolution chemical mapping, and (d) bridging multiple length scales by combining the MOF atomically defined scale with the nano dimension for plasmonic structures, thus realizing new chemical and physical functions. In this way, it would be possible to construct mesoscopic assemblies where the MOF and the plasmonic nanocrystals are linked across multiple length scales yet operate differently and synergistically. (Reproduced with permission from *J. Am. Chem. Soc.* **2015**, 137, 2199. Copyright 2015 American Chemical Society.)

Although efforts to grow MOFs on inorganic nanocrystals have been made, a general method addressing all four challenges has not emerged.¹⁻¹⁵ In this work, a general method has been developed to overcome these four challenges using atomic layer deposition (ALD) technique where a thin metal oxide film is deposited onto plasmonic silver nanocrystals and used as a metal ion source to nucleate the desired MOF when the appropriate organic linker is added (Scheme 1). We show that ALD allows control of MOF thickness by controlling the metal oxide thickness, while the slow release of metal ions from the metal oxide layer results in control of crystallinity of MOF and ultimately its orientation on the silver nanocrystals. The MOF crystallinity, orientation, and the pristine interface thus produced enabled metalation and linker variation chemistry to be carried out on the MOF-silver nanocrystal mesoscopic construct. Integration of MOF onto nanocrystal surfaces further enables the direct probing of such chemistry by surface enhanced Raman spectroscopy (SERS) using the plasmonic silver nanocrystal substrates. Specifically, we show that the course of metalation in a porphyrin based MOF can be tracked and, in addition, different chemical signatures within MOF can be imaged at high spatial resolution down to a single nanoparticle level.

On a fundamental level, this system is an illustrative example of how two materials of self-similar structures can be combined into a mesoscopic ensemble of heterogeneous construction yet endowed with precisely defined chemical, spatial and metric characteristics. This coupled to the demonstrated ability to make mesoscopic constructs of these MOF-inorganic nanocrystals

provides an unparalleled opportunity for tracking, probing and mapping of passing molecules; an aspect that is expected to be a boon for catalytic chemical conversions, sensing and imaging applications.

Our strategy to overcome the functionalization problem involves making silver nanoparticle-MOF constructs (O_h -nano-Ag@MOF) in which silver nanoparticles are wrapped by MOF enclosures. Silver octahedra were synthesized by the polyol method: silver nitrate salt is reduced by a pentanediol solvent and polyvinylpyrrolidone (PVP) employed as a surfactant.¹⁶ Silver nanocrystals are selected as a model plasmonic metal nanostructure as they have intense local surface plasmon resonances in the visible range and have been extensively studied as SERS substrates.^{17,18} The chosen MOF is $\text{Al}_2(\text{OH})_2(\text{TCPP})$ [H_4TCPP : 4,4',4'',4'''-(porphyrin-5,10,15,20-tetrayl) tetrabenzoic acid], which consists of chains of corner-sharing aluminum octahedra running along the b -axis and connected by the TCPP units through the carboxylate groups (Fig. 1).¹⁹ This MOF was initially synthesized in bulk by reacting H_4TCPP with AlCl_3 in water at 180°C to give large, microcrystalline powder.

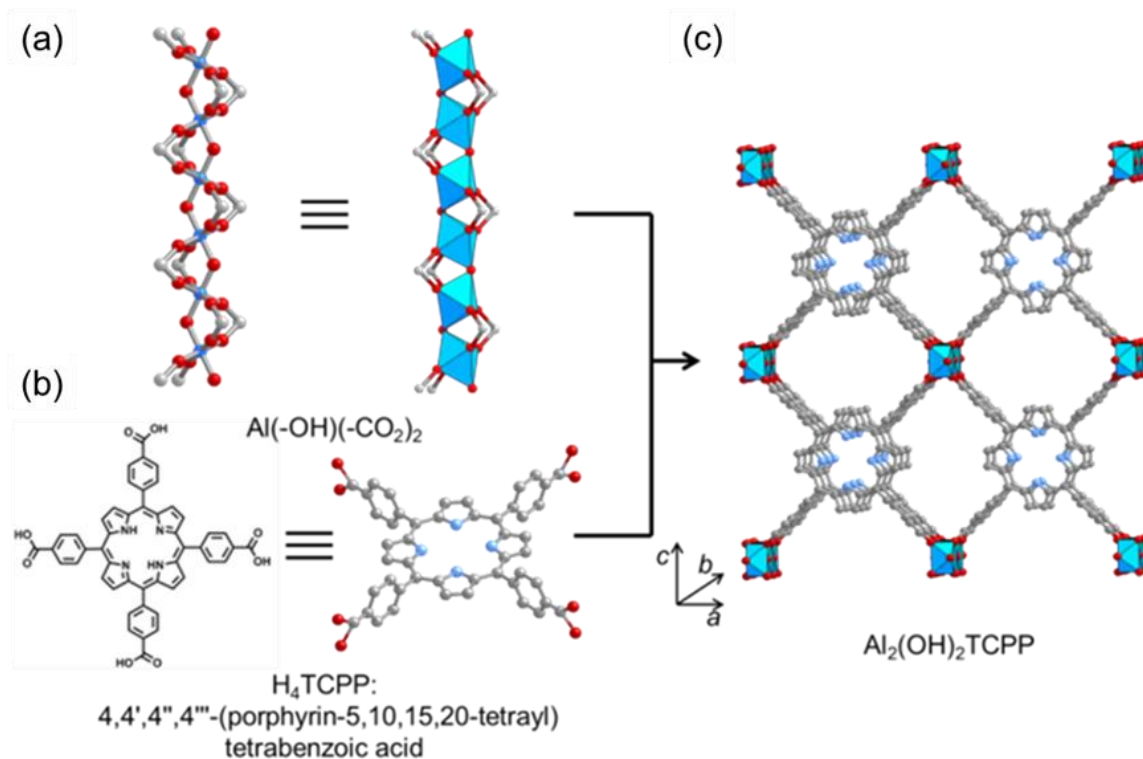


Figure 2.1. The structure of $\text{Al}_2(\text{OH})_2\text{TCPP}$ MOF. Construction of $\text{Al}_2(\text{OH})_2\text{TCPP}$ MOF from (A) rod-shaped aluminum oxide units linked by (B) porphyrin units (H_4TCPP) to give a three-dimensional MOF (C) having $0.11 \times 0.60 \text{ nm}^2$ opening along the b -axis. Al, blue octahedral polyhedra and blue spheres in (A); N, blue spheres; O, red spheres; C, gray spheres. Hydrogen atoms are omitted for clarity.

Section 2.2 Experimental Section

Section 2.2.1 Methods and Materials

N,N-Dimethylformamide (DMF) (99.8%), dimethyl sulfoxide (DMSO) (99.5%), anhydrous acetonitrile, trimethyloxonium tetrafluoroborate, hexadecyltrimethylammonium bromide (CTAB) (98%) and cobalt(II) acetate tetrahydrate were purchased from Sigma Aldrich. Aluminum chloride hexahydrate (99.9%) was purchased from Fluka. Ethanol is purchased from Koptec. 4,4',4'',4'''-(porphyrin-5,10,15,20-tetrayl)tetrabenzic acid (H₄TCP) was purchased from TCI. 2-Methylimidazole (99%) and biphenyl-4,4'-dicarboxylic acid (97%) were purchased from Aldrich. Trimethylaluminum, trimethylindium, and diethylzinc were purchased from Strem chemicals. Hydrochloric acid and anhydrous DMF were purchased from EMD Millipore. Sodium hydroxide and methanol were purchased from Fischer Chemical.

Attenuated total reflectance (ATR) FTIR spectra of neat samples were performed on a Bruker ALPHA Platinum ATR-FTIR Spectrometer equipped with a single reflection diamond ATR module. High resolution electrospray ionization mass (HR-ESI) was acquired on an Finnigan LTQ FT (Thermo Electron Corporation) instrument, using positive mode and by direct injection of methanol solutions of the samples using a syringe pump. Powder x-ray diffraction (PXRD) patterns were recorded using a Rigaku Miniflex 600 diffractometer (Bragg-Brentano geometry, Cu K α radiation, $\lambda = 1.54056 \text{ \AA}$) and a Bruker D8 Advance diffractometer (K α radiation, $\lambda = 1.54056 \text{ \AA}$). The optical absorption spectra were recorded using an UV-Vis-NIR scanning spectrophotometer equipped with an integration sphere (Shimadzu UV-3101PC). SEM images were recorded on a Zeiss Gemini Ultra-55 Analytical scanning electron microscope with accelerating voltage of 5 kV. The low voltage SEM images were obtained using a JEOL JSM-7800F prime field emission SEM with an accelerating voltage of 5.3 kV, a specimen bias of -5 kV, and a landing energy of 300 eV. The working distance is 2 mm.

Raman spectroscopic measurements were performed on a Horiba Labram JY HR 800 with an Olympus SMPLN 100X objective. A 532 nm laser with an output power of 150 mW was used in all measurements. A D4 neutral density filter is placed in the laser path to decrease the intensity of the laser by a factor of 10^4 to minimize damage to the samples.

For transmission electron microscopy (TEM), the specimens were prepared by scraping the samples wafers and directly dispersed the powders on to the TEM grid. A JEM-2010F equipped with a CEOS post-specimen spherical aberration corrector (*C*_s corrector) was operated at 120 kV for high-resolution transmission electron microscopy (HRTEM) imaging. The electron beam damage to the specimen was minimized as much as possible (in this study, the beam density during the observations was measured to be from 50 to 130 electrons/(nm²·s)). Sequences of images (up to 20 frames) were recorded, with a 1 second exposure time for each frame. After drift correction, some frames were superimposed to increase the signal-to-noise (S/N) ratio for display. Some of the TEM studies are also performed on a Hitachi H-7650 TEM operating at 120 kV. Energy dispersive x-ray spectroscopy (EDS) mapping is performed on a FEI TitanX Microscope operated in STEM mode with acceleration voltage of 120 kV and 2 minutes acquisition time was used for EDS mapping.

The GIWAXS data was obtained using Pilatus 2M (Dectris) instrument on beamline 7.3.3 at the Advanced Light Source (ALS), Lawrence Berkeley National Laboratory ($\lambda = 1.24 \text{ \AA}$). GIWAXS measurements were taken at incident angles of 0.12° . The sample-detector distance and beam center were calibrated using silver behenate. 1-D scattering profiles were reduced from the 2-d data using the Nika package for IGOR Pro (Wavemetrics) (26, 27). The 1-D plot shown in this material are plotted from GIWAXS data converted to 2 theta values assuming $\lambda = 1.54 \text{ \AA}$.

Section 2.2.2 Synthesis of $\text{Al}_2(\text{OH})_2(\text{TCPP})$ MOFs and O_h -nano-Ag@MOF Mesoscopic Constructs

Synthesis of $\text{Al}_2(\text{OH})_2(\text{TCPP})$ MOFs. These MOFs are synthesized using a hydrothermal method according to previous literature reports.¹⁹ H_4TCPP or $\text{H}_4\text{TCPP-Co}$ (70 mg) and aluminum chloride hexahydrate (150 mg) are dispersed in 15 mL of H_2O by sonication. The mixture is next heated to 160°C for 40 min under microwave irradiation and filtered. The solid is washed six times with DMF and six times with acetone, then heated to 100°C under vacuum to remove remaining solvent.

Removal of PVP on Silver Nanocrystals. The silver nanocrystals were dispersed in ethanol and drop cast on 1 cm^2 silicon substrate. Next, in oxygen free glove box the substrate was soaked in 1 mL of a 40 mg/mL trimethyloxonium tetrafluoroborate anhydrous acetonitrile solution for 20 min.²⁰ After this, 1 mL of DMF was added to the solution and the substrate kept immersed for another 20 min. The substrate was then washed with DMF and ethanol and air dried.

Atomic Layered Deposition. Deposition of Al_2O_3 thin films was performed in a customized thermal ALD reactor. The precursors used for Al_2O_3 deposition were trimethylaluminum and water. The aluminum precursor was held in a customized vessel that allowed for pulsed doses using nitrogen as a delivery gas through the vessel, which was maintained at room temperature. The aluminum and water sources were maintained at room temperature. The substrate temperature for Al_2O_3 deposition was 60°C . Typical pulse times for the alumina precursor and water were 1.5 and 1.0 s, respectively. Nitrogen was used as a carrier and purge gas in both processes at a flow rate of 10 standard cubic centimeters per minute (sccm).

$\text{Al}_2(\text{OH})_2(\text{TCPP})$ MOF Nucleation on Silver Nanocrystals. The conversion of the alumina into MOF is performed in CEM Discover-SP W/Activent microwave reactor. The substrate coated with alumina is put into 10 mL microwave vessel. 5 mg (6.32 mmol) of the H_4TCPP is dissolved in 1.5 mL DMF and 0.5 mL H_2O . This solution is added to the vessel, which is then heated to 140°C for 10 min. After the reaction, the substrate is washed with DMF and ethanol extensively and air dried. For metallated and multivariate MOF enclosure, corresponding linker or linker combination

Post-synthetic Metalation of $\text{Al}_2(\text{OH})_2(\text{TCPP})$ Enclosure on Silver Nanocrystals. The metalation of $\text{Al}_2(\text{OH})_2(\text{TCPP})$ MOF is carried out under microwave irradiation. 2 mL of 10 mg/mL methanol solution of cobalt acetate is added to a 10 mL glass microwave vessel and purged with nitrogen. The substrate with O_h -nano-Ag@MOF is soaked in the solution and heated to 100°C for desired time.

Section 2.3 Results and Discussion

Section 2.3.1 Fabrication of O_h -nano-Ag@MOF Mesoscopic Constructs

With the eventual goal of creating thin films of this MOF on the silver surface, we chose to use ALD thin films as a localized metal precursor source. The fabrication procedure of the O_h -nano-Ag@MOF begins with the deposition of Al_2O_3 films on the silver nanocrystals as the aluminum source for the MOF synthesis. The silver nanocrystal is drop cast on a silicon substrate for conformal, thickness-controlled alumina deposition at a deposition rate of 0.1 nm/cycle. On silver nanocrystals, the ALD is carried out at 60°C to prevent the silver nanocrystals from melting. The

ALD growth rate was in this study calibrated by TEM measurements and was determined to be 0.1 nm/cycle, using silver nanocrystals coated with 30 cycles alumina coating. A coating of 150 cycles was also measured and gave the same growth rate. Using this calibration, we estimated the thickness of the ALD alumina on FTO and carbon disk substrates. The ALD of ZnO and In₂O₃ are calibrated using a similar method and are determined to be 0.15 nm/cycle and 0.05 nm/cycle, respectively.

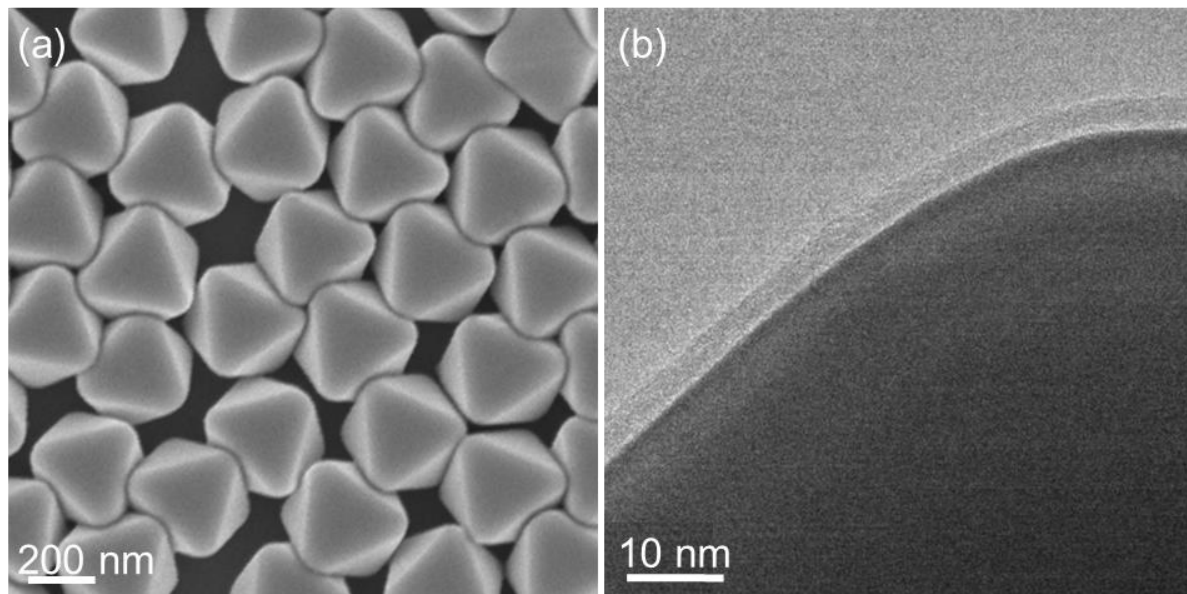


Figure 2.2. SEM images of silver nanocrystals after 30 cycles ALD (a). The growth rate of Al₂O₃ was calibrated by measuring its thickness on silver nanocrystals by TEM (b).

The alumina coated silver nanocrystals are converted to MOF by reacting with the TCPP linker. However, the original hydrothermal condition used to synthesize this MOF would not be appropriate as the high temperature will melt the silver nanocrystals and the TCPP linker is not soluble enough in water to sufficiently react with alumina. Considering this, the reaction temperature was reduced to 140°C, and *N,N*-dimethylformamide (DMF) water mixed solvent is used. The conversion of alumina to MOF was carried out in a sealed glass tube in a microwave reactor using, in the initial runs, 20 nm thick layers of alumina. Unfortunately, an interfacial 10 nm thick alumina layer between the MOF and the silver was observed instead of the desired pristine interface. This lead us to reduce the alumina layer thickness to below 3 nm and found it to be sufficient to eliminate the interfacial alumina layer while enabling the fabrication of conformal and thin MOF enclosures.

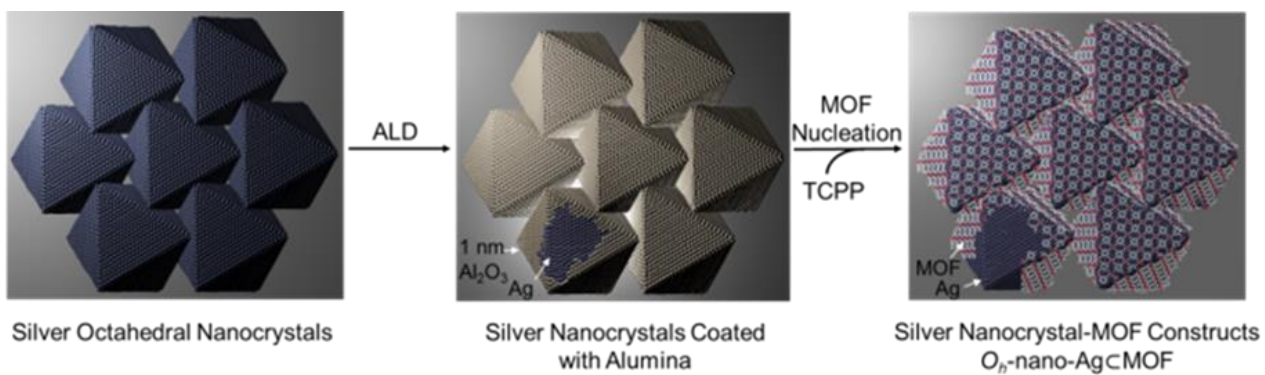


Figure 2.3. The fabrication of MOF enclosure on silver nanocrystals.

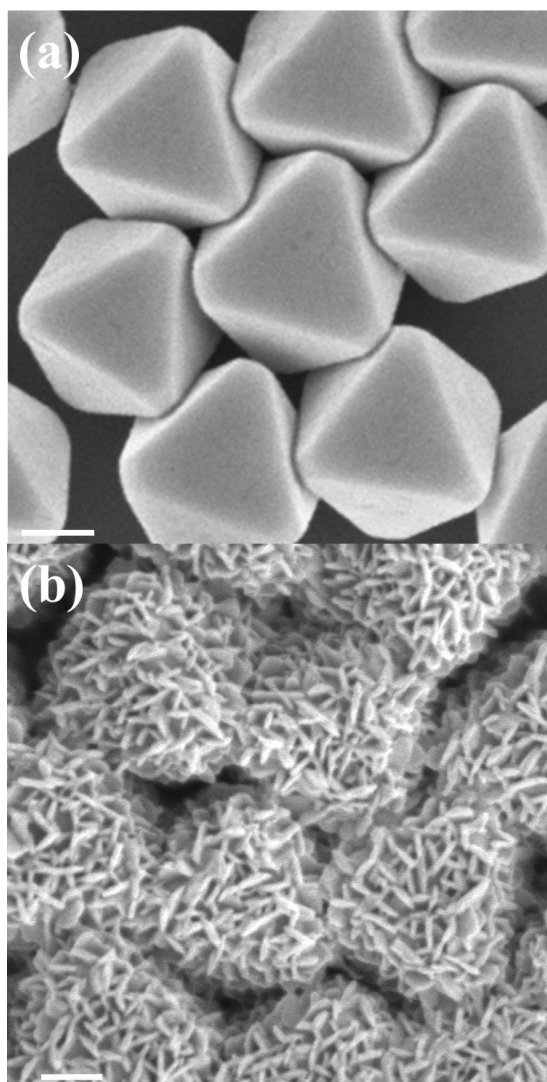


Figure 2.4. The SEM and TEM images of the O_h -nano-Ag@MOF particles. Octahedral silver nanocrystals (a) are subjected to ALD deposition of alumina followed by addition of TCPP linkers to make MOF enclosed silver nanocrystals, O_h -nano-Ag@MOF, (b).

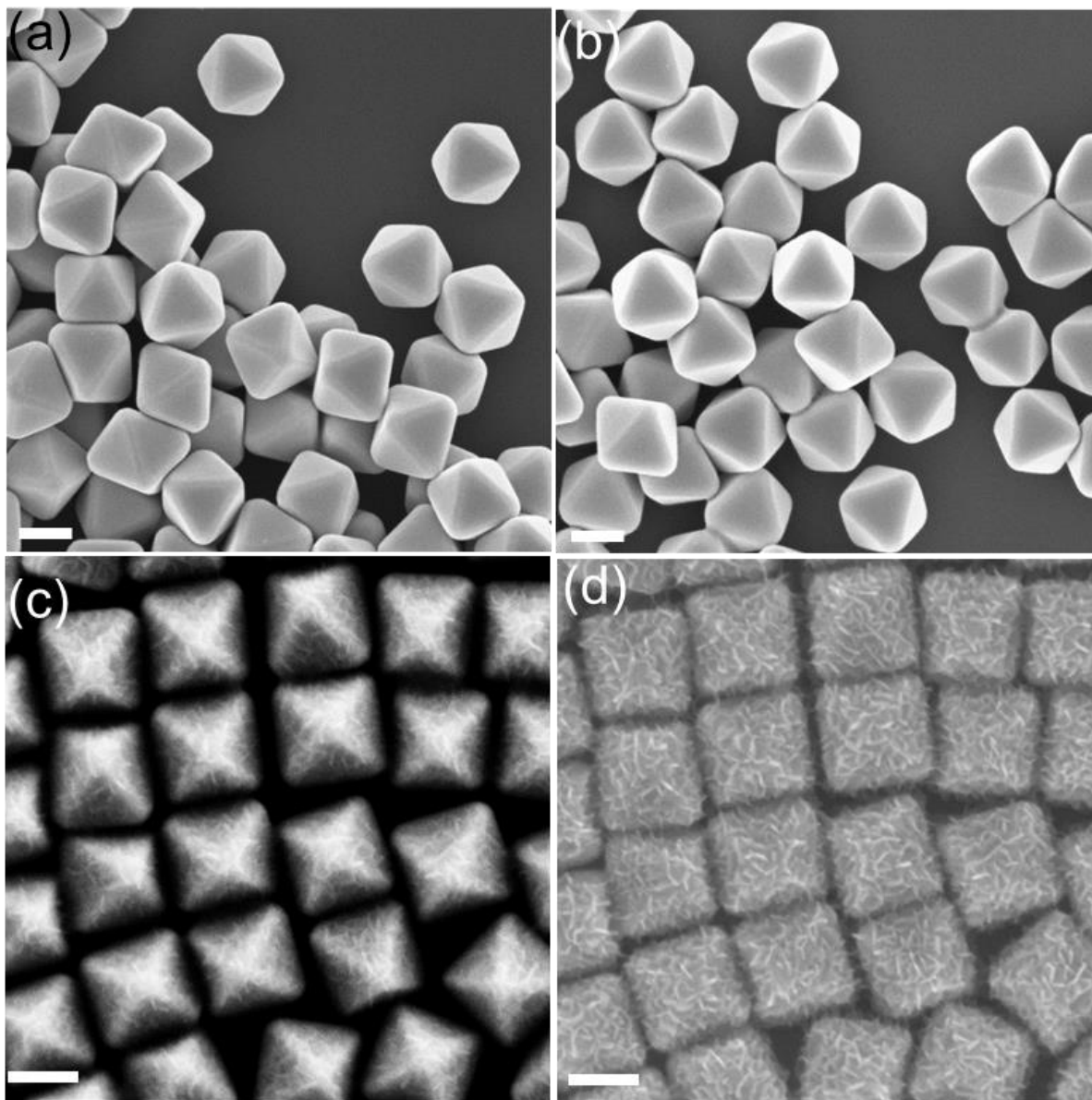


Figure 2.5. The SEM images of the silver nanocrystals at different stage of the fabrication procedure: (a) after PVP ligand removal (b) after 5 cycles of alumina ALD (c) MOF obtained from 5 cycles ALD alumina using a secondary electron detector and (d) an in-lens detector. Scale bar 200 nm

The phase purity and high crystallinity of the MOF enclosures synthesized using 1, 5, and 30 cycles of ALD Al_2O_3 is confirmed by grazing incidence wide angle x-ray scattering (GIWAXS) measurements. Scanning electron microscopy (SEM) was used to characterize the morphology of O_h -nano-Ag@MOF, and showed that the shape of the silver nanocrystal is retained throughout the process of fabrication and crystalline plate-like MOF regions are visible on the silver nanocrystal surface.

We proceeded to quantify the thickness control of the resulting MOF enclosures by controlling the ALD layer thickness. Figure 2.6 shows typical SEM and transmission electron microscopy (TEM) images of MOF films obtained from alumina layer thicknesses of 3, 0.5, and 0.1 nm. With increased cycles of alumina, the size and coverage of MOF crystallites on the Ag surface as well as the overall MOF layer thickness increases. The average thickness of the MOF enclosures is approximately 50 nm, 25 nm, and 10 nm for 30 cycles, 5 cycles, and 1 cycle ALD alumina, respectively. At the lowest limits of the ALD precursor film thickness of less than one nanometer, highly crystalline MOF enclosures as thin as several nanometers were made. The crystallite size and morphology of the MOF was finely tuned by varying the reaction conditions: a water:DMF ratio of 3:1 solvent mixture results in a more uniform, conformal MOF enclosure in contrast to the plate-like structure.

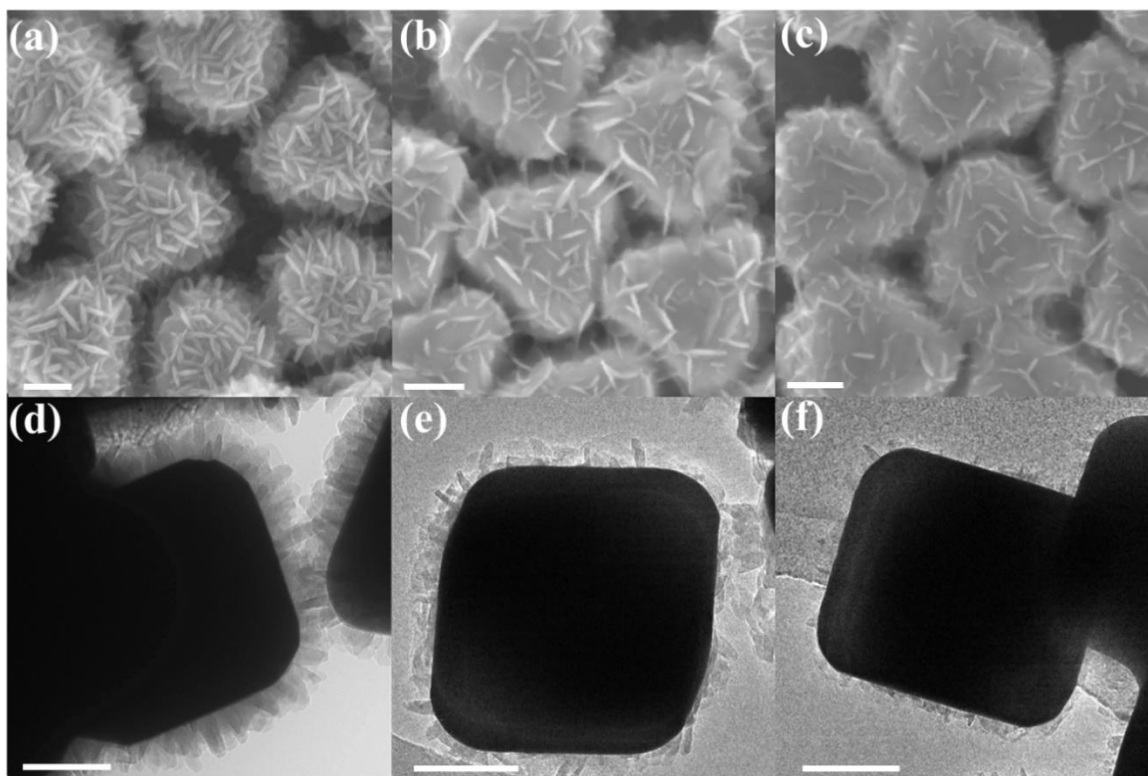


Figure 2.6. Thickness control of MOF enclosures. Variation in the alumina thickness from 3 to 0.5 to 0.1 nm allows control of MOF coverage on the silver nanocrystals with their SEM shown respectively (a to c) and the corresponding TEM (d to f) where the thickness and coverage of the MOF is further confirmed. Scale bars are all 50 nm.

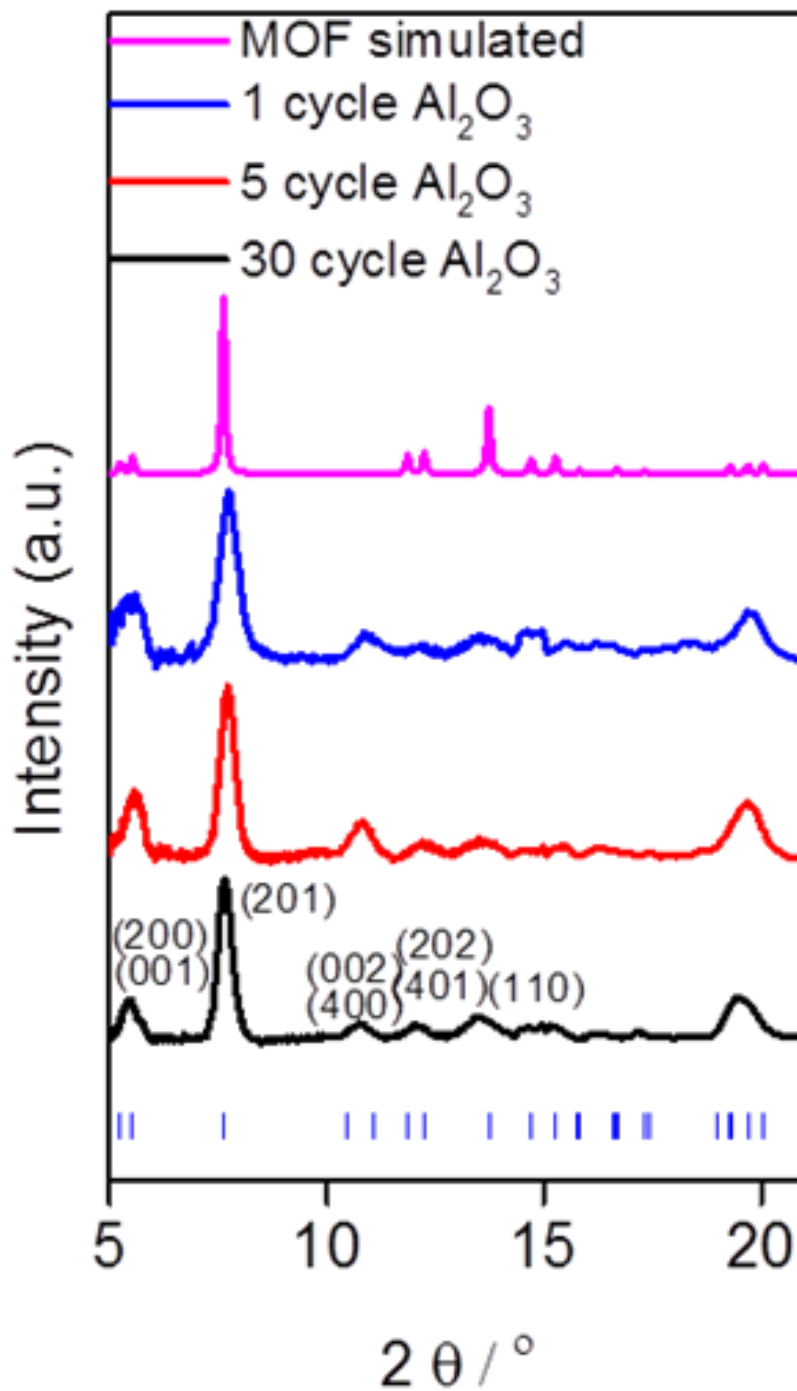


Figure 2.7. The 1-D scattering profiles of GIWAXS pattern of the $\text{Al}_2(\text{OH})_2(\text{TCPP})$ MOF enclosures. Due to the resolution of the detector, the (001) and (200) planes, the (002) and (400) planes, the (401) and (202) planes are too close to be resolved and are indistinguishable in the GIWAXS pattern. However, this does not affect the determination of the phase purity of the MOF.

Section 2.3.2 Determination of the Orientation of MOF Enclosure

The MOF crystallinity and orientation at the interface was examined by high resolution TEM. When imaging under the accelerating voltage of 120 kV with a low electron dosage, MOF lattice fringes were observed. This confirmed, at a microscopic level, the high crystallinity of the MOF enclosure at the interface and the fact it is pristine. The orientation of the MOF regions was determined from the TEM images, where the lattice fringes of 1.60 nm correspond to the MOF (200) planes parallel to the interface. This indicates that the porphyrin units of the MOF are perpendicular to the silver surface. The two-dimensional lattice fringes of 1.16 nm, which correspond to MOF (201) planes, are also observed, and thus provide an unambiguous determination of the MOF orientation being perpendicular to the silver surface. No evidence of porphyrin units oriented parallel to the silver surface was found among the TEM images. Here we analyze the silver and MOF orientation in details.

The MOF structure and various set of planes are illustrated in figure 2.8. Fundamentally, the essence of determining the orientation of MOF enclosure is to elucidate the relative orientation of the porphyrin units and silver surface. In this perspective, the ($h00$) and MOF ($00l$) planes are equivalent, as they are both parallel to the direction where the porphyrin rings are stacked. As the length of a -axis is very similar to two times of that of c -axis, the lattice spacing of some planes are very similar [for example, the lattice spacing of (200) planes is very similar to that of (001)] and the assignment of the lattice fringes are performed based on structure factor. However, this does affect the determination of the porphyrin orientation.

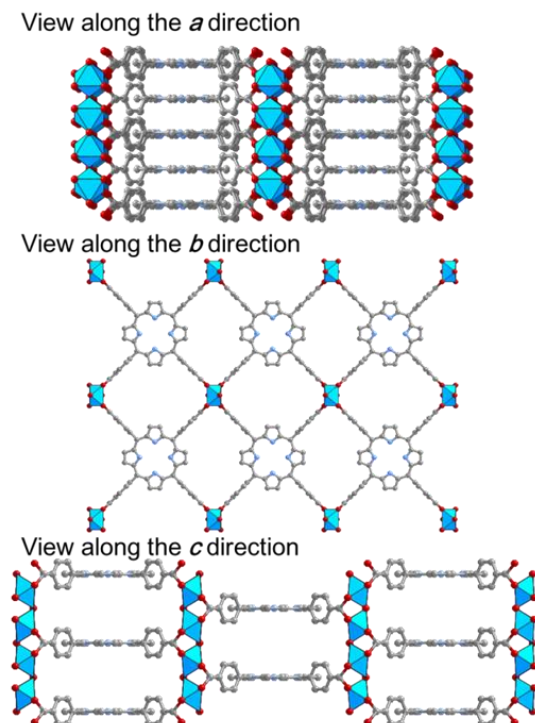


Figure 2.8. Crystal structures of $\text{Al}_2(\text{OH})_2(\text{TCPP})$ viewed along different axes.

The silver nanocrystal orientation on the TEM grid can be obtained from the TEM images. The dark square shape is the projection of the silver octahedra when illuminated from $\langle 100 \rangle$ direction.

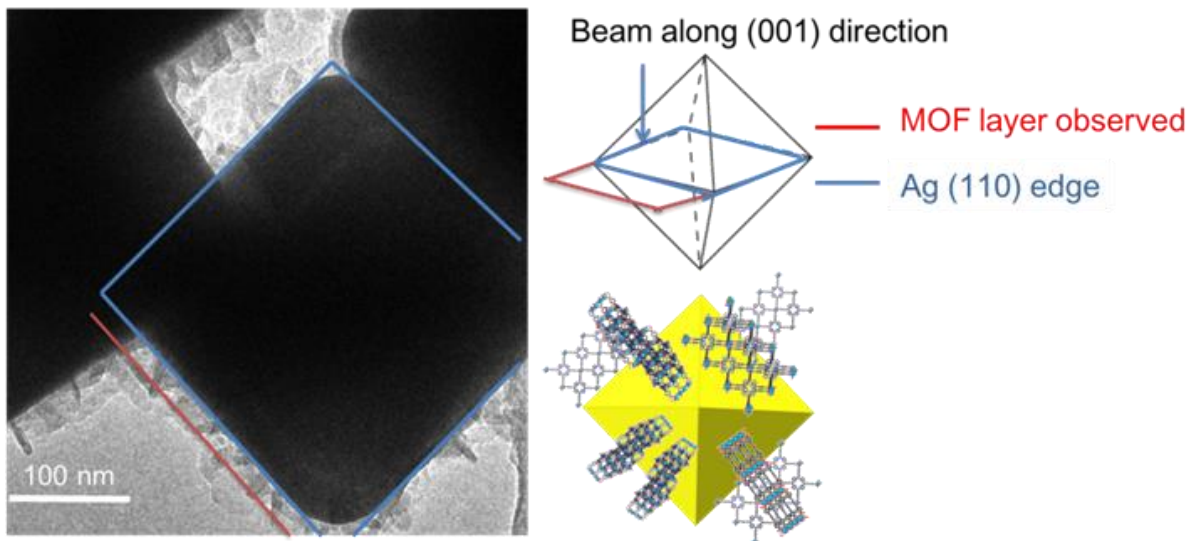


Figure 2.9. TEM image showing the overall orientation of the O_h -nano-Ag@MOF.

When the MOF (200) lattice fringes are parallel to the silver nanocrystal surface, with the lattice fringes along the other direction absent, there is ambiguity in the absolute orientation of the MOF. The MOF crystalline domain could rotate along the $\langle 200 \rangle$ direction and still give the same TEM image. However, this does not affect the conclusion that in this case the porphyrin unit is perpendicular to the silver surface. When the MOF (200) lattice fringes are perpendicular to the silver nanocrystal surface the MOF orientation could not be determined. The MOF orientation could be the same, but now the MOF could rotate along the $\langle 001 \rangle$ direction and give the same TEM image. This prevents us from obtaining the orientation of the porphyrin units.

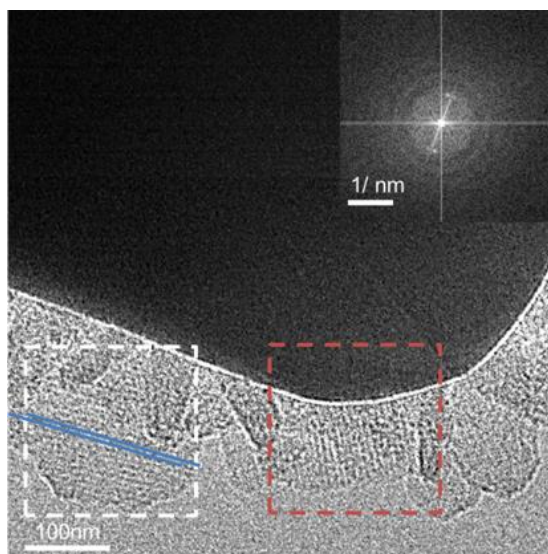


Figure 2.10. High-resolution TEM image of the MOF crystalline domains on silver nanocrystal and its FFT image. In the two squares, lattice fringes of MOF (200) plane are observed, where in the white square and its being parallel to the silver nanocrystal surface and in the red one it is perpendicular to silver surface.

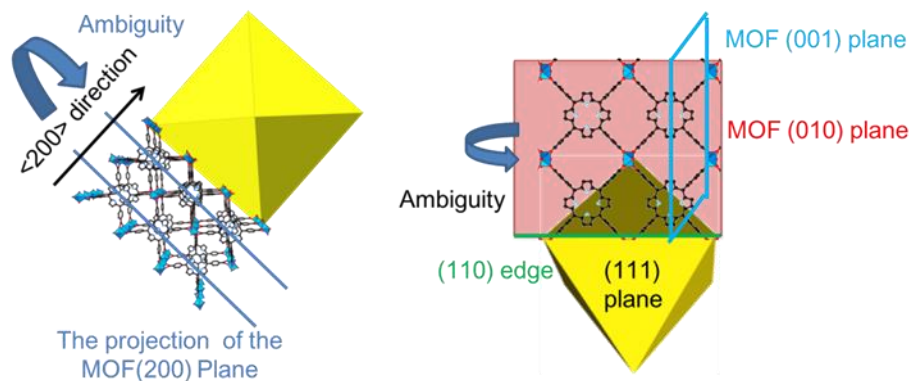


Figure 2.11. The structure model of the interface in discussed in O_h -nano-Ag@MOF. The silver octahedra exposed their (111) plane.

When the two-dimensional lattice fringes corresponding to MOF (201) planes can be observed, we could determine the MOF structure unambiguously where porphyrin units are perpendicular to the silver surface (Figure 2.12). The structural models only have one porphyrin crystallites drawn for simplicity, and a more realistic model would have MOF crystallites cover all the facets of the silver nanocrystal.

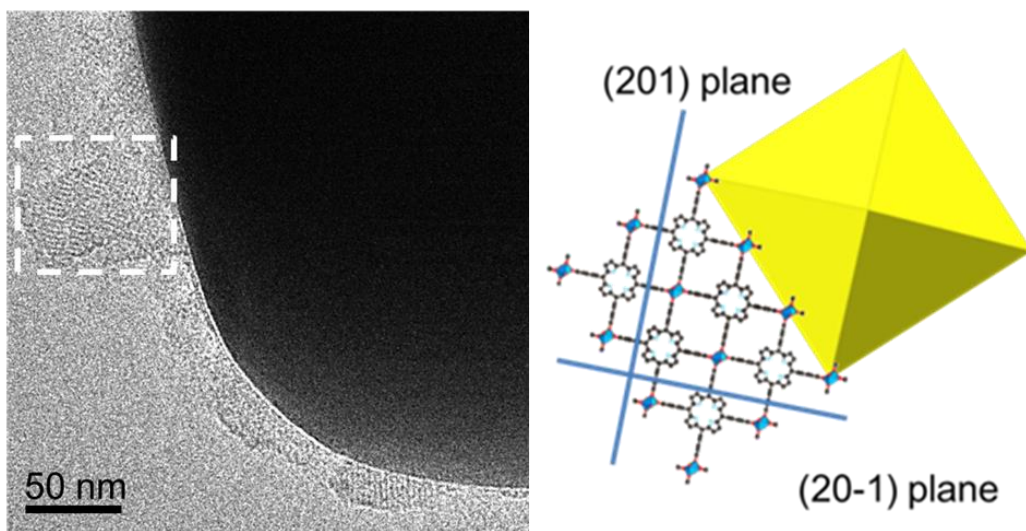


Figure 2.12. The TEM images showing two-dimensional lattice fringes corresponding to MOF (201) planes and corresponding structural model of the interface.

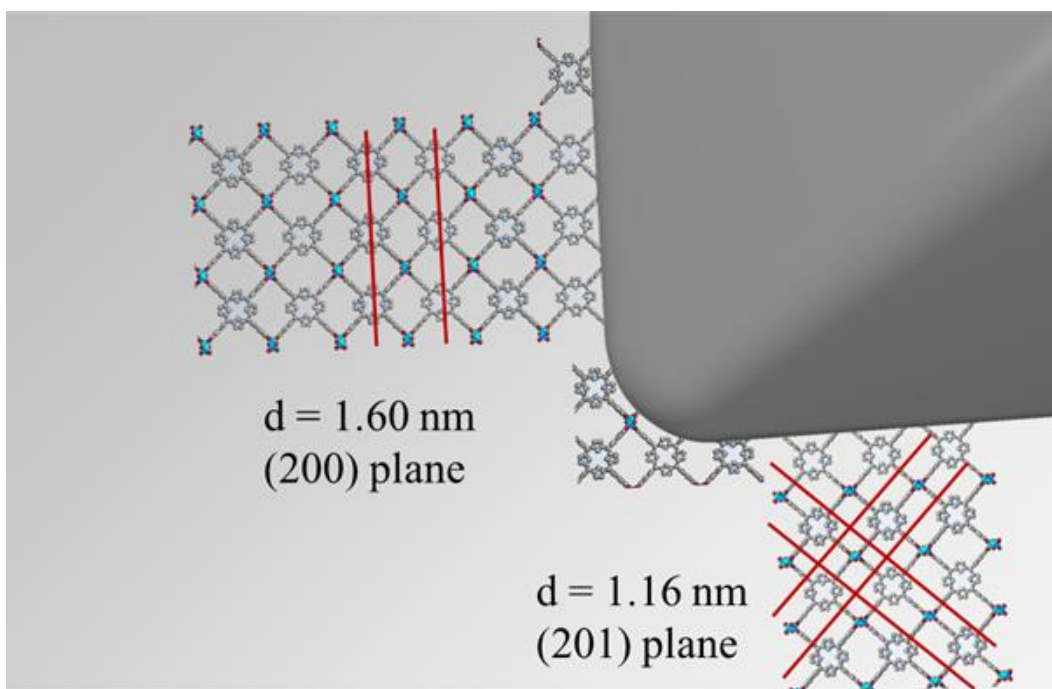


Figure 2.13. Summary of MOF orientation on silver nanocrystal with porphyrin units perpendicular to the interface.

This observation of porphyrin orientation is further supported by the high resolution low voltage SEM images of the O_h -nano-Ag@MOF, where plate-like MOF crystallites are observed growing vertically on the silver nanocrystal. Combining the crystal structure of the MOF and the information from the TEM images, we can confirm that the b -axis of the MOF is parallel to the silver surface and the porphyrin unit is perpendicular to the silver surface.

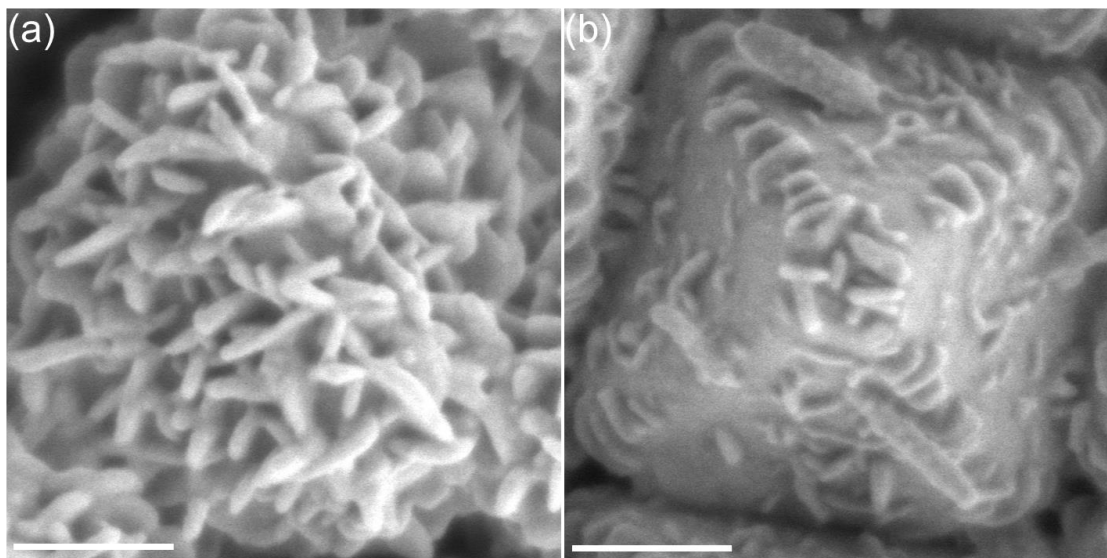


Figure 2.14. The high-resolution SEM images of the O_h -nano-Ag@MOF. The MOF enclosures are obtained from 5 cycles ALD alumina (a) and 1 cycle ALD alumina, respectively.

GIWAXS structural analysis was performed on a macroscopic level using a flat silicon substrate for MOF growth to further confirm the crystallinity and orientation of the MOF at an ensemble level. The spot pattern on GIWAXS image matches that expected for the preferred orientation of the MOF with the porphyrin units being perpendicular to the substrate (MOF [200] direction perpendicular to the substrate). A random orientation of the MOF would result in a ring rather than a spot pattern in the GIWAXS image. The GIWAXS pattern confirmed the structural model of the MOF-substrate interface, in which the porphyrin units of the MOF are perpendicular to the interface. This clearly demonstrates that this synthetic approach is well-suited for fabricating crystalline and precisely oriented MOF enclosures on inorganic nanocrystals.

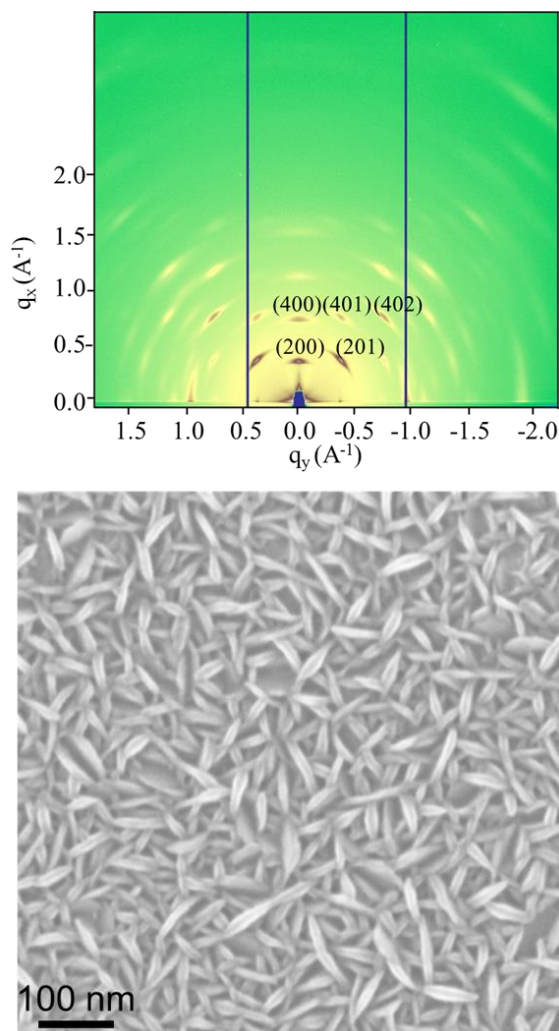


Figure 2.15. The GIWAXS pattern and SEM image of MOF grown on silicon substrate. In this case, the porphyrin units are also perpendicular to the substrate. When grown on flat substrate, the MOF nanocrystals form a thin film. In the next section, we demonstrate that this orientation of MOF is consistent among different substrates.

Section 2.3.3 Tracking Post-synthetic Metalation of $\text{Al}_2(\text{OH})_2(\text{TCPP})$ MOF Enclosure on O_h -nano-Ag@MOF by SERS

The metalation of $\text{Al}_2(\text{OH})_2(\text{TCPP})$ MOF is carried out under microwave irradiation. 2 mL of 10 mg/mL methanol solution of cobalt acetate is added to a 10 mL glass microwave vessel and purged with nitrogen. The substrate with O_h -nano-Ag@MOF is soaked in the solution and heated to 100°C for desired time. The completion of the metalation process is confirmed by UV-Vis absorption spectroscopy and energy dispersive x-ray (EDS) spectroscopies where in the latter, elemental mapping is utilized to further confirm the enclosed structure of the O_h -nano-Ag@MOF. For the UV-Vis absorption measurement, the MOF was deposited on a transparent glass slide.

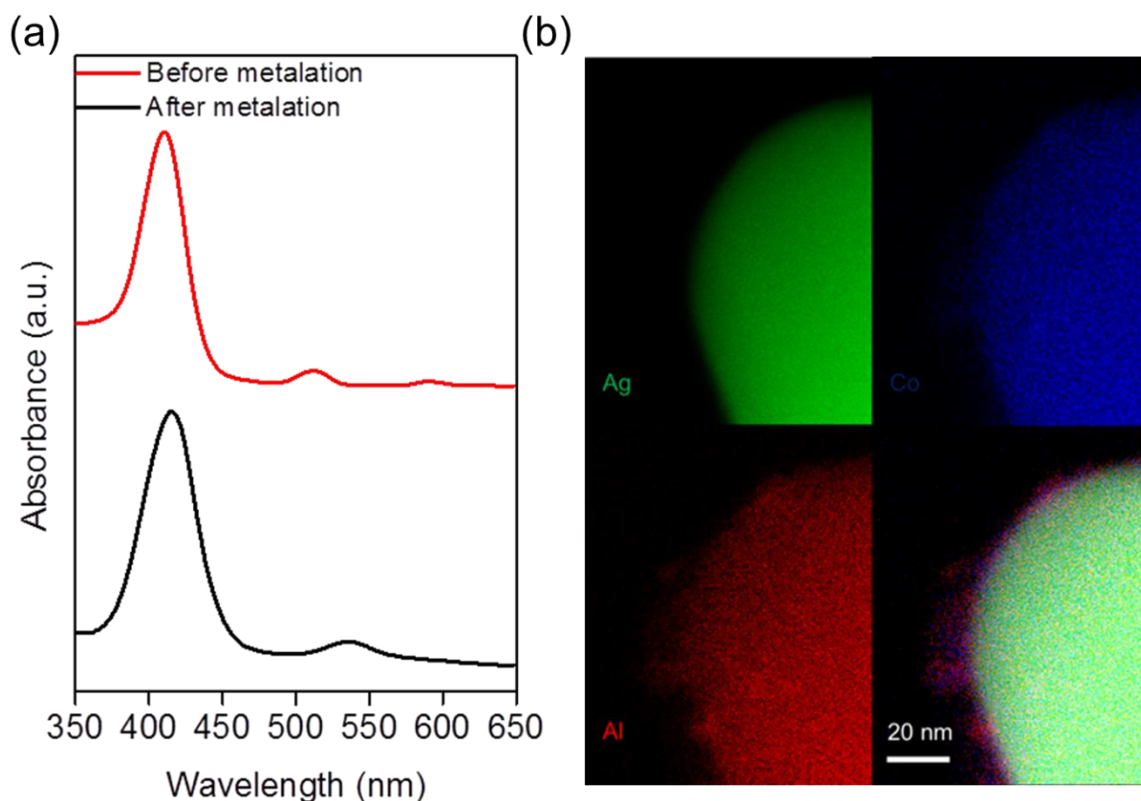


Figure 2.16. Characterization of metalated $\text{Al}_2(\text{OH})_2(\text{TCPP})$ MOF enclosures. UV-Vis spectrum of cobalt metallated MOF [$\text{Al}_2(\text{OH})_2(\text{TCPP-Co})$] after 50 min metalation compared to that of the MOF before metalation. EDS mapping of the O_h -nano-Ag@MOF after metallation.

With the ability to form thin MOF enclosures on plasmonic nanocrystals without an interfacial surfactant layer, unprecedented opportunities emerge in high resolution probing of chemical processes in MOF using SERS. The pristine interface enables the synergistic effects between the MOF enclosure and the silver nanocrystals. In an O_h -nano-Ag@MOF sample, all peaks in the SERS spectrum match those of the bulk MOF and the TCPP molecule and can be assigned according to previous literature studies of porphyrin molecules.

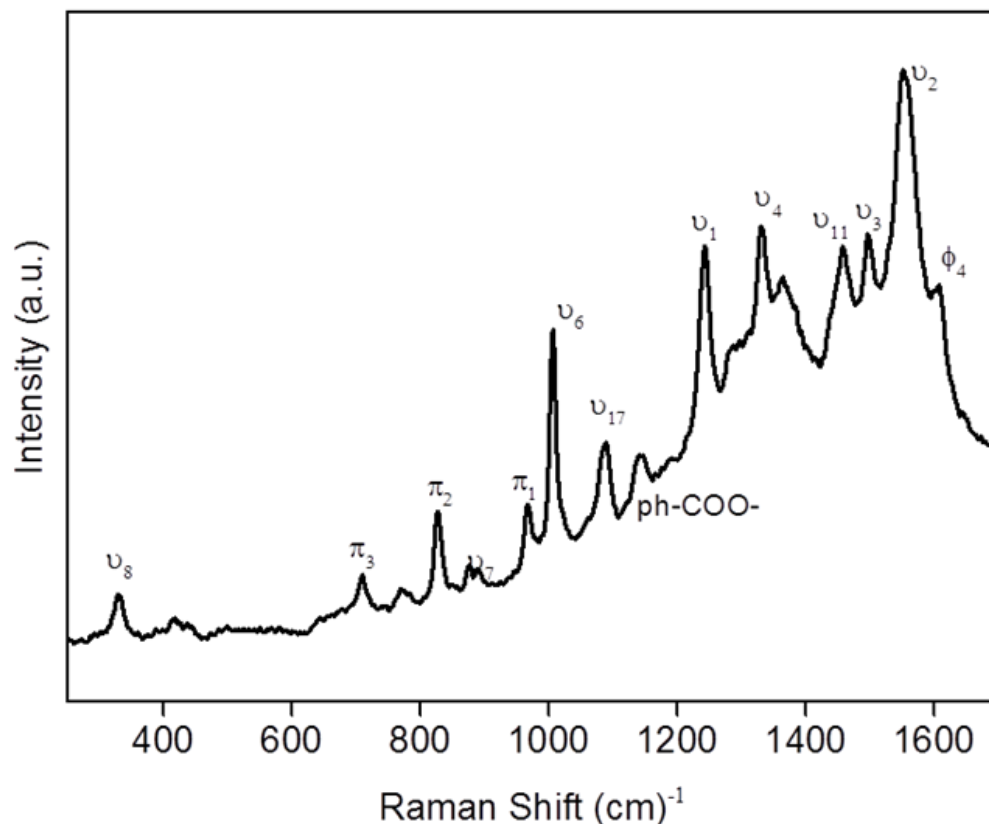


Figure 2.17. The Raman spectra of O_h -nano-Ag@MOF [$\text{Al}_2(\text{OH})_2(\text{TCPP})$] and the assignment of the main peaks. This assignment is based on previous literature studies.^{21,22} It is worth noticing that all these peaks match with the literature reported SERS spectrum of H_4TCPP .

This spectroscopic handle allowed us to track the metalation of the porphyrin units within the MOF enclosure. Metalation was carried out by heating the O_h -nano-Ag@MOF in a 10 mg/mL cobalt acetate methanol solution at 100°C , and SERS spectra of the mesoscopic construct were measured after different reaction time. Within the enclosure of MOF, this post-synthetic metalation was tracked with SERS and found to be complete within 50 minutes; thus, pointing to the facile diffusion of the cobalt acetate reagent due to the porosity of the MOF and access to the silver interface.

The metalation of the porphyrin molecule was evidenced mainly by the decline of the ν_8 mode corresponding to the free base porphyrin at 330 cm^{-1} and the rise of the ν_8 mode of the metalated porphyrin at 390 cm^{-1} . The validity of using the 330 cm^{-1} and the 390 cm^{-1} peaks to distinguish the metalated and un-metalated linkers is confirmed by comparing the SERS spectrum of the MOF with the Raman spectra of the corresponding MOF and porphyrin linker in powder form. The Raman spectrum of the un-metalated linker shows the ν_8 mode at 330 cm^{-1} and the spectrum of the metalated linker shows the ν_8 mode at 390 cm^{-1} .

In the metalation process, the 330 cm^{-1} peak gradually declined, and at the same time the 390 cm^{-1} peak emerged in the SERS spectra of the O_h -nano-Ag@MOF construct. After 50 minutes, the 330 cm^{-1} peak disappeared completely, indicating the metalation is completed. The evolution of other peaks in the SERS spectra is also consistent with the metalation process.

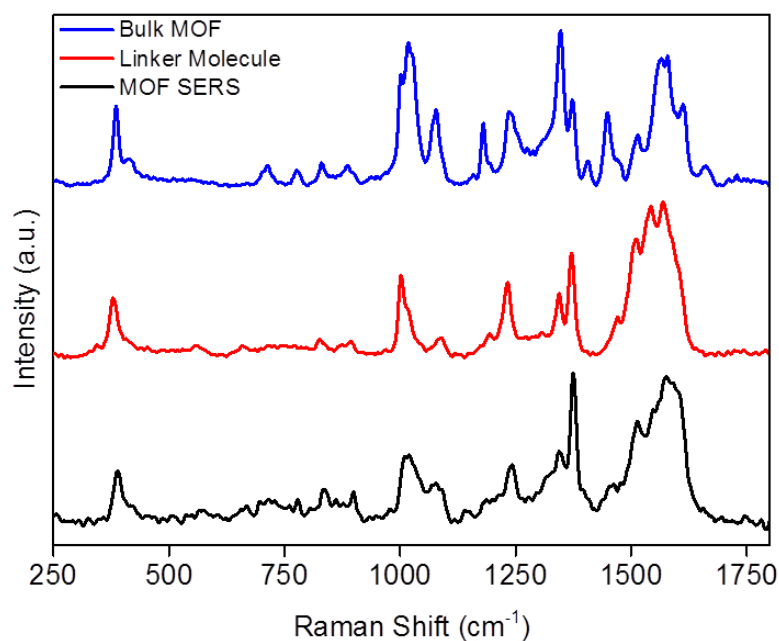


Figure 2.18. Raman spectra of the all-metalated MOF on silver (SERS) compared to H₄TCPP-Co linker and bulk all-metalated MOF model compound.

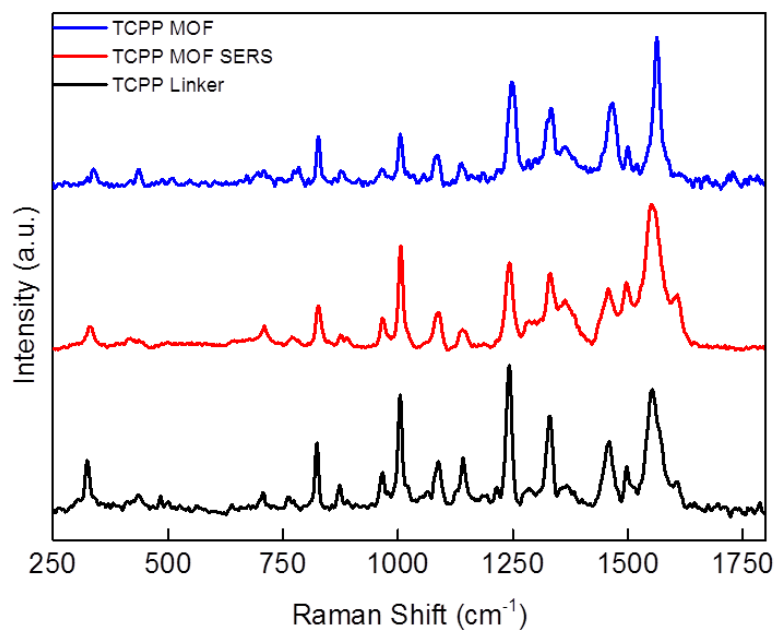


Figure 2.19. Raman spectrum of the un-metalated MOF on silver (SERS) compared to the H₄TCPP linker and bulk un-metalated Al₂(OH)₂(TCPP) MOF model compound.

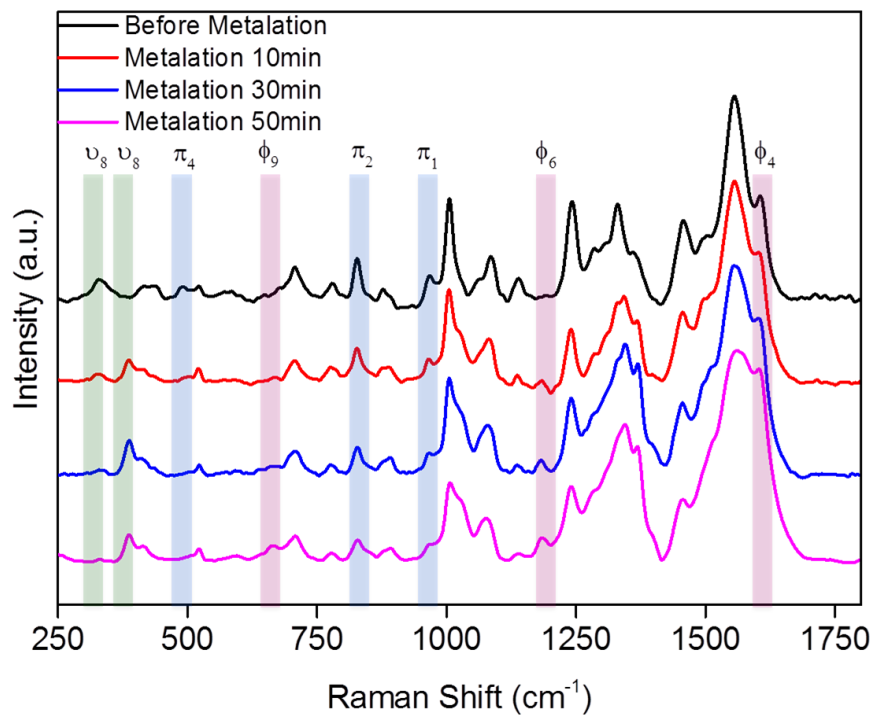


Figure 2.20 The Raman spectra of the MOF enclosure after different metalation times.



Figure 2.21 Illustration of vibrational modes of the H₄TCPP molecule.

In addition to the shift of ν_8 mode, the metalation process is also evident by a series of peak evolutions that are consistent with the literature. Most of the phenyl ring out-of-plane decrease in intensity while the phenyl ring in-plane modes increase in intensity during the metalation process, which is attributed to the change of symmetry from D_{2h} to D_{4h} after the metalation.

Section 2.3.4 Mapping of Metalated Linker Distribution in MOF Enclosure by SERS

Confocal SERS mapping was next applied to study heterogeneous MOF enclosures on silver nanocrystals and the unique capability of this system to generate spatially resolved chemical information. The size of an O_h -nano-Ag@MOF octahedron is 300 nm, which is similar to the diffraction limited spatial resolution possible with a 532 nm laser in a confocal microscopy setup. Therefore, chemical information at the limit of a single silver nanoparticle can be obtained. The multivariate approach, in which different organic linkers are incorporated into the same framework, is a powerful technique to introduce heterogeneity and complexity into MOFs and one that has presented challenges to its characterization due to lack of techniques capable of deciphering the spatial arrangement of the linkers.^{23,24} Here, pre-metalated porphyrin linker, cobalt(II) 4,4',4''',4''''-(porphyrin-5,10,15,20-tetrayl)tetrabenzoic acid, was mixed with the un-metalated TCPP linker in a 1:3 ratio in the precursor solution and reacted with the alumina coated silver nanocrystals under the conditions described above to give a multivariate MOF enclosure. The pre-metalated linker was also used to synthesize fully metalated MOF enclosure as reference material in this study. In the synthesis, the alumina coated silver nanocrystals were soaked in a 10 mL glass microwave vessel filled with 2 mL stock solution containing 5.5 mg H₄-TCPP-Co, 1.5 mL DMF and 0.5 mL H₂O (for multivariate MOF enclosure, 3.75 mg H₄TCPP, 1.32 mg H₄TCPP-Co 1.5 mL DMF and 0.5 mL H₂O were used). The alumina to MOF conversion is carried out under microwave irradiation under 140°C for 10 min. Following this, the substrate was extensively rinsed with DMF and ethanol.

The phase purity and crystallinity of the MOF enclosures were determined through electron microscopy and GIWAXS pattern. The presence of both linkers in the multivariate MOF enclosure was confirmed by UV-Vis absorption spectroscopy, which shows the Q band of both types of linkers. The EDS mapping confirms the presence of cobalt in the MOF films.

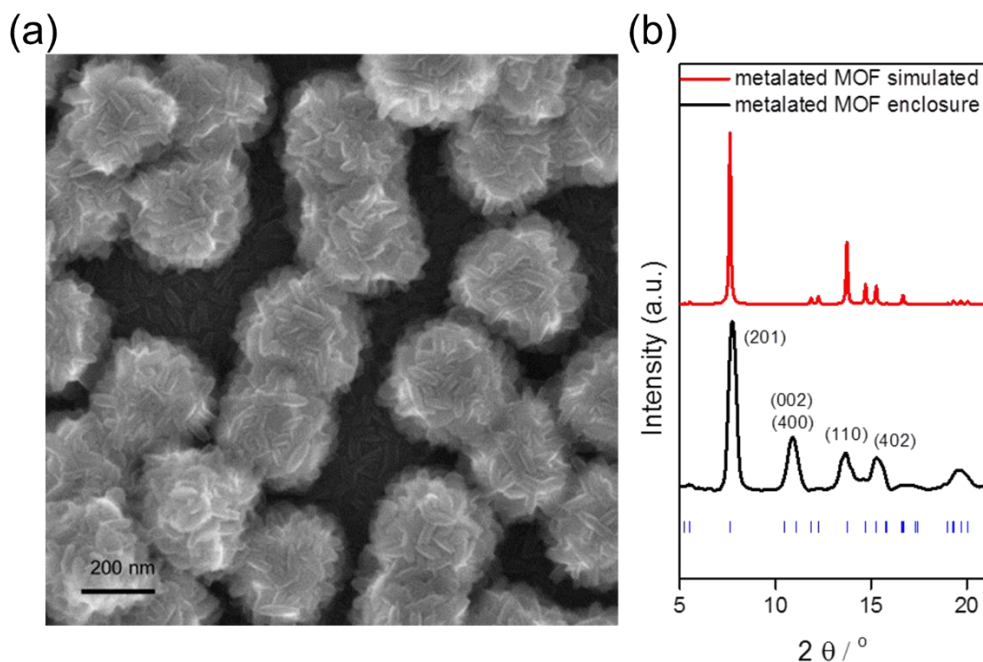


Figure 2.22. The SEM image and XRD of fully metalated MOF on silver. The 1-D scattering profiles of GIWAXS pattern of all-metalated MOF enclosure on silver confirms its crystallinity.

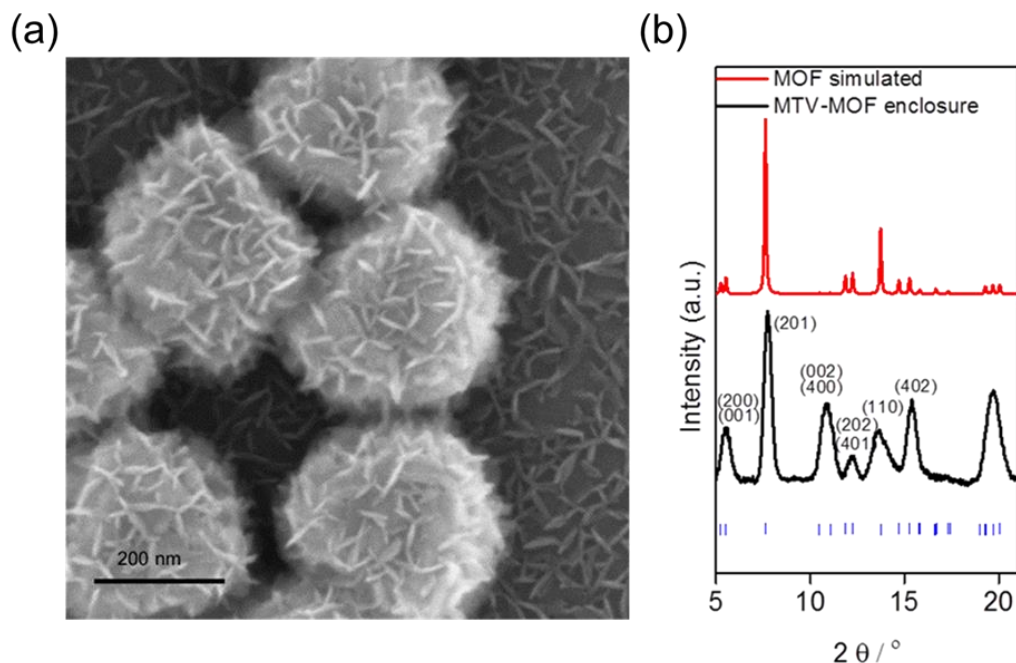


Figure 2.23. The SEM image and XRD of multivariate metalated MOF on silver. The 1-D scattering profiles of GIWAXS pattern of all-metalated MOF enclosure on silver confirms its crystallinity.

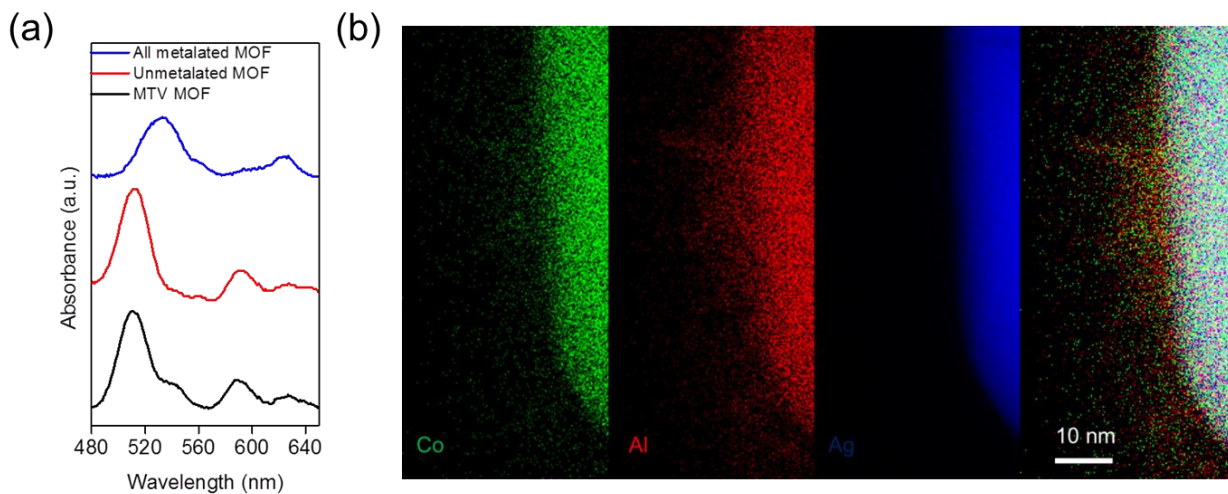


Figure 2.24. Characterization of MTV MOF enclosure by UV-Vis spectra and EDS mapping. The UV-Vis absorption spectrum (a) and EDS mapping (b) of the MTV MOF showing the presence of both metalated and un-metalated linker in the MOF enclosure.

The SERS spectrum was measured on clusters of O_h -nano-Ag@MOF particles, and found to have peaks attributable to ν_8 mode of both the metalated and un-metalated forms of the porphyrin unit. One of the fundamental difficulties in nano-MOF chemistry is to decipher whether the nanoparticles as a whole are homogenous in their composition, especially when a multivariate approach in metalation or mixing of linkers is employed in the synthesis of the MOF. The materials prepared here allow us to address this issue. Mapping of the metalated and un-metalated linkers in

a monolayer of O_h -nano-Ag@MOF using SERS reveals a well-mixed porphyrin system. In that, on the single particle level there is no segregation of metalated and un-metalated regions of the MOF. This is quantified by the ratio of the Raman scattering intensity of the two ν_8 modes for the metalated and un-metalated. This ratio is obtained from integrating the corresponding peaks areas and it is found to lie at 1.5 which is in between all-metalated and all un-metalated scenarios, which indicates that the distribution is homogenous from particle to particle as evidenced from mapping 7 μm regions.

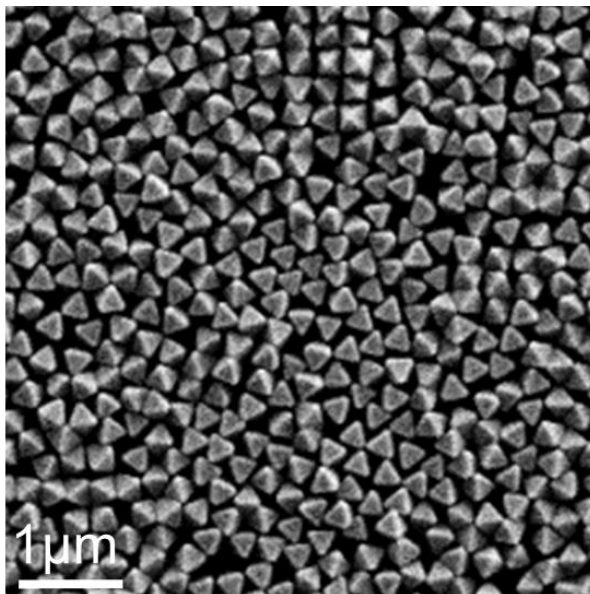


Figure 2.25. Monolayer of closed packed O_h -nano-Ag@MOF mapped by SERS

The mapping of single particle and clusters is performed on a substrate with drop cast silver nanocrystals on a silicon substrate. The mapping of discrete particles and clusters is performed with spatial increment of 120 nm and integration time of 7 seconds. It is worth noting that for the mapping of discrete particles, both the substrate and the silver nanocrystals are coated with the MOF and their Raman spectra are shown in figure 2.26. The Raman spectrum taken on the MOF on silicon substrate is shown as “background”.

The silver nanocrystal monolayer is prepared using the Langmuir-Blodgett approach. For quantitative Raman mapping of a silver monolayer, a 350 nm spatial increment with a 7 second integration time is used to minimize damage to the sample. The spectrum is acquired twice on each pixel and averaged. In the 7 μm region mapped, each pixel corresponds to an area of approximately one single nanoparticle. In other words, the data of each pixel represents the chemical information of the MOF enclosure on the length scale of a single O_h -nano-Ag@MOF. Mapping of the ν_8 mode ratios of the two pure-linker MOFs (un-metalated and all-metalated) and the MTV MOF gives similar standard deviation of this ratio throughout the region (7 μm , 400 data points). This shows that the un-metalated and metalated linkers are homogeneously distributed on this length scale. The 3D map in figure 2.26 visualizes this uniform ratio distribution.

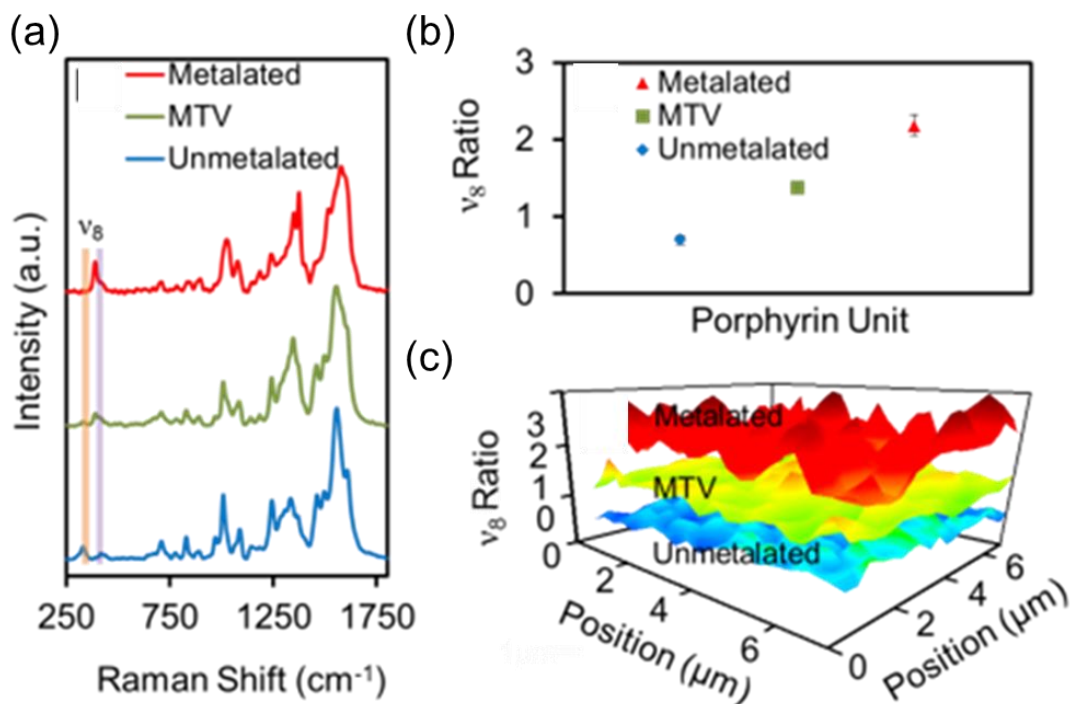


Figure 2.26. The SERS spectra for metalated, un-metalated, and multivariate metalated O_h -nano-Ag@MOF (a) showing the system is multivariate (MTV, mixed metalated and un-metalated MOF enclosures). The ratio of metalated and un-metalated linkers (b), and the homogeneity of these in the O_h -nano-Ag@MOF particles packed into a monolayer is mapped (c) (color going from blue to red corresponding to the value of the v_8 mode ratio going from 0.5 to 3.5).

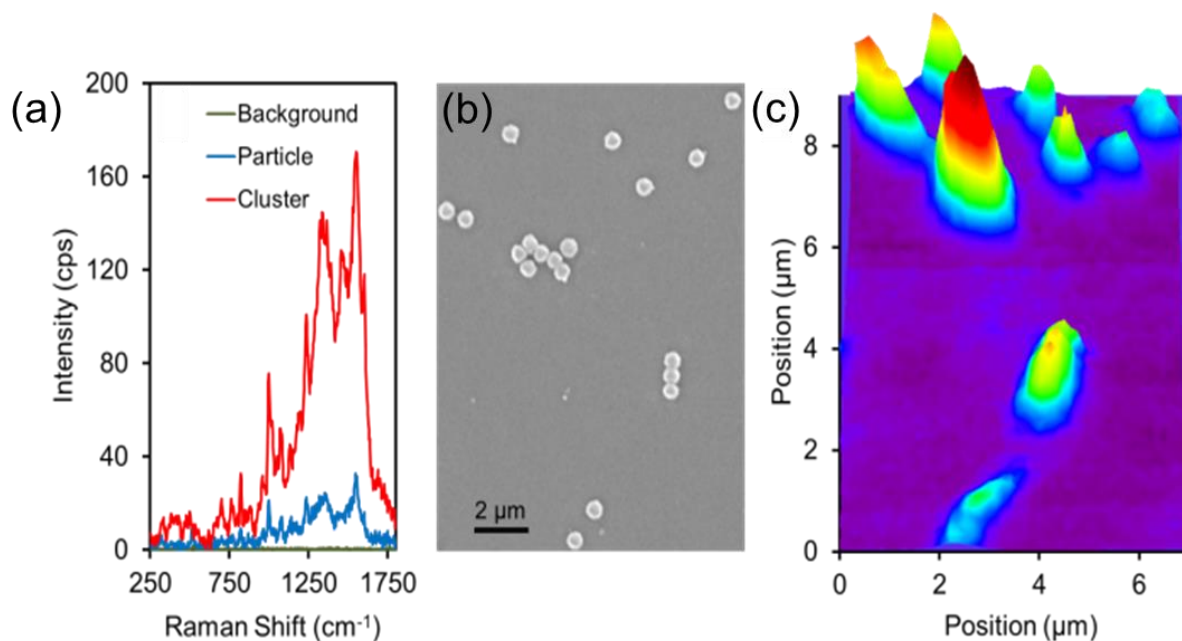


Figure 2.27. The SERS enhancement shown for single particles and clusters of O_h -nano-Ag@MOF (a), SEM of spatially resolved discrete O_h -nano-Ag@MOF (b), and the result of their SERS mapping (c) showing the one-to-one correspondence.

To illustrate the power of combining MOF and plasmonic nanocrystal into one mesoscopic construct, O_h -nano-Ag@MOF, we examined an area occupied by multiple discrete particles for their chemical composition using confocal Raman spectroscopy. It is very clear that because of the thin enclosure of MOF around the silver, it is possible to observe strong SERS signals for each of the particles and furthermore within each such particle the metallated and un-metallated porphyrin units in the MOF can be observed. This is possible because the MOF is grown on a plasmonic inorganic nanocrystal with a clean interface. Figure 2.27 (b) and (c) shows the area of particles and their corresponding SERS maps, respectively. Comparison of them also reveals that the SEM and SERS mapping are consistent in providing a highly-resolved picture of the spatial arrangement of the mesoscopic O_h -nano-Ag@MOF particles.

Section 2.4 Conclusion

We overcome the ‘functionalization problem’ of inorganic nanocrystals by enclosing them with metal-organic frameworks as well-defined units for which the spatial arrangement of functional organic and inorganic units, porosity, density and thickness can be precisely controlled. We addressed this problem by developing a new synthetic approach that overcomes the four challenges: (a) a pristine interface between inorganic nanocrystals and MOFs that is free of surfactants and other surface ligands to take advantage of synergistic effects at the interface, (b) well-ordered and precisely oriented MOF enclosures around the inorganic nanocrystals to impart high degree of spatial control over the desired functional groups, (c) sufficiently thin MOF enclosures for facile diffusion and high resolution chemical mapping, and (d) bridging multiple length scales by combining the MOF atomically defined scale with the nano dimension, thus realizing new chemical and physical functions.

We demonstrate this synthetic approach by constructing a mesoscopic construct O_h -nano-Ag@MOF, where silver octahedra were wrapped with $Al_2(OH)_2$ TCPP MOF enclosure. The MOF enclosures have controllable thickness from 5-50 nm, attach directly to the silver nanocrystals, and have well-defined orientation on the nanocrystal substrates. In the MOF enclosure, the porphyrin units were determined to be perpendicular to the substrates, which can be inorganic nanocrystals or nanostructures.

The construction of O_h -nano-Ag@MOF mesoscopic construct allows us to study the synergy between silver nanocrystal and MOF enclosure in structural characterization of MOF by SERS. We monitored post-synthetic metalation of $Al_2(OH)_2$ TCPP MOF by SERS and concluded that due to facile diffusion, this chemistry could be completed in 50 minutes. Furthermore, the distribution of metallated and unmetallated porphyrin linker in multivariate MOF enclosure was found to be uniform on 300 nm length scale by SERS. Additionally, the enhancement of MOF Raman signal was clearly demonstrated by comparing the Raman spectroscopic mapping and SEM images of the same $49 \mu m^2$ area, where the spatial arrangement of silver nanocrystals (O_h -nano-Ag@MOF mesoscopic construct) matches the spot on the Raman mapping where intense $Al_2(OH)_2$ TCPP MOF signal was recorded.

Section 2.5 References

- (1) He, L.; Liu, Y.; Liu, J.; Xiong, Y.; Zheng, J.; Liu, Y.; Tang, Z., *Angew. Chem. Int. Ed.* **2013**, *52*, 3741-3745.
- (2) Hu, P.; Zhuang, J.; Chou, L.-Y.; Lee, H. K.; Ling, X. Y.; Chuang, Y.-C.; Tsung, C.-K., *J. Am. Chem. Soc.* **2014**, *136*, 10561-10564.
- (3) Hu, Y.; Liao, J.; Wang, D.; Li, G., *Anal. Chem.* **2014**, *86*, 3955-3963.
- (4) Jin, S.; Son, H.-J.; Farha, O. K.; Wiederrecht, G. P.; Hupp, J. T., *J. Am. Chem. Soc.* **2013**, *135*, 955-958.
- (5) Khaletskaya, K.; Reboul, J.; Meilikhov, M.; Nakahama, M.; Diring, S.; Tsujimoto, M.; Isoda, S.; Kim, F.; Kamei, K.-i.; Fischer, R. A.; Kitagawa, S.; Furukawa, S., *J. Am. Chem. Soc.* **2013**, *135*, 10998-11005.
- (6) Kreno, L. E.; Greeneltch, N. G.; Farha, O. K.; Hupp, J. T.; Van Duyne, R. P., *Analyst* **2014**, *139*, 4073-4080.
- (7) Kreno, L. E.; Hupp, J. T.; Van Duyne, R. P., *Anal. Chem.* **2010**, *82*, 8042-8046.
- (8) Liu, N.; Yao, Y.; Cha, J.; McDowell, M.; Han, Y.; Cui, Y., *Nano Res.* **2012**, *5*, 109-116.
- (9) Lu, G.; Li, S.; Guo, Z.; Farha, O. K.; Hauser, B. G.; Qi, X.; Wang, Y.; Wang, X.; Han, S.; Liu, X.; DuChene, J. S.; Zhang, H.; Zhang, Q.; Chen, X.; Ma, J.; Loo, S. C. J.; Wei, W. D.; Yang, Y.; Hupp, J. T.; Huo, F., *Nat. Chem.* **2012**, *4*, 310-316.
- (10) Reboul, J.; Furukawa, S.; Horike, N.; Tsotsalas, M.; Hirai, K.; Uehara, H.; Kondo, M.; Louvain, N.; Sakata, O.; Kitagawa, S., *Nat. Mater.* **2012**, *11*, 717-723.
- (11) Shekhah, O.; Wang, H.; Strunskus, T.; Cyganik, P.; Zacher, D.; Fischer, R.; Wöll, C., *Langmuir* **2007**, *23*, 7440-7442.
- (12) So, M. C.; Jin, S.; Son, H.-J.; Wiederrecht, G. P.; Farha, O. K.; Hupp, J. T., *J. Am. Chem. Soc.* **2013**, *135*, 15698-15701.
- (13) Sugikawa, K.; Furukawa, Y.; Sada, K., *Chem. Mater.* **2011**, *23*, 3132-3134.
- (14) Zhan, W.-w.; Kuang, Q.; Zhou, J.-z.; Kong, X.-j.; Xie, Z.-x.; Zheng, L.-s., *J. Am. Chem. Soc.* **2013**, *135*, 1926-1933.
- (15) Furukawa, H.; Cordova, K. E.; O’Keeffe, M.; Yaghi, O. M., *Science* **2013**, *341*, 974.
- (16) Tao, A.; Sinsersuksakul, P.; Yang, P., *Angew. Chem. Int. Ed.* **2006**, *45*, 4597-4601.
- (17) Tao, A.; Sinsersuksakul, P.; Yang, P., *Nat. Nanotechnol.* **2007**, *2*, 435-440.
- (18) Tao, A. R.; Ceperley, D. P.; Sinsersuksakul, P.; Neureuther, A. R.; Yang, P., *Nano Lett.* **2008**, *8*, 4033-4038.
- (19) Fateeva, A.; Chater, P. A.; Ireland, C. P.; Tahir, A. A.; Khimiyak, Y. Z.; Wiper, P. V.; Darwent, J. R.; Rosseinsky, M. J., *Angew. Chem. Int. Ed.* **2012**, *51*, 7440-7444.

(20) Rosen, E. L.; Buonsanti, R.; Llordes, A.; Sawvel, A. M.; Milliron, D. J.; Helms, B. A., *Angew. Chem. Int. Ed.* **2012**, *51*, 684-689.

(21) Vlckova, B.; Matejka, P.; Simonova, J.; Cermakova, K.; Pancoska, P.; Baumruk, V., *J. Phy. Chem.* **1993**, *97*, 9719-9729.

(22) Li, X. Y.; Czernuszewicz, R. S.; Kincaid, J. R.; Su, Y. O.; Spiro, T. G., *J. Phy. Chem.* **1990**, *94*, 31-47.

(23) Kong, X.; Deng, H.; Yan, F.; Kim, J.; Swisher, J. A.; Smit, B.; Yaghi, O. M.; Reimer, J. A., *Science* **2013**, *341*, 882-885.

(24) Deng, H.; Doonan, C. J.; Furukawa, H.; Ferreira, R. B.; Towne, J.; Knobler, C. B.; Wang, B.; Yaghi, O. M., *Science* **2010**, *327*, 846-850.

Section 2.6 Appendix

Section 2.6.1 Synthesis of H₄TCPP-Co

The H₄TCPP-Co is synthesized with slight modification of the literature reports (28). H₄TCPP (H₄TCPP is the un-metalated form of the porphyrin unit, which is the abbreviated form of H₄TCPP-H₂) (72 mg) and cobalt chloride hexahydrate (25 mg) are dissolved in 30 mL of DMSO solvent and heated to reflux under nitrogen for 12 hours. The solution is then cooled to room temperature and 60 mL of 1 M HCl is added. The solid precipitates are collected by centrifugation, washed with HCl and water, and dissolved in 20 mL 0.1 M NaOH aqueous solution. The solution is next acidified with HCl, and the solid precipitates are washed with water and dried. Figure A2.1 illustrates the ESI-HR mass spectroscopic results for the H₄TCPP-Co: calcd. 847.12 found 847.12. FTIR $\nu = 1684$ (s), 1603 (s), 1397(m), 1220 (m), 1173(m), 1093(m), 1018(m), 962(s), 865 (m), 792 (s) cm^{-1}

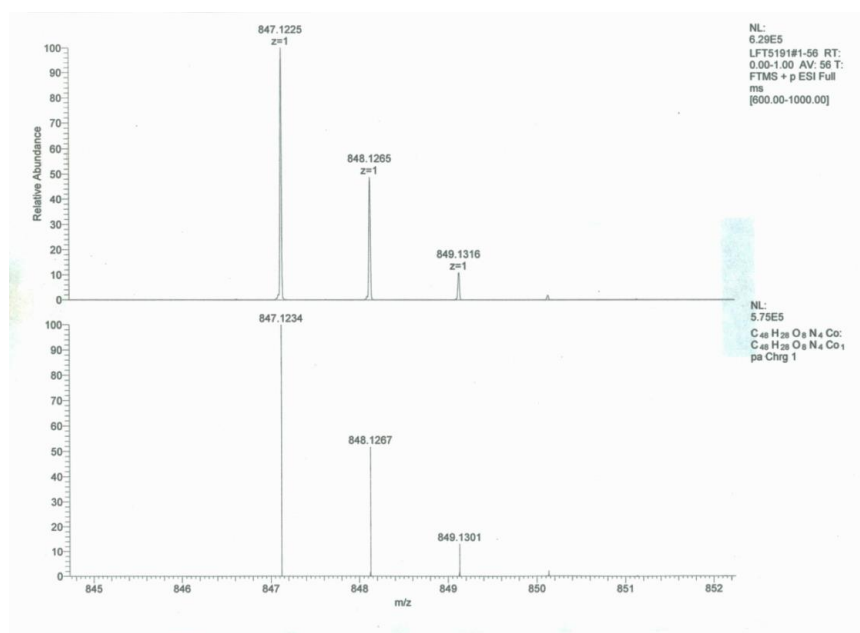


Figure A2.1. ESI-HR mass spectrum of H₄TCPP-Co molecule.

Section 2.6.2 XRD Patterns of $\text{Al}_2(\text{OH})_2\text{TCPP}$ and $\text{Al}_2(\text{OH})_2\text{TCPP-Co}$

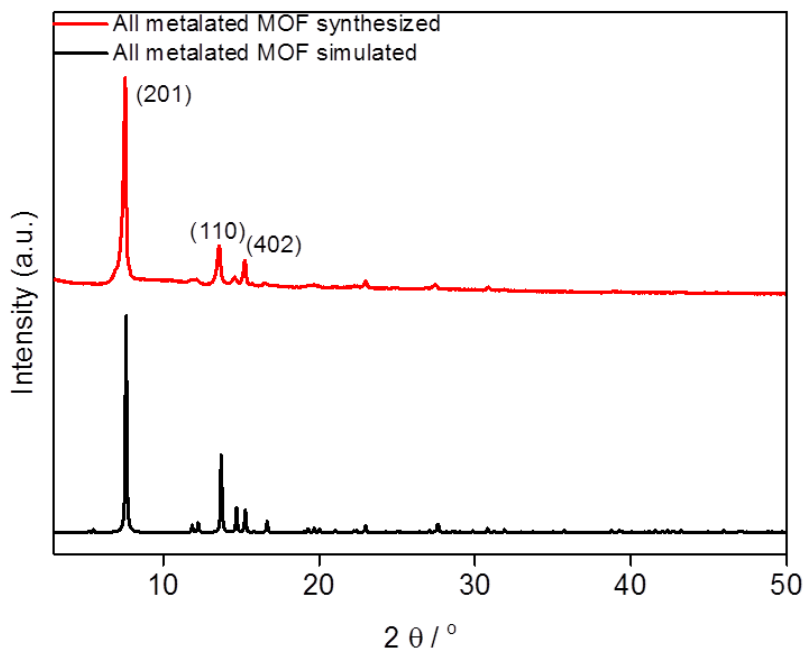


Figure A2.2 PXRD pattern of all-metalated $\text{Al}_2(\text{OH})_2\text{TCPP-Co}$ MOF

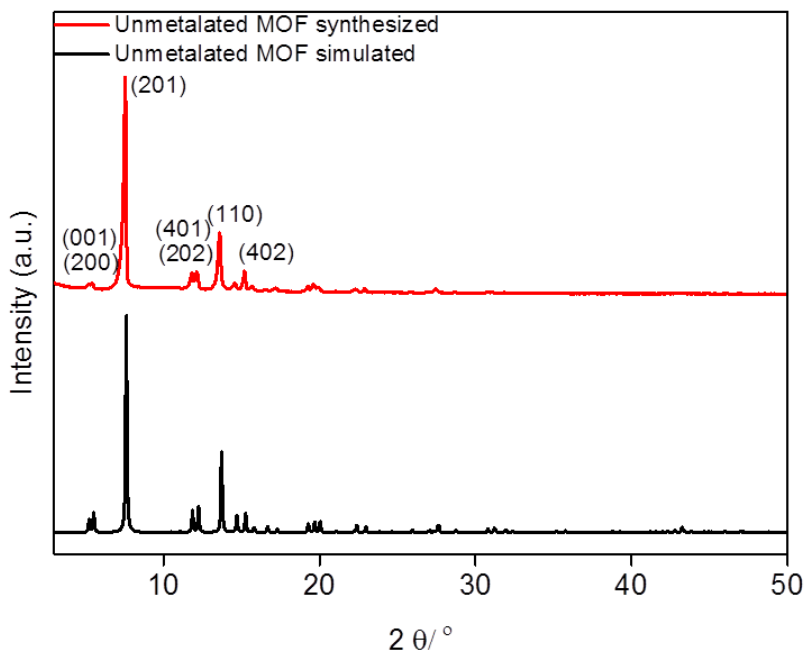


Figure A2.3 PXRD pattern of $\text{Al}_2(\text{OH})_2\text{TCPP-Co}$ MOF

Section 2.6.3 Morphological Control of $\text{Al}_2(\text{OH})_2\text{TCPP}$ MOF Enclosure by Solvent

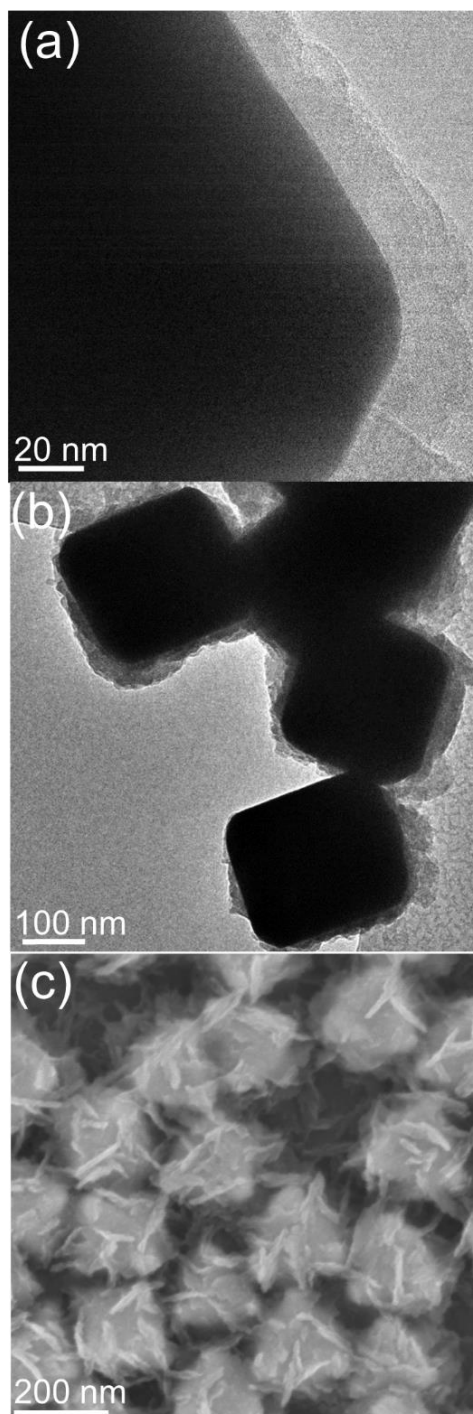


Figure A2.4. The HRTEM image (a), TEM image (b) and SEM image (c) of the $\text{Al}_2(\text{OH})_2(\text{TCPP})$ MOF enclosure synthesized in a water rich solvent condition (75% water 25% DMF) with other conditions the same as above.

Section 2.6.4 Removal of PVP on Silver Nanocrystals

As the PVP layer at the interface between the silver and MOF would give a strong Raman signal that overwhelm the spectrum of MOF, an additional surface cleaning step using a Meerwein's salt treatment to remove PVP surfactant was employed before coating the silver with alumina to ensure a pristine interface between the MOF and Ag nanocrystal (Figure A2.5). The evolution of PVP signal is monitored by SERS. These spectra are sampled on the same spot of silver nanocrystal island by using a marked silicon substrate. The PVP signal declined after the Meerwein salt treatment and the ALD process. In the ALD process both heating under vacuum and the growth of alumina on the silver surface further reduce the PVP signal. The signal intensity and peak position of the SERS spectrum of the MOF both confirm that the final spectrum is free from PVP signal.

It is worth noting that prolonged treatment of Meerwein salt would result in deformation of the silver nanocrystals and after PVP removal the silver nanocrystals are prone to oxidation if left in air. Without the passivation of PVP, the silver nanocrystals would also melt at lower temperature (around 150 °C).

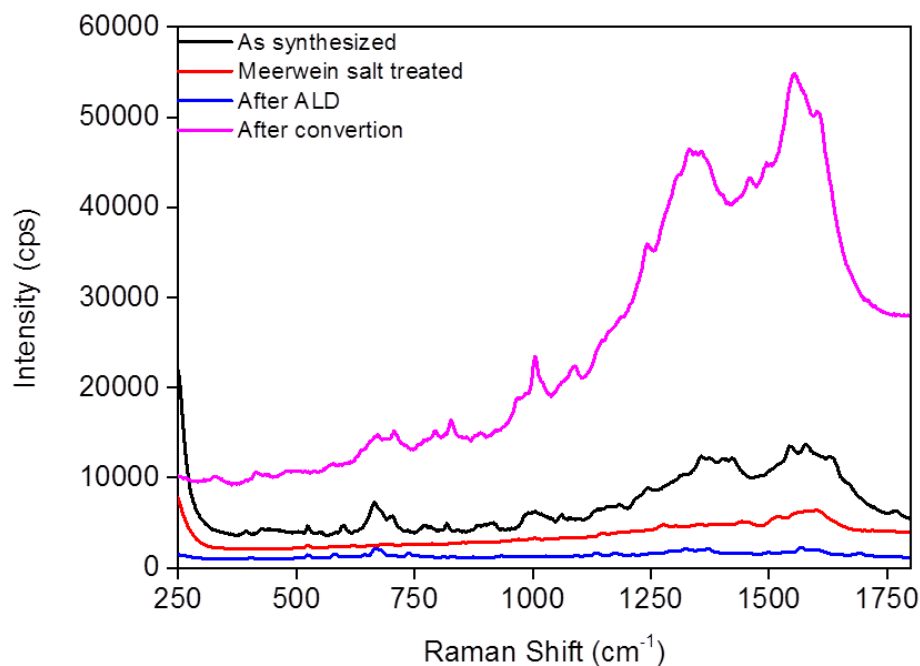


Figure A2.5. The Raman spectrum of the silver-MOF construct at different stage of the fabrication. As synthesized silver nanocrystal shows strong signal of PVP, which is significantly reduced after Meerwein salt treatment and ALD deposition of alumina. It is clear that the features in the Raman spectrum that emerge after MOF nucleation originate from the MOF enclosure on silver nanocrystals.

Section 2.6.5 Fabrication of $\text{Al}_2(\text{OH})_2(\text{TCPP})$ MOF on Other Substrates

This approach for making mesoscopic constructs can also produce MOF films on other substrates such as carbon disk with the same morphology and crystallinity. The carbon disk, silicon wafer, FTO substrates are directly put in the ALD chamber and coated with alumina using the same alumina ALD parameters as for the $\text{Al}_2(\text{OH})_2(\text{TCPP})$ MOF. The substrates are each soaked in a 10 mL sealed glass microwave vessel with a stock solution of 5 mg H_4TCPP , 1.5 mL DMF, and 0.5 mL H_2O . The alumina to MOF conversion is carried out under microwave irradiation at 140°C for 10 min. Following this, the substrates are extensively rinsed with DMF and ethanol. The control over MOF thickness by controlling the thickness of alumina through ALD can also be applied on these substrates.

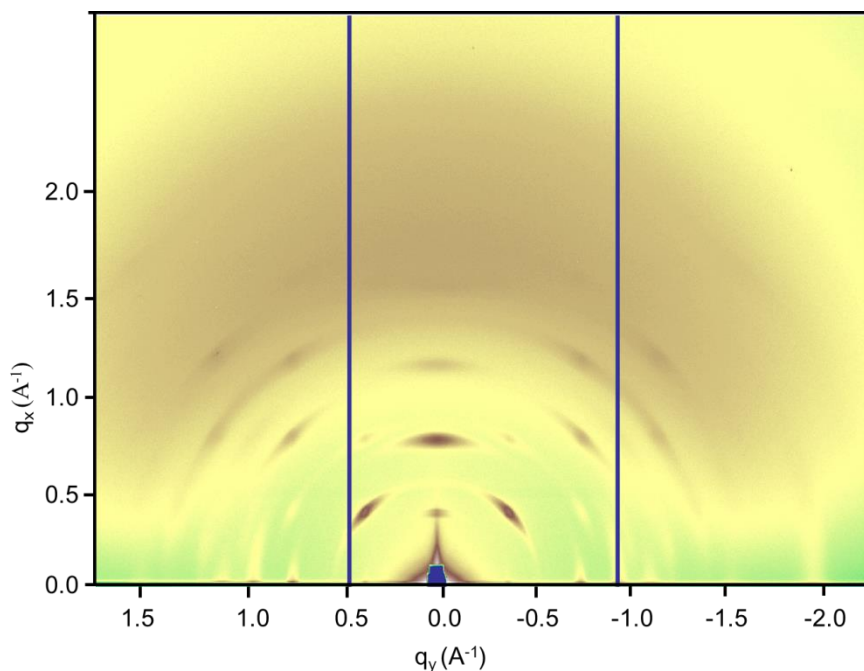


Figure A2.6. The GIWAXS pattern of $\text{Al}_2(\text{OH})_2(\text{TCPP})$ MOF on FTO coated glass showing the same orientation as on silicon substrate and the surface of silver nanocrystals.

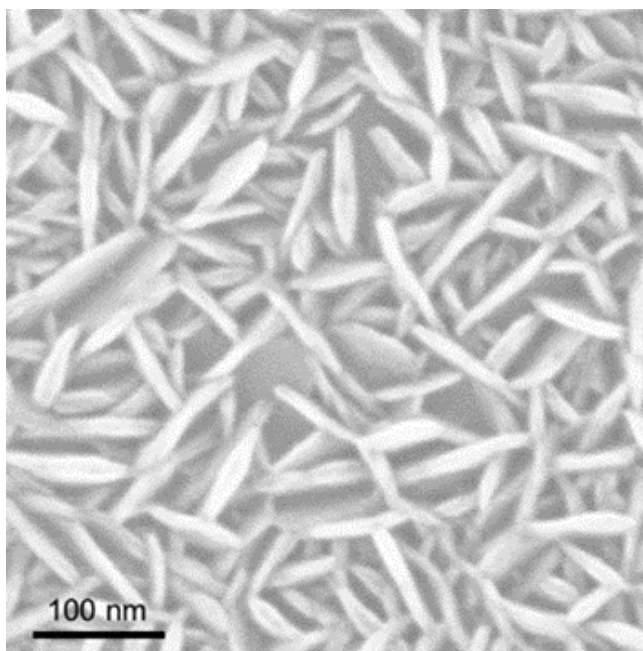


Figure A2.7. SEM image of Al₂(OH)₂(TCPP) MOF obtained from 30 cycles ALD alumina on a silicon substrate.

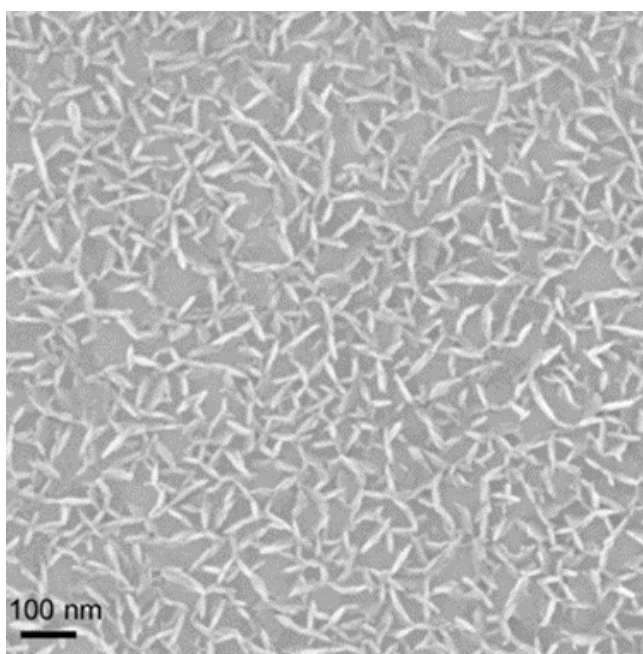


Figure A2.8. SEM image of Al₂(OH)₂(TCPP) MOF obtained from 5 cycles ALD alumina on silicon.

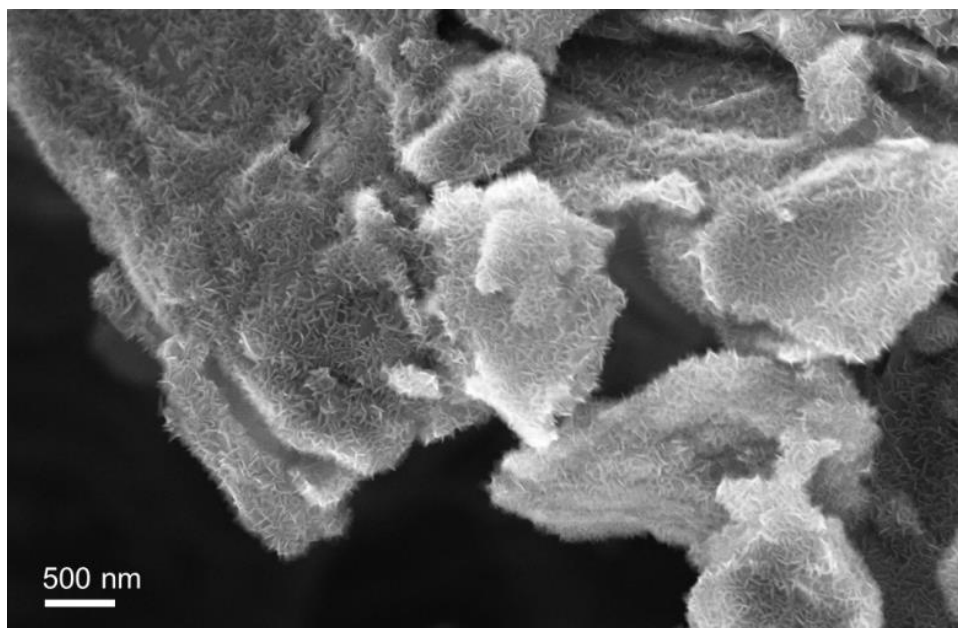


Figure A2.9. SEM image of $\text{Al}_2(\text{OH})_2\text{TCPP}$ MOF obtained from 30 cycles ALD alumina on a carbon disk substrate.

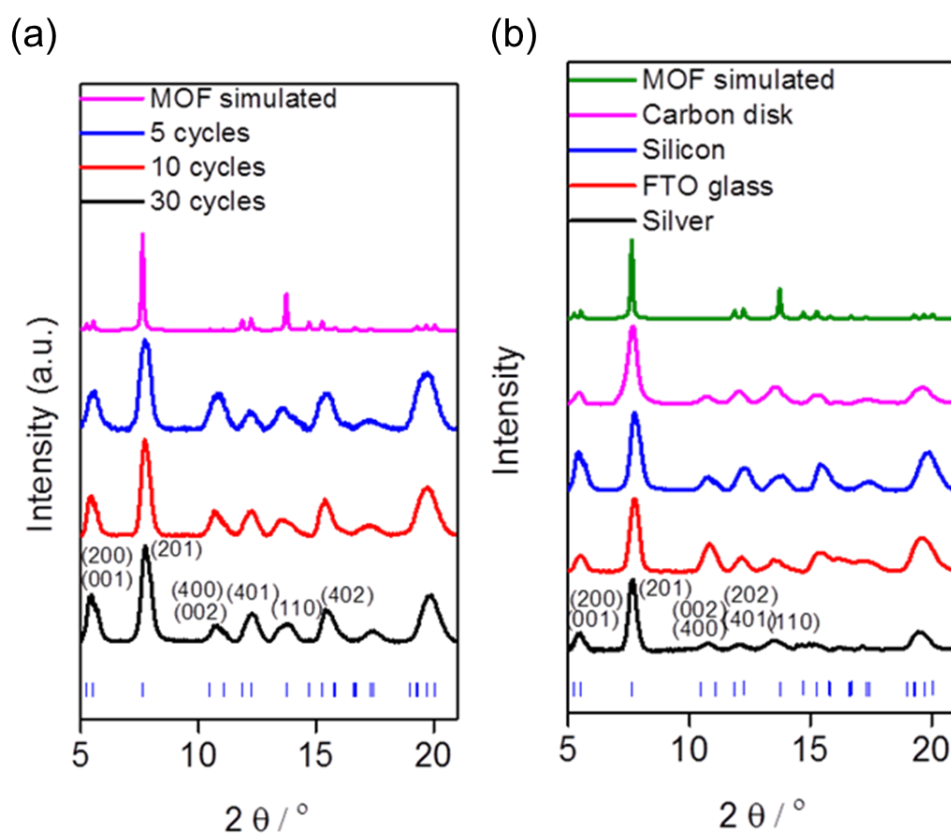


Figure A2.10. 1-D scattering profiles of GIWAXS data of $\text{Al}_2(\text{OH})_2(\text{TCPP})$ MOF obtained from different thickness of ALD alumina on silicon (a) and on various substrates (b).

Section 2.6.6 Fabrication of Other MOFs on Silver Nanocrystals

This method of MOF fabrication is also applicable to a variety of MOFs made up of other metals. Here, the appropriate metal oxide could be used as a precursor. For example, a film of ALD indium oxide was used as the metal precursor to react with H₄TCPP to give an isorecticular (having the same net topology) indium MOF as the present aluminum MOF. Different linkers could also be used to react with the same oxide to give the corresponding MOF, as in the case of DUT-5⁷, in which biphenyl-4,4'-dicarboxylic acid was used. A member of a subclass of MOFs, ZIF-8, could also be fabricated using ALD zinc oxide. We expect that since this MOF fabrication approach is substrate independent, it is generalizable and can be extended to produce multiple oriented and ordered MOF enclosures on a variety of inorganic nanostructures.

In₂(OH)₂TCPP. The ALD of In₂O₃ is carried out at 150°C. The indium precursor used is trimethylindium. Typical pulse times for the indium precursor and water were both 2 s. Nitrogen was used as a carrier and purge gas in both processes at a flow rate of 10 sccm. In our experiments, indium oxide is deposited as an amorphous film. The indium oxide coated silver nanocrystals are then soaked in a stock solution of H₄TCPP (5 mg in 1.75 mL DMF, 0.25 mL H₂O). The indium oxide to In-TCPP MOF (which is assumed to have the same net topology as the Al(OH)₂(TCPP) MOF with the indium substituting the aluminum) nucleation is carried out under microwave irradiation at 140°C for 10 min. After the reaction, the substrate is rinsed extensively with DMF and ethanol.

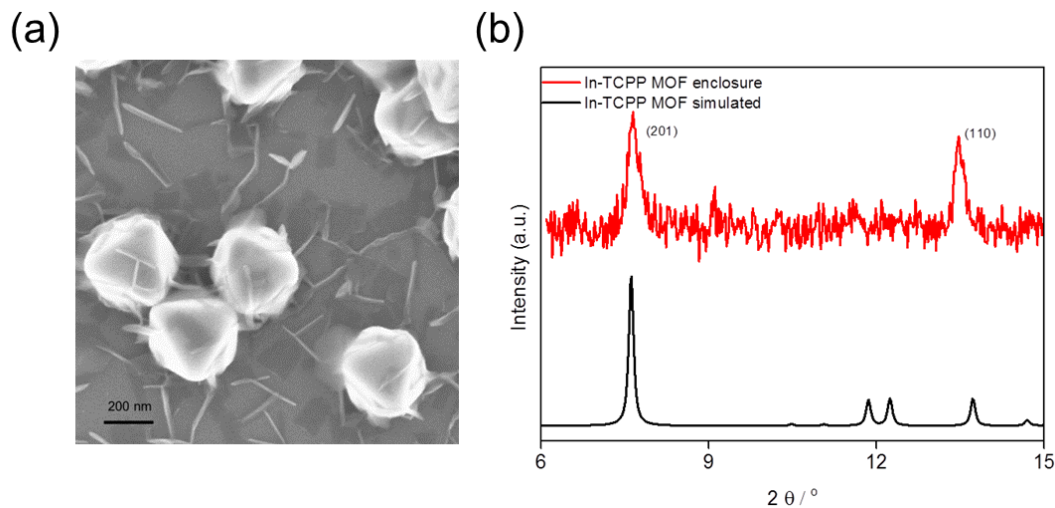


Figure A2.11. SEM image (a) and PXRD pattern (b) of In-TCPP MOF enclosures on silver nanocrystal.

DUT-5. Alumina is deposited on the ligand removed silver using the same ALD parameter. The alumina to MOF conversion is performed under microwave irradiation: the substrate is put into a 10 mL glass microwave vessel with 30 mg of the biphenyl-4,4'-dicarboxylic acid, 1.5 mL DMF and 0.5 mL H₂O and heated to 160°C for 20 min. The substrate is then taken out of the vessel and extensively washed with DMF and ethanol.

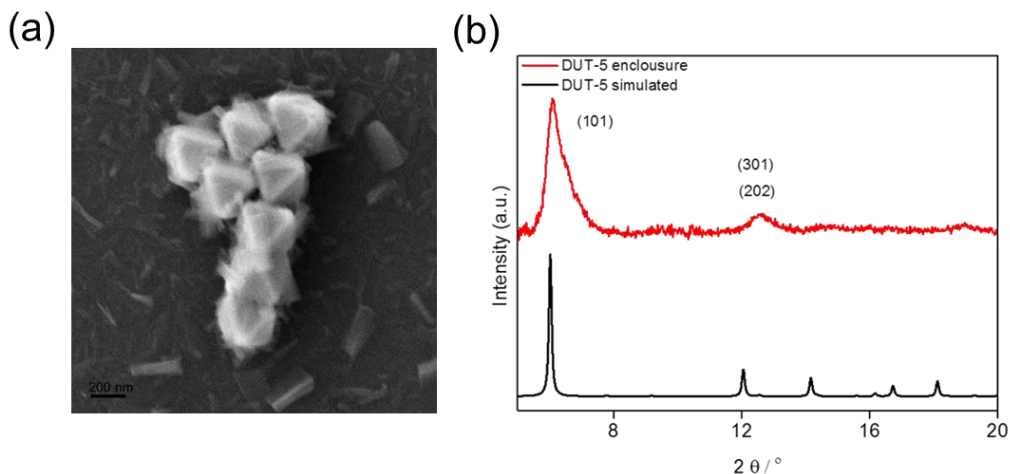


Figure A2.12. SEM image (a) and PXRD pattern (b) of DUT-5 enclosures on silver nanocrystal.

ZIF-8. The ALD of ZnO is carried out at 85°C. The zinc precursor used is diethylzinc, which is held at room temperature. Typical pulse times for the zinc precursor and water were 100 ms and 200 ms, respectively. Nitrogen was used as a carrier and purge gas in both processes at a flow rate of 10 sccm. The ZnO coated silver nanocrystals are then soaked in a 10 mL glass microwave vessel with 2 mL stock solution of 2-methylimidazole and CTAB (5.45g 2-methylimidazole, 11.1 mg CTAB dissolved in 70 mL H₂O). The addition of CTAB is not necessary but is used in this case as a modulator to give a cubic shaped MOF. The ZnO to MOF conversion is performed under microwave irradiation at 85°C for 10 min. The substrate is then washed extensively with water and ethanol.

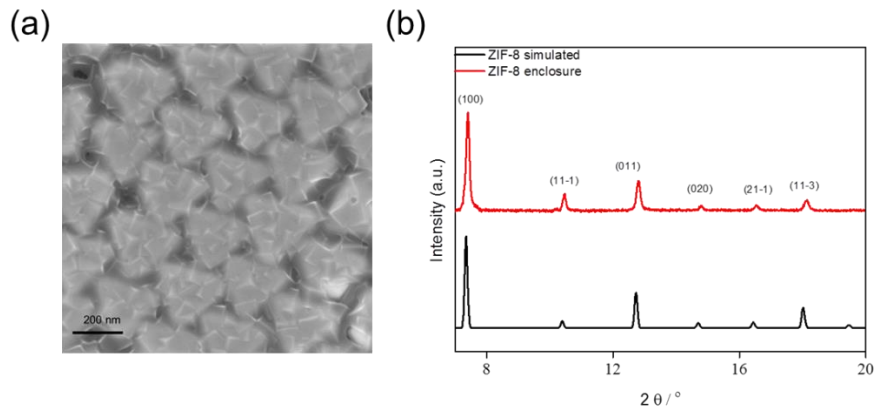


Figure A2.13. SEM image (a) and PXRD pattern (b) of ZIF-8 enclosures on silver nanocrystal.

Chapter 3. Application of MOF Thin Film in Electrochemical CO₂ Reduction

Section 3.1 Introduction

One of the most attractive approaches towards providing carbon-neutral energy is the electrochemical conversion of atmospheric carbon dioxide (CO₂) into energy dense carbon compounds to be used as fuels and chemical feedstock.¹⁻⁴ Extensive efforts have been devoted to the development of homogeneous and heterogeneous catalysts for this purpose. The outstanding challenges remain in the design of catalyst systems featuring (I) selectivity for CO₂ reduction in water with minimum H₂ generation, (II) long term stability, (III) catalytic efficiency at low electrochemical overpotential and (IV) compositions of earth abundant materials. In this report, we show that nanosized metal-organic frameworks (MOFs) meet these criteria and also present additional opportunities due to the modular nature of MOFs in which their organic and inorganic components can be functionalized and modified prior to precisely arranging in the MOF crystal structure.⁵⁻¹² We chose a stable cobalt porphyrin MOF where these porphyrin units are linked with aluminum oxide rods to form a three-dimensional porous structure with pores of 6 × 11 Å. Electrochemical CO₂ reduction studies were performed on thin films of this MOF, which was found to convert CO₂ to CO selectively (76% Faradaic efficiency) and with high turnover number (TON = 1400). *In situ* spectroelectrochemical measurements revealed that the Co(II) centers are reduced to Co(I) throughout the MOF and subsequently reduce CO₂. This is the first MOF catalyst construct for the electrocatalytic conversion of aqueous CO₂ to CO, and its high-performance characteristics are encouraging for the further development of this approach. (Reproduced with permission from *J. Am. Chem. Soc.* **2015**, 137, 14129. Copyright 2015 American Chemical Society.)

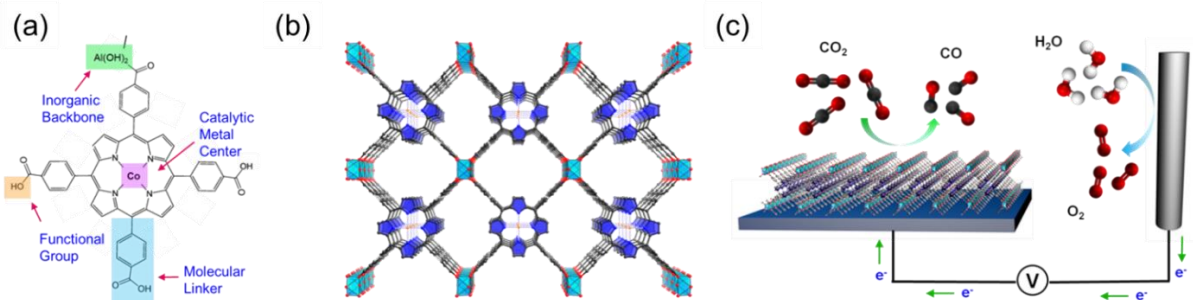


Figure 3.1. MOF catalyst allows for modulation of metal centers, molecular linkers, and functional groups at the molecular level (a). The organic building units, in the form of cobalt metalated TCPP, are assembled into a 3-dimensional MOF, Al₂(OH)₂TCPP-Co with variable inorganic building blocks (b). Co, orange spheres; O, red spheres; C, black spheres; N, blue spheres; Al, light blue octahedra; pyrrole ring, blue. In this structure, each carboxylate from (a) is bound to the aluminum inorganic backbone. The MOF is integrated with a conductive substrate to achieve a functional CO₂ electrochemical reduction system (c).

In the context of aqueous electrocatalytic CO₂ reduction studies where heterogeneous catalysts, such as metal foils,¹³⁻¹⁷ metal nanostructures,¹⁸⁻²⁶ oxide derived metals,²⁷⁻²⁹ 2-dimensional materials,³⁰ carbon nanomaterials,³¹⁻³³ as well as bio-inspired catalysts,³⁴⁻³⁸ and homogenous molecular catalysts³⁹⁻⁴⁸ are used; MOFs combine the favorable characteristics of both heterogeneous and homogeneous catalysts. Exploration of MOFs and COFs for CO₂ reduction has just begun through their use as photocatalysts in colloidal dispersions with the aid of sacrificial reagents,⁴⁹⁻⁵³ and MOFs have only recently been utilized as electrocatalysts for CO₂ reduction.⁵⁴⁻⁵⁷

Our strategy to construct the MOF-based electrochemical CO₂ reduction system was to select MOFs with catalytic linker units and fabricate them into thin films covering conductive substrates (Figure 3.1): appropriate catalytic linker units (Figure 3.1a) are assembled into a porous thin film MOF (Figure 3.1b) which is grown on a conductive substrate (Figure 3.1c). We first screened MOFs with systematically varied building blocks and then chose the most promising MOF catalyst for in depth electrochemical studies. The thickness of the selected MOF was next optimized to yield the final CO₂ reduction system, which was shown to be active, selective, and stable towards CO production. We also demonstrate that the majority of cobalt centers are reduced from Co(II) to Co(I) during the electrochemical process through *in situ* spectroelectrochemical measurements. Using MOFs as heterogeneous electrocatalysts represents an efficient strategy to reticulate catalytic molecular units into a porous network in which the number of active sites is maximized and both charge and mass transported could be simultaneously balanced by controlling the nanoscopic MOF morphology and thickness.

Section 3.2 Experimental Section

Section 3.2.1 Methods and Materials

Chemicals: *N,N*-Dimethylformamide (DMF) (99.8%), dimethyl sulfoxide (DMSO) (99.5%), anhydrous acetonitrile, potassium bicarbonate and cobalt(II) acetate tetrahydrate were purchased from Sigma Aldrich. FTO substrates (7 ohm/sq) were purchased from Sigma Aldrich and cut on-site into desirable dimensions. Aluminum chloride hexahydrate (99.9%) was purchased from Fluka. Ethanol was purchased from KOPTEC. 4,4',4'',4'''-(porphyrin-5,10,15,20-tetrayl)tetrabenzoic acid (H₄TCPP) was purchased from TCI. 2-Methylimidazole (99%) and biphenyl-4,4'-dicarboxylic acid (97%) were purchased from Aldrich. Trimethylaluminum and trimethylindium were purchased from Strem chemicals. Hydrochloric acid and anhydrous DMF were purchased from EMD Millipore. Sodium hydroxide and methanol were purchased from Fischer chemical. Carbon disk substrates are purchased from Ted Pella. All chemicals were used as received without further purification.

Atomic Layer Deposition: Atomic layer deposition (ALD) was performed with a home build thermal ALD system. Trimethylaluminum, trimethylindium, and water were used as aluminum, indium, and oxygen sources, respectively. Precursors were held in customized vessels to allow for pulsed delivery. Alumina deposition was carried out at 150 °C and indium oxide deposition was carried out at 200 °C. Pulse times for trimethylaluminum, trimethylindium, and water were 1.0, 2.0, and 0.5 seconds, respectively. Nitrogen functioned as both a purge and carrier gas and was flowed at a rate of 10 standard cubic centimeters per minute. Following the desired amount of ALD cycles, the chamber was purged with nitrogen and the samples were taken out and allowed

to cool naturally to room temperature in an air environment. The calibration of the amorphous alumina growth rate was previously performed with TEM measurements on a variety of surfaces and was consistently 0.1 nm/cycle.

Powder X-ray Diffraction: Powder X-ray diffraction (PXRD) patterns were acquired with a Bruker D8 Advance diffractometer (Cu K α radiation, $\lambda = 1.54056 \text{ \AA}$).

UV-Vis Spectroscopy: The optical absorption spectra were recorded using an UV-Vis-NIR scanning spectrophotometer equipped with an integration sphere (Shimadzu UV-3101PC). A quartz cuvette functioned as a one-compartment electrochemical cell with a Ag/AgCl reference and Pt wire counter electrode.

Section 3.2.2 Preparation, Characterization and Electrochemical Study of MOF Catalyst

MOF Synthesis: Following the ALD coating on the desired substrate, no further modifications were made and the substrate as-made was put through the MOF synthesis. MOF synthesis was performed in pyrex microwave vials using a CEM Discover-SP W/Activent microwave reactor. In a typical synthesis, the desired ALD coated sample was mixed with 5 mg of the H4TCPP, 1.5 mL DMF, and 0.5 mL water. The vessel is heated to 140 °C for 10 minutes. Following this, the sample is allowed to naturally cool to room temperature and washed with DMF and ethanol. Further purification is carried out by soaking the sample for 4 days in DMF and exchanging the liquid daily. After the DMF soak, the samples are soaked in acetone for 1 day and held under vacuum at room temperature for one more day. The growth of the MOF thin films is believed to occur via a dissolution-recrystallization mechanism. XRD, UV-Vis absorption, HRTEM, and GIWAXS measurements all confirm the identity and phase purity of the MOF.

Electrochemistry: For all experiments, 0.5 M potassium carbonate was used as the electrolyte. Prior to electrochemical testing, the electrolyte was purified overnight by applying 2V potential difference between a working and counter Ti foil electrodes to remove trace metals salts and organic species. A standard 3 electrode setup was employed with a titanium counter electrode and Ag/AgCl reference electrode. For product quantification, a home-built 2 compartment setup was used that featured a nafion membrane separating the working and counter compartments. All current densities are normalized by projected surfaces area.

Gas Chromatography: A home-built electrochemical cell was utilized for quantitative product measurement. The cell had two compartments separated by a nafion membrane to prevent product oxidation at the counter electrode. A flow mode was used to quantify gas products. Liquid products were quantified after the electrochemical measurement. During the chronoamperometric measurement, gas from the cell was directed through the sampling loop of a gas chromatograph (SRI) and was analyzed in 20 min intervals. The gas chromatograph was equipped with a molecular sieve 13X and hayesep D column with Ar (Praxair, 5.0 Ultra high purity) flowing as a carrier gas. The separated gas products were analysed by a thermal conductivity detector (for H₂) and a flame ionization detector (for CO and gaseous hydrocarbons). Liquid products were analyzed afterwards by quantitative NMR (Bruker AV-500) using dimethyl sulphoxide as an internal standard.

ICP-AES: ICP-AES is performed on a PerkinElmer optical emission spectrometer Optima 7000DV instrument. Carbon disk (5.25 cm²) coated with the MOF is put in the bottom of a 20 mL glass vial with an acid resistance cap. 2 mL of 99.5% nitric acid is then added to the vial and reacted violently with the carbon disk, where the carbon disk is exfoliated and deformed.

Substantial amount of heat is released during the process and orange smoke, presumably NO₂, is generated. 2 minutes later, 2 mL deionized water is added to dilute the acid so that the oxidation of the carbon disk is terminated. This solution is kept for 3 days to completely digest the MOF. Next, 4 mL of deionized water is added to the vial to further dilute the nitric acid. The clear solution for ICP measurement is obtained by centrifuging this carbon-nitric acid mixture at 4400 rpm for 1 minute and collecting the supernatant. The concentration of cobalt in this solution is determined to be 3.8 ppm with approximately 10% error, giving a total cobalt amount of 30.4 micrograms, which is calculated to be 5.1×10^{-7} molar. Considering the overall surface area of 5.25 cm² on the carbon disk, the cobalt loading on carbon disk is 6.1×10^{16} cobalt atom per square centimeter.

Spectroelectrochemistry: Fluorine-doped tin oxide (FTO) coated glass (7 ohm/sq) was utilized as a transparent conducting substrate for in situ spectroelectrochemical measurements. The alumina deposition and conversion to MOF procedure was identical as to the carbon disk substrate. A quartz 5 mL cell served as one compartment electrochemical cell, with Ag/AgCl and Pt serving as reference and counter electrodes, respectively. The cell was filled with 0.5 M carbonate buffer saturated with carbon dioxide prior to measurements, and a carbon dioxide atmosphere was maintained throughout. The FTO working electrode was held at the desired potential for 3 minutes to reach steady state conditions before acquiring a spectrum. A Shimadzu-3101 PC spectrometer fitted with an integrating sphere was used for all measurements.

Raman Spectroscopy: Raman measurements are performed on a Horiba Labram JY HR 800 with an Olympus SMPLN 100X objective. A 532 nm diode laser was utilized as an excitation source. An open one compartment cell served as the in situ cell for the measurement with Ag/AgCl and Pt functioning as the reference and counter electrodes, respectively. The electrolyte used was 0.5 M potassium carbonate, saturated with carbon dioxide. Surface enhanced Raman spectroscopy (SERS) substrates were fabricated through electrochemically roughening silver films. First, 300 nm of silver was thermally evaporated onto a titanium foil substrate. Next, the silver was electrochemically roughened through oxidation-reduction cycles in 3 M potassium chloride electrolyte. The silver coated titanium electrode was cycled 10 times between -1.2 V and 0.3 V vs. RHE at 50 mV/second. All SERS measurements were conducted at steady state conditions.

Grazing Incidence Wide Angle X-ray Scattering (GIWAXS): GIWAXS spectra were acquired with a Pilatus 2M (Dectris) instrument on beamline 7.3.3 at the Advanced Light Source, Lawrence Berkeley National Laboratory ($\lambda = 1.24 \text{ \AA}$). The incidence angle was held at 0.12° to optimize signal collection. Silver behenate was used to calibrate the sample-detector distance and the beam center. The Nika package for IGOR Pro (Wavemetrics) was utilized to reduce the acquired 1-D raw data to a 2D format.

Due to the fact that the carbon disks are covered by the salt precipitating from the electrolyte after electrolysis, the GIWAXS measurements on those samples are not successful due to the strong scattering of the residue salts near the surface on high angle saturating the detector. The SEM images are also influenced by the presence of the salt.

MOF Stability Characterization: Due to the fact that the carbon disks are covered by the salt precipitating from the electrolyte after electrolysis, the GIWAXS measurements on those samples are not successful due to the strong scattering of the residue salts near the surface on high angle saturating the detector. The SEM images are also influenced by the presence of the salt.

Section 3.3 Results and Discussion

Section 3.3.1 Catalytic Activity Screening of $\text{Al}_2(\text{OH})_2\text{TCPP-M}'$ MOFs

The catalysts we selected in this work are the $\text{Al}_2(\text{OH})_2\text{TCPP-H}_2$ series [TCPP- $\text{H}_2 = 4,4',4'',4'''$ - (porphyrin-5,10,15,20-tetrayl)tetrabenzoate],⁵⁸ which incorporate the porphyrin-based molecular units previously reported as selective and efficient homogeneous CO_2 reduction electrocatalysts.^{40,59,60} Specifically, the cobalt metalated porphyrin units are known to be of particular interest for CO_2 reduction and are explored in detail in this work.⁶¹⁻⁶³ The advantage over using molecular porphyrins as homogeneous catalysts is that each active site is simultaneously exposed to the electrolyte and electrically connected to the conductive support. We employ our previously developed methodology for thin-film MOF synthesis,⁶⁴ which involves the ALD deposition of metal oxide thin films as metal precursors onto the electrode and subsequent MOF creation through reacting the coated electrode with the appropriate linker in a DMF solvent in a microwave reactor.⁶⁵

Initially, we studied the effect of employing different metal centers in the porphyrin units on the catalytic properties of the MOF. We began with 50 ALD cycles of alumina thin films (thickness of 5 nm) deposited onto conductive carbon disk electrodes, and converted the alumina film to porphyrin-containing MOF [$\text{Al}_2(\text{OH})_2\text{TCPP-M}'$] structures with free-base porphyrin as well as porphyrin centers metalated with $\text{M}' = \text{Zn, Cu, and Co}$. Cyclic voltammetry (CV) measurements of the synthesized metalated porphyrin containing MOFs under an argon or carbon dioxide environment were used to screen the MOF catalytic performance. The voltammogram traces feature redox waves attributed to the reduction of the metal centers and catalytic peaks stemming from the reduction of either protons or aqueous CO_2 , qualitatively matching the behavior of previously studied analogous porphyrin homogeneous catalysts.⁵⁹ Notably, the cobalt metalated MOF exhibits the highest relative increase in current density after saturating the solution with carbon dioxide (1 atm, 33 mM concentration), increasing from 3.5 to 5.9 mA/cm^2 . Hence, this particular catalyst is chosen for further in-depth examination. Previous works have reported differences in activity and selectivity amongst porphyrins and porphyrin analogues with different metal centers and cobalt was consistently among the best.^{66,67} The increase in current density under a CO_2 atmosphere for this catalyst may be due to the preferred binding to CO_2 and increased kinetics of CO_2 reduction relative to hydrogen generation for this active site. To exhibit a further layer of modularity with our MOF-based catalyst design, we modified the inorganic backbone to prepare cobalt metalated [$\text{M}_2(\text{OH})_2\text{TCPP-Co}$, $\text{M} = \text{Al and In}$] MOFs (Appendix, Figure A3.2). The In and In-Al based MOF catalysts also exhibit significant current density increases under a CO_2 saturated aqueous bicarbonate electrolyte relative to an argon bubbled electrolyte, suggesting that the porphyrin units are the essential catalytic active center and the inorganic backbone may be tuned for additional purposes.

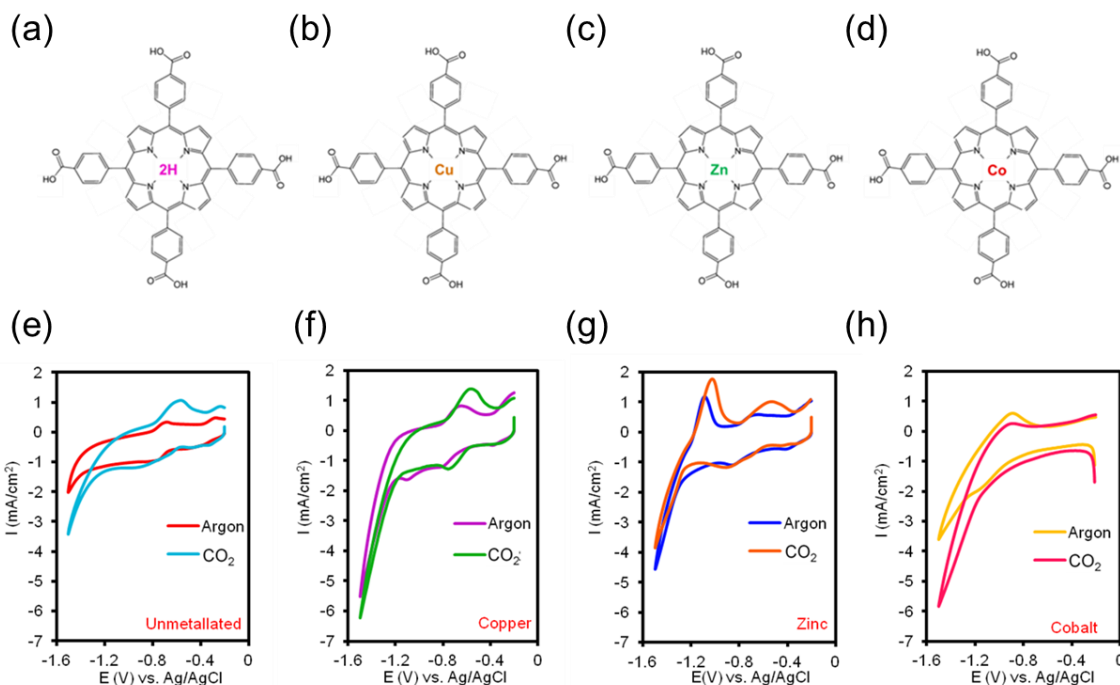


Figure 3.2. Catalytic performance screening of $\text{Al}_2(\text{OH})_2\text{TCPP-M}$ series of MOFs. The electrochemical performance of thin film MOFs with catalytic units comprised of porphyrins that were un-metalated (a) or metalated with copper (b), zinc (c), and cobalt (d) was evaluated. Each MOF displayed an increase in current density in a CO_2 saturated solution (e-h), with the cobalt metalated system showing the biggest increase

Section 3.3.2 Catalytic Performance of $\text{Al}_2(\text{OH})_2\text{TCPP-Co}$ MOF Thin Films

Based on our initial catalyst screening, we focused our subsequent investigation on the $[\text{Al}_2(\text{OH})_2\text{TCPP-Co}]$ MOF. The voltammogram trace of this MOF showed an enhanced current density under a CO_2 saturated solution relative to argon saturated solution and displayed a redox couple in addition to an irreversible catalytic peak (Figure 3.3a). Increasing the CV scan rates (Figure 3.3b) illustrated that a cathodic wave centered roughly -0.4 to -0.5 V vs. reversible hydrogen electrode (RHE), an irreversible catalytic peak immediately following, and an anodic peak at -0.2 V vs. RHE increase in magnitude linearly proportional to the square root of the sweep rate, indicative of a diffusion limited process (Figure 3.3c).^{68,69} The first cathodic wave and the lone anodic wave are likely due to counter ion diffusion to balance a Co(II/I) redox change and the irreversible cathodic peak, which is not voltammetric, at the most negative potentials stems from the diffusion and subsequent reduction of carbon dioxide. The anodic-cathodic wave separation increased from ~100 mV to ~250 mV with increasing sweep rate, which provided further evidence that the underlying reaction is not a simple reversible redox process. Previous electrochemical studies of cobalt porphyrins have attributed a cathodic wave at approximately -0.5 V vs. RHE to the reduction of the Co(II) to Co(I) center and we see similar behavior for the homogeneous $\text{H}_4\text{TCPP-Co}$ (Appendix, Figure A3.5).⁷⁰ Spectroelectrochemical studies confirmed the chemical nature of this cathodic wave as discussed below.

Balancing reactant diffusion and charge transport is essential for electrochemical catalysis. To this end, the thickness of the MOF catalyst film was tuned to optimize the performance of the MOF catalyst by varying the starting ALD alumina layer thickness from 0.5 to 10 nm (Figure 3.3d). Upon testing a carbon disk electrode with only 5 layers (0.5 nm) of ALD precursor converted to the MOF, resulting in a ~10 nm thick MOF layer, we observed a two-fold increase in the catalytic current density (measured at -0.57 V vs. RHE at a sweep rate of 100 mV/s) relative to the bare carbon disk substrate. The performance of the MOF catalyst increased with increasing active site loading until reaching a maximum at 50 ALD cycles (MOF thickness of ~30-70 nm). Inductively coupled plasma atomic emission absorption (ICP-AES) was utilized to quantify the total cobalt loading on this sample and indicated an upper limit of 6.1×10^{16} cobalt atoms (1.1×10^{-7} mol) per cm^2 . The performance decrease observed for higher active site loading is likely limited by charge transport limitations from the electrode to the MOF periphery or impedance through a thin insulating alumina layer not fully converted to the MOF. This result highlights the strength of our ALD-based MOF conversion technique, which allows nanometer precision of catalyst loading to balance active site density with mass/charge transfer.

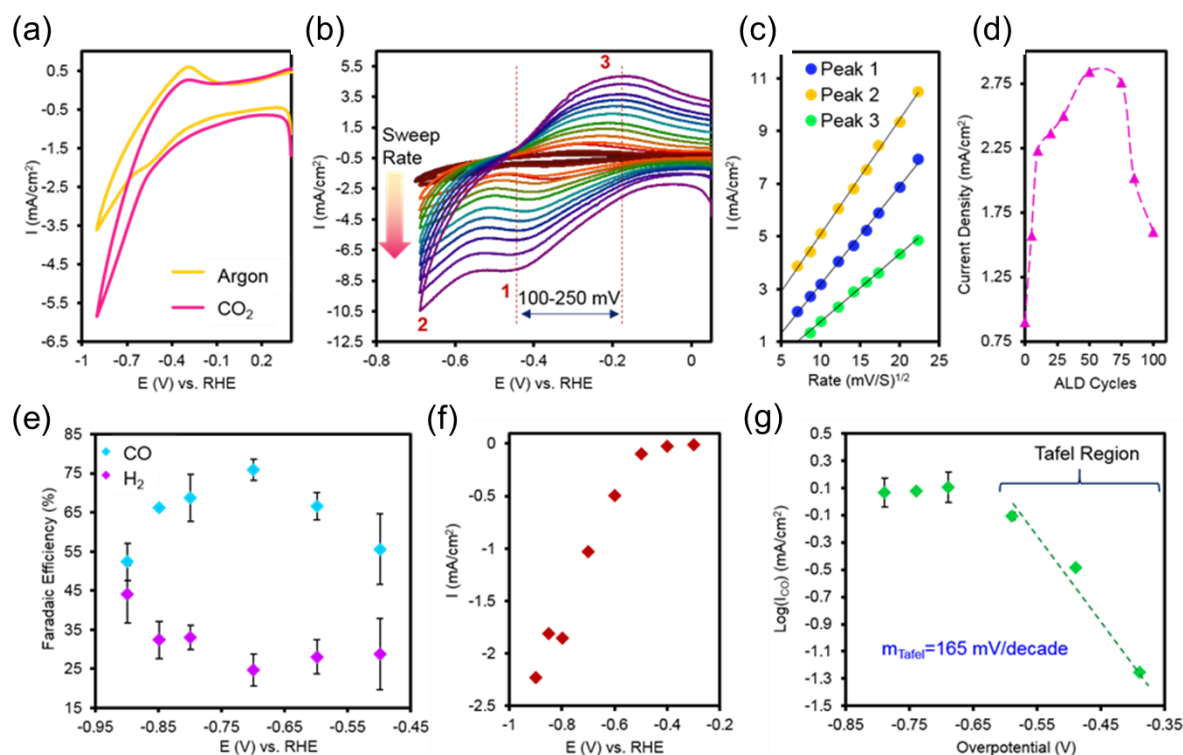


Figure 3.3. Electrochemical CO_2 reduction catalyzed by $\text{Al}_2(\text{OH})_2\text{TCPP-Co}$ MOF thin films. The voltammogram trace of the MOF catalyst exhibits a current increase in a CO_2 environment relative to an argon saturated environment (a). As the scan rate is systematically increased in a CO_2 saturated electrolyte (b), the electrochemical waves increase in magnitude proportional to the square root of the scan rate (c), indicative of a diffusion limited process. The MOF catalytic performance is maximized at a starting layer thickness of 50 ALD cycles (d), which offers a balance of charge transport, mass transport, and active site density. The selectivity for each product is tested over a potential range of -0.5 to -0.9 vs. RHE (e) and reaches upwards of 76% for CO. The steady state current density for product quantification is illustrated in (f). In the low overpotential region, the Tafel slope of 165 mV/decade is closest to that of a one-electron reduction from CO_2 to the CO_2^- rate limiting step (g).

Comprehensive product analysis using gas chromatography (GC) and nuclear magnetic resonance (NMR) was carried out to reveal the nature of the chemical processes occurring within our MOF catalysts (Figure A3.6). As illustrated in Figure 3.3e, the two main products measured were CO and H₂, with current selectivity for CO reaching up to 76% at -0.7 V vs. RHE. The average steady state current density from these measurements is displayed in Figure 3.3f. In contrast, the un-metallated MOF produces primarily H₂ (Figure A3.7). When plotting the partial current density for CO production on a logarithmic scale vs. the thermodynamic overpotential (Figure 3.3g) we obtain a Tafel slope of 165 mV/decade in the low overpotential region, which points to a one electron reduction of CO₂ to form the CO₂⁻ radical as a probable rate limiting step, though the reaction is likely to be at least in part diffusion limited.^{16,71-73} However, the exact nature of the rate limiting step is difficult to determine from the Tafel slope alone, especially in a more complicated system such as ours. For comparison, studies of porphyrin homogeneous catalysts have measured Tafel slopes ranging from 100 to 300 mV/decade; thus, the rate limiting step and mechanism may depend on more than just the active site itself.⁷⁴⁻⁷⁶ We stress that this is the first incarnation of our MOF electrocatalyst and efforts are being undertaken to further exploit the modular nature of such systems for the next generation of catalyst.

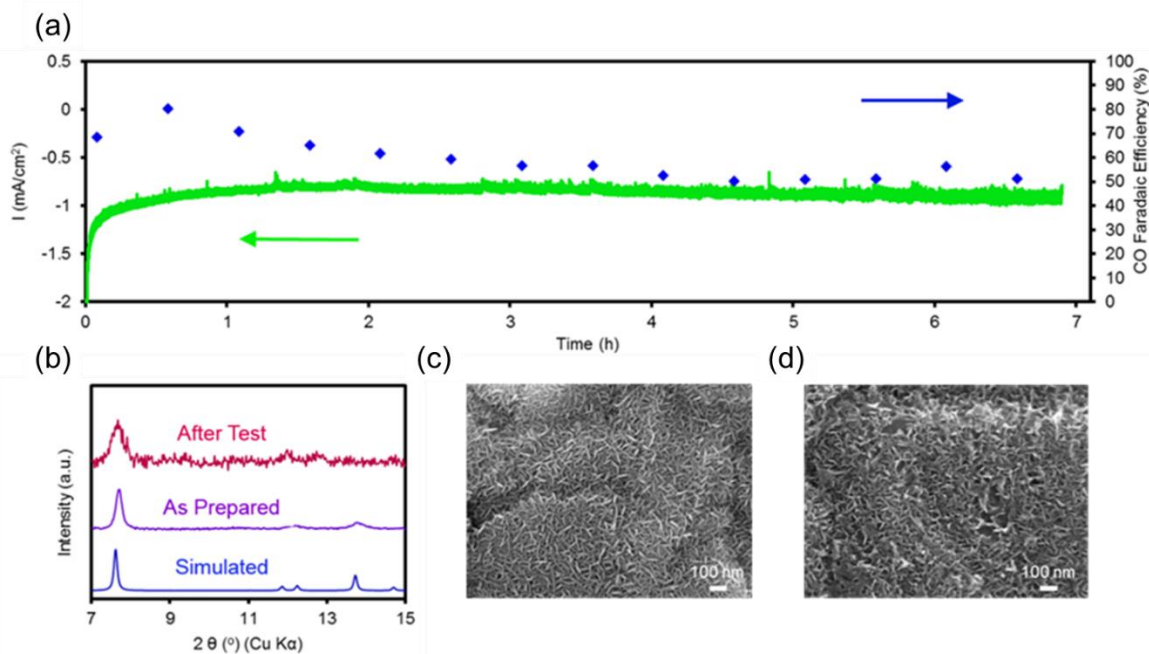


Figure 3.4. The stability of the Al₂(OH)₂TCPP-Co MOF catalyst. The catalyst stability was evaluated through chronoamperometric measurements in combination with faradaic efficiency measurements (a) The green trace represents geometric current density and blue diamonds denote CO Faradaic efficiency. XRD analysis indicates that the MOF retains its crystalline structure after chronoamperometric measurement (b). SEM images of the MOF catalyst film before (c) and after electrolysis (d) reveal the retention of the plate-like morphology.

The stability of the MOF catalyst was next tested over an extended period of time. In controlled potential electrolysis at -0.7 V vs. RHE in carbon dioxide-saturated aqueous bicarbonate buffer, the current density reached a stable state after several minutes and subsequently showed no sign of decrease for up to 7 h, generating 16 mL of CO (0.71 mmol, 5.25 cm² substrate) (Figure 3.4a). The lower limit of the TON of the MOF catalyst is quantified through ICP analysis of the electrode after a testing and is measured to be 1400 assuming every cobalt atom is an electrochemically

active site (Turnover frequency (TOF) = $\sim 200 \text{ h}^{-1}$). The MOF largely retains its crystallinity after electrolysis and preservation of the framework was evidenced through the retention of the major powder X-ray diffraction (XRD) peaks (Figure 3.4b). Furthermore, scanning electron microscopy (SEM) analysis reveals the plate-like morphology has been retained (Figure 3.4c, d). *In situ* surface enhanced Raman spectroscopy (SERS) was utilized to confirm the integrity of the organic units throughout the catalytic process (Figure A2.10). At each applied potential, the primary SERS peaks attributed to the porphyrin linker remain in the SERS spectrum.

Section 3.3.3 Oxidation State Study of $\text{Al}_2(\text{OH})_2\text{TCPP-Co}$ Catalyst

In situ spectroelectrochemical testing was next employed to ascertain the cobalt oxidation state under operating conditions. Such techniques have proven valuable for studying the electronic structure of porphyrins.^{70,77-83} We grew the MOF on a transparent conductive fluorine-doped tin oxide (FTO) substrate and measured the film UV-Vis absorbance for a series of applied electrochemical potentials (Figure 3.5a). A typical absorption of the cobalt-metalated $[\text{Al}_2(\text{OH})_2\text{TCPP-Co}]$ MOF in open circuit states featured a Soret band ($S_0 \rightarrow S_2$) at 422 nm and a Q-band ($S_0 \rightarrow S_1$) at 530 nm. The increase in absorbance at lower wavelengths has also been attributed to the back-donation of Co(I) into the porphyrin system.⁶² Upon applying increasingly negative potential (0 to -0.7 V vs. RHE) to the FTO/MOF electrode in a CO_2 saturated electrolyte, the Soret band at steady state conditions decreases in intensity at 422 nm and increases at 408 nm, with isosbestic points at 413 nm and 455 nm (Figure 3.5a). Plotting the difference spectra (Figure 3.5b) illustrates the band bleach and increase in the aforementioned spectral regions, which is subsequently quantified to deduce the formal redox potential ($E_{1/2}$) of the cobalt center in our system. The peak in the first derivative of the difference magnitude in these two wavelengths signified the formal reduction potential of the cobalt porphyrin unit in the MOF at -0.4 V vs. RHE (Figure 3.5c), which is consistent with the position of the first cathodic wave in the voltammogram trace. However, even at more positive potentials than -0.4 V vs. RHE, a fraction of the cobalt centers are still reduced and are likely to be participating in the catalytic conversion of CO_2 to CO .

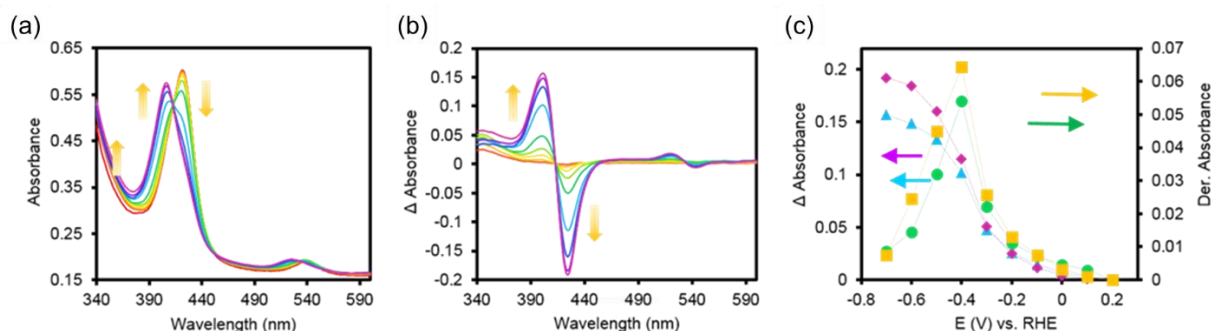


Figure 3.5. *In situ* spectroelectrochemical analysis reveals the oxidation state of the cobalt porphyrin unit of the MOF under reaction conditions. Upon varying the voltage from 0.2 to -0.7 V vs. RHE, the Co(II) Soret band decreases at 422 nm and is accompanied by a Co(I) Soret band increase at 408 nm (a). This change is quantified (b) and plotted to elucidate a formal redox potential of the Co center, which is deemed to be at the peak of the first derivative (c) of the Co(II) bleach and Co(I) enhancement.

The buildup of a Co(I) species under operating conditions and a Tafel slope of 165 mV/decade indicates that the rate limiting step in our reaction mechanism may be either a CO₂ molecule adsorbing onto a Co(I) porphyrin coupled with a one electron reduction or a one electron reduction of a Co(I)-CO₂ adduct. We stress the importance of this spectroelectrochemical data in signifying that the majority of the cobalt centers are electrically connected to the electrode and are reduced to the catalytically active Co(I) state.

Section 3.4 Conclusion

We have adapted the method to fabricate the MOF enclosure on *O_h*-nano-Ag@MOF mesoscopic constructs to prepare thickness controlled thin film of Al₂(OH)₂TCP-*M'* (*M'*=Co, Zn, Cu, H₂) MOF on carbon disks. We further applied this approach to fabricate M(OH)₂TCP-Co MOF (*M*=Al, In) with controllable aluminum and indium distribution on carbon disk and silicon nanowire. We screened the M₂(OH)₂TCP-*M'* MOF as catalysts for electrochemical carbon dioxide reduction and found that composition of the inorganic building block of MOF (aluminum or indium) gave similar catalytic performance, while cobalt metalated porphyrin gave best catalytic performance among other metalated porphyrin linkers.

The catalytic performance of the Al₂(OH)₂TCP-Co MOF thin film was subjected to in-depth study. The thickness of the film was optimized according to the catalytic current. With increasing film thickness, the current first increase due to higher catalyst loading then decreased due to limitation in electron and CO₂ transport in the MOF layer, thus giving an optimized thickness of 50 nm. For MOF film of optimized thickness, the faradic efficiency of CO reach 76% at -0.7 V vs. RHE with TOF of 200 h⁻¹. The catalyst was stable for at least 7 h giving a TON of 1400.

In the catalytic conversion, the cobalt center of the MOF linker was first reduced to Co(I) before reducing CO₂ to CO. The MOF thin film was found to be fully electrocatalytically active by *in situ* spectroelectrochemical measurements.

This study verified the applicability of MOF-integrated catalytic systems as modular platforms for the electrochemical reduction of aqueous CO₂. This study represents the development of the first generation of MOF-based CO₂ reduction electrocatalysts in which the active site, inorganic backbone, and thickness/loading were rationally chosen and the resulting MOF integrated onto a conductive support. The modularity of these systems yields many opportunities to further improve performance and open new directions in electrocatalysis.

Section 3.5 References

- (1) Appel, A. M.; Bercaw, J. E.; Bocarsly, A. B.; Dobbek, H.; DuBois, D. L.; Dupuis, M.; Ferry, J. G.; Fujita, E.; Hille, R.; Kenis, P. J. *Chem. Rev.* **2013**, 113, 6621.
- (2) Aresta, M.; Dibenedetto, A.; Angelini, A. *Chem. Rev.* **2013**, 114, 1709.
- (3) Costentin, C.; Robert, M.; Savéant, J.-M. *Chem. Soc. Rev.* **2013**, 42, 2423.
- (4) Quadrelli, E. A.; Centi, G.; Duplan, J. L.; Perathoner, S. *ChemSusChem* **2011**, 4, 1194.
- (5) Yaghi, O. M.; Li, H.; Davis, C.; Richardson, D.; Groy, T. L. *Acc. Chem. Res.* **1998**, 31, 474.

- (6) Yaghi, O. M.; O'Keeffe, M.; Ockwig, N. W.; Chae, H. K.; Eddaoudi, M.; Kim, J. *Nature* **2003**, 423, 705.
- (7) Lee, J.; Farha, O. K.; Roberts, J.; Scheidt, K. A.; Nguyen, S. T.; Hupp, J. T. *Chem. Soc. Rev.* **2009**, 38, 1450.
- (8) Zhou, H.-C.; Long, J. R.; Yaghi, O. M. *Chem. Rev.* **2012**, 112, 673.
- (9) Kuppler, R. J.; Timmons, D. J.; Fang, Q.-R.; Li, J.-R.; Makal, T. A.; Young, M. D.; Yuan, D.; Zhao, D.; Zhuang, W.; Zhou, H.-C. *Coord. Chem. Rev.* **2009**, 253, 3042.
- (10) Wang, Z.; Cohen, S. M. *Chem. Soc. Rev.* **2009**, 38, 1315.
- (11) An, J.; Rosi, N. L. *J. Am. Chem. Soc.* **2010**, 132, 5578.
- (12) Kitagawa, S.; Kitaura, R.; Noro, S. i. *Angew. Chem. Int. Ed.* **2004**, 43, 2334.
- (13) Hori, Y.; Murata, A.; Takahashi, R. *J. Chem. Soc. Faraday Trans. 1* **1989**, 85, 2309.
- (14) DeWulf, D. W.; Jin, T.; Bard, A. J. *J. Electrochem. Soc.* **1989**, 136, 1686.
- (15) Rosen, B. A.; Salehi-Khojin, A.; Thorson, M. R.; Zhu, W.; Whipple, D. T.; Kenis, P. J.; Masel, R. I. *Science* **2011**, 334, 643.
- (16) Kuhl, K. P.; Cave, E. R.; Abram, D. N.; Jaramillo, T. F. *Energy Environ. Sci.* **2012**, 5, 7050.
- (17) Hoshi, N.; Kato, M.; Hori, Y. *J. Electroanal. Chem.* **1997**, 440, 283.
- (18) Kim, D.; Resasco, J.; Yu, Y.; Asiri, A. M.; Yang, P. *Nat. Commun.* **2014**, 5, 4948.
- (19) Zhu, W.; Michalsky, R.; Metin, O. n.; Lv, H.; Guo, S.; Wright, C. J.; Sun, X.; Peterson, A. A.; Sun, S. *J. Am. Chem. Soc.* **2013**, 135, 16833.
- (20) Zhu, W.; Zhang, Y.-J.; Zhang, H.; Lv, H.; Li, Q.; Michalsky, R.; Peterson, A. A.; Sun, S. *J. Am. Chem. Soc.* **2014**, 136, 16132.
- (21) Zhang, S.; Kang, P.; Meyer, T. J. *J. Am. Chem. Soc.* **2014**, 136, 1734.
- (22) Manthiram, K.; Beberwyck, B. J.; Alivisatos, A. P. *J. Am. Chem. Soc.* **2014**, 136, 13319.
- (23) Gao, D.; Zhou, H.; Wang, J.; Miao, S.; Yang, F.; Wang, G.; Wang, J.; Bao, X. *J. Am. Chem. Soc.* **2015**, 137, 4288.
- (24) Medina-Ramos, J.; Pupillo, R. C.; Keane, T. P.; DiMeglio, J. L.; Rosenthal, J. *J. Am. Chem. Soc.* **2015**, 137, 5021.
- (25) Medina-Ramos, J.; DiMeglio, J. L.; Rosenthal, J. *J. Am. Chem. Soc.* **2014**, 136, 8361.
- (26) Lu, Q.; Rosen, J.; Zhou, Y.; Hutchings, G. S.; Kimmel, Y. C.; Chen, J. G.; Jiao, F. *Nat. Commun.* **2014**, 5, 3242.
- (27) Li, C. W.; Kanan, M. W. *J. Am. Chem. Soc.* **2012**, 134, 7231.
- (28) Chen, Y.; Kanan, M. W. *J. Am. Chem. Soc.* **2012**, 134, 1986.

- (29) Chen, Y.; Li, C. W.; Kanan, M. W. *J. Am. Chem. Soc.* **2012**, 134, 19969.
- (30) Asadi, M.; Kumar, B.; Behranginia, A.; Rosen, B. A.; Baskin, A.; Repnin, N.; Pisasale, D.; Phillips, P.; Zhu, W.; Haasch, R. *Nat. Commun.* **2014**, 5, 4470.
- (31) Wu, J.; Yadav, R. M.; Liu, M.; Sharma, P. P.; Tiwary, C. S.; Ma, L.; Zou, X.; Zhou, X.-D.; Yakobson, B. I.; Lou, J. *ACS Nano* **2015**, 9, 5364.
- (32) Zhang, S.; Kang, P.; Ubnoske, S.; Brennaman, M. K.; Song, N.; House, R. L.; Glass, J. T.; Meyer, T. J. *J. Am. Chem. Soc.* **2014**, 136, 7845.
- (33) Kumar, B.; Asadi, M.; Pisasale, D.; Sinha-Ray, S.; Rosen, B. A.; Haasch, R.; Abiade, J.; Yarin, A. L.; Salehi-Khojin, A. *Nat. Commun.* **2013**, 4, 2819.
- (34) Liu, C.; Gallagher, J. J.; Sakimoto, K. K.; Nichols, E. M.; Chang, C. J.; Chang, M. C.; Yang, P. *Nano Lett.* **2015**, 15, 3634.
- (35) Torella, J. P.; Gagliardi, C. J.; Chen, J. S.; Bediako, D. K.; Colón, B.; Way, J. C.; Silver, P. A.; Nocera, D. G. *Proc. Natl. Acad. Sci. U. S. A.* **2015**, 112, 2337.
- (36) Reda, T.; Plugge, C. M.; Abram, N. J.; Hirst, J. *Proc. Natl. Acad. Sci. U. S. A.* **2008**, 105, 10654.
- (37) Schuchmann, K.; Müller, V. *Science* **2013**, 342, 1382.
- (38) Nichols, E. M.; Gallagher, J. J.; Liu, C.; Su, Y.; Resasco, J.; Yu, Y.; Sun, Y.; Yang, P.; Chang, M. C.; Chang, C. J. *Proc. Natl. Acad. Sci. U. S. A.* **2015**, 112, 11461.
- (39) Seshadri, G.; Lin, C.; Bocarsly, A. B. *J. Electroanal. Chem.* **1994**, 372, 145.
- (40) Costentin, C.; Drouet, S.; Robert, M.; Savéant, J.-M. *Science* **2012**, 338, 90.
- (41) Smieja, J. M.; Sampson, M. D.; Grice, K. A.; Benson, E. E.; Froehlich, J. D.; Kubiak, C. P. *Inorg. Chem.* **2013**, 52, 2484.
- (42) Fujita, E.; Haff, J.; Sanzenbacher, R.; Elias, H. *Inorg. Chem.* **1994**, 33, 4627.
- (43) Thoi, V. S.; Kornienko, N.; Margarit, C. G.; Yang, P.; Chang, C. J. *J. Am. Chem. Soc.* **2013**, 135, 14413.
- (44) Kang, P.; Cheng, C.; Chen, Z.; Schauer, C. K.; Meyer, T. J.; Brookhart, M. *J. Am. Chem. Soc.* **2012**, 134, 5500.
- (45) Schneider, J.; Jia, H.; Kobiro, K.; Cabelli, D. E.; Muckerman, J. T.; Fujita, E. *Energy Environ. Sci.* **2012**, 5, 9502.
- (46) Tornow, C. E.; Thorson, M. R.; Ma, S.; Gewirth, A. A.; Kenis, P. J. *J. Am. Chem. Soc.* **2012**, 134, 19520.
- (47) Richardson, R. D.; Holland, E. J.; Carpenter, B. K. *Nat. Chem.* **2011**, 3, 301.
- (48) Lacy, D. C.; McCrory, C. C.; Peters, J. C. *Inorg. Chem.* **2014**, 53, 4980.
- (49) Wang, C.; Xie, Z.; deKrafft, K. E.; Lin, W. *J. Am. Chem. Soc.* **2011**, 133, 13445.

- (50) Fu, Y.; Sun, D.; Chen, Y.; Huang, R.; Ding, Z.; Fu, X.; Li, Z. *Angew. Chem., Int. Ed.* **2012**, 124, 3420.
- (51) Liu, Y.; Yang, Y.; Sun, Q.; Wang, Z.; Huang, B.; Dai, Y.; Qin, X.; Zhang, X. *ACS Appl. Mater. Interfaces* **2013**, 5, 7654.
- (52) Li, L.; Zhang, S.; Xu, L.; Wang, J.; Shi, L.-X.; Chen, Z.-N.; Hong, M.; Luo, J. *Chem. Sci.* **2014**, 5, 3808.
- (53) Wang, D.; Huang, R.; Liu, W.; Sun, D.; Li, Z. *ACS Catal.* **2014**, 4, 4254.
- (54) Hinogami, R.; Yotsuhashi, S.; Deguchi, M.; Zenitani, Y.; Hashiba, H.; Yamada, Y. *ECS Electrochem. Lett.* **2012**, 1, H17.
- (55) Kumar, R. S.; Kumar, S. S.; Kulandainathan, M. A. *Electrochem. Commun.* **2012**, 25, 70.
- (56) Hod, I.; Sampson, M. D.; Deria, P.; Kubiak, C. P.; Farha, O. K.; Hupp, J. T. *ACS Catal.* **2015**, 5, 6302.
- (57) Lin, S.; Diercks, C. S.; Zhang, Y.-B.; Kornienko, N.; Nichols, E. M.; Zhao, Y.; Paris, A. R.; Kim, D.; Yang, P.; Yaghi, O. M. *Science* **2015**, 349, 1208.
- (58) Fateeva, A.; Chater, P. A.; Ireland, C. P.; Tahir, A. A.; Khimyak, Y. Z.; Wiper, P. V.; Darwent, J. R.; Rosseinsky, M. J. *Angew. Chem. Int. Ed.* **2012**, 124, 7558.
- (59) García, M.; Aguirre, M. J.; Canzi, G.; Kubiak, C. P.; Ohlbaum, M.; Isaacs, M. *Electrochim. Acta* **2014**, 115, 146.
- (60) Bonin, J.; Chaussemier, M.; Robert, M.; Routier, M. *ChemCatChem* **2014**, 6, 3200.
- (61) Leung, K.; Nielsen, I. M.; Sai, N.; Medforth, C.; Shelnut, J. A. *J. Phys. Chem. A* **2010**, 114, 10174.
- (62) Behar, D.; Dhanasekaran, T.; Neta, P.; Hosten, C.; Ejeh, D.; Hambright, P.; Fujita, E. *J. Phys. Chem. A* **1998**, 102, 2870.
- (63) Ramírez, G.; Lucero, M.; Riquelme, A.; Villagrán, M.; Costamagna, J.; Trollund, E.; Aguirre, M. J. *J. Coord. Chem.* **2004**, 57, 249.
- (64) Zhao, Y.; Kornienko, N.; Liu, Z.; Zhu, C.; Asahina, S.; Kuo, T.-R.; Bao, W.; Xie, C.; Hexemer, A.; Terasaki, O.; Yang, P.; Yaghi, O. M. *J. Am. Chem. Soc.* **2015**, 137, 2199.
- (65) Reboul, J.; Furukawa, S.; Horike, N.; Tsotsalas, M.; Hirai, K.; Uehara, H.; Kondo, M.; Louvain, N.; Sakata, O.; Kitagawa, S. *Nat. Mater.* **2012**, 11, 717.
- (66) The Journal of Physical Chemistry C Tripkovic, V.; Vanin, M.; Karamad, M.; Björketun, M. r. E.; Jacobsen, K. W.; Thygesen, K. S.; Rossmeisl, J. *J. Phys. Chem. C* **2013**, 117, 9187.
- (67) Qiao, J.; Liu, Y.; Hong, F.; Zhang, J. *Chem. Soc. Rev.* **2014**, 43, 631.
- (68) Bard, A. J.; Faulkner, L. R. *Electrochemical methods: fundamentals and applications*; Wiley New York, 1980.

- (69) Newman, J.; Thomas-Alyea, K. E. *Electrochemical systems*; John Wiley & Sons: Hoboken, New Jersey, 2012.
- (70) Ahrenholtz, S. R.; Epley, C. C.; Morris, A. J. *J. Am. Chem. Soc.* **2014**, 136, 2464.
- (71) Russell, P.; Kovac, N.; Srinivasan, S.; Steinberg, M. *J. Electrochem. Soc.* **1977**, 124, 1329.
- (72) Bandi, A. *J. Electrochem. Soc.* **1990**, 137, 2157.
- (73) Hatsukade, T.; Kuhl, K. P.; Cave, E. R.; Abram, D. N.; Jaramillo, T. F. *Phys. Chem. Chem. Phys.* **2014**, 16, 13814.
- (74) Riquelme, M.; Isaacs, M.; Lucero, M.; Trollund, E.; Aguirre, M.; Canales, J. *J. Chil. Chem. Soc.* **2003**, 48, 89.
- (75) Najafi, M.; Sadeghi, M. *ECS Electrochem. Lett.* **2013**, 2, H5.
- (76) Manbeck, G. F.; Fujita, E. *J. Porphyrins Phthalocyanines* **2015**, 19, 45.
- (77) Kung, C.-W.; Chang, T.-H.; Chou, L.-Y.; Hupp, J. T.; Farha, O. K.; Ho, K.-C. *Chem. Commun.* **2015**, 51, 2414.
- (78) Kadish, K.; Boisselier-Cocolios, B.; Coutsolelos, A.; Mitaine, P.; Guillard, R. *Inorg. Chem.* **1985**, 24, 4521.
- (79) Wei, Z.; Ryan, M. D. *Inorg. Chim. Acta.* **2001**, 314, 49.
- (80) Lin, X.; Boisselier-Cocolios, B.; Kadish, K. *Inorg. Chem.* **1986**, 25, 3242.
- (81) Quezada, D.; Honores, J.; García, M.; Armijo, F.; Isaacs, M. *New J. Chem.* **2014**, 38, 3606.
- (82) Kadish, K. M.; Van Caemelbecke, E. *J. Solid State Electrochem.* **2003**, 7, 254.
- (83) Kadish, K. M.; Smith, K. M.; Guillard, R. *The porphyrin handbook*; Academic Press, Amsterdam, 1999.

Section 3.6 Appendix

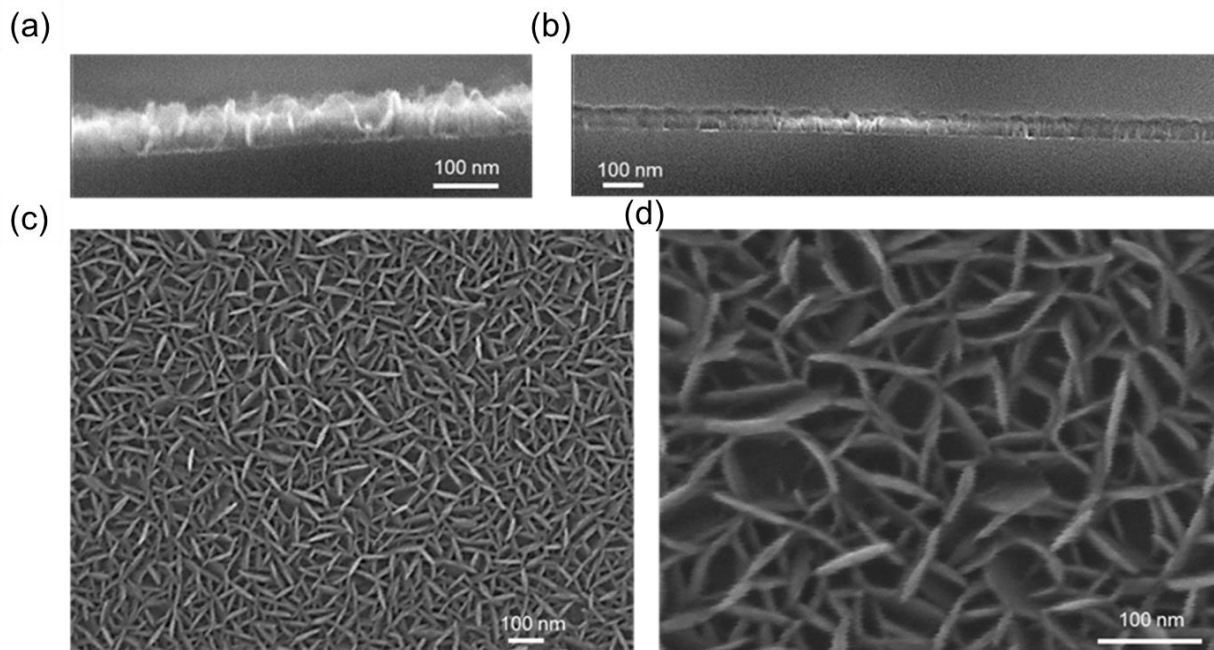


Figure A3.1. The typical morphology of the thin film MOF catalyst prepared from 50 cycles of ALD alumina as the starting material. Cross section (a,b) and top down (c,d) views depict a flake-like morphology of 30-70 nm thickness.

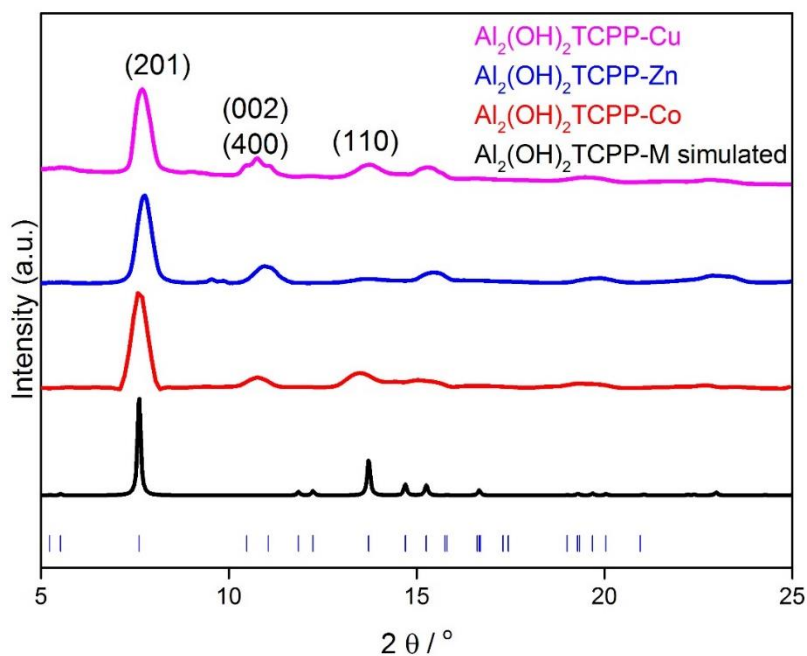


Figure A3.2 Integrated GIWAXS spectra reveal that the MOF with un-metalated and Co, Cu, and Zn metalated linkers grows in the same phase and crystallographic orientation. The X-axis of the spectra is converted to 2-theta values ($\text{Cu K}\alpha$).

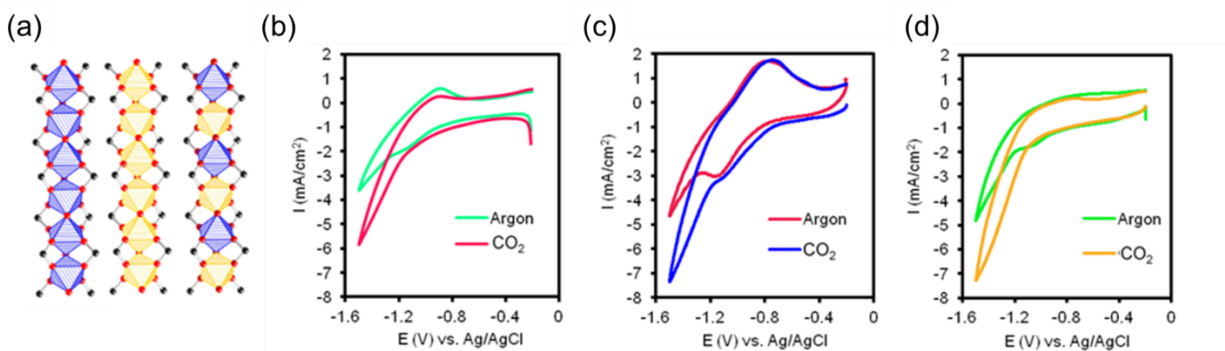


Figure A3.3. The one-dimensional MOF SBU is varied (a) between aluminum (blue) indium/aluminum (blue/yellow) and indium (yellow). MOFs featuring aluminum (b), aluminum/indium (c), and indium (d) SBUs all feature enhanced current density under the presence of CO₂.

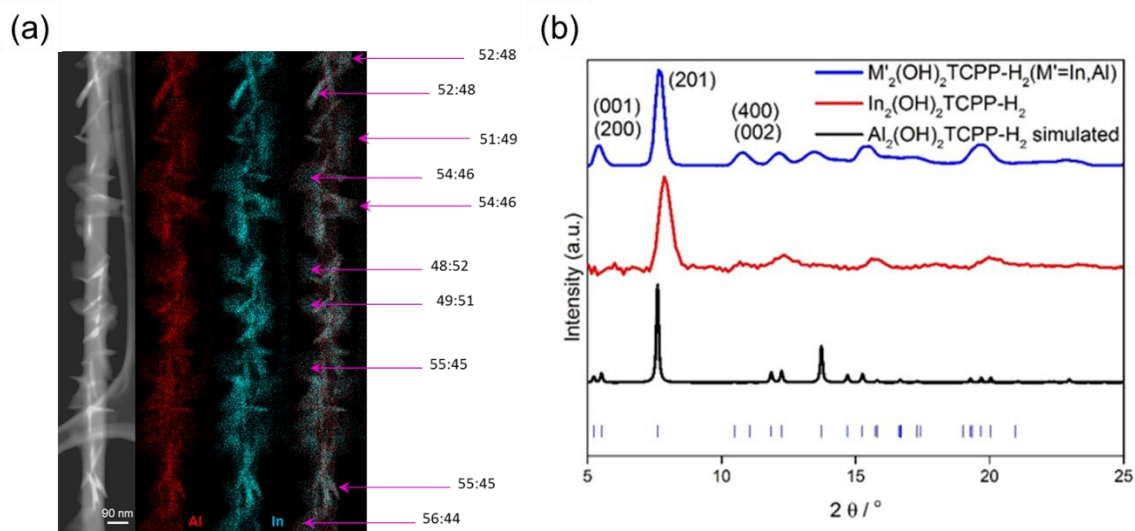


Figure A3.4. (a) Elemental mapping is utilized to demonstrate a uniform distribution of the indium/aluminum mixed metal MOF. Silicon nanowires were used as a platform for mapping because of their compatibility with transmission electron microscope energy dispersive spectroscopy. The ratio displayed signifies the atomic ratio of aluminum:indium. The ALD deposition and MOF conversion procedure used in this sample are the same as that for the carbon disk electrode. (b) Integrated GIWAXS spectra reveal the MOFs with indium and mix-metal SBU has the same phase as the Al₂(OH)₂TCPP MOF.

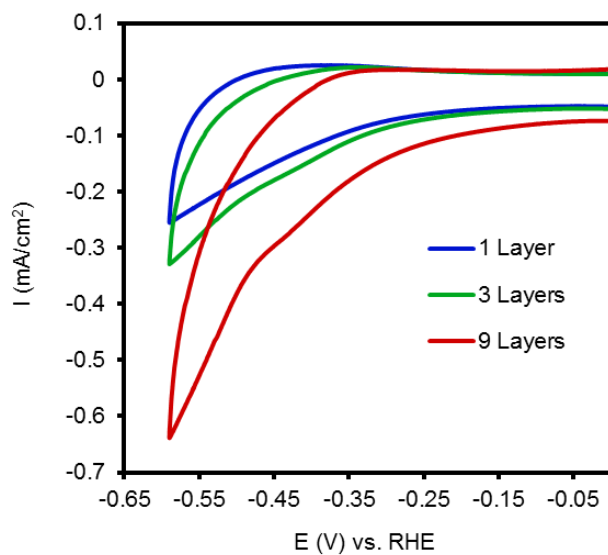


Figure A3.5. CV scans of the Co-TCPP linker drop cast on titanium foil at 100 mV/s under a CO₂ atmosphere also displayed a cathodic peak at -0.4 V vs. RHE preceding an irreversible catalytic peak.

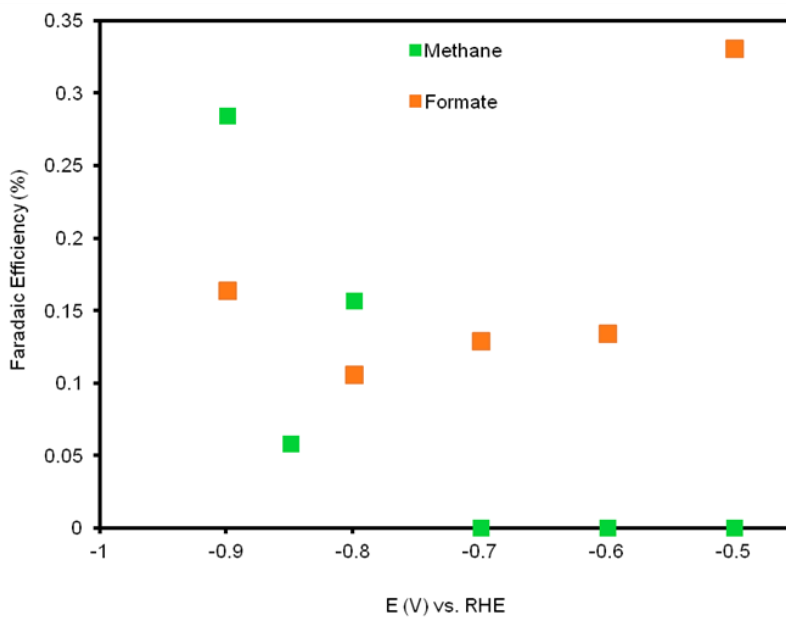


Figure A3.6. Formate and methane were quantified in trace quantities through GC and NMR analysis.

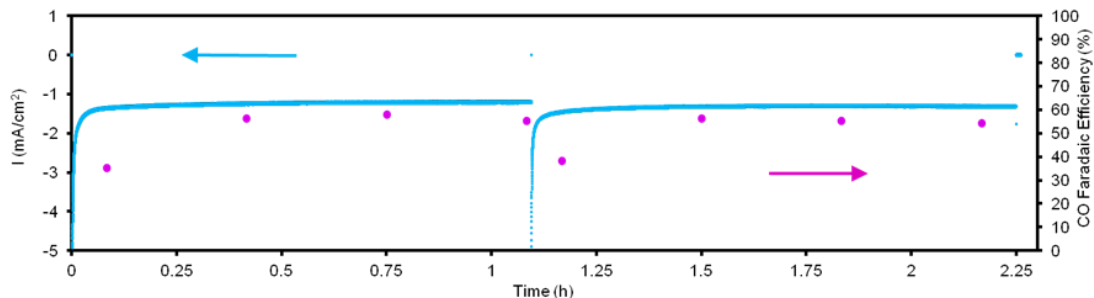


Figure A3.7. The MOF activity is stable under -0.8 V vs. RHE for over 2 hours. Upon changing the electrolyte after 1.1 hours of electrolysis, the activity is similar as before, decreasing the likelihood of a homogeneous catalyst being responsible for the CO_2 reduction.

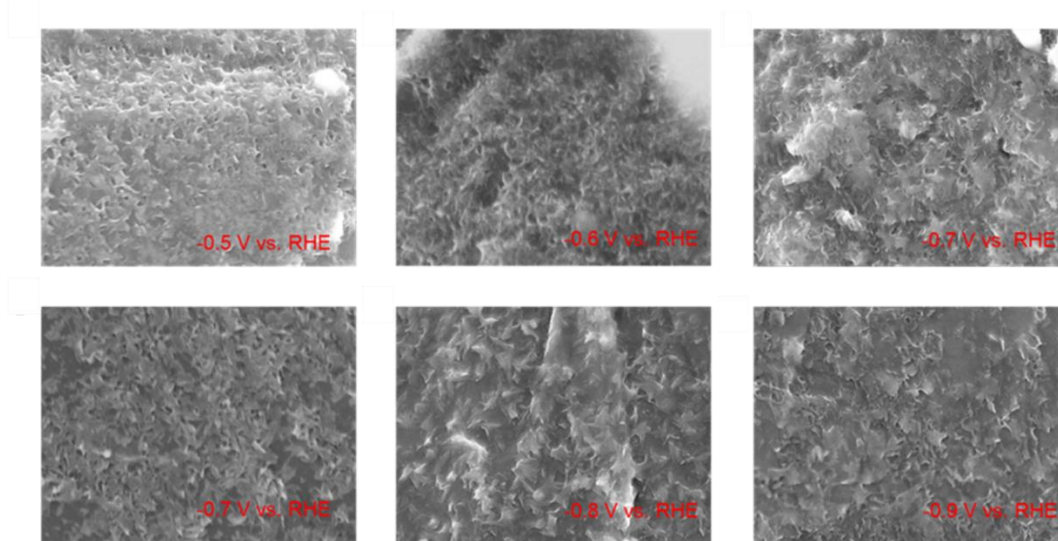


Figure A3.8. The MOF retains its plate-like morphology after 1.5 hours of electrolysis at reducing potentials of -0.5 to -0.9 V vs. RHE.

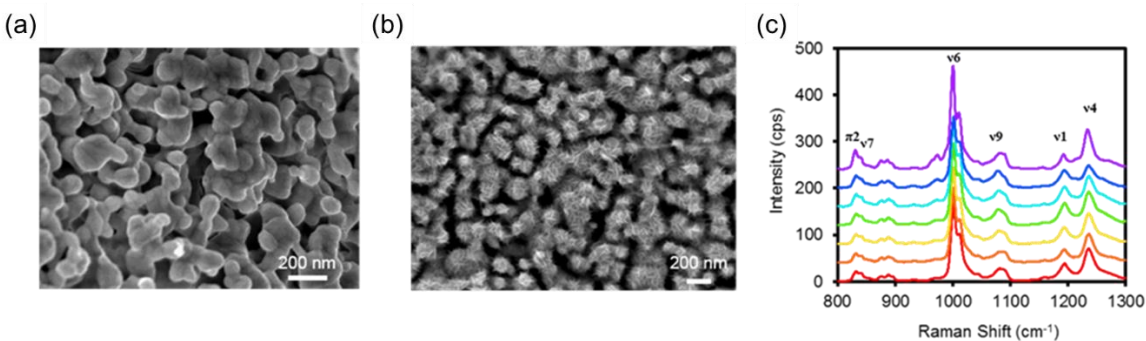


Figure A3.9. Electrochemically roughened SERS platforms before (a) and after (b) MOF coating. The roughened silver served as a clean, surfactant-free substrate which allowed us to acquire clean spectra of the MOF catalyst during testing. The SERS spectrum (d), after holding for 15 minutes at each potential increment from -1.1 V vs. RHE (bottom trace) to -0.7 V vs. RHE (top trace) further indicates structural preservation of the MOF for this time frame. The SERS spectra were taken under the same conditions as electrochemical testing. π peaks represent phenyl out of plane modes and v peaks represent porphyrin core mo

Chapter 4. Synthesis of Glassy Metal-organic Frameworks

Section 4.1 Introduction

Conceptually, MOF glasses with permanent porosity can be constructed by applying the concept of reticular chemistry to conventional glasses (e.g. silicate glasses),¹⁻⁴ where the silicon atom is replaced by a metal cluster (metal node) and the bridging oxygen atom is replaced by a ditopic organic linker (organic strut) that linked to the metal node. According to constraint theory,⁵⁻⁷ the stability of this expanded network should then be equivalent to that of the conventional glass in terms of the balance between constraints and degrees of freedom. However, in this case, similar to the 'isoreticular expansion' known in crystalline MOFs, the void volume of the system should become a strong function of the length of the strut, the size of the cluster node, and the manner of connection between them. Thus, we should be able to combine the maximum (strain-free) rigidity condition with a large empty space condition, thereby producing nanoporous glasses. Consequently, we now expect the range of nanoporous MOF glass compositions to greatly exceed those found in atomic systems such as the classical Ge-As-Se system for which the original "magic" stability condition, $\langle r \rangle = 2.4$, ($\langle r \rangle$, the average bond density) was deduced.⁵ (Reproduced with permission from *J. Am. Chem. Soc.* **2016**, 138, 10818. Copyright 2016 American Chemical Society.)


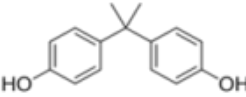
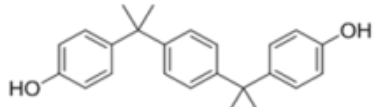
Previously, reports of MOF glasses were based on destructive treatments (*i.e.* thermally induced amorphization) of crystalline MOFs.⁸⁻¹² However, these treatments exclusively lead to compromised porosity and these MOF glasses were not accessible to gases (no surface area based on N₂ isotherm have been reported).¹³ Other reported amorphous MOFs, although sometimes have gas uptake, are essentially amorphous mass, the light scattering by which excludes any description as a "glass".^{14,15} Glasses can be taken through a thermodynamic cycle which includes passage into the liquid state, and returned to the same state they started in provided the same thermal protocol is followed. Another class of solution processible porous material, polymers with intrinsic porosity (PIMs) is of pure organic composition and consists of irregularly packed organic chains,¹⁶ thus are fundamentally different from the 3D MOF frameworks developed in this report.

Herein, we use a constructive approach to obtain monolithic, transparent nanoporous MOF glasses, which relies on a solvent-modulator that dissolves the organic linker and competitively coordinates to the metal nodes. This solvent-modulator is analogous to mono-dentate modulators used to tune the morphology and crystallinity of MOFs (e.g. acetic acid in the synthesis of UiO-66).¹⁷ The synthetic procedure we developed start with dissolving the metal nodes and organic linker in the solvent-modulator to form a liquid. The gradual removal of the solvent-modulator from the liquid by evaporation enables the linker to coordinate to the metal nodes and form MOF networks with increasing completeness (or connectivity). This process proceeds until the liquid turns into a glassy solid, which has the robustness and porosity of a MOF but the shape of a liquid.

The organic linkers we chose to demonstrate this chemistry are bisphenols (Table 1), and the corresponding modulator, *m*-cresol is an extraordinary solvent for polymeric compounds (to keep

the dynamically forming network dissolved) and volatile enough for facile evaporation.¹⁸ The metal-nodes we used are titanium-oxo (Ti-oxo) clusters,^{19,20} which form labile covalent bond with phenols that can support a 3D porous network but at the same time allows for the necessary dynamic ligand exchange.²⁰⁻²² In particular, the $Ti_{16}O_{16}(OEt)_{32}$ cluster is known to undergoes facile ligand exchanges with phenol and alcohols without the decomposition of the $Ti_{16}O_{16}$ core.²⁰

Table 4.1. Various bisphenol struts used in glassy MOF synthesis

strut character	Structure formula and chemical name (common name)	Abbreviation	T_m (°C)	T_g (°C)
rigid	 1,4-benzenediol (Hydroquinone)	HQ	171	-
rigid	 2,2-Bis(4-hydroxyphenyl)propane (Bisphenol-A)	BPA	158	35.8
semi-rigid	 4,4'-(1,4-Phenylenediisopropylidene)bisphenol (Bisphenol-A)	BPP	193	44.1

Section 4.2 Experimental Section

Section 4.2.1 Methods and Materials

Chemicals. 2,2-Bis(4-hydroxyphenyl)propane (BPA) and 2,2-Bis(4-hydroxyphenyl)propane (BPP) were purchased from Tokyo Chemical Industry Co., Ltd. *m*-Cresol, titanium ethoxide [Ti(OEt)₄] titanium isopropoxide [Ti(*i*-OPr)₄], 5,10,15,20-tetrakis(4-hydroxyphenyl)porphyrin (TPPP), anhydrous acetone and ethanol were purchased from Sigma-Aldrich Co. Tetrahydrofuran (THF), *N,N*-dimethylformamide (DMF), tetraethylene glycol and methanol were purchased from Fisher Scientific International Inc.

Analytical techniques and instrument. low-pressure gas adsorption experiments (up to 760 torr) were carried out on a Quantachrome AUTOSORB-1 automatic volumetric instrument ('volumetric', contrary to 'gravimetric' represents the method used for determining equilibrium gas-solid adsorption isotherms: In the volumetric method, pressure is measured before and after gas expansions from a chamber with known volume to the chamber containing the adsorbent at bath temperature; In the gravimetric method, the mass of the sample is measured by a suspension balance as pressure is increased). Ultrahigh-purity-grade N₂ and He gases were used in all adsorption measurements. The N₂ (77 K) isotherms were measured using a liquid nitrogen bath (77 K). The backbone density of the glasses is measured by pycnometry on a Quantachrome upyc 1200e V5.04 instrument using He gas. Powder X-ray diffraction patterns (PXRD) were recorded using a Rigaku Miniflex 600 (Bragg-Brentano geometry, Cu K α radiation $\lambda = 1.54056 \text{ \AA}$) instrument. Solution ¹H NMR spectra were acquired on a Bruker AVB-400 NMR spectrometer. Elemental microanalyses (EA) were performed in the Microanalytical Laboratory of the College of Chemistry at UC Berkeley, using a Perkin Elmer 2400 Series II CHNS elemental analyzer. Attenuated total reflectance (ATR) FTIR spectra of neat samples were performed in-house on a Bruker ALPHA Platinum ATR-FTIR Spectrometer equipped with a single reflection diamond ATR module. Electron microscopy was performed on a 200-kV Tecnai G220S-TWIN TEM equipped with a Gatan Orius SC200 CCD camera. The heat capacity studies were carried out on a Perkin Elmer DSC-7 instrument with the scans conducted at 20 K/min.

Section 4.2.2 Synthesis and Activation of MOF Glasses

The synthesis of Ti-BPA from Ti₁₆O₁₆(OEt)₃₂ cluster. 2.5 g Ti(OEt)₄ was reacted with 107 mg water in 2.5 mL ethanol at 100 °C in a sealed tube for 2 days to give single crystals of Ti₁₆O₁₆(OEt)₃₂ cluster. 154 mg of Ti₁₆O₁₆(OEt)₃₂ and 228 mg of BPA is dissolved in 10 mL THF and heated at reflux overnight. The yellow precipitate is filtered off and dissolved in 2 mL of DMF/cresol 1:1 mixture with heating. This solution was heated to 140 °C, casted into a petri dish, and kept at 140 °C until the solvent evaporates and the glass solidified.

The synthesis of Ti-BPP and Ti-BPA from Ti(O-*i*Pr)₄ or Ti(OEt)₄. 228 mg of BPA and 284 mg of Ti(O-*i*Pr)₄ [or 228 mg of Ti(OEt)₄] were dissolved in 5 mL of THF respectively, the two solutions are mixed in a 20 mL vial, which was heated briefly with heat gun (until yellow precipitate formed) and placed in an oven preheated to 85 °C for 30 minutes. The yellow precipitate was then collected and dissolved in 2 mL *m*-cresol/DMF = 1/1 mixture and heated to 140 °C. This mixture was poured in a petri dish preheated to around 150 °C. The solvents (DMF and cresol) rapidly evaporated (almost boiling), thus lowering the temperature of the petri dish and prevent

the continuous boiling of the mixture. The petri dish was then kept at 140 °C until the glass hardened (typically took 5 to 10 minutes). Prolonged heating or overheating in the cresol evaporation step can lead to oxidation of cresol (evident by a dark red color of the glass), formation of bubbles in the glass, and loss of transparency or porosity of the glass.

The Ti-BPP glass can be synthesized using a similar procedure as Ti-BPA glass. 300 mg of BPP and 90 mg of Ti(OEt)₄ were dissolved in 5 mL of THF respectively, the two solutions are mixed in a 20 mL vial, which was heated briefly with heat gun (until yellow precipitate formed) and placed in an oven preheated to 85 °C for 30 minutes. The yellow precipitate was then collected and dissolved in 2 mL *m*-cresol/DMF =1/1 mixture and heated to 140 °C. This mixture was poured in a petri dish preheated to around 150 °C. The solvents (DMF and cresol) rapidly evaporated (almost boiling), thus lowering the temperature of the petri dish and prevent the continuous boiling of the mixture. The petri dish was then kept at 140 °C until the glass hardened (typically took 5 to 10 minutes).

In general, the process of MOF synthesis is robust and insensitive to the stoichiometry of the reactants. Empirically, excess bisphenol linkers would be removed after the MOF formation by solvent exchange (see below, activation process) as evidenced by the chemical composition analysis; inadequate amount of bisphenol linkers relative to titanium would give glass prone to decomposition in the solvent exchange process.

preparation of MOF glass solutions for glass transition characterization. BPA and Ti(OEt)₄ with stoichiometry of Ti:BPA=1:2 were dissolved in THF and heated at reflux overnight to form yellow precipitates. This THF suspension was then dried and all the resulting solid was dissolved in cresol with controlled weight. This solution with known composition was evaporated to the specified cresol content in and measured for glass transition temperature.

For the heating-in-tube experiment, activated MOF glass solids and designated amount of cresol were put in the bottom of a Pyrex tube, which was flame sealed under vacuum and put in an oven pre-heated to 200 °C overnight.

The synthesis of mixed linker MOFs. Different ratio of tetraethylene glycol and BPA were mixed in THF to react with Ti(O-*i*Pr)₄ keeping the overall molar ratio of Ti:BPA=1:1. The precipitate was collected by filtration and dissolved in 1:1 cresol/DMF mixtures, which was then heated and casted according to the procedure mentioned above.

For TPPP and cobalt TPPP (Co-TPPP) doped MOF glass, 20 mg of TPPP (or Co-TPPP) and 102 mg of BPA was reacted with 142 mg of Ti(*i*-OPr)₄ in THF. The precipitate was collected by filtration and dissolved in 1:1 cresol/DMF mixtures, which was then heated and casted according to the procedure mentioned above.

Activation of the MOF glasses. The activation of the titanium bisphenol glasses started with solvent exchange. The glass was collected from the petri dish, transferred into a 20 mL vial and soaked in 15 mL anhydrous acetone for 3 hours. The acetone was then refreshed three times with the interval of at least three hours to allow for adequate diffusion of the cresol into acetone. Then the acetone was replaced with anhydrous ethanol or methanol (also refreshed 3 times), which turned slightly yellow after soaking the glass. In this process, the alcohol not only removed residue free cresol but also replaced bonded *m*-cresol (phenoxide) by competing for titanium coordination,

which further opened up the pore and facilitated the diffusion of *m*-cresol and unbounded BPP out of the interior of the glass. Subsequently, the alcohol was replaced by anhydrous acetone again (refreshed three times) to remove all unbounded alcohols. At this point, the interior of the glass was filled with acetone, which can be exchanged with supercritical CO₂. The wet glass was then transferred to a supercritical CO₂ drier, in which the sample was washed five times with liquid CO₂ with the interval of half hour (liquid CO₂ was refreshed every half hour for five times). The system was heated up to 45 °C and the CO₂ reached critical point. The supercritical CO₂ was bled for 3 hours in very slow flow rate to ambient pressure. The sample was then heated at 120 °C under dynamic vacuum overnight to completely remove CO₂ adsorbed in the pore. This activated sample was then ready for N₂ uptake measurement.

The absence of unbounded cresol molecules are evidenced by the absence of –OH vibrations above 3600 cm⁻¹ in the IR spectrum. Also in the digested NMR spectrum, the amount of cresol is quantified and shown to be of stoichiometric amount, which indicates the cresol found in the NMR reside as bounded cresolate in the activated glass. The detailed analysis of the activation process can be found below.

Section 4.2.3 EXAFS Study of Ti-BPA Glass

Extended x-ray absorption fine structure (EXAFS) data was collected at the Advanced Light Source Beamline 10.3.2. The x-ray wavelength was monochromatized by a Si(111) double-crystal, fixed exit monochromator. The intensity of the incident x-ray radiation, I_0 , and the transmitted intensity, I_t , were monitored with nitrogen filled ionization chambers. The data was collected at the Ti *K*-edge and all spectra were calibrated with a Ti foil measured in transmission mode and aligned according to a glitch in I_0 near the absorption edge. The EXAFS of the Ti MOF was collected in transmission mode because the sample could be poured into a film that, when hardened, produced an even thickness ideal for transmission.

EXAFS data reduction was performed in Athena.^{S1} Edge step normalization for each spectrum was performed by subtracting the pre-edge and post-edge backgrounds. For EXAFS background removal, a cubic spline was fit to the data and the *k*-space data was Fourier transformed resulting in an *R*-space spectrum which was fit in Artemis with multiple *k*-weight fitting (k^1, k^2, k^3). EXAFS data was fit to the following EXAFS function:

$$\chi(k) = S_0^2 \sum_{i=1}^{shells} \frac{N_i}{kR_i^2} F_i(k) e^{-2k^2\sigma_i^2} e^{-2R_i/\lambda(k)} \sin[2kR_i - \varphi_i(k)]$$

Each coordination shell included in the fit has a specific amplitude contribution to the EXAFS function that is summed to generate a fit to the data. S_0^2 represents an amplitude reduction factor which is typically assumed to be chemically transferable and is affected by shake-up effects at the absorbing atom. N_i and R_i are the coordination number and half-path length between the central absorbing atom and a scattering atom, respectively. Since S_0^2 and N_i are correlated, it is only possible to fit the data with one of the two. In this case, being limited by the number of fitting parameters that could be used in a multi-shell fit, the coordination number was fixed to that from the model and the S_0^2 was varied. The mean-square disorder in the distance from the central absorbing atom to a given shell due to thermal fluctuation and structural disorder is represented by σ_i^2 and is also a fitted parameter. The photoelectron mean free path is represented by λ . Lastly,

$F_i(k)$ is the backscattering amplitude and $\varphi_i(k)$ is the phase factor for a given coordination shell, i . These parameters are calculated through *ab initio* methods using FEFF6 as embedded in Artemis and Atoms.

Section 4.3 Result and Discussion

Section 4.3.1 Chemical Composition and Building Blocks Analysis of MOF Glasses

The Ti-oxo cluster was synthesized according to literature reports,²⁰ where titanium ethoxide was reacted with water in ethanol give single crystals of $\text{Ti}_{16}\text{O}_{16}(\text{OEt})_{32}$ cluster. This cluster was then reacted with BPA linkers in THF at reflux overnight, at which condition ethoxide ligand was replaced by phenolates to form a network. This network can be dissolved in cresol with heating and the subsequent evaporation of the cresol at 140 °C gives monolithic, transparent glasses. It was during this process that the Ti-cresolate type bonds of the broken network were systematically replaced by bridging bonds of the Ti-O-(strut)-O-Ti type, as can be followed by monitoring the glass transition temperature *vs.* weight fraction of *m*-cresol (see below). This MOF glass can also be obtained by using titanium alkoxide as precursor and the Ti-oxo clusters can be formed in-situ during the reaction. The transparent orange monolithic glassy product of this process is shown in Figure 4.1b. This Ti-BPA MOF glass is insoluble in water and common organic solvents such as DMF, acetonitrile, THF, acetone and only soluble in cresol when heated, indicating the glass is an extended network instead of an irregular assembly of molecular oligomers.

Removal of solvent to vitrify an assembly of large molecules has actually been used as a means of preparing glassy solids. The solvent removal plays a role analogous to that of cooling a liquid of fixed composition, by decreasing the configurational freedom of the large molecules in a solution. Then, according to the celebrated Adam-Gibbs equation, the viscosity rises exponentially with configurational entropy (S_c) decrease,²³ until the shear relaxation time reaches the order of minutes and the structure "freezes" for experiments of that time scale. In the MOF glasses case, the configurational restrictions are accelerated by the formation of the covalent bridging node-to-node linkages. There are some similarities in our process to the formation of hydrocarbon-containing silicas(ormosils).^{24,25} However, the organic components of ormosils were highly flexible hydrocarbon chain fragments, and quite different in their function from that of the Table 1 struts. No generation of porosity was sought nor detected.

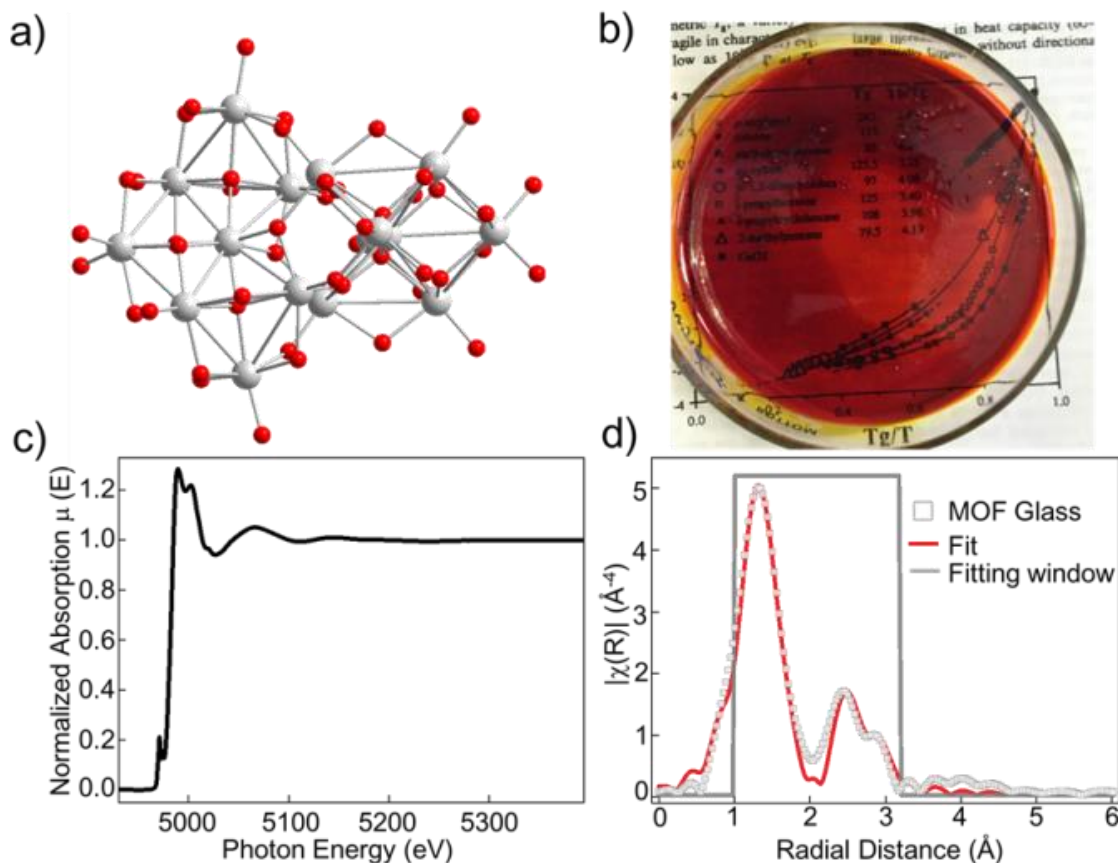


Figure 4.1. MOF glasses consist of Ti-oxo clusters linked up with bisphenol linkers. (a) the structure core of $\text{Ti}_{16}\text{O}_{16}(\text{OEt})_{32}$, Ti, gery; oxygen, red; ethoxides are omitted for clarity. (b) Photograph of monolithic MOF glass in a 10 cm diameter Petri dish, following vitrification by *m*-cresol evaporation. (c) The X-ray absorption spectrum of the MOF glass and (d) the fitting of $\text{Ti}_{16}\text{O}_{16}(\text{OEt})_{32}$ structure model to EXAFS of the MOF glass.

We confirmed the presence of Ti-oxo clusters as metal nodes in the MOF glasses by X-ray absorption spectroscopy at the Ti *K*-edge. The pre-edge feature is similar to that of Neptunite and indicates the Ti is six coordinated, which is consistent with the chemical environment of Ti in the Ti-oxo cluster $\text{Ti}_{16}\text{O}_{16}(\text{OEt})_{32}$ (Figure 4.1c). Also, the position, area and line shape of the pre-edge peak contradicts known phases of TiO_2 . The extended X-ray absorption fine structure (EXAFS) also supported the presence of Ti-oxo clusters, as the $\text{Ti}_{16}\text{O}_{16}(\text{OEt})_{32}$ model cluster can be successfully fit to the EXAFS data acquired for the MOF glass. Specifically, the path length for the first Ti-Ti scattering was found to be around 3.04-3.07 Å, which resembles the path lengths of Ti-Ti scatterers in the Ti-oxo cluster and the number of Ti-Ti scatters found confirmed the absence of Ti-O-Ti dimers typically found in Ti-phenol networks.²⁶

The EXAFS data of the Ti-BPA MOF clearly shows scattering paths of oxygen at ~ 1.4 Å and a second and third shell peak at ~ 2.5 and 2.9 Å (distances not corrected for a phase factor). Fits to the data were attempted for both the Ti-oxo cluster and rutile TiO_2 , though there is no evidence of crystalline TiO_2 formation. These two models have different symmetry but similar coordination shells, with the main differences being the path lengths and that the first and second oxygen

coordination numbers in the Ti-oxo cluster are 2 and 4 respectively, while in rutile TiO₂ they are reversed. In addition, the shortest Ti-Ti scattering paths have lower symmetry in the Ti-oxo cluster, meaning not every scattering path could be included due to the limitation on the number of parameters allowed in the fit which was dictated by the number of independent points used. For both models, the first two oxygen scattering paths and two shells of Ti scattering paths were included. Both models fit the data with similar accuracy, but the results for the fitting parameters demonstrate that the Ti MOF EXAFS better resembles the coordination of the Ti-oxo cluster, with its successful fitting being limited by the number of scattering paths which can be included. As shown in Table S1, using either model resulted in a path length for the first Ti-Ti scattering path of ~3.04-3.07 Å. This resembles the path lengths of Ti-Ti scatterers in the Ti-oxo cluster and not in rutile TiO₂, which has a path length of ~2.96 Å. For either model, the fitted S_0^2 value was ~0.6, which has been found in other fits to Ti EXAFS data. A first-shell fit was then performed in which the S_0^2 was fixed to the result from the multi-shell fit. This was required due to the limitation in the number of parameters allowed in the first-shell fit. It can be seen in Table S2 that when the coordination number of the second oxygen is set to 2 in the case of rutile TiO₂, the σ^2 value for that path was fitted to an unreasonably low value to compensate for the lower amplitude contributed by the smaller coordination number. The first-shell fit to the Ti-oxo cluster produced physically reasonable values, demonstrating that the first two shells of oxygen resembled the distorted octahedron motif of the Ti-oxo cluster, not rutile TiO₂. The analysis by X-ray absorption spectroscopy clearly showed that the MOF glass is composed of Ti-oxo clusters as the metal node, although though it cannot rule out the presence of other Ti-oxo clusters with similar structure to Ti₁₆O₁₆(OEt)₃₂ [*e.g.* Ti₁₂O₁₆(O-iPr)₁₆].¹⁹

Table 4.2. Multiple-shell EXAFS fitting results for fits to the Ti-BPA MOF.

Shell	Ti-oxo model			Rutile TiO ₂ model		
	N	R (Å)	σ^2 (10 ⁻³ Å ²)	N	R (Å)	σ^2 (10 ⁻³ Å ²)
O.1	2	1.80(3)	1.7(4.8)	4	1.85(2)	4.7(3.4)
O.2	4	1.96(2)	5.2(5.1)	2	2.01(3)	1.7(4.6)
Ti.1	3	3.07(3)	10.1(3.9)	2	3.04(2)	6.4(2.9)
Ti.2	2	3.35(6)	10.6(7.1)	8	3.32(5)	34.3(9.9)

Fitting was carried out with the Ti-oxo cluster or rutile TiO₂ FEFF models. The fitting ranges are $\Delta k = 2-11$ Å⁻¹ and $\Delta R = 1-3.2$ Å. The fitted S_0^2 values were 0.61 ± 0.12 (Ti-oxo) and 0.59 ± 0.10 (TiO₂). The fitted energy parameters were $\Delta E_0 = -5.76 \pm 2.11$ (Ti-oxo) and $\Delta E_0 = -5.46 \pm 1.69$ (TiO₂).

Table 4.3. First-shell EXAFS fitting results for fits to the Ti-BPA MOF.

Shell	Ti-oxo model			Rutile TiO ₂ model		
	N	R (Å)	σ ² (10 ⁻³ Å ²)	N	R (Å)	σ ² (10 ⁻³ Å ²)
O.1	2	1.80(3)	1.2(2.9)	4	1.84(3)	4.3(2.2)
O.2	4	1.95(3)	4.8(3.3)	2	2.00(4)	0.6(3.2)

Fitting was carried out with the Ti-oxo cluster or rutile TiO₂ FEFF models. The fitting ranges are $\Delta k = 2-11 \text{ \AA}^{-1}$ and $\Delta R = 1.0-2.0 \text{ \AA}$. The S_0^2 values were fixed to those from the multiple-shell fits. The fitted energy parameters were $\Delta E_0 = -6.46 \pm 2.87$ (Ti-oxo) and $\Delta E_0 = -6.99 \pm 2.69$ (TiO₂).

The presence of Ti-oxo clusters also is consistent with the chemical composition analysis of the MOF glass, where elemental analysis, 'digested' NMR (Figure 4.2 and 4.3) and ICP-AES were combined to give a typical chemical formula of Ti₁₆O₁₆(BPA)_x(OR)_{32-x} [$x \sim 4$, OR is cresolate, hydroxide, and ethoxide]. Infrared spectroscopy was used to confirm the incorporation and integrity of the BPA and BPP linkers in the glass. Thus, from X-ray absorption spectroscopy and chemical composition analysis, we confirmed that the Ti-BPA and Ti-BPP MOF glasses are composed of Ti-oxo clusters linked up with BPA and BPP linkers respectively.

For a typical Ti-BPA glass sample, elemental analysis (CHN analysis by combustion) and inductively coupled plasma atomic emission spectroscopy (ICP-AES) were combined to give Ti 30.7%, C 33.9%, H 3.9% and O 31.5%. Since the glass had been activated under dynamic vacuum at 120 °C overnight to remove all free solvent, the carbon in the Ti-BPA glass can be attributed to deprotonated alcohols and phenols (*i.e.* alkoxides and phenoxides), which are: deprotonated BPA (C₁₅H₁₄O₂²⁻), cresolate (C₇H₇O⁻), and ethoxide (C₂H₅O⁻). Their ratio was calculated from the NMR spectrum of the "digested" glass in DCI-DMSO mixture to be BPA/cresol/ethanol = 1/0.66/0.58. Thus, the chemical formula of this batch of the Ti-BPP glass was determined to be Ti₁₆O₁₆[(BPA)_{3.40}(cresolate)_{2.25}(ethoxide)_{1.81}(OH)_{20.96}], which can be represented as Ti₁₆O₁₆[(BPA)_x(OR)_{32-2x}]($x=3.4$). This formula is coincident with the titanium cluster, Ti₁₆O₁₆(OEt)₃₂. The analysis of Ti-BPP glass gave similar results, where their chemical formulae can be represented by Ti₁₂O₁₆(BPP)_x(RO)_{16-2x} or Ti₁₆O₁₆(BPP)_x(OR)_{32-2x}, with x varying from around 3 to 5 [Ti₁₂O₁₆(O-*i*Pr)₁₆ is also a well-known titanium-oxo cluster synthesized in similar condition to Ti₁₆O₁₆(OEt)₃₂].

The high Ti/bisphenol ratios found for our MOFs make it necessary to propose a Ti-O cluster node (as opposed to the single atom node in silicate glasses). These are linked together by bisphenol struts to give a highly cross-linked, rigid network that allows for the presence and accessibility of pores in the glass.

Here we describe in detail the procedure of chemical composition analysis using a Ti-BPP glass as example. The elemental analysis gave relative amount of carbon and hydrogen in the material, which is 51.44 and 5.07 wt%, respectively. Then 11.6 mg of the Ti-BPP glass was dissolved in concentrated nitric acid to form a clear solution, which was then diluted to 150 mL in volume. The

titanium concentration of this solution was determined by ICP-AES to be 18.19 ppm, which corresponded to 23.5 % weight percentage of titanium in the Ti-BPP glass. As the Ti-BPP glass is composed of Ti, H, C, O, the oxygen weight percent could be obtained as 20 wt%. This yields an empirical formula for the Ti-BPP glass of $\text{TiC}_{8.8}\text{H}_{10}\text{O}_{2.8}$ ($\text{Ti}_{12}\text{C}_{106}\text{H}_{120}\text{O}_{33}$). Since the glass had been activated under dynamic vacuum at 120°C overnight to remove all free solvent (in one case, at 180 °C), the carbon in the Ti-BPP glass can be attributed to deprotonated BPP ($\text{C}_{24}\text{H}_{24}\text{O}_2^{2-}$), *m*-cresol ($\text{C}_7\text{H}_7\text{O}^-$), and ethanol ($\text{C}_2\text{H}_5\text{O}^-$), the ratio between which was determined by digested NMR. In digested NMR, the MOF glasses were dissolved in DCl-DMSO mixture (typically 1-3 mg glass in 0.1 mL DCl and 0.6 mL DMSO- d_6 mixture) overnight and the ^1H NMR spectrum of this clear solution was acquired. The integration of peaks corresponding to BPP, ethanol, and cresol in this NMR spectrum gave their relative ratio, which, in this case, was BPP/cresol/Ethanol = 1/0.78/0.73. The assignment of carbon to deprotonated BPP, ethanol and cresol gives their relative amount with respect to titanium, which also accounted for the majority of hydrogen and part of oxygen in the material. The residue hydrogen and oxygen in the empirical formula were assigned to be OH^- and bridging oxygen with the consideration of overall charge balance. Thus, the chemical formula of this batch of the Ti-BPP glass was determined to be $\text{Ti}_{12}\text{O}_{16}[(\text{OH})_4(\text{C}_{24}\text{H}_{24}\text{O}_2)_{3.45}(\text{C}_7\text{H}_7\text{O})_{2.55}(\text{C}_2\text{H}_5\text{O})_{2.55}]$. This is equivalent to $\text{Ti}_{12}\text{O}_{16}(\text{BPP})_{3.5}(\text{RO})_9$, where the RO^- is hydroxide, ethoxide and cresolate.

Chemical composition analysis of the MOF glasses after each synthetic step. The precipitate from reacting BPP and titanium alkoxide in THF was analyzed in a similar manner to give C 69.88% H 6.83% Ti 10.88% O 12.41%. Combining the result from digested NMR, a typical chemical formula of this powder is $\text{TiO}(\text{BPP})(\text{THF})_{0.54}$. This matches well with the chemical composition of crystalline networks formed by reacting titanium alkoxide with other ditopic phenols in THF reported in literature. After dissolving the powder in cresol and casting of the glass, the overall amount of titanium and BPP is preserved as no solid is removed in this process.

The as casted Ti-BPP glass typically has 40 wt % cresol, 60 wt% polymer with composition Ti:BPP=1:1 [143 mg BPP, 19 mg Ti, 120 mg cresol]. After washing with acetone, 7 wt% cresol (15 mg) was left and after washing with methanol around 38 mg of BPP was left to give the final activated product. These results are based on weight analysis on the Ti-BPP glass after each step of activation and the corresponding analysis of Ti-BPA gave similar result. Some qualitative conclusions can be made from this analysis: (a) during the entire process, titanium is always incorporated in the solid and negligible amount of titanium is lost; (b) In the THF heating step, the titanium alkoxide starts to hydrolyze, only one equivalent of BPP (for BPA, typically 1.5 equivalent) is incorporated in the precipitate, also, the alkoxide ligand can be completely removed in this step; (c) after the glass is casted, most residue cresol can be removed by acetone, consistent with the fact these cresol are not chemically bounded; (d) Most of the residue bisphenol can only be removed by methanol wash, indicating that these bisphenol molecules are likely to be chemically bond. It is reasonable to speculate that these bisphenols bound to the titanium cluster with one hydroxyl group and dangling in the pores; (e) during the methanol wash, methanol molecules replace bonded cresol and dangling bisphenol molecules, making the pores accessible.

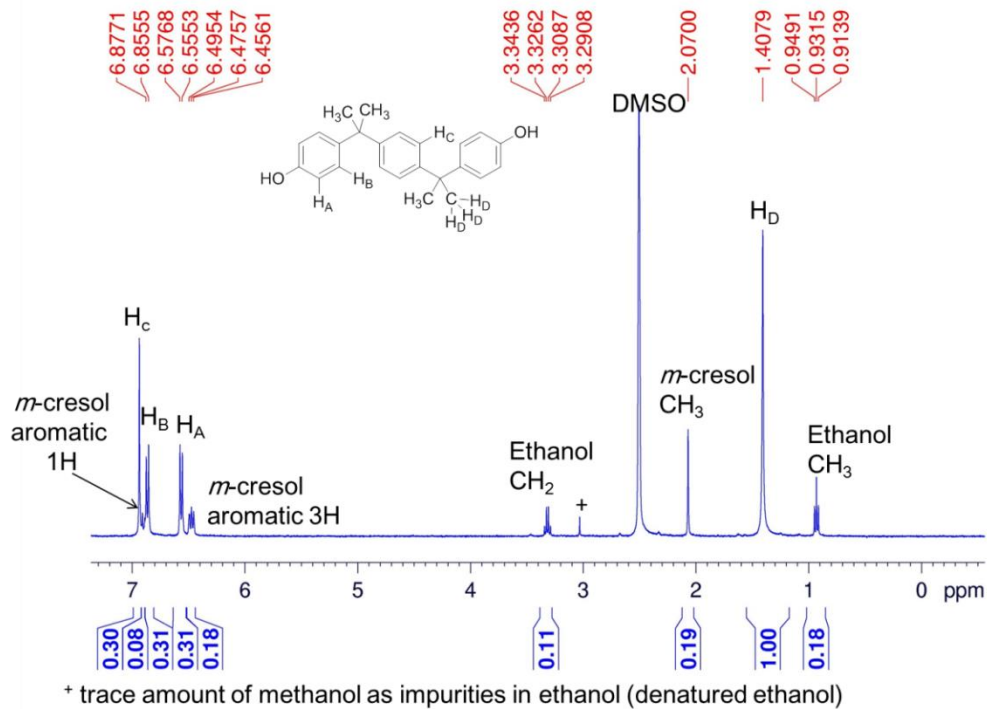


Figure 4.2. Digested NMR spectrum of activated Ti-BPP glass

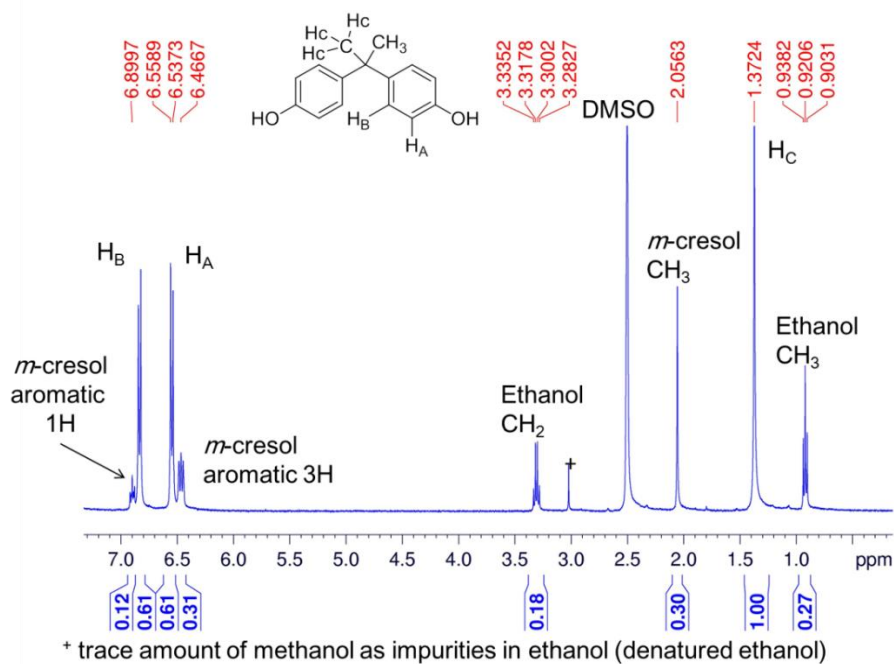


Figure 4.3. Digested NMR spectrum of activated Ti-BPA glass

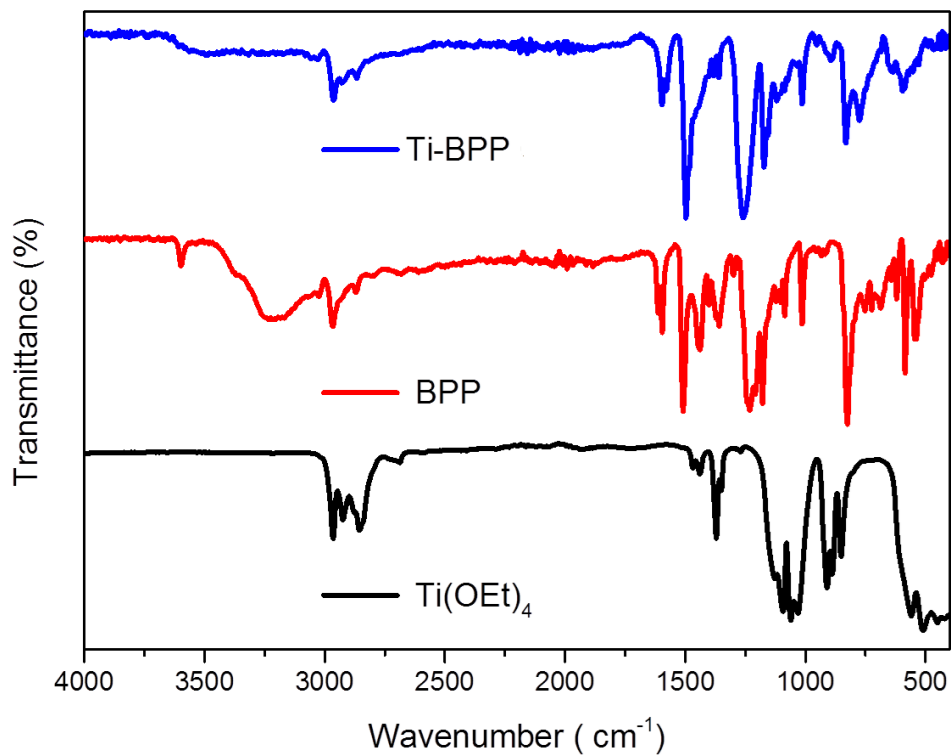


Figure 4.4. IR spectrum of activated Ti-BPP glass

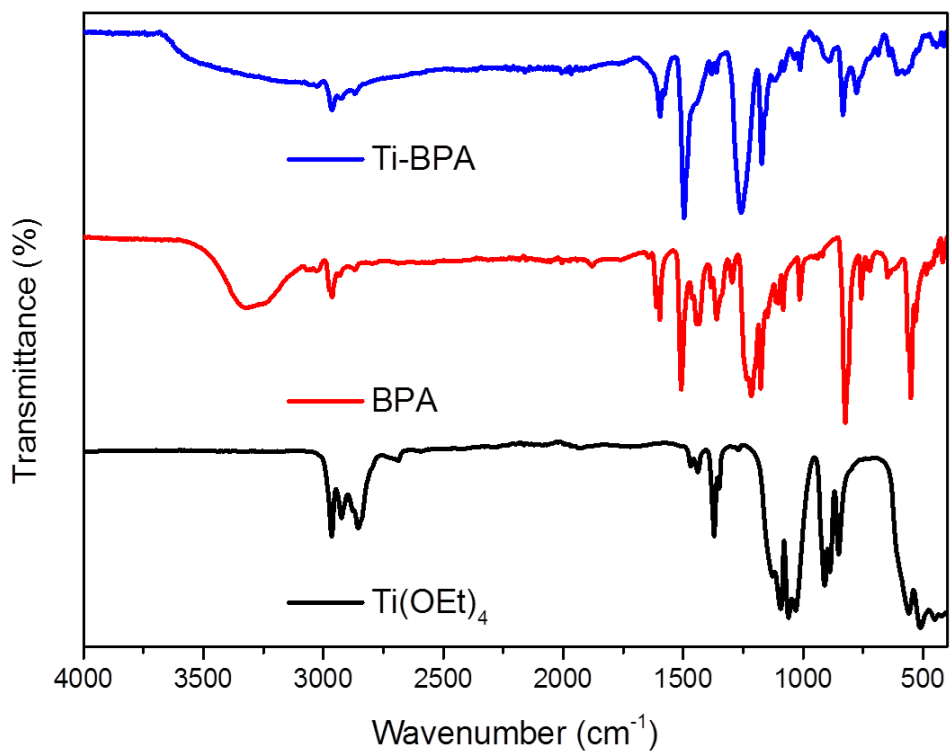


Figure 4.5. IR spectrum of activated Ti-BPA glass

Section 4.3.2 Structural and Porosity Characterization of Ti-BPP and Ti-BPA Glass

The structures of the above mentioned Ti-BPA glass and its derivative Ti-BPP glass were characterized by X-ray powder diffraction, which gave dominant low angle peaks in the vicinity of $2\theta = 2-5^\circ$, corresponding to pore-pore separations of about 2 nm comparable to those known for crystalline zeolite A (Figure 4.6a).²⁷ Transmission electron microscopy (TEM) was employed to confirm the absence of crystallinity, as no lattice fringes are observed for both the Ti-BPP and Ti-BPA glasses, with a typical image shown in Figure 4.6b.

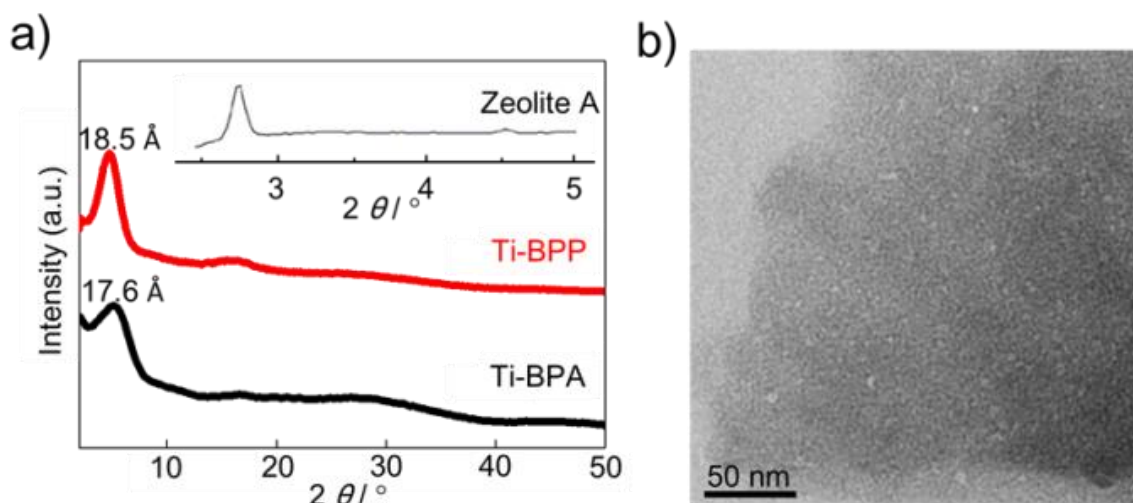


Figure 4.6 Structural characterization of the MOF glasses. (a) XRD pattern for MOF glasses with (i) BPP struts and (ii) BPA struts, compared with the low angle line of zeolite A (known internal pore dimension = 25 Å).²⁷ The prominent low angle peaks $2\theta = 4.8^\circ$ for (i) and 5.0° for (ii) would correspond to 18.5 Å and 17.6 Å d-spacings in a crystalline material. (b) The typical TEM image of the MOF glass (Ti-BPP) showing the absence of lattice fringes.

The accessible internal surface of the MOF glasses is clearly demonstrated by N₂ adsorption isotherm. According to the adsorption isotherm shapes of Figure 4.7, the accessible internal surface is heterogeneously distributed, which is hardly surprising for a glassy material. The total internal surface area, which is the important quantity, amounts to some 330 m²/g for the Ti-BPA MOF glass and 267 m²/g for the Ti-BPP MOF glass. The latter result has been obtained for three separate preparations of this material. Its lower value than for the Ti-BPA material shows that the naive picture of a strut-length dependent internal surface is inaccurate, no doubt due to the non-rigid nature of the single oxygen link to the node combined with the extra *sp*³ carbon in the strut. It is reasonable to expect that the dissolution-evaporation vitrification principle that we have introduced here will permit extensions to more rigid node-strut connections. Either of the above compares favorably with the most porous glass that has previously been made by physical methods (Corning "thirsty glass", 250 m²/g, made by laborious phase separation and leaching method).²⁸ In the case of the BPA struts, the gas uptake is quite reversible. The hysteresis so often encountered is only in evidence for the higher uptake levels, and even then, is not very pronounced.

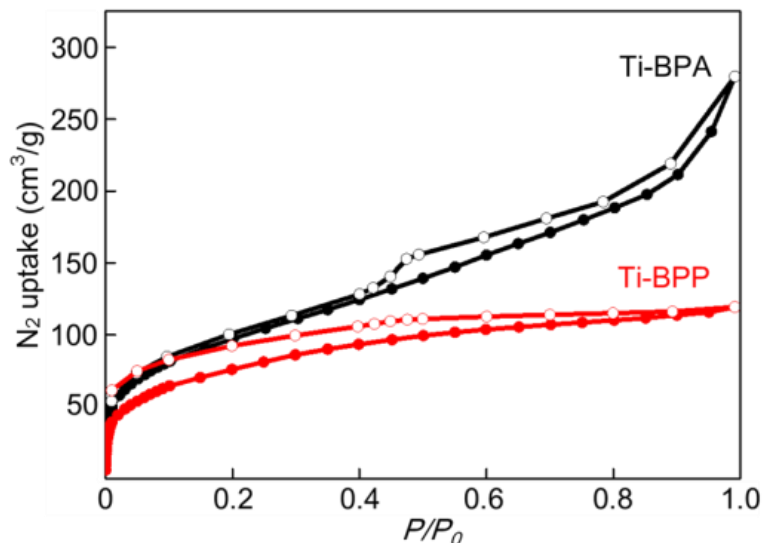


Figure 4.7 N_2 adsorption isotherms of MOFs glasses. The Ti-BPA g-MOF shows highly reversible behavior at low gas uptake. From these data we calculate internal surface values of 330 and 267 m^2/g . Due to the high backbone density measured by He pycnometry, *i.e.* 2.7 g/cm^3 for Ti-BPP, these MOFs are actually more porous than the surface area indicates. In the case of Ti-BPP, it has free volume of 0.33 cm^3/cm^3 , with volumetric N_2 uptake of 216 cm^3/cm^3 .

The internal surface of our MOF glass can be better understood when the high density of the framework is taken into account and a volumetric measure for porosity is used. The framework density can be obtained by the helium pycnometry method which, applied to our Ti-BPP g-MOF samples, yields a value of 2.7 g/cm^3 . From this we can derive a nitrogen uptake volume of 216 cm^3/cm^3 of glass corresponding to 33 % open space; a value that places g-MOF at higher porosity than the first porous MOF (MOF-2, 11 %) and in the range of typical MOFs (MOF-5, 60 %).²

Section 4.3.3 Glass Transition in MOF Glasses

We further consider an interesting aspect of the glass transition signature (T_g) by which the cohesive energy of a glassy phase is commonly assessed,²⁹ and by which the properties of the liquid phase above T_g are commonly scaled.^{30,31} In this respect the Ti-BPA and Ti-BPP glasses, with 3-dimensional network structure, prove to imitate very dry silica,³² vitreous water in its low-density polyamorphic (LDA) form,³³ and also most of the common ambers (highly cross-linked organic glasses from geologically distant times). These are all problematic because their T_g 's are undetectable except by very sensitive measurements. In the known cases, like the present one, they seem to become systematically non-existent as the modulator (or network breaking component) is removed. The significance of vanishing T_g to theory of the glass transition is currently at the center of debate. For fragile liquids, configurational heat capacities [$C_{p(\text{conf})}$] are usually increasing as T_g is approached whereas, for the smaller number of very strong liquids, the opposite is true, with $C_{p(\text{conf})}$ disappearing in some cases. In the "superstrong" cases of water and a-silicon, "ubiquitous" glass signatures disappear,^{34,35} including excess entropy in the case of LDA water,³⁶ meaning its glass is in a unique low entropy state ("perfect" glass).³⁶⁻³⁸ Thus the disappearing C_p in our g-MOF case is intriguing and will be the focus of future investigation.

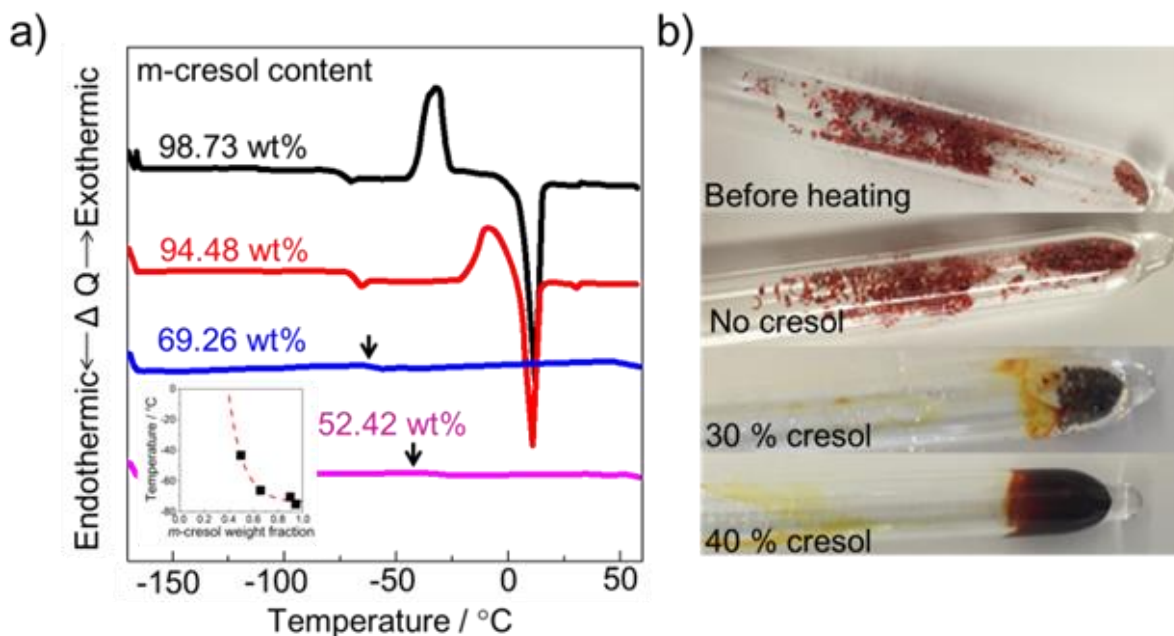


Figure 4.8 Glass transition temperature of Ti-BPA solution. (a) Differential scanning calorimetry (DSC) thermograms of Ti-BPA in *m*-cresol solutions. The thermogram shows the glass transition followed by *m*-cresol crystallization, followed by *m*-cresol remelting at the high *m*-cresol contents. As *m*-cresol content drops to 69.3 wt% *m*-cresol no longer crystallizes and both the overshoot and magnitude of the glass transition have greatly diminished. Concomitant increases in the liquid viscosity suggest greatly increased network formation, which is evidently almost completed at 50 % *m*-cresol. Insert: T_g vs. *m*-cresol wt fraction. T_g of pure BPP is 44.2 °C. (b) Indirect characterization of the glass transition of Ti-BPA with cresol content less than 50%. These Ti-BPA samples have same morphology before heating, as the overall cresol volume is small. After heating the 40% cresol sample vitrified, the 30% cresol sample clumped.

Figure 4.8 shows the behavior of Ti-BPA solution in cresol, as the wt % of the Ti-BPA network was increased from effectively zero (1.27 wt %) to the 50 wt % domain. As in polymer-plus-plasticizer phenomenology,³⁹ a highly non-linear relationship between T_g and macromolecule content was found but, quite unlike the chain polymer case, the strength of the glass transition is also diminishing. Indeed beyond 50 wt % Ti-BPA the glass transition cannot be detected by calorimetry but can only be qualitatively speculated by observing the morphology change of the MOF glasses upon heating. By heating the MOF glasses with different cresol composition at 200 °C overnight, the sample with no cresol retained its morphology, while the one with 30% cresol clumped and the one with 40% cresol vitrified, indicating the trend of glass transition diminishes with the decrease in cresol content holds throughout all cresol content. This is more like the classic behavior of alkali silicate glass formers as the alkali oxide component is evaporated off, or of organic polymers as crosslink density is maximized. The fact that the T_g disappears (Figure 4.8) while there is still so much *m*-cresol present, strongly suggests that the network is already complete at 50 % cresol, and the remaining solvent is sequestered, in a dynamic plasticizing role, in the intra-network pore spaces.

This constructive approach to synthesize MOF glasses is highly versatile, as multi-dentate alcohols and phenols can be used to substitute the BPA and BPP strut and still produce monolithic glasses. For example, flexible organic linkers, such as tetraethylene glycol, can also be

incorporated in monolithic glasses (Appendix, Figure A4.3 and A4.4). Additionally, functional molecule with hydroxyl groups can be mixed with BPA struts to produce functionalized MOF glasses, as exemplified by the incorporation of tetrakis-(4-hydroxyphenyl)-porphine (TPPP) molecule in the Ti-BPA glasses. In this experiment, 10% TPPP is mixed with BPA a give a purple glass with slightly higher porosity (Figure A4.4).

Section 4.4 Conclusion

Glassy metal-organic frameworks with intrinsic porosity were synthesized for the first time with titanium-oxo cluster as inorganic nodes and bisphenol linkers are organic strut by a solvent-modulator approach. In this synthetic process, the inorganic nodes and organic struts were dissolved in *m*-cresol solvent, which has the same phenol functional group as the bisphenol struts and thus capped the inorganic nodes and prevent the formation of extended MOF framework. The evaporation of *m*-cresol led to the formation of monolithic and translucent MOF glass, where the inorganic nodes were linked by the organic struts with residue solvents filling the pore.

Activation of these MOF glasses by removing solvent from the pore gave rise to accessible internal surface of approximately 300 m²/g, which is comparable to the early crystalline MOFs. The glass transition temperature of these MOF glasses was found to increase exponentially with decreasing amount of cresol filling the pore. This feature allowed the MOF glasses to be processed as liquid in the preparation process and had high thermal stability after hardened by solvent evaporation.

Section 4.5 Reference

- (1) Kitagawa, S. *Chem. Soc. Rev.* **2014**, 43, 5415.
- (2) Furukawa, H.; Cordova, K. E.; O’Keeffe, M.; Yaghi, O. M. *Science* **2013**, 341, 123044.
- (3) Park, K. S.; Ni, Z.; Côté, A. P.; Choi, J. Y.; Huang, R.; Uribe-Romo, F. J.; Chae, H. K.; O’Keeffe, M.; Yaghi, O. M. *Proc. Natl. Acad. Sci.* **2006**, 103, 10186.
- (4) Yaghi, O. M.; O’Keeffe, M.; Ockwig, N. W. E. A. *Nature* **2003**, 423, 705.
- (5) Phillips, J. C. *J. Non-Cryst. Solids* **1979**, 34, 153.
- (6) Thorpe, M. F. *J. Non-Cryst. Solids* **1983**, 57, 355.
- (7) He, H.; Thorpe, M. F. *Phys. Rev. Lett.* **1985**, 54, 2107.
- (8) Bennett, P. D.; Goodwin, A. L.; Dove, M. T.; Keen, D. A.; Tucker, M. G.; Barney, E. R.; Soper, A. K.; Bithell, E. G.; Tan, J.-C.; Cheetham, A. K. *Phys. Rev. Lett.* **2010**, 104, 115503.
- (8) Chen, W.; Horike, S.; Umeyama, D.; Ogiwara, N.; Itakura, T.; Tassel, C.; Goto, Y.; Kageyama, H.; Kitagawa, S. *Ange. Chem. Int. Ed.* **2016**, 55, 5195.
- (9) Bennett, T. D.; Tan, J.-C.; Yue, Y.-Z.; Baxter, E.; Ducati, C.; Terrill, N. J.; Cheetham, A. K.; Greaves, G. N. *Nat. Commun.* **2015**, DOI: 10.1038/ncomms9079.

- (10) Bennett, T. D.; Yue, Y.; Li, P.; Qiao, A.; Tao, H.; Greaves, N. G.; Richards, T.; Lampronti, G. I.; Redfern, S. A. T.; Blanc, F.; Farha, O. K.; Hupp, J. T.; Cheetham, A. K.; Keen, D. A. *J. Am. Chem. Soc.* **2016**, 138, 3484.
- (11) Umeyama, D.; Horike, S.; Inukai, M.; Itakura, T.; Kitagawa, S. *J. Am. Chem. Soc.* **2015**, 137, 864.
- (12) Thornton, A. W.; Jelfs, K. E.; Konstas, K.; Doherty, C. M.; Hill, A. J.; Cheetham, A. K.; Bennett, T. D. *Chem. Commun.* **2016**, 52, 3750.
- (13) Chapman, K. W.; Halder, G. J.; Chupas, P. J. *J. Am. Chem. Soc.* **2009**, 131, 17546.
- (14) Bennett, T. D.; Cheetham, A. K. *Acc. Chem. Res.* **2014**, 47, 1555.
- (15) McKeown, N. B.; Budd, P. M. *Chem. Soc. Rev.* **2006**, 35, 675.
- (16) Schaate, A.; Roy, P.; Godt, A.; Lippke, J.; Waltz, F.; Wiebcke, M.; Behrens, P. *Chem. Eur. J.* **2011**, 17, 6643.
- (17) Suematsu, K.; Nakamura, K.; Takeda, *Colloid Polym. Sci.* **1983**, 261, 493.
- (18) Day, V. W.; Eberspacher, T. A.; Klemperer, W. G.; Park, C. W. *J. Am. Chem. Soc.* **1993**, 115, 8469.
- (19) Fornasieri, G.; Rozes, L.; Le Calvé, S.; Alonso, B.; Massiot, D.; Rager, M. N.; Evain, M.; Boubekeur, K.; Sanchez, C. *J. Am. Chem. Soc.* **2005**, 127, 4869.
- (20) Scolan, E.; Magnenet, C.; Massiot, D.; Sanchez, C. *J. Mater. Chem.* **1999**, 9, 2467.
- (21) Soler-Illia, G. J. d. A. A.; Rozes, L.; Boggiano, M. K.; Sanchez, C.; Turrin, C.-O.; Caminade, A.-M.; Majoral, J.-P. *Angew. Chem. Int. Ed.* **2000**, 39, 4249.
- (22) Adam, G.; Gibbs, J. H. *J. Chem. Phys.* **1965**, 43, 139.
- (23) Schmidt, H. *J. Non-Cryst. Solids* **1985**, 73, 681.
- (24) MacKenzie, J. D.; Bescher, E. P. *J. Sol-Gel Sci. Technol.* **1998**, 13, 371.
- (25) Farges, F.; Brown, G. E.; Rehr, J. J. *Phys. Rev. B* **1997**, 56, 1809.
- (26) Vaid, T. P.; Tanski, J. M.; Pette, J. M.; Lobkovsky, E. B.; Wolczanski, P. T. *Inorg. Chem.* **1999**, 38, 3394.
- (27) Greaves, G. N.; Meneau, F.; Sapelkin, A.; Colyer, L. M.; ap Gwynn, I.; Wade, S.; Sankar, G. *Nat. Mater.* **2003**, 2, 622.
- (28) Elmer, T. H. *ASM International, Engineered Materials Handbook.* **1991**, 4, 427.
- (29) Cohen, M. H.; Turnbull, D. *Nature* **1964**, 203, 964.
- (30) Martinez, L. M.; Angell, C. A. *Nature* **2001**, 410, 663;
- (31) Angell, C. A. *Science* **1995**, 267, 1924.

- (32) Yue, Y.-Z. *Front. Mater.* **2014**, 2, 1.
- (33) Amann-Winkel, K.; Gainaru, C.; Handle, P. H.; Seidl, M.; Nelson, H.; Böhmer, R.; Loerting, T. *Proc. Nat. Acad. Sci.* **2013**, 110, 17720.
- (34) Agladze, N. I.; Sievers, A. J. *Phys. Rev. Lett.* **1998**, 80, 4209.
- (35) Liu, X.; Queen, D. R.; Metcalf, T. H.; Karel, J. E.; Hellman, F. *Phys. Rev. Lett.* **2014**, 113, 025503.
- (36) Whalley, E.; Klug, D. D.; Handa, Y. P. *Nature* **1989**, 342, 782.
- (37) Greaves, G. N.; Sen, S. *Adv. Phys.* **2007**, 56, 1.
- (38) Angell, C. A.; Moynihan, C. T.; Hemmati, M. *J. Non-Cryst. Solids* **2000**, 274, 319.
- (39) Ellis, T. S.; Karasz, F. E.; Brinke, G. T. *J. Appl. Polym. Sci.* **1983**, 28, 23.

Section 4.6 Appendix



Figure A4.1. Image of the activated Ti-BPP glass. The glass tube in the picture is 1.5 cm in diameter

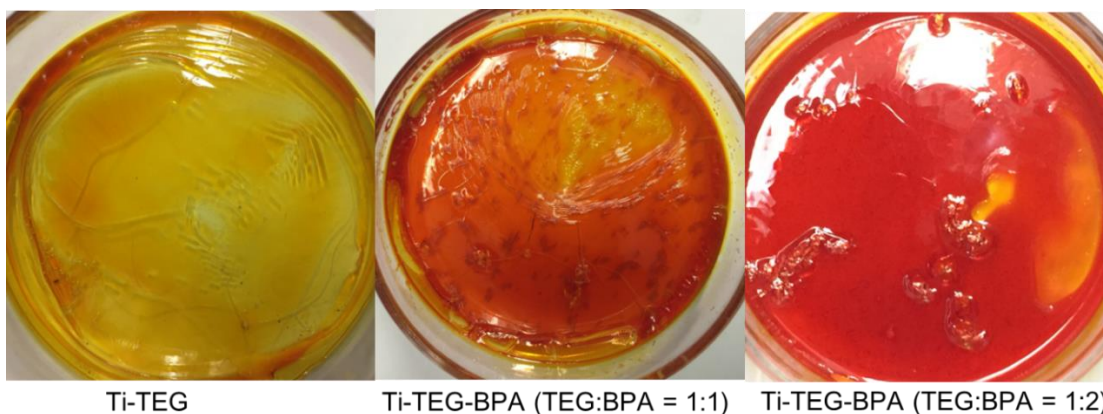


Figure A4.2. Image of as-casted MOF glasses incorporating tetraethylene glycol (TEG) linker in different ratio

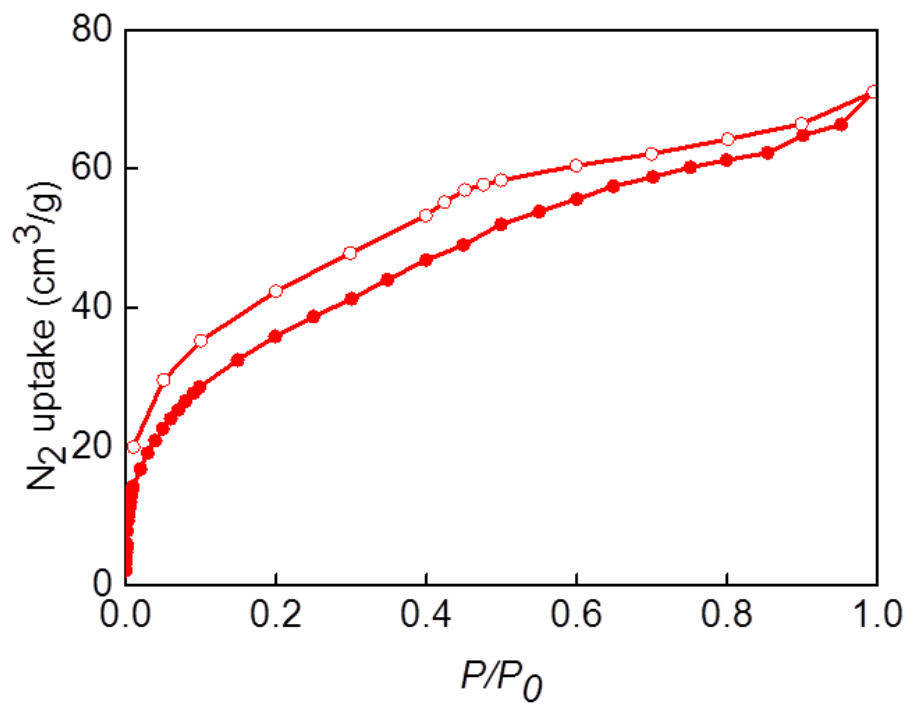


Figure A4.3. N₂ sorption isotherm of Ti-TEG-BPA (TEG:BPA = 1:1) mixed linker MOF glasses.

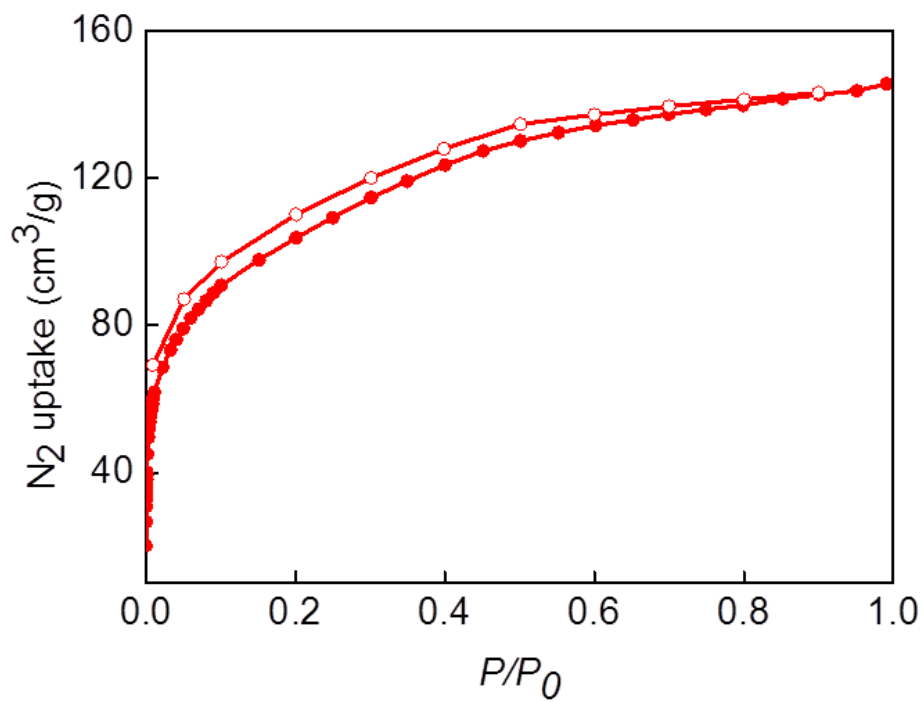


Figure A4.4. N₂ sorption isotherm of Ti-TPPP-BPA mixed linker MOF glasses

Chapter 5. Reticular Design of Woven Frameworks

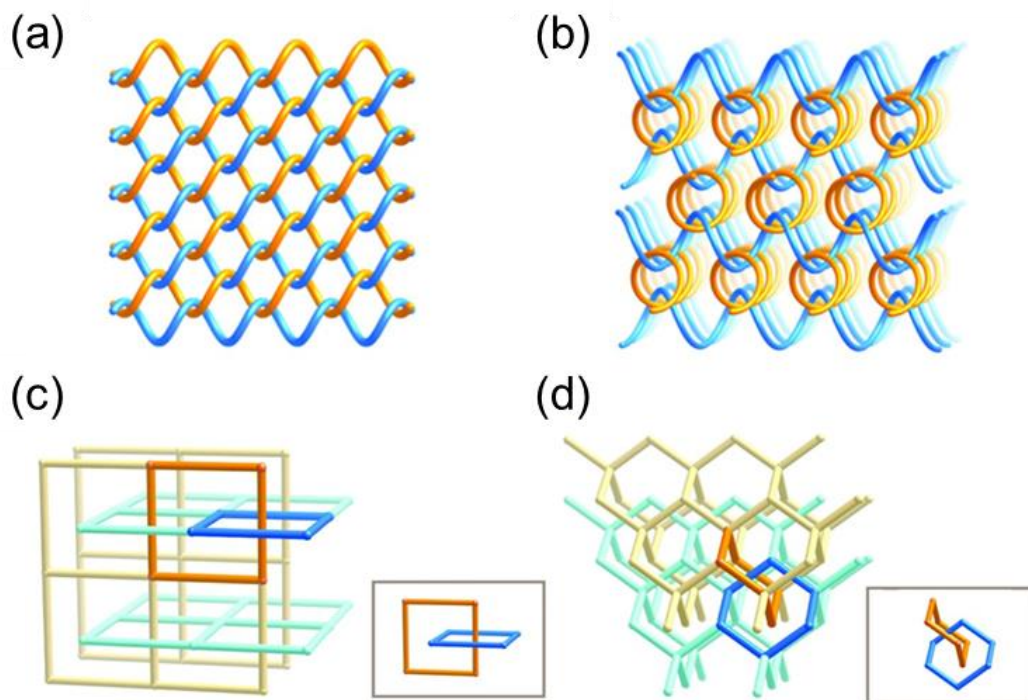
Section 5.1 Introduction

Weaving, the mutual interlacing of long threads (Scheme 5.1a), is one of the oldest and most enduring methods of making fabric. The equivalent of this important design concept is yet to be emulated in extended chemical structures. Learning how to link molecular building units by strong bonds using reticular synthesis into weaving forms would be a boon to making materials with exceptional mechanical properties and dynamics.¹ In order to successfully design weaving of chains into two- and three-dimensional chemical structures, long threads of covalently linked molecules (i.e. one-dimensional units) must be able to cross at regular intervals. It would also be desirable if such crossings serve as points-of-registry so that the threads can have many degrees of freedom to move away and back to such points without collapsing the overall structure.

The concept of weaving in chemistry has long been sought after and examples are known of structures made from weaving of metal-organic chains.² However, it remains a challenge to achieve well-defined materials and to assemble their structures by design. In addition, weaving in crystalline inorganic or covalent organic extended structures is undeveloped. Herein, we report a general strategy and its implementation for the designed synthesis of the first weaving material (covalent organic framework-505, COF-505). This COF has helical organic threads interlacing to make a weaving crystal structure with the basic topology of Scheme 5.1b, and show that this material has an unusual behavior in elasticity. Although terms such as interweaving³ and interpenetrating^{4,5} have been used to describe interlocking of two- and three-dimensional extended objects (Scheme 5.1c and d), most commonly found in metal-organic frameworks, we reserve the term weaving to describe exclusively the interlacing of one-dimensional units to make two- and three-dimensional structures (Scheme 5.1a and b). Weaving is distinctly different from the commonly observed interpenetrating frameworks as the latter is topologically interlocking (*i.e.* interlocking rings, Scheme 5.1, insets), while the weaving constructs we envision have many more degrees of freedom for enormous spatial deviations, by each of the threads, to take place independently and still preserve the underlying topology. We believe this freedom is necessary for reversible control over the mechanical properties of materials.

Our synthetic strategy for making weaving structures by design is based on the reticular synthesis of COFs. In this synthetic design, aldehyde (amine) functionalized derivative of tetra-topic metal complexes, where the position of the aldehyde (amine) groups approximates a tetrahedral geometry are used in reticular COF synthesis as the tetrahedral building block. This building block would be linked with di-topic amine (aldehyde) to give a diamond topology framework with interlacing imine-bonded molecular threads with the counter ions (*i.e.* tetrafluoroborate anions) occupying the pores.

Scheme 5.1. Illustrations of weaving and entanglement. Weaving of threads in two- (a) and three-dimensions (b) and entanglements of sheets (c), three-dimensional networks (d), and interlocking of rings (insets).



Section 5.2 Experimental Section

Section 5.2.1 Methods and Materials

Chemicals. Tetrahydrofuran (HPLC grade, Aldrich) was passed through a PureSolv MD 7 Solvent Purification System before use. 4,4'-(1,10-Phenanthroline-2,9-diyl)dibenzaldehyde was synthesized according to published literature.⁶ $\text{Co}(\text{BF}_4)_2 \cdot 6\text{H}_2\text{O}$ (purity $\geq 99\%$), $\text{Fe}(\text{BF}_4)_2 \cdot 6\text{H}_2\text{O}$ (purity $\geq 97\%$), *p*-phenylenediamine (PDA, purity $\geq 99\%$), polyvinylpyrrolidinone (PVP, M_w 10,000, and M_w 360,000), ethanol (anhydrous, purity $\geq 99.5\%$), and triethylamine (TEA, purity $\geq 99.5\%$) were obtained from Sigma-Aldrich. 1,3,5-Triformylbenzene (TFBZ, purity $\geq 98\%$), 4-(*tert*-butoxycarbonylamino)-aniline (NBPDA, purity $\geq 97\%$), acetone (anhydrous, purity $\geq 99.8\%$), isopropanol (anhydrous, purity $\geq 99.8\%$) were obtained from Acros Organics. 2,6-Pyridinedicarboxaldehyde (PCBA, purity $\geq 98\%$) was obtained from TCI. Toluene (anhydrous purity $\geq 99.8\%$), acetonitrile (purity $\geq 99.8\%$), glacial acetic acid (purity 100%) and trifluoroacetic acid (TFA, purity $\geq 99.7\%$) were obtained from EMD Millipore Chemicals.

All reactions were performed at ambient laboratory conditions, and no precautions taken to exclude oxygen or atmospheric moisture, unless otherwise specified. Pyrex glass tube charged with reagents and flash frozen with liquid N_2 were evacuated using a Schlenk line by fitting the open end of the tube inside a short length of standard rubber hose that was further affixed to a ground glass tap which could be close to insulate this assembly from dynamic vacuum when the

desired internal pressure was reached. Tubes were sealed under the desired static vacuum using an oxygen propane torch.

Analytical techniques and instrument. Gas adsorption experiments (up to 760 torr) were carried out on a Quantachrome AUTOSORB-1 automatic volumetric instrument. Ultrahigh-purity-grade N₂ and He gases were used in all adsorption measurements. The N₂ (77 K) isotherms were measured using a liquid nitrogen bath (77 K). The backbone density of the COF-112 was measured by pycnometry on a Quantachrome-UPYC 1200e V5.04 instrument using He gas. Powder X-ray diffraction (PXRD) patterns were recorded using a Rigaku Miniflex 600 (Bragg-Brentano geometry, Cu K_α radiation $\lambda = 1.54 \text{ \AA}$) instrument. Solution ¹H NMR spectra were acquired on a Bruker AVB-400 and AV-600 NMR spectrometer. Elemental microanalyses (EA) were performed in the Microanalytical Laboratory of the College of Chemistry at UC Berkeley, using a Perkin Elmer 2400 Series II CHNS elemental analyzer. The amount of Co, Fe and B in COF-112 was analyzed by an ICP–AES spectrometer with Optima 7000 DV (PerkinElmer) instrument. Attenuated total reflectance (ATR) FTIR spectra of neat samples were performed on a Bruker ALPHA Platinum ATR-FTIR Spectrometer equipped with a single reflection diamond ATR module. Scanning electron microscope (SEM) images were recorded on a Zeiss Gemini Ultra-55 analytical scanning electron microscope with accelerating voltage of 5 kV. Optical refractive index was measured using ellipsometer (Gaertner Scientific Corporation). Single crystal X-ray diffraction data was collected using synchrotron radiation on beamline 11.3.1 at the Advanced Light Source (ALS) at Lawrence Berkeley National Lab (LBNL), equipped with a Bruker Photon 100 CMOS area detector using synchrotron radiation (16 keV) and Bruker D8 Venture diffractometer equipped with a fine-focus Mo target X-ray tube operated at 40 W power (40 kV, 1 mA) and a PHOTON 100 CMOS detector. Samples were mounted on MiTeGen[®] kapton loops and placed in a 100 K nitrogen cold stream unless otherwise specified. Grazing-Incidence Wide-Angle X-ray Scattering (GIWAXS) patterns were acquired with a Pilatus 2 M (Dectris) instrument on beamline 7.3.3 at the ALS ($\lambda = 1.24 \text{ \AA}$). The incidence angle was held at 0.120° to optimize signal collection. Silver behenate was used for calibration. The Nika package for IGOR Pro (Wavemetrics) was used to reduce the acquired 1D raw data to a 2D format.

A cold field emission JEM-2100F equipped with a DELTA C_s corrector operated at 60 kV was used for HRTEM imaging. Since COF materials are electron beam sensitive, the electron beam damage to the specimen was minimized as much as possible (in this study, the beam density during the observations was less than 500 electrons/(nm²·s)). A Gatan 894 CCD camera was used for digital recording of the HRTEM images. A single HRTEM image with an exposure time of 2 seconds or a sequence of images (up to 20 frames) was recorded, with a 1 or 2 seconds exposure time for each. After drift compensation, some frames can be superimposed to increase the signal-to-noise (SN) ratio for display. HRTEM images are filtered by a commercial software named HREM-Filters Pro (HREM Research Inc. Japan). COF crystals were dispersed into ethanol by ultrasonic oscillation and dropped on a carbon film supported TEM grid. 3D electron diffraction tomography (3D-EDT) data were collected on a JEOL JEM-2100, with LaB6 filament and the control of EDT-collect program.⁷ The data was further processed by EDT-process program.

Model building in Material Studio: The rough positions of metal ions were obtained at the maxima of reconstructed 3D potential map from Fourier analysis of HRTEM image. metal complex molecules were put into one unit cell as a rigid body with metal ion positions fixed. The

orientation of complex was initially refined using PXRD pattern at first. To make it an extended structure, one metal complexes was connected to its four neighbors through corresponding COF building blocks. Then the crystal structure was optimized through energy and geometrical minimization. Anions BF_4^- were located during Rietveld refinement using PXRD patterns.

Section 5.2.3 Synthesis and Characterization of COF-505

Synthesis of $\text{Cu}(\text{PBD})_2 \cdot [\text{Cu}(\text{CH}_3\text{CN})_4]\text{BF}_4$ (388 mg, 1.00 mmol) was dissolved in anhydrous CH_3CN (8 mL) under a N_2 atmosphere and added to a solution of 4,4'-(1,10-phenanthroline-2,9-diyl)dibenzaldehyde (157 mg, 0.500 mmol) in CHCl_3 (16 mL), affording a dark red solution, which was stirred at room temperature for 30 min. The solution was then concentrated under vacuum to afford an analytically pure compound as a red solid (545 mg, quantitative). ^1H NMR (400 MHz, CDCl_3) δ 9.69 (s, 4H), 8.29 (d, $^3J = 7.9$ Hz, 8H), 8.18 (d, $^3J = 8.4$ Hz, 4H), 8.07 (d, $^3J = 8.4$ Hz, 4H), 7.70 (d, $^3J = 7.9$ Hz, 8H), 7.60 (s, 4H). ESI-MS for $[\text{C}_{52}\text{H}_{32}\text{CuN}_4\text{O}_4]^+$ (Calcd. 839.17): $m/z = 839.17$ ($[\text{M}]^+$, 100%); Elemental analysis: Calcd. For $\text{C}_{100}\text{H}_{68}\text{BCuF}_4\text{N}_8$: C, 67.36; H, 3.48; N, 6.04%. Found: C, 66.34; H, 3.37; N, 5.81%.

Synthesis and Activation of COF-505. A Pyrex tube measuring 10×8 mm (o.d \times i.d) was charged with $\text{Cu}(\text{PBD})_2$ (15 mg, 0.016 mmol), BZ (6.0 mg, 0.032 mmol), 1 mL of anhydrous THF and 0.1 mL of 6 M aqueous acetic acid solution. The tube was flash frozen at 77 K (liquid N_2 bath), evacuated to an internal pressure of 50 mTorr and flame sealed. Upon sealing, the length of the tube was reduced to 18-20 cm. The reaction was heated at 120 °C for 72 h yielding a brown solid at the bottom of the tube which was isolated by centrifugation and washed with anhydrous THF and dried at 120 °C under 50 mTorr for 12 h. This material is insoluble in water and common organic solvents such as hexanes, methanol, acetone, tetrahydrofuran, *N,N*-dimethylformamide, and dimethyl sulfoxide, indicating the formation of an extended structure. Yield: 18.7 mg, 94.4% based on $\text{Cu}(\text{PBD})_2$. Elemental analysis: for $\text{C}_{76}\text{H}_{48}\text{BCuF}_4\text{N}_8 \cdot 4\text{H}_2\text{O}$: Calcd. C, 70.45; H, 4.36; N, 8.65%. Found: C, 70.13; H, 4.03; N, 8.50%.

Synthesis of the molecular analogue of COF-505, $\text{Cu}(\text{I})\text{-bis}[(1E,1'E)\text{-}1,1'\text{-}((1,10\text{-phenanthroline-2,9-diyl})\text{bis}(4,1\text{-phenylene}))\text{bis}(N\text{-}([1,1'\text{-biphenyl}]\text{-4-yl})\text{methanimine})\text{tetrafluoroborate}$ [$\text{Cu}(\text{PBM})_2$]: A mixture of $\text{Cu}(\text{PBD})_2$ (50.0 mg, 0.108 mmol) and 4-phenylaniline (110 mg, 0.648 mmol) in anhydrous *p*-xylene and chloroform 1:1 mixture (15 mL) was stirred under reflux with a Dean-Stark apparatus over 24 h. A dark grey solid was precipitated by adding additional *p*-xylene after cooling down the mixture to room temperature, which was then collected by filtration and dried under vacuum (49 mg, 99% yield). ^1H NMR (600 MHz, $\text{DMSO-}d_6$) δ 8.81 (d, $^3J = 8.1$ Hz, 4H), 8.33 (s, 4H), 8.19 (d, $^3J = 8.2$ Hz, 4H), 8.12 (s, 4H), 7.76 (d, $^3J = 7.8$ Hz, 8H), 7.72 (d, $^3J = 7.5$ Hz, 8H), 7.60 (d, $^3J = 7.9$ Hz, 8H), 7.49 (t, $^3J = 7.7$ Hz, 8H), 7.39 (s, 4H), 7.37 (d, $^3J = 7.5$ Hz, 8H), 7.13 (d, $^3J = 7.7$ Hz, 8H). ESI-MS for $[\text{C}_{100}\text{H}_{68}\text{CuN}_8]^+$ (Calcd. 1444.49): $m/z = 1444.48$ ($[\text{M}]^+$, 100%); Elemental analysis: Calcd. For $\text{C}_{100}\text{H}_{68}\text{BCuF}_4\text{N}_8$: C, 78.40; H, 4.47; N, 7.31%. Found: C, 76.25; H, 4.55; N, 6.92%.

X-ray single-crystal structure analysis of $\text{Cu}(\text{PBD})_2$. Single-crystals of the complex were crystallized by the slow diffusion of hexane vapor into a CH_2Cl_2 solution of $\text{Cu}(\text{PBD})_2$. A red block-shaped crystal ($0.150 \times 0.120 \times 0.100$ mm) was measured and the specimen was cooled to -123 °C using an Oxford Cryosystem chilled by liquid nitrogen. Bruker APEX2 software package was used for data collection; SAINT software package was used for data reduction; SADABS was

used for absorption correction; no correction was made for extinction or decay. The structure was solved by direct methods in a triclinic space group $P-1$ with the SHELXTL software package and further refined with least squares method. The details of crystallography data are shown in Appendix (Table A5.1).

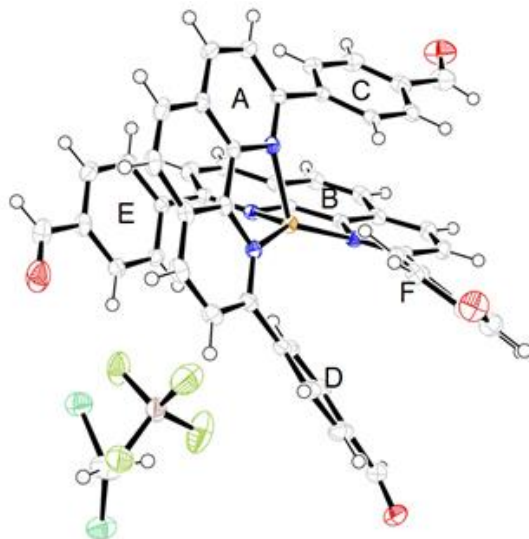


Figure 5.1 Crystal structure of Cu(PBD)_2 . Thermal ellipsoids are shown with 50% probability.

Solid-State ^{13}C CP-MAS nuclear magnetic resonance spectroscopy. Solid-state nuclear magnetic resonance (NMR) spectra were recorded at ambient pressure on a Bruker AV-500 spectrometer using a standard Bruker magic angle-spinning (MAS) probe with 4 mm (o.d.) zirconia rotors. The magic angle was adjusted by maximizing the number and amplitudes of the signals of the rotational echoes observed in the ^{79}Br MAS FID signal from KBr. The transmitter frequency of ^{13}C NMR is 125.80 MHz.

The solid-state ^{13}C NMR spectra were acquired using cross-polarization (CP) MAS technique with the ninety degree pulse of ^1H with 4.2 μs pulse width. The CP contact time was 2 ms. High power two-pulse phase modulation (TPPM) ^1H decoupling was applied during data acquisition. The decoupling frequency corresponded to 32 kHz. The MAS sample spinning rates was 11 kHz. Recycle delays between scans were 2 s. The ^{13}C chemical shifts are given relative to neat tetramethylsilane as zero ppm, calibrated using the methylene carbon signal of adamantane assigned to 38.48 ppm as secondary reference.

The experimental setup for cross-polarization and polarization inversion (CPPI) spectral editing is the same as the CPMAS experiment. Pulse sequences are included in work by Zilm and co-workers (14). Spectral editing parameters were determined as ^1H with 6 μs pulse width, cross-polarization times of 2 ms, and a polarization inversion time of 40 μs .

Demetalation and remetalation of COF-505. To a suspension of COF-505 powder was added a 0.3 M KCN solution in a 1:5 mixture of CH_3OH and H_2O , and was heated at 90 $^\circ\text{C}$. The solution was replaced by a fresh solution of KCN every 24 h and this procedure was repeated three times. Control experiment without KCN solution was also conducted under otherwise identical conditions. Subsequently, both samples were washed with anhydrous CH_3OH and dried at 120 $^\circ\text{C}$

under 50 mTorr for 12 h. The demetalated material was observed to be pale-yellow in color, in contrast to the dark brown color of COF-505.

The remetalation process was carried out in similar conditions with the complexation reaction to yield complex Cu(PBD)₂. Dried powder of the demetalated material was immersed in anhydrous CHCl₃, to which was added a 0.01 M Cu(CH₃CN)BF₄ solution. This mixture was stirred for 12 h under N₂ at room temperature and dark brown color was recovered.

Inductively coupled plasma atomic emission spectroscopy (ICP-AES) was used to determine the copper component in these materials. Samples were dissolved in OPTIMA grade nitric acid. The stock solutions were then diluted to 1:10 (v/v) with H₂O, which were analyzed on an Agilent 7500ce ICP-AES using helium collision gas mode. The copper content in COF-505 (C₇₆H₄₈BCuF₄N₈·4H₂O) is calculated to be 4.9% and measured to be 4.8%, while in the demetalated material, it was determined to be in the range of 0.15% to 0.38%, approximately 3-8% of the original Cu concentration. After remetalation, the Cu content was determined to be 3.9% to 4.2%, which is 82-88% of COF-505.

Mechanical studies of COF-505 by atomic force microscope (AFM). Nano-indentation based on AFM (Nanoscope Dimension 3100) was employed to measure Young's modulus of COF-505 and the demetalated material.⁸ AFM images of the particles were first acquired under non-contact mode, followed by indentation at the summit of the aggregate which is relatively flat.

Following the standard procedure of nano-indentation, the Young's modulus is related to the indentation curve by Eq. (1):

$$S = \frac{dP}{dh} = \beta \frac{2}{\pi} E_{eff} \sqrt{A} \quad (1)$$

For COF-505, we found the indentation curve is close to pure elastic deformation at small depth described by Hertz theory. Its Young's modulus is calculated to be 12.5 GPa using a tip radius of 15 nm, and Poisson's ratio of $\nu = 0.3$. This value lies within the typical range of MOFs.⁹ The measured Young's moduli of other COF-505 particles and remetalated COF-505 are within 30% deviation. On the contrary, the demetalated material is very soft and shows significant plastic deformation under moderate force. Applying Eq. (1) we obtained its Young's modulus around 1.3 GPa, assuming a tip radius of 15 nm and a tip angle of 30°.

Section 5.2.3 Synthesis and Characterization of COF-112

Synthesis of 2,6-pyridinedicarboxaldehydebis-(*p*-aminophenylimine) (NH₂-DIP): 2,6-pyridine-dicarboxaldehyde (270 mg, 2 mmol) was dissolved in 16 mL of anhydrous isopropyl alcohol under nitrogen. This solution was added dropwise into 1,4-benzenediamine (648 mg, 6 mmol) in 16 mL of ethanol. The reaction mixture was stirred for 30 min and filtered. The precipitate was washed with ethanol thoroughly and dried to give compound NH₂-DIP (518 mg, 82%). ¹H NMR (400 MHz, d-DMSO) δ 8.64 (s, 2H), 8.11 (d, 3J = 7.6 Hz, 2H), 7.98 (t, ³J = 8.0 Hz, 1H), 7.25 (d, ³J = 8.8 Hz, 4H), 6.62 (d, ³J = 8.4 Hz, 4H), 5.43 (s, 4H). HRMS (ESI⁺) for [C₁₉H₁₈N₅]⁺ (M+H⁺): m/z Calcd. 316.3875, found =316.1557.

Synthesis of 2,6-pyridinedicarboxaldehydebis-(*p*-aminophenylimine) (NHBoc-DIP): 2,6-pyridine-dicarboxaldehyde (128 mg, 0.95 mmol) was dissolved in 5 mL of isopropyl alcohol

purged with nitrogen. This solution was added dropwise into 4-(tert-butoxycarbonylamino)-aniline (396 mg, 1.90 mmol) in 5 mL of ethanol. The reaction mixture was stirred for 30 min and filtered. The precipitate was washed with ethanol thoroughly and dried to give compound **NHBoc-DIP** (387.0 mg, 79%). ¹H NMR (600 MHz, d-acetone δ 8.71 (s, 2H), 8.56 (s, 2H), 8.30 (d, ³J = 7.8 Hz, 2H), 8.01 (t, ³J = 7.8 Hz, 1H), 7.67 (d, ³J = 8.4 Hz, 4H), 7.40 (d, ³J = 8.4 Hz, 4H), 1.50 (s, 18H). HRMS (ESI⁺) for [C₂₉H₃₃O₄N₅]⁺ (M+H⁺): *m/z* = Calcd 516.6215, found 516.2611.

Synthesis of Co(NH₂-DIP)₂(BF₄)₂. Co(BF₄)₂·6H₂O (102.2 mg, 0.3 mmol) was dissolved in 5 mL of MeCN and added to a solution of NH₂-DIP (188.2 mg, 0.6 mmol) in 5 mL of CH₂Cl₂, affording a dark brown solution, which was stirred under N₂ at room temperature for 30 min. The solution was then concentrated under vacuum to afford this compound as a dark brown solid (258 mg, quantitative). HRMS (ESI⁺) for [C₃₈H₃₄N₁₀Co₁]²⁺ *m/z* = Calcd 344.6144, found 343.1152. This complex was further studied by single crystal X-ray diffraction (Figure A5.1).

Synthesis of Co(NHBoc-DIP)₂(BF₄)₂. Co(BF₄)₂·6H₂O (128 mg, 0.375 mmol) was dissolved in 5 mL of MeCN and added to a solution of NHBoc-DIP (387 mg, 0.75 mmol) in 5 mL of CH₂Cl₂, affording a dark brown solution, which was stirred under N₂ at room temperature for 30 min. The solution was then concentrated under vacuum to afford an analytically pure title compound as a dark brown solid (473.0 mg, quantitative). HRMS (ESI⁺) for [C₅₈H₆₆O₈N₁₀Co₁]²⁺ *m/z* = Calcd 544.7193, found 544.7194.

Synthesis of Fe(NH₂-DIP)₂(BF₄)₂. Fe(BF₄)₂·6H₂O (101.2 mg, 0.3 mmol) was dissolved in 5 mL of MeCN and added to a solution of NH₂-DIP (188.2 mg, 0.6 mmol) in 5 mL of CH₂Cl₂, affording a dark solution, which was stirred under N₂ at room temperature for 30 min. The solution was then concentrated under vacuum to afford the title compound as a dark brown solid (256.0 mg, quantitative). HRMS (ESI⁺) for [C₃₈H₃₄N₁₀Fe]²⁺ *m/z* = Calcd 343.1153, found 343.1152.

One-pot homogeneous synthesis route to COF-112-Co. A Pyrex tube measuring 10 × 8 mm (o.d × i.d) was charged with 2,6-pyridinedicarboxaldehyde (5.4 mg, 0.04 mmol), 4-(tert-butoxycarbonylamino)-aniline (8.3 mg, 0.04 mmol), Co(BF₄)₂·6H₂O (6.8 mg, 0.02 mmol), 0.3 mL of anhydrous MeCN, 0.4 mL of anhydrous toluene and 0.05 mL of aqueous trifluoroacetic acid solution (trifluoroacetic acid: water: 1:4). The tube was flash frozen at 77 K (liquid N₂ bath), evacuated to an internal pressure of 50 mTorr and flame sealed. Upon sealing, the length of the tube was reduced to 18-20 cm. The reaction was heated at 85 °C for 48 h, yielding brown solids at the bottom of the tube which was isolated by centrifugation and washed with anhydrous acetone and dried at 120 °C under 50 mTorr for 12 h. This material is insoluble in water and common organic solvents such as hexanes, methanol, acetone, tetrahydrofuran, *N,N*-dimethylformamide, and dimethyl sulfoxide, indicating the formation of an extended structure. C₂₆H₁₈N₆Co₁B₂F₈·2H₂O: Calcd.: C, 45.72; H, 3.25; N, 12.30; Co, 8.63; B, 3.17; F, 22.25; O, 4.68%. Found: C, 45.57; H, 3.81; N, 12.05; Co, 8.41; B, 3.14%.

Metal-complex synthetic route to COF-112-Co with Co(NH₂-DIP)₂(BF₄)₂. A Pyrex tube measuring 10 × 8 mm (o.d × i.d) was charged with Co(NH₂-DIP)₂(BF₄)₂ (8.6 mg, 0.01 mmol), 2,6-pyridine-dicarboxaldehyde (2.7 mg, 0.02 mmol), Co(BF₄)₂·6H₂O (3.4 mg, 0.01 mmol), 0.4 mL of anhydrous MeCN, 0.6 mL of anhydrous toluene and 0.1 mL of 6 M aqueous acetic acid solution. The tube was flash frozen at 77 K (liquid N₂ bath), evacuated to an internal pressure of 50 mTorr and flame sealed. Upon sealing, the length of the tube was reduced to 18-20 cm. The reaction was

heated at 120 °C for 72 h, yielding brown solids at the bottom of the tube. The solids were isolated by centrifugation and washed with anhydrous acetone and dried at 120 °C under 50 mTorr for 12 h.

Homogeneous synthesis of COF-112-Co with Boc-protected complex Co(NHBoc-DIP)₂(BF₄)₂. A Pyrex tube measuring 10 × 8 mm (o.d × i.d) was charged with Co(NHBoc-DIP)₂(BF₄)₂ (12.6 mg, 0.01 mmol), 2,6-pyridine-dicarboxaldehyde (2.7 mg, 0.02 mmol), Co(BF₄)₂·6H₂O (3.4 mg, 0.01 mmol), 0.3 mL of anhydrous MeCN, 0.4 mL of anhydrous toluene and 0.05 mL of aqueous trifluoroacetic acid solution (trifluoroacetic acid: water: 1:4). The tube was flash frozen at 77 K (liquid N₂ bath), evacuated to an internal pressure of 50 mTorr and flame sealed. Upon sealing, the length of the tube was reduced to 18-20 cm. The reaction was heated at 100 °C for 48 h yielding brown solids at the bottom of the tube.

Synthesis of COF-112-Fe. A Pyrex tube measuring 10 × 8 mm (o.d × i.d) was charged with Fe(NH₂-DIP)₂(BF₄)₂ (8.6 mg, 0.01 mmol), 2,6-pyridinedicarboxaldehyde (2.7 mg, 0.02 mmol), Fe(BF₄)₂·6H₂O (3.3 mg, 0.01 mmol), 0.4 mL of anhydrous EtOH, 0.6 mL of anhydrous toluene and 0.1 mL of 6 M aqueous acetic acid solution. The tube was flash frozen at 77 K (liquid N₂ bath), evacuated to an internal pressure of 50 mTorr and flame sealed. Upon sealing, the length of the tube was reduced to 18-20 cm. The reaction was heated at 120 °C for 72 h yielding black solids at the bottom of the tube which was isolated by centrifugation and washed with anhydrous acetone and dried at 120 °C under 50 mTorr for 12 h. This material is insoluble in water and common organic solvents such as hexanes, methanol, acetone, tetrahydrofuran, *N,N*-dimethylformamide, and dimethyl sulfoxide, indicating the formation of an extended structure. Elemental analysis: C₂₆H₁₈N₆Fe₁B₂F₈H₂O: Calcd.: C, 45.18; H, 3.05; N, 12.70; Fe, 8.44; B, 3.27; F, 22.96; O, 2.42%. Found: C, 47.03; H, 3.68; N, 12.15; Fe, 8.95; B, 3.07%.

Synthesis of Non-Metallated Polyimine Chain and Amorphous counter part of COF-112. PCBA and PDA were condensed without cobalt under conventional heterogeneous imine COF synthesis condition to give a crystalline polyimine, the PXRD pattern of which differs from COF-112. From well-known polymer chemistry, linear polymers often pack in parallel manner instead of interlacing manner. Thus, although the exact structure of the polyimine could not be solved from powder X-ray diffraction, it is clear that it has a structure substantially different from COF-112. When reacting the crystalline polyimine with cobalt salt under the same heterogeneous imine COF synthesis condition, metalation took place (the powder become reddish brown) and the powder X-ray diffraction peaks disappeared, indicating the reversible imine condensation enable the partially metallated polyimine chain to change its configuration but not sufficiently to arrive in the complete woven structure of COF-112. We believe this experiment rationalizes the failure of one-pot heterogeneous route to get COF-112, where the partially metallated polyimine chain would first form upon mixing of reagents, followed by metalation. Solvent annealing in this case would also be insufficient to correct defects and yield crystalline COF-112.

Section 5.3 Result and Discussion

Our synthetic strategy for making weaving structures by design is shown in Scheme 3, where we start with the aldehyde functionalized derivative of the well-known Cu(I)-bis[4,4'-(1,10-phenanthroline-2,9-diyl)dibenzaldehyde] tetrafluoroborate, Cu(PDB)₂(BF₄) complex salt (Scheme 3A). The position of the aldehyde groups approximates a tetrahedral geometry and therefore can be used in reticular synthesis as a building block to be linked with benzidine (BZ) and make imine-bonded PDB-BZ threads weaving arrangement with the tetrafluoroborate anions occupying the pores (Scheme 3B). The fact that the PDB units are oriented in a mutually interlacing fashion ensures that the threads produced from linking of the building units are entirely independent, with the copper(I) ions serving as templates (points-of-registry) to bring those threads together in a precise manner at well-defined intervals. Since the PDB-BZ threads are topologically independent of the copper ions, the resulting weaving structure is formally a COF (termed COF-505). The overall tetrahedral geometry of the aldehyde units ensures the assembly of the threads into a three-dimensional framework (Figure 5.1). In the present case, the topology of the framework is that of diamond as expected from the principles of reticular chemistry. In this study, we show that by removing the copper(I) ions, the structure and its topology remain intact regardless of how the threads deviate from their points-of-registry, and upon remetaling the overall structure is reversibly restored. We find a ten-fold increase in elasticity when going from the metalated to the demetalated forms of the material.

The copper(I)-bisphenanthroline core of the Cu(PDB)₂ has been studied extensively as a discrete molecule for the formation of supramolecular complexes;¹⁰⁻¹² however, as yet it has not been used to make extended structures especially of the type discussed here. The tolerance for robust reaction conditions makes this complex suitable for imine COF synthesis,^{10,13} especially in weak acidic conditions. Thus, the tetrahedral building unit, Cu(PDB)₂, was designed bearing aldehyde groups in the *para* positions of the two phenyl substituents (Figure 5.2a). The synthesis of Cu(PDB)₂(BF₄) molecular complex was carried out by air-free copper(I) complexation of 4,4'-(1,10-phenanthroline-2,9-diyl)dibenzaldehyde according to a previously reported procedure.⁶ The single crystal structure of this complex reveals a distorted tetrahedral geometry around copper(I) center, where a dihedral angle of 57° is found between the two phenanthroline planes.

COF-505 was synthesized using imine condensation reactions by combining a mixture of Cu(PDB)₂(BF₄) (15 mg, 0.016 mmol) and BZ (6.0 mg, 0.032 mmol) in tetrahydrofuran (THF, 1 mL) and aqueous acetic acid (6 mol/L, 100 μL). The reaction mixture was sealed in a Pyrex tube and heated at 120 °C for 3 days. The resulting precipitate was collected by centrifugation, washed with anhydrous THF, and then evacuated at 120 °C for 12 h to yield 18.7 mg [94.4% based on Cu(PDB)₂(BF₄)] of a dark brown crystalline solid (COF-505), which was found to be insoluble in common polar and nonpolar organic solvents.

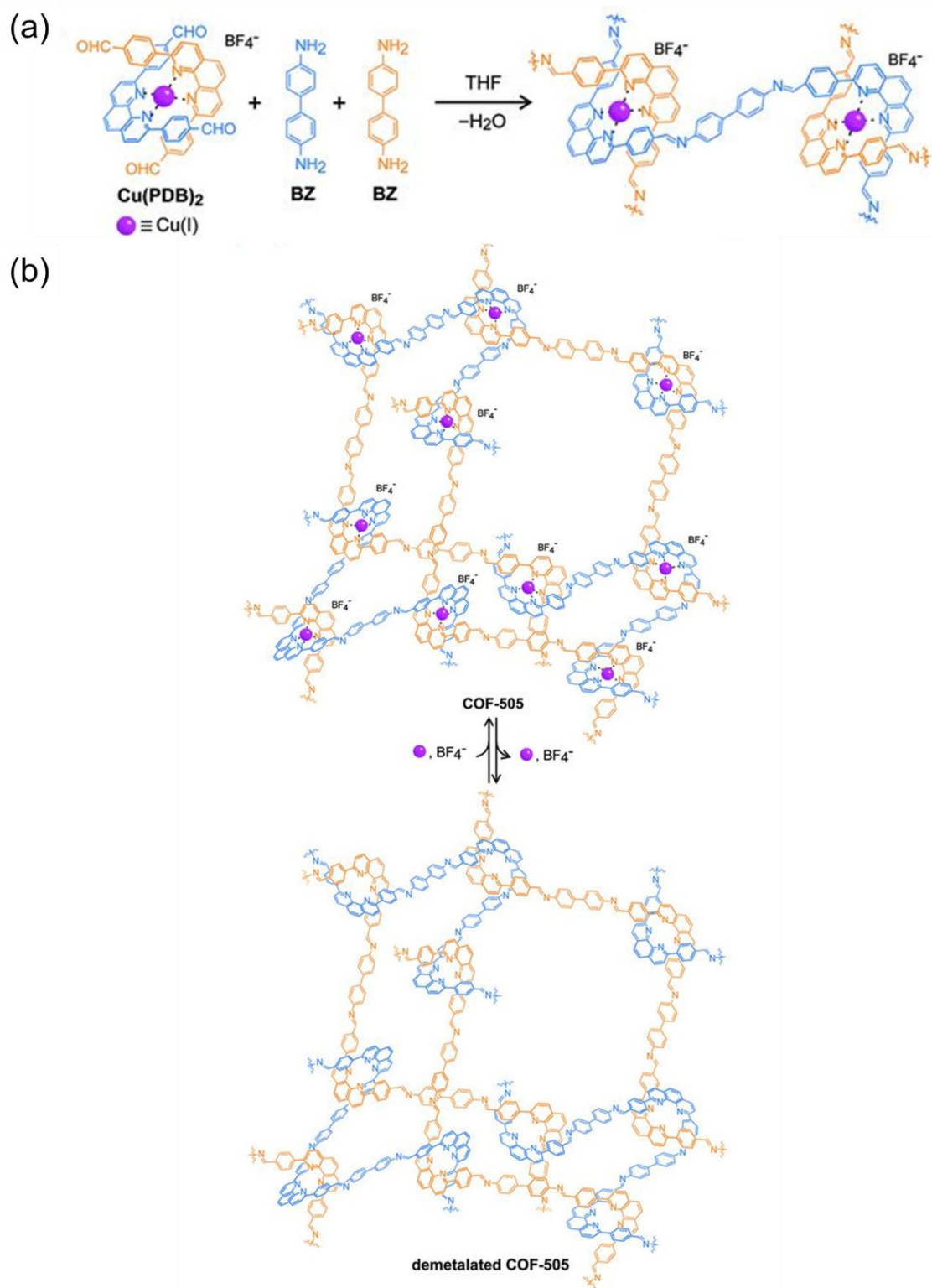


Figure 5.2. A general strategy for the design of weaving structures from organic threads using copper(I) as a template (a) to make extended weaving structure (b).

FT-IR and solid-state NMR spectroscopy studies were performed on COF-505 to confirm the formation of imine linkages (Figure A5.2-A5.4). A molecular analogue of COF-505 fragment, Cu(I)-bis[(1,10-phenanthroline-2,9-diyl)bis(phenylene)bis(biphenyl)methanimine] tetrafluoroborate, $\text{Cu}(\text{PBM})_2(\text{BF}_4)$, was used as a model compound and synthesized by condensation of $\text{Cu}(\text{PDB})_2(\text{BF}_4)$ and 4-aminobiphenyl (Figure A5.3). The FT-IR spectrum of COF-505 shows peaks at 1621 and 1196 cm^{-1} [1622 and 1197 cm^{-1} for $\text{Cu}(\text{PBM})_2(\text{BF}_4)$], which are characteristic C=N stretching modes for imine bonds.^{14,15} Furthermore, the ^{13}C cross-polarization with magic-angle spinning (CPMAS) solid-state NMR spectrum acquired for COF-505 displays a series of peaks from 140 to 160 ppm, similar in shape and occurring at chemical shifts characteristic of those expected for C=N double bonds. In order to differentiate imine bonds from C=N double bonds of the phenanthroline unit, a cross-polarization and polarization inversion (CPPI) technique was applied, which leaves the signal for quaternary ^{13}C groups unchanged, while the residual tertiary ^{13}CH signal should approach zero.¹⁶ The observation of decreased intensity for the ^{13}CH signal under these conditions confirmed the existence of imine CH=N double bond (Figure A5.4). Overall, these observations served as initial confirmation of having covalently linked imine extended threads in COF-505.

Prior to determining the single crystal structure of COF-505, we studied the morphology and purity of the as-synthesized material. We found, using scanning electron microscopy (SEM), crystallites of approximately 200 nm are aggregated into spheres of 2 μm in diameter (Figure 5.3), which is possibly due to weak interactions of the synthesized material with the solvent, THF. No other phase was observed from SEM images taken throughout the material.

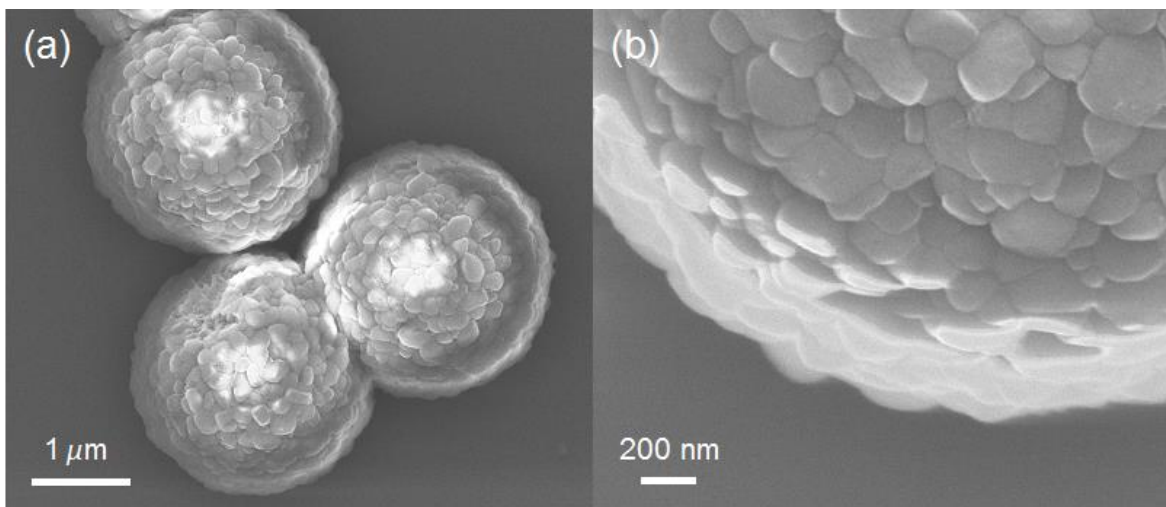


Figure 5.3. Morphology of COF-505 studied by SEM. (a) Crystalline spheres from aggregated crystallites. (b) Crystal plates on the surface of a sphere.

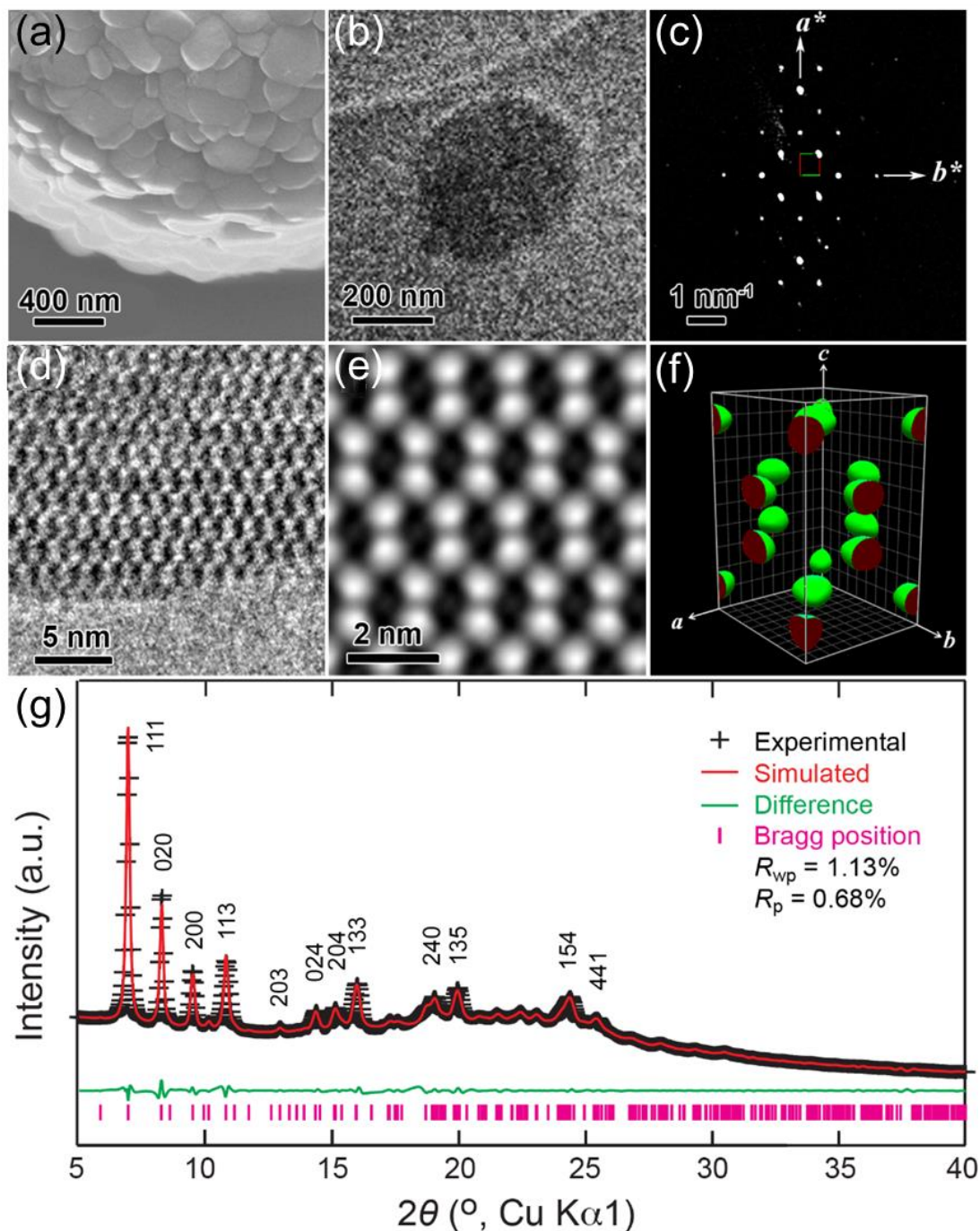


Figure 5.4. Structural characterizations of COF-505. (a) Crystallites aggregated on a crystalline sphere observed by SEM. (b) TEM image of a single sub- μm crystal used for 3D-EDT. (c) 2D projection of the reconstructed reciprocal lattice of COF-505 obtained at 298 K from a set of 3D-EDT data (the inset shows image of used crystal). (d) HRTEM image of COF-505 taken with the $[1-10]$ incidence. (e) 2D projected potential map obtained by imposing pgg plane group symmetry on figure 5.4d. (f) Reconstructed 3D electrostatic potential map (threshold: 0.8). (g) Indexed PXRD pattern of the activated sample of COF-505 (black) and the Pawley fitting (red) from the modeled structure.

A single sub- μm crystal (Figure 5.4b) from this sample was studied by three-dimensional electron diffraction tomography (3D-EDT), which is a powerful tool for solving structures of nano-scale single crystal.^{7,17,18} One EDT data set was collected from the COF-505 (Figure 5.4c) by combining specimen tilt and electron-beam tilt in the range of -41.3° to $+69.1^\circ$ with a beam-tilt step of 0.2° . From the acquired data set 3D reciprocal lattice of COF-505 was constructed that was identified as a *C*-centered orthorhombic Bravais lattice. The unit cell parameters were determined to be $a = 18.9 \text{ \AA}$, $b = 21.3 \text{ \AA}$, $c = 30.8 \text{ \AA}$ and $V = 12399 \text{ \AA}^3$ which can be used to index reflections observed in both powder X-ray diffraction (PXRD) pattern and Fourier diffractograms of high-resolution TEM images (Figure 5.4d). Later, the unit cell parameters were further refined to be $a = 18.6 \text{ \AA}$, $b = 21.4 \text{ \AA}$, $c = 30.2 \text{ \AA}$, $V = 12021 \text{ \AA}^3$ by Pawley refinement of PXRD pattern (figure 5.4g). The observed reflection conditions were summarized as *hkl*: $h+k = 2n$; *hk0*: $h, k = 2n$; *h0l*: $h = 2n$; *0kl*: $k = 2n$, suggesting five possible space groups, *Cm2a* (No. 39), *Cmma* (No. 67), *Cmca* (No. 64), *Cc2a* (No. 41) and *Ccca* (No. 68). Three of them, *Cm2a*, *Cmma*, and *Ccca*, were excluded, as their projected symmetries along [1-10] did not coincide with that of HRTEM image, *pgg* (figure 5.4e). Furthermore, by performing Fourier analysis of the HRTEM images and imposing symmetry to the reflections, copper(I) positions were determined from the reconstructed 3D potential map (figure 5.4f). The structure of COF-505 was built in Materials Studio by putting Cu(PDB)₂ units at copper positions and connecting them through biphenyl (reacted BZ) molecules. The chemical compositions are determined by elemental analysis, therefore once the number of copper atoms in one unit cell is obtained, the numbers of other elements in one unit cell are also determined, which indicates that the unit-cell framework is constructed by 8 Cu(PDB)₂ and 16 biphenyl units. However, symmetry operations of the space group *Cmca* requires two PDB units connected to one copper onto a mirror plane perpendicular to *a* axis, which is not energetically favorable geometry. Therefore, the final space group was determined to be *Cc2a*, according to which a structure model was built and optimized. The PXRD pattern calculated from this model is consistent with the experimental pattern of activated COF-505.

According to the refined model, COF-505 crystallizes in a diamond (**dia**) network with the distorted tetrahedral building units Cu(PBD)₂ and biphenyl linkers BZ through *trans* imine bonds. As a result, adamantane-like cages of $19 \times 21 \times 60 \text{ \AA}^3$ are obtained and elongated along the *c*-axis (dimensions are calculated based on copper-to-copper distances). This allows for two diamond networks of identically weaving frameworks to form the crystal. In other words, two weaving frameworks are mutually weaving in COF-505 crystals along the *c* direction, with the two frameworks related by a C₂ rotation on the *b*-axis, leaving sufficient space for BF₄⁻ counter-ions.

Fundamentally, each of the threads making up a framework is a helix (Figure 5.5a). For clarity, only a fragment of one weaving framework is shown (Figure 5.5b and c). The helices are entirely made of covalently linked organic threads. As expected, they are weaving and being held by copper ions at their points-of-registry. These threads are propagating in two different directions along [110] and [-110]. Although the helices are chemically identical, they have opposite chirality giving rise to an overall racemic and weaving framework of the same topology as in Scheme 5.1b.

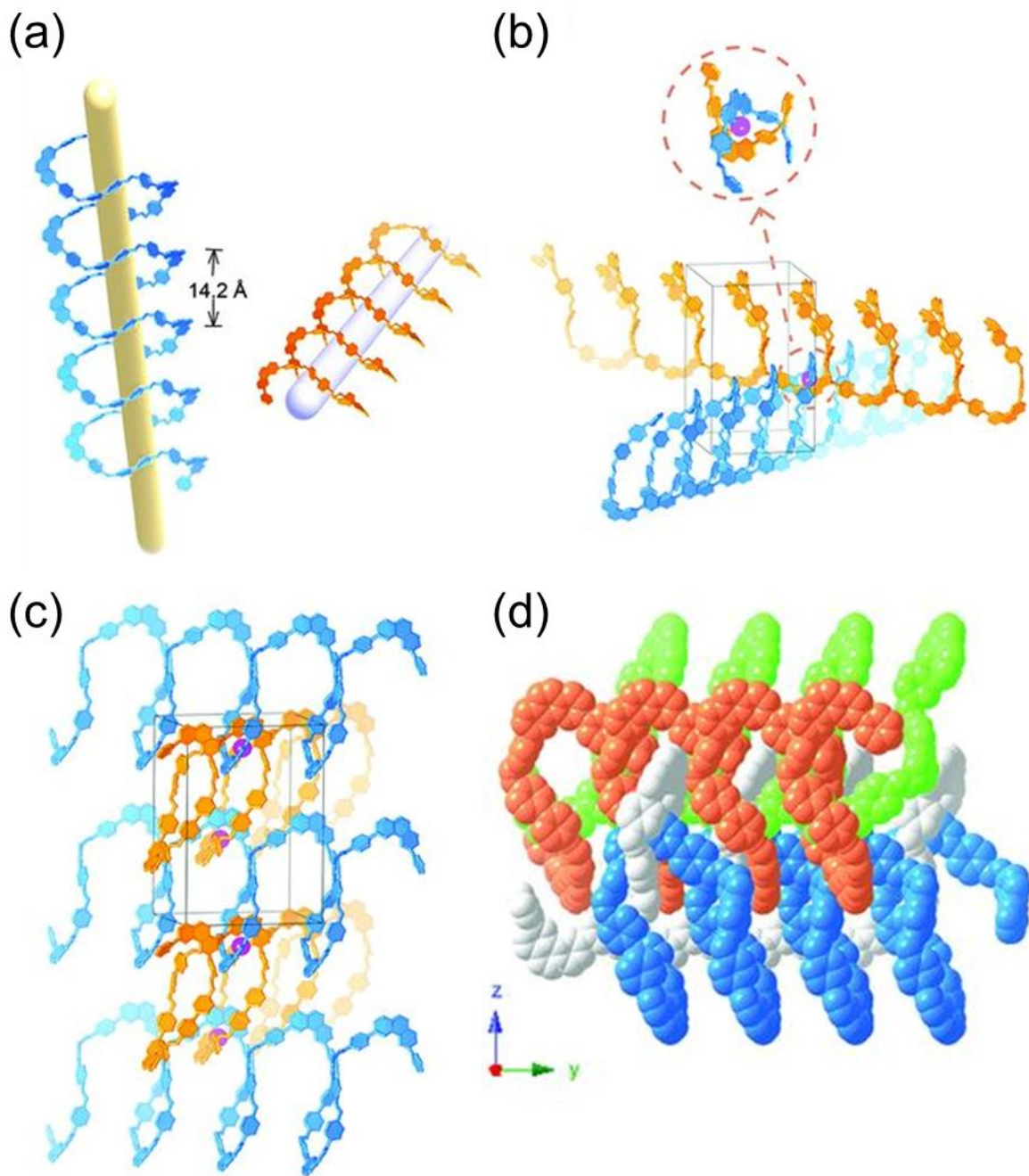


Figure 5.5. The woven structure of COF-505. The woven COF-505 consists of chemically identical helices (marked in blue and orange because they are of opposite chirality) with the pitch of 14.2 Å (a). The orange helices propagate in the [1-10] direction, whereas the blue helices propagate in the [110] direction with copper (I) ions as the points of registry (b). Neighboring blue helices are woven with the orange helices to form the overall framework (c). Blue and orange helices and their C₂symmetry-related green and gray copies are mutually woven (d). Additional parallel helices in (c) and (d) are omitted for clarity.

Since COF-505 structure is a weaving of helices, we sought to remove the copper centers and examine the properties of the material before and after demetalation. Heating COF-505 in a KCN methanol-water solution results in a significant decrease of copper content in the resulting demetalated material. Using inductively coupled plasma (ICP) analysis, we find up to 97% of the copper ions have been removed. The dark brown color of COF-505, due to the copper-phenanthroline metal-to-ligand charge transfer (MLCT),¹⁹ changed to pale-yellow as demetalation proceeded. Despite the fact that the crystallinity of demetalated material was decreased in comparison to that of COF-505, SEM images show similar morphology before and after demetalation (Appendix Figure A5.5). Additionally, the imine linkages were also maintained. FT-IR peaks at 1621 and 1195 cm^{-1} (Figure A5.7 and A5.8), which are representative of C=N stretching modes for imines, are consistent with COF-505 (1621 and 1196 cm^{-1}). Furthermore, the material can be remetalated with copper(I) ions by stirring in a CHCl_3 and CH_3OH solution of $\text{Cu}(\text{CH}_3\text{CN})_4(\text{BF}_4)$ to give back crystalline COF-505. This remetalated COF-505 has identical crystallinity to the original as-synthesized COF-505 as evidenced by the full retention of the intensity and positions of the peaks in the PXRD. In the FT-IR spectrum, the peak representing imine C=N stretch was retained, indicating that the framework is chemically stable and robust under such reaction conditions. This demonstrates that the open phenanthroline sites in the demetalated material can be complexed again with copper ions, and that the process of demetalation and remetalation is chemically reversible.

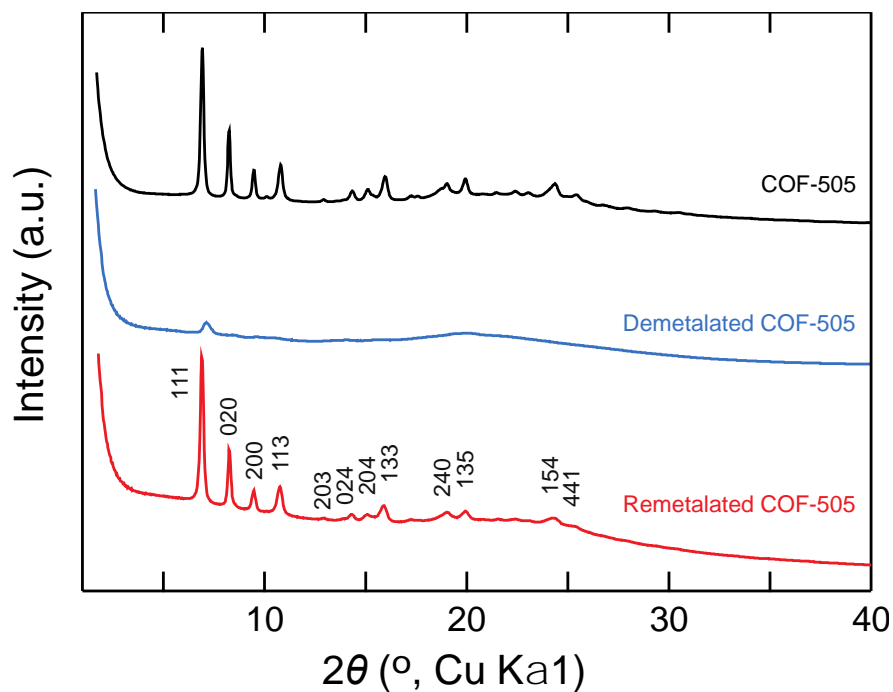


Figure 5.6. PXRD patterns of as-synthesized COF-505, the demetalated and remetalated materials. The crystallinity of COF-505 decreases upon demetalation and can be fully restored after remetalation with copper(I) ions.

Given the facility with which demetalation can be carried out and the full retention of the structure upon remetalation, we examined the elastic behavior of the metalated and demetalated COF-505. Using nano-indentation atomic force microscope, a single particle of each of these two samples was indented by a conical tip and the load-displacement curves were recorded for both loading and unloading process.⁸ The effective Young's moduli (neglecting the anisotropy of the elasticity) of the two COF-505 materials were measured to be approximately 12.5 GPa and 1.3 GPa for the metalated and demetalated particles, respectively (Figure 5.7). Remarkably, this ten-fold increase in elasticity upon demetalation of COF-505 is similar to the increase found in going from porous MOFs to polyethylene.⁹ The distinct increase of elasticity could be attributed to the loose interaction between the threads upon removal of copper. Moreover, the elasticity of the original COF-505 could be fully recovered after the process of demetalation and remetalation, being facilitated by the unique structure of weaving helical threads that easily 'zip' and 'unzip' at their points-of-registry. It is worth noting that the large difference in elasticity modulus is caused by loss of copper(I) ions, which in total only represent a minute mole percentage (0.67 mol%) of the COF-505 structure.

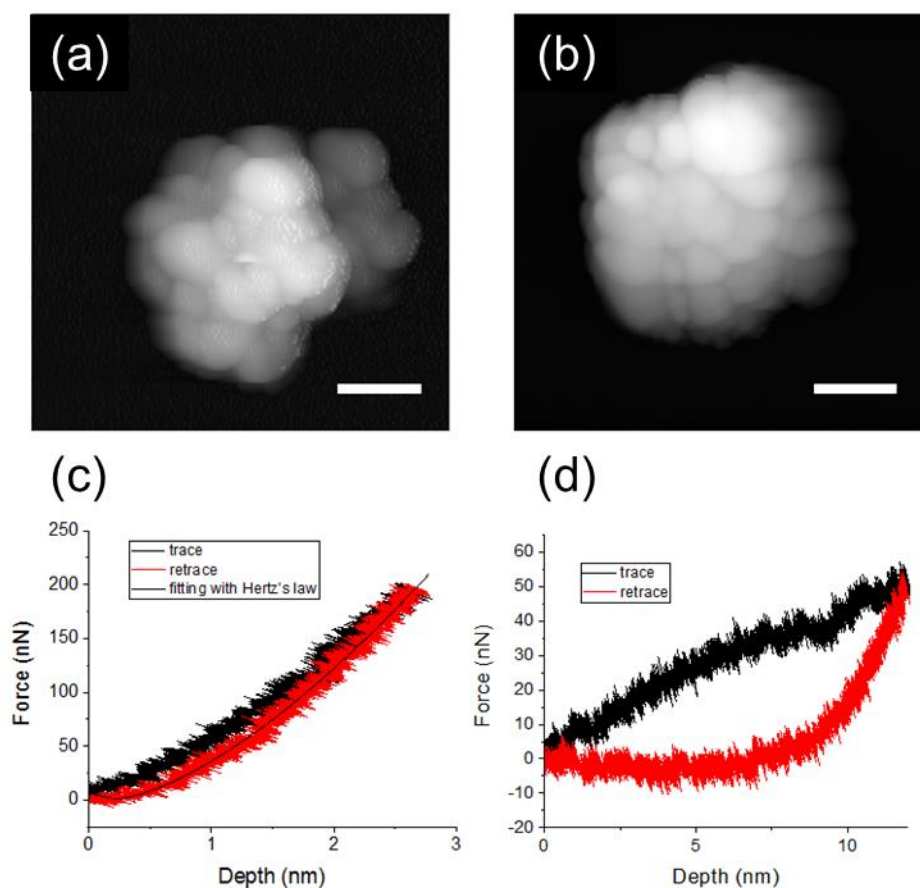


Figure 5.7. AFM study of the as-synthesized and demetalated COF-505. AFM images are shown for COF-505 (a) before and (b) after demetalation. Scale bar: 200 nm. Grey scale range: 240 nm. (c) The load of indentation P for COF particles before and (d) after demetalation as a function of elastic displacement Δh .

The weaving strategy reported here is potentially applicable to the conversion of other network topologies to weaving structures as illustrated in figure 5.8. In addition to the **dia** net of COF-505, a variety of other two- and three-dimensional topologies can also be achieved by weaving of threads (variously colored) using metal ions as points-of-registry. Tetrahedrally coordinated metal complexes with two ligands can be employed as tetratopic building units in reticular synthesis to construct weaving structures of corresponding topologies (*e.g.* **pnf**, **qtz** and **sod**). Metal ions with an octahedral coordination geometry, which provides another type of points-of-registry by coordinating three ligands, can also be used to synthesize weaving structures (*e.g.* **kgm** and **pcu**).

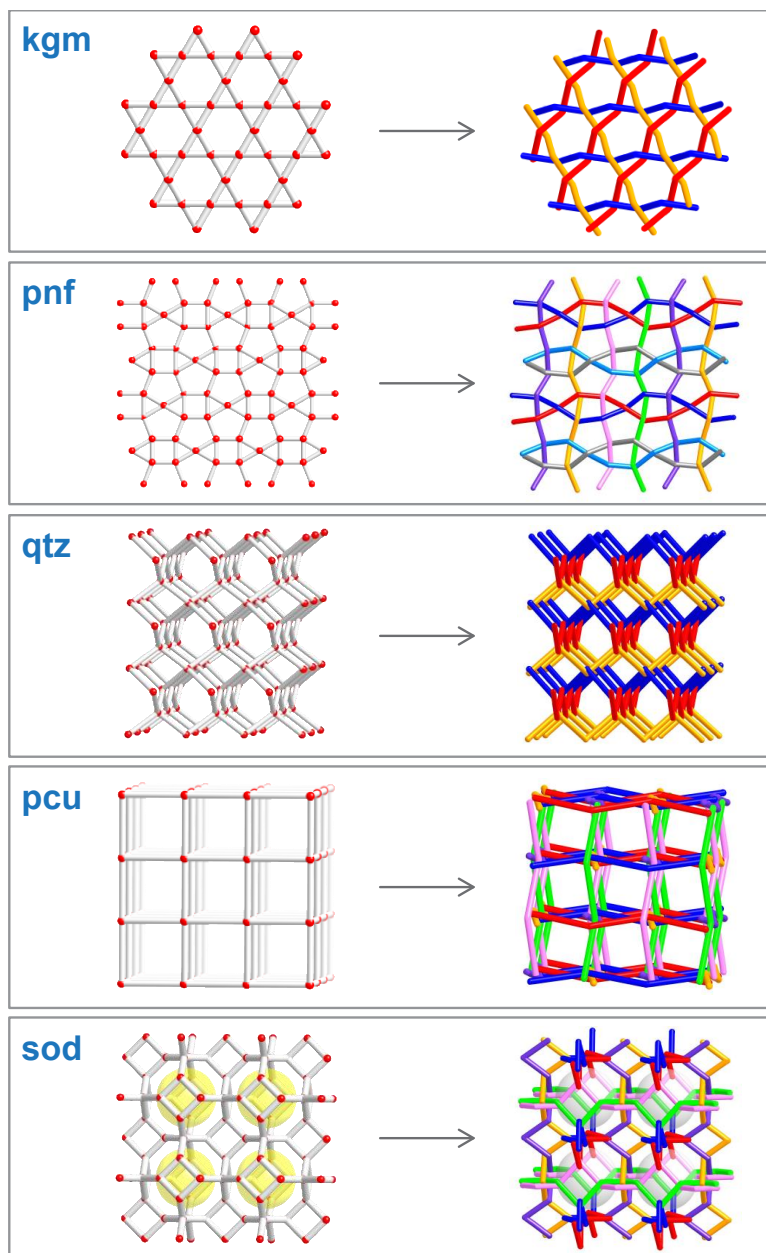
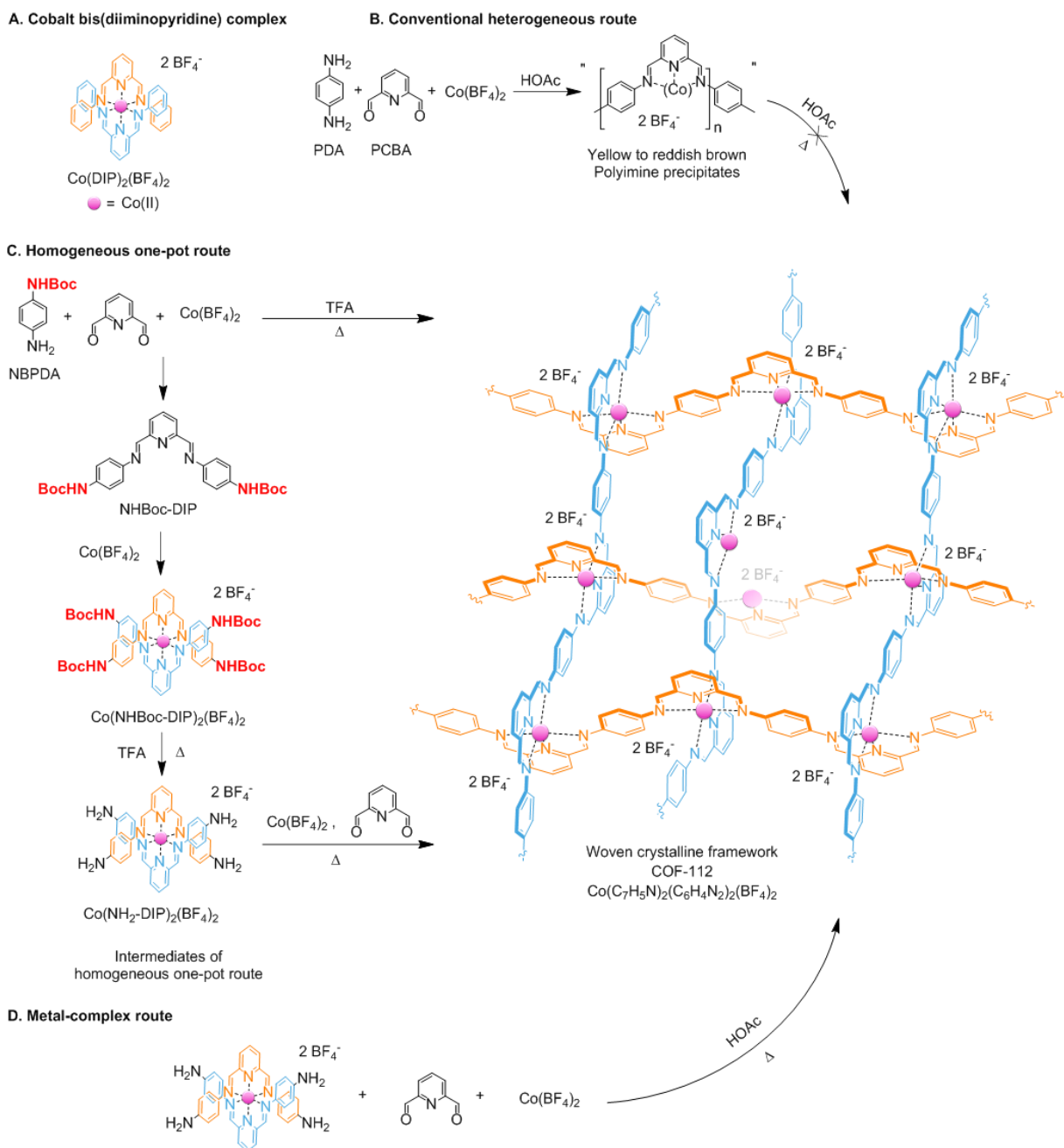


Figure 5.8. Weaving molecular threads into frameworks of various two- and three-dimensional topologies

Before attempting to synthesis frameworks of these complex topologies with more than two sets of threads, we first explored other designs of woven framework with **dia** topology but more ideal woven structure where the molecular threads can be straight and not mutually woven. In COF-505, the 57° dihedral angle between the two phenanthroline rings gives a distorted tetrahedral coordination geometry of copper(I) ion and directs the polyimine chains to be helical and mutually woven in the COF structure. With a less distorted tetrahedral building unit, more symmetrical arrangement of the organic threads can be expected which would give ideal woven structures. This can be realized by employing cobalt bis(diiminopyridine) complexes as the tetrahedral building unit, where the dihedral angles between the two pyridine rings can be close to the ideal angle of 90°. ²⁰⁻²² As the Schiff base diiminopyridine (DIP) ligand can be synthesized through imine condensation, conventional one-pot COF synthesis was initially set up with PDA, PCBA and Co(BF₄)₂·6H₂O as starting materials. However, this yielded no crystalline product despite testing a wide range of synthetic parameters. Throughout this process, we observed that yellow precipitates often formed initially, which quickly turned reddish brown, indicating the imine condensation proceeded to give polyimines before the coordination of cobalt ions by the *in situ* formed DIP motifs. As the non-metallated polyimine threads can pack into structures dramatically different from that of the woven framework (Figure A5.9), we speculated that defect correction with conventional solvent annealing is insufficient to afford crystalline products. Consequently, to obtain crystalline woven COF, the formation of polyimine precipitates would need to be avoided to allow the metal complexes to direct the propagation and entanglement of the polyimine chains. Thus, we employed NBPDA as the starting material where one of the two amine groups in PDA is protected with Boc group, which can form the DIP ligand and corresponding cobalt complexes rapidly at room temperature yet avoid the precipitation of polyimine. (Reproduced with permission from *J. Am. Chem. Soc.*, submitted for publication. Unpublished work copyright 2017 American Chemical Society.)

The one-pot homogeneous synthesis of COF-112 was thus carried out with NBPDA, PCBA and Co(BF₄)₂ as starting materials in a solvent mixture of acetonitrile and toluene with trifluoroacetic acid as the catalyst for imine condensation and the deprotection reagent for the Boc group (Scheme 1C). This clear solution was heated in a sealed Pyrex tube at 85 °C for 48 h, to yield reddish brown microcrystals. In this synthetic route, NBPDA and PCBA first undergo imine condensation to form the Boc-protected diiminopyridine ligand (NHBoc-DIP, Scheme 1C). This rapidly binds cobalt ions to form the Co(NHBoc-DIP)₂(BF₄)₂ complex giving the red color to the homogeneous solution. While being heated, crystalline solids emerged from this red solution as the *in situ* deprotected amine groups reacted with the remaining PCBA to form the interlacing one-dimensional polyimine chains and the COF-112 structure (Scheme 1). In this homogeneous synthetic route to COF-112, the building up of the molecular threads is being directed by the metal complex leading to successful crystallization. This is in contrast with the unsuccessful heterogeneous route, where the polyimine chains formed prior to metal complexation (Scheme 1B). To further compare the homogeneous and heterogeneous synthesis routes, the deprotected amine intermediate [Co(NH₂-DIP)₂(BF₄)₂] of the homogeneous route was used to react with PCBA and the cobalt salt (Scheme 1D) in an imine COF synthesis similar to that leading to COF-505. This metal-complex route also gave crystalline COF-112; indicating the initial cobalt complex formation in the homogeneous one-pot route is the key to obtaining crystallinity.

Scheme 5.2. The conventional heterogeneous, homogeneous (one-pot), and metal-complex route for crystalline woven covalent organic framework-112.



We found that reacting the polyimine precipitate, resulting from PCBA and PDA (in the absence of cobalt), with $\text{Co}(\text{BF}_4)_2$ in the presence of acid catalyst gave amorphous product. Thus, we concluded that the utilization of the protected amine homogenizes imine COF synthesis and enables metal-ligand coordination reaction to occur prior to polyimine chain formation and this leads to the successful crystallization of woven COF-112. It is worth noting, that the $\text{Co}(\text{NH}_2\text{-DIP})_2(\text{BF}_4)_2$ used in the metal-complex route should be perceived as an isolated reaction intermediate instead of an amine building block, as it was observed to dynamically disassemble under the *de novo* COF synthesis (Figure A5.10 and 5.11). The crystallites produced in this metal-complex route were also small and highly aggregated (Figure 5.9), while the homogeneous one-pot route with NBPDA gave larger, discrete crystals that can be studied by 3D electron diffraction tomography (3D-EDT) for COF structural determination.¹⁴

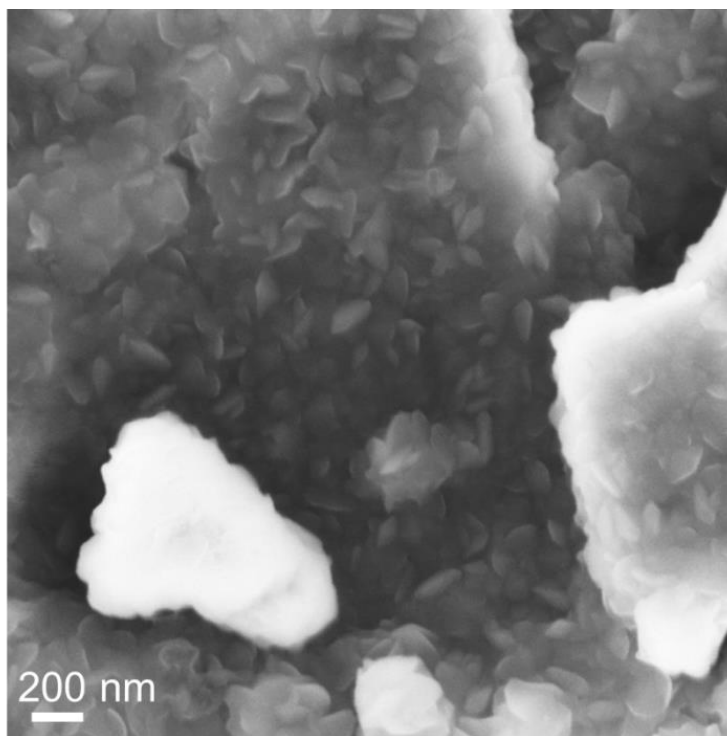
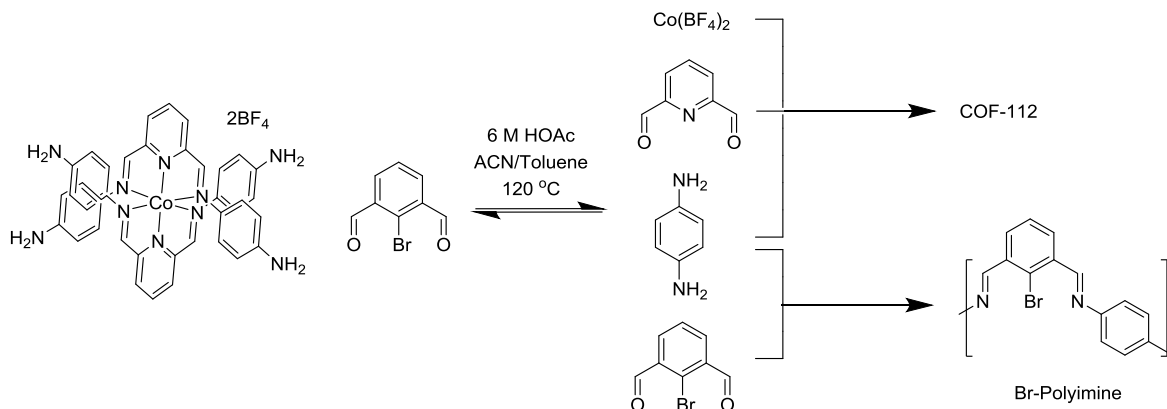


Figure 5.9. The SEM images of COF-112 crystallites synthesized in the metal-complex route. The the crystallites were highly aggregated and not separable by sonication.

Furthermore, the $\text{Co}(\text{NH}_2\text{-DIP})_2(\text{BF}_4)_2$ used in the metal-complex route should be perceived as an isolated reaction intermediate instead of an amine building block, as it was observed to dynamically disassemble under the COF synthesis conditions used and thus cannot be used to condense with other aldehyde building blocks to give different imine COFs. The dynamic nature of the $\text{Co}(\text{NH}_2\text{-DIP})_2(\text{BF}_4)_2$ in imine COF synthesis condition can be best demonstrated by its reaction with bromine substituted Br-PCBA, which is unlikely to form or be incorporated in COF-112 due to the steric hindrance of Br. Under conventional imine COF synthesis, the reaction yielded a mixture of COF-112 and presumably a crystalline phase of Br-polyimine, as evidenced by the PXRD pattern of the product (Figure A5.11) containing diffraction lines of both COF-112 and an unknown phase with small d-spacing, presumably a packed polyimine.

Scheme 5.3. Dynamic nature of $\text{Co}(\text{NH}_2\text{-DIP})_2(\text{BF}_4)_2$ in imine COF synthesis



The product mixture of the above reaction was further studied by SEM, which reveals the COF 112 phase that does not contain any Br and a polymer phase that contains Br but no cobalt. Similar phenomena were also observed when terephthalaldehyde or biphenyl-4,4'-dicarbaldehyde was used instead of Br-PCBA to react with $\text{Co}(\text{NH}_2\text{-DIP})_2(\text{BF}_4)_2$ in the attempt to construct other imine COFs with $\text{Co}(\text{NH}_2\text{-DIP})_2(\text{BF}_4)_2$ as amine building block, where COF-112 and the presumably corresponding polyimine phase coexisted in the product mixture. This further confirms the above-mentioned conclusion that the $\text{Co}(\text{NH}_2\text{-DIP})_2(\text{BF}_4)_2$ starting material in the metal-complex route is unstable in imine COF synthesis and should be perceived as an intermediate rather than a stable amine building block.

The completeness of the imine condensation to make COF-112 was assessed by IR spectroscopy where no vibrational modes were observed for any unreacted amine, aldehyde, and Boc protecting group (Figure 5.10). The presence of the DIP motif was further supported by comparing the IR spectrum with $\text{Co}(\text{NH}_2\text{-DIP})_2(\text{BF}_4)_2$ (Figure 5.11). Solid state UV-Vis spectroscopy (Figure A5.12) combined with inductively coupled plasma atomic emission spectroscopy (ICP-AES) and elemental analysis further confirmed the composition of COF-112.

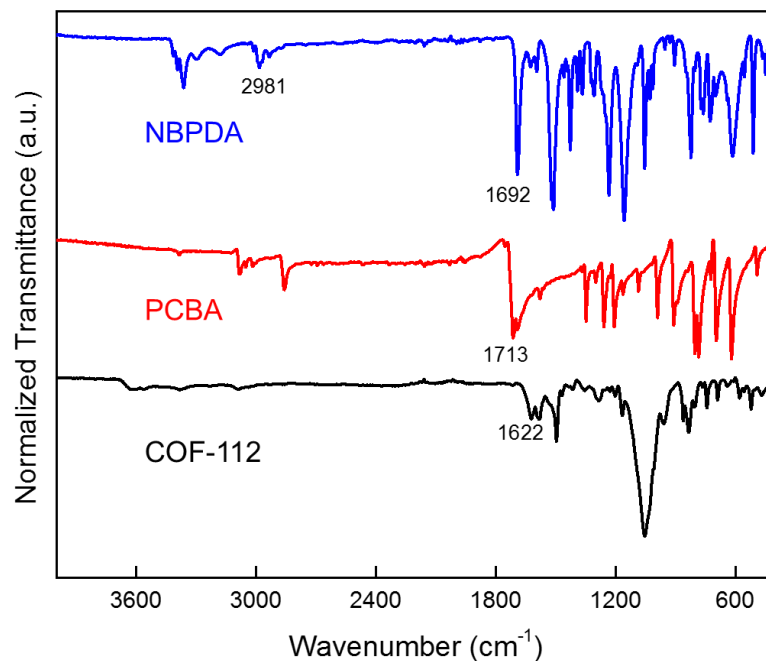


Figure 5.10. Infrared spectrum of COF-112 and its starting material. It is clear that the Boc group (characteristic vibration C=O, 1692 cm^{-1} , CH₃, 2981 cm^{-1}) and amine group (N-H, beyond 3000 cm^{-1}) in NBPDA and aldehyde group in PCBA (C=O, 1713 cm^{-1}) are absent in COF-112.

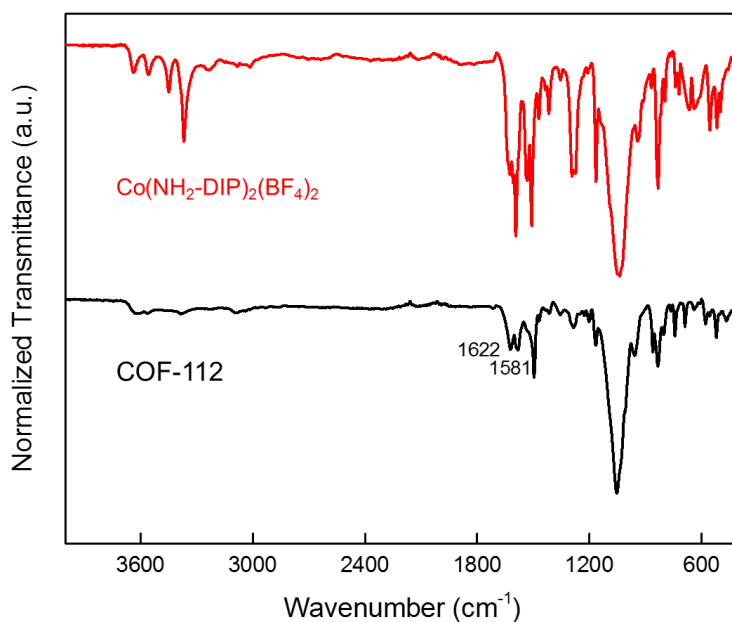


Figure 5.11. Infrared spectrum of COF-112 and $\text{Co}(\text{NH}_2\text{-DIP})_2(\text{BF}_4)_2$. The two compounds display similar vibrational modes, where in COF-112 the vibrational mode of N-H stretch (beyond 3200 cm^{-1}) disappear and that of imine bond (1622 cm^{-1}) strengthened, both consistent with their slight structural difference.

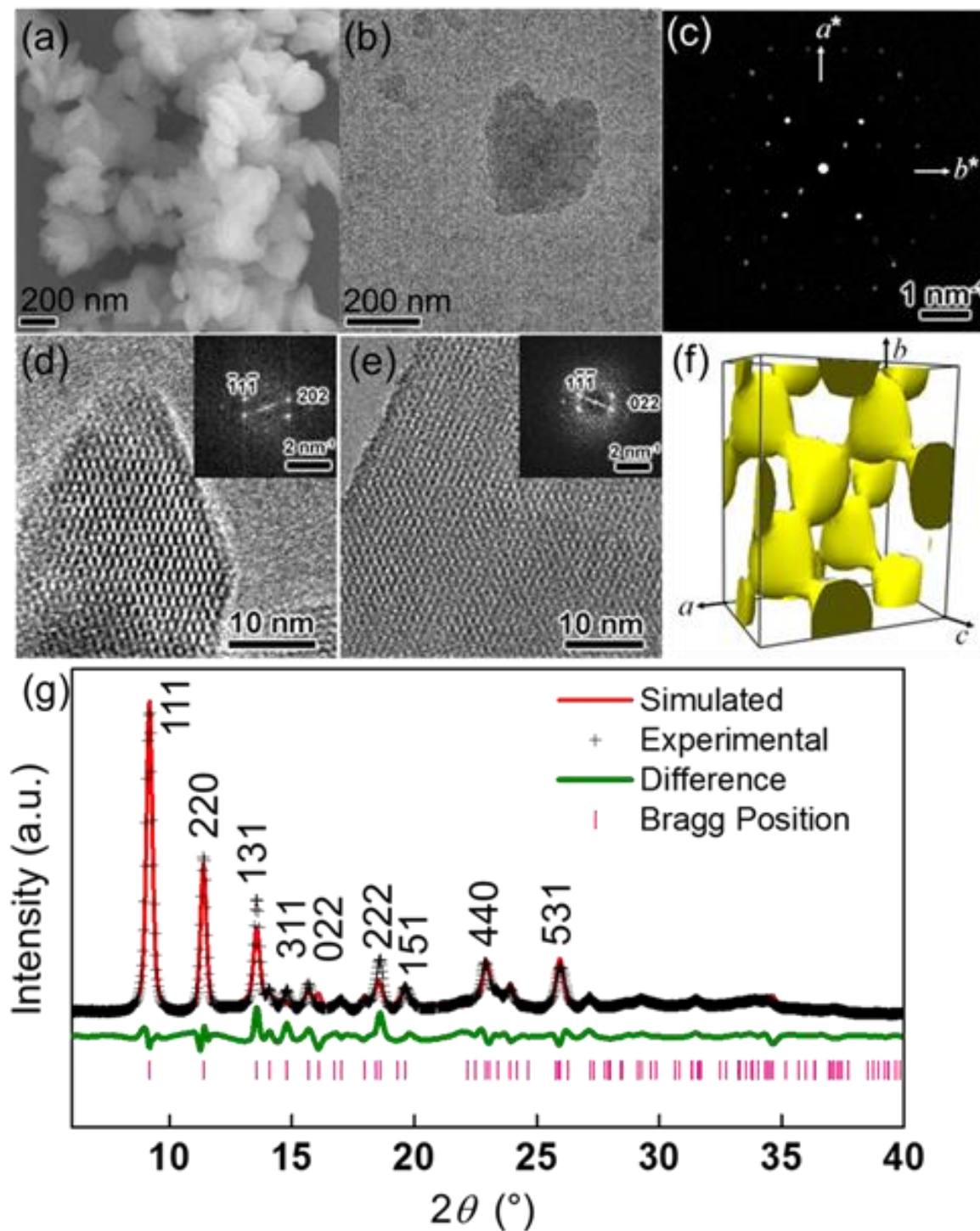


Figure 5.12. Structural determination of COF-112. The COF-112 crystals were 200 nm in size as observed by SEM (a). 3D-EDT study (b) and (c) gave the unit cell parameters a and b , from which the unit cell can be determined by Pawley refinement of the powder X-ray diffraction pattern. High resolution TEM images (d) and (e) were combined to give the cobalt positions by Fourier analysis (f). The COF-112 structural model was thus built and optimized by Rietveld refinement with R_p and R_{wp} values of 1.66% and 2.48% respectively.

The crystal structure of COF-112 was solved by a combination of X-ray and electron crystallographic studies (Figure 5.12). One three-dimensional electron diffraction tomography dataset was collected from a submicron crystal by using a goniometer tilt of 3° and an electron-beam tilt of 0.3° (Figure 5.12a, b and c). From the reconstruction of the reciprocal lattice, two of the unit cell parameters were uniquely determined, while the third one remained uncertain due to insufficient reflections and possible twinning. Subsequently, the PXRD pattern was indexed confirming an orthorhombic lattice, and providing the third cell parameter. Pawley refinement was then conducted with the data from the PXRD pattern, resulting in unit cell parameters $a = 19.74 \text{ \AA}$, $b = 25.13 \text{ \AA}$, $c = 12.26 \text{ \AA}$. The first four strong reflections in the PXRD pattern can be indexed as (111), (220), (131) and (040). The observed reflection conditions from electron diffraction and PXRD patterns were summarized as $hkl: h+k, h+l, k+l = 2n$; $0kl: k, l = 2n \& k+l = 4n$, which indicated an F-center Bravais lattice and the most likely space group of $Fdd2$. Two HRTEM images of COF-112 were taken along the $[-101]$ and $[0-11]$ incidences (Figure 5.12d and e). The Fourier analysis of two HRTEM images after imposing the space group symmetry indicated the positions of the cobalt centered complexes, which was consistent with that given by the electron density map reconstructed by applying the charge flipping method with the reflection intensities extracted from the PXRD pattern (Figure 5.12f). Moreover, with the unit cell and space group determined, the position of cobalt atoms can also be confirmed from the measured sample density of 1.4 g/cm^3 . This indicates one unit cell has only eight cobalt atoms, and their coordinates can be determined from the Wyckoff positions. The structural model of COF-112 was thus built and geometrically optimized using Materials Studio software by putting the diiminopyridine ligand around these cobalt atoms under the constraint of $Fdd2$ symmetry. This model was further optimized by Rietveld refinement against the experimental PXRD pattern to give the COF-112 structure.

The structure of the COF-112 consists of two sets of one-dimensional zig-zag polyimine chains, which propagate linearly along $[110]$ and $[-110]$ direction of the crystal and weave at the coordinated cobalt ions as the point of registry at regular interval of 1.6 nm (Figure 5.13). This structure is an ideal example of molecular weaving, which represents one of the simplest three-dimensional woven structures as it involves only two sets of threads that are straight and parallel and one point of registry. Topologically, COF-112 is a non-interpenetrated COF with **dia** topology, with the $\text{Co}(\text{DIP})_2^{2+}$ complex considered as the tetrahedral building unit. It is worth noting that the two sets of polyimine chains cross at an angle of 77.3° , which is very similar to the 80° dihedral angle between the two pyridine rings in the $\text{Co}(\text{NH}_2\text{-DIP})_2(\text{BF}_4)_2$ complex (Figure A5.1), supporting our initial design principle that the coordination geometry of the metal template would direct the propagation of the molecular threads. Additionally, an isostructural COF-112-Fe can be also constructed with iron(II) instead of cobalt(II) as the point of registry, which demonstrates the versatility of the *bis*-diiminopyridine metal complex templates in woven COF synthesis (Figure A5.13-A5.15). Fundamentally, the COF-112 framework is an example of constructing a highly complex structure from simple building blocks, where metal coordination and imine condensation reactions take place coherently in a one-pot reaction enabled by a homogenized imine COF synthetic route.

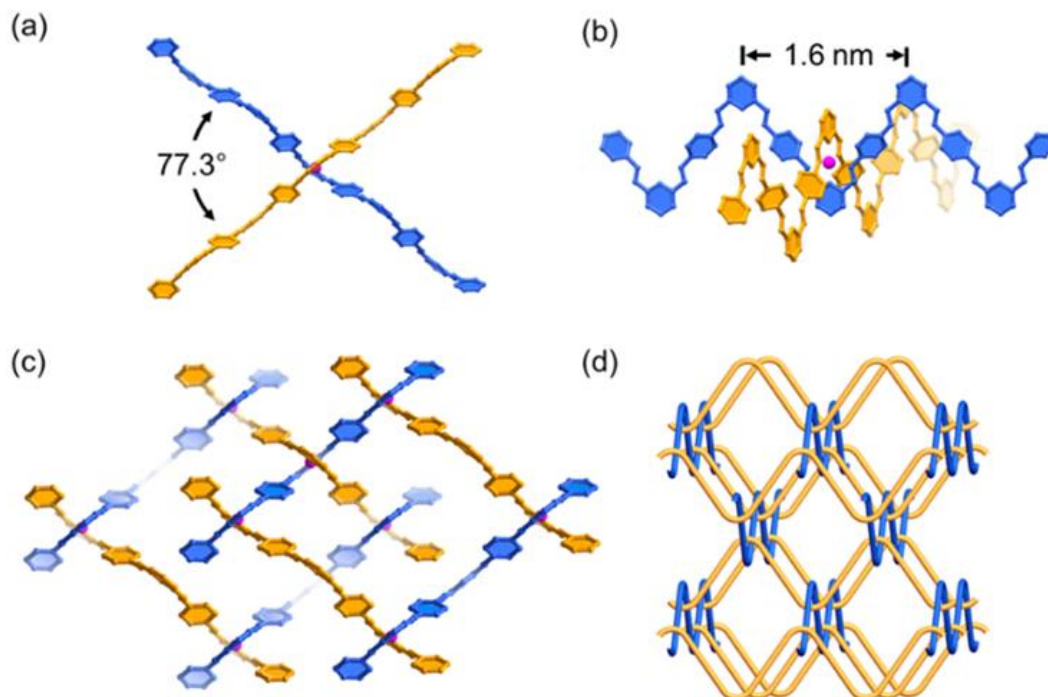


Figure 5.13. The structure of COF-112. (a) COF-112 is composed of two sets of interlacing polyimine threads (marked blue and orange for their different propagating directions) crossing at 77.3° angle (a). The threads are weaved with cobalt(II) ions as point of registry at regular interval of 1.6 nm (b), which form a three-dimensional framework (c) that represents a simple 3D woven network (d). Additional parallel threads are omitted for clarity in (c).

Section 5.4 Conclusion

Molecular weaving has been achieved by interlacing organic threads into crystalline covalent organic frameworks. Two woven frameworks of diamond topology, COF-505 and COF-112, were successfully synthesized by applying metal templation in COF chemistry, and both consist of interlacing polyimine threads weaved around metal ions as the point of registry at regular interval. For COF-505, an aldehyde functionalized derivative of the copper *bis*-phenanthroline complex where the position of the aldehyde groups approximates a tetrahedral geometry was linked with benzidine to form the woven framework with mutually woven helical organic threads; for COF-112, a one-pot three-component reaction was developed to crystalline the woven framework which has straight organic threads and non-mutual woven structure.

The spatial arrangement of coordinating ligands (phenanthroline and diiminopyridine in COF-505 and COF-112, respectively) around the metal ion template directs the structure of the woven framework, which can be solved by a combination of electron diffraction tomography (EDT), high-resolution TEM (HRTEM) imaging and X-ray crystallography. In structure determination of the woven frameworks, we also developed a systematic structure analysis process: (a) EDT was first used to obtain unit cell parameters; (b) Fourier analysis of HRTEM images was employed to obtain the position of metal centers; (c) structure model can be built by placing the organic threads around the metal centers in a manner consistent with the PXRD pattern; (d) counter ion positions refined by Rietveld refinement.

Section 5.5 Reference

- (1) Yaghi, O. M.; O'Keeffe, M.; Ockwig, N. W.; Chae, H. K.; Eddaoudi, M.; Kim, J., *Nature* **2003**, 423, 705-714.
- (2) Leong, W. L.; Vittal, J. J., *Chem. Rev.* **2011**, 111, 688-764.
- (3) Chen, B.; Eddaoudi, M.; Hyde, S. T.; O'Keeffe, M.; Yaghi, O. M., *Science* **2001**, 291, 1021-1023.
- (4) James, S. L., *Chem. Soc. Rev.* **2003**, 32, 276-288.
- (5) Maji, T. K.; Matsuda, R.; Kitagawa, S., *Nat. Mater.* **2007**, 6, 142-148.
- (6) Linke, M.; Chambron, J. C.; Heitz, V.; Sauvage, J. P.; Encinas, S.; Barigelletti, F.; Flamigni, L., *J. Am. Chem. Soc.* **2000**, 122, 11834-11844.
- (7) Gemmi, M.; Oleynikov, P., *Z. Kristallogr.* **2013**, 228, 51-58.
- (8) Olivera, W. C.; Pharra, G. M., *J. Mater. Res.* **2004**, 19, 3-20.
- (9) Tan, J. C.; Cheetham, A. K., *Chem. Soc. Rev.* **2011**, 40, 1059-1080
- (10) Dietrich-Buchecker, C. O.; Sauvage, J.-P., *Angew. Chem. Int. Edit.* **1989**, 28, 189-198.
- (11) Dietrich-Buchecker, C. O.; Sauvage, J. P.; Kern, J. M., *J. Am. Chem. Soc.* **1984**, 106, 3043-3045.
- (12) Jimenez, M.-C.; Dietrich-Buchecker, C.; Sauvage, J.-P., *Angew. Chem. Int. Ed.* **2000**, 39, 3284.
- (13) Pakhomova, S. V.; Proskurnin, M. A.; Chernysh, V. V.; Kononets, M. Y.; Ivanova, E. K., *J. Anal. Chem.* **2001**, 56, 1042-1049.
- (14) Zhang, Y.-B.; Su, J.; Furukawa, H.; Yun, Y.; Gandara, F.; Duong, A.; Zou, X.; Yagh, O. M., *J. Am. Chem. Soc.* **2013**, 135, 16336-16339.
- (15) Uribe-Romo, F. J.; Hunt, J. R.; Furukawa, H.; Klöck, C.; O'Keeffe, M.; Yaghi, O. M., *J. Am. Chem. Soc.* **2009**, 131, 4570-4571.
- (16) Wu, X.; Zilm, K. W., *J. Mag. Reson.* **1993**, 102, 205-213.
- (17) Mugnaioli, E.; Andrusenko, I.; Schüler, T.; Loges, N.; Dinnebier, R. E.; Panthöfer, M.; Tremel, W.; Kolb, U., *Angew. Chem. Int. Ed.* **2012**, 51, 7041-7045.
- (18) Sun, Q.; Ma, Y.; Wang, N.; Li, X.; Xi, D.; Xu, J.; Deng, F.; Yoon, K. B.; Oleynikov, P.; Terasaki, O.; Yu, J., *J. Mater. Chem. A* **2014**, 2, 17828-17839.
- (19) Scaltrito, D. V.; Thompson, D. W.; O'Callaghan, J. A.; Meyer, G. J., *Coord. Chem. Rev.* **2000**, 208, 243-266.
- (20) Blake, A. J.; Lavery, A. J.; Hyde, T. I.; Schroder, M. J. *Chem. Soc., Dalton Trans.* **1989**, 5, 965-970.

- (21) Vance, A. L.; Alcock, N. W.; Heppert, J. A.; Busch, D. H. *Inorg. Chem.* **1998**, *37*, 6912-6920.
- (22) Leigh, D. A.; Lusby, P. J.; Teat, S. J.; Wilson, A. J.; Wong, J. K. *Angew. Chem. Int. Ed.* **2001**, *40*, 1538-1543.

Section 5.6 Appendix

Table A5. 1 Single crystal diffraction of Cu(PBD)₂

Compound	Cu(PBD) ₂
Chemical formula	C ₅₃ H ₃₄ BCl ₂ CuF ₄ N ₄ O ₄
Formula mass	1012.09
Crystal system	triclinic
Space group	<i>P</i> -1
λ (Å)	0.7107(3)
<i>a</i> (Å)	12.987(5)
<i>b</i> (Å)	12.995(5)
<i>c</i> (Å)	14.074(5)
α (°)	88.288(7)
β (°)	81.131(7)
γ (°)	67.000(6)
<i>Z</i>	2
Size /mm ³	0.150 × 0.120 × 0.100
Measured reflections	73691
Unique reflections	7962
<i>R</i> _{int}	0.1378
θ range (°)	1.465-25.427
<i>R</i> ₁ , <i>wR</i> ₂	0.0399, 0.0999
Max/min res. dens. (e/Å ³)	0.78/-0.49

Table A5.2 Crystal data and structure determination for Co(NH₂-DIP)₂(BF₄)₂

Compound	Co(NH ₂ -DIP) ₂ (BF ₄) ₂
Chemical formula	C ₄₂ H ₄₀ B ₂ CoF ₈ N ₁₂
Formula mass	945.41
Crystal system	triclinic
Space group	<i>P</i> -1
λ (Å)	0.7749(1)
<i>a</i> (Å)	12.1126(16)
<i>b</i> (Å)	14.208(2)
<i>c</i> (Å)	15.083(2)
<i>a</i> (°)	113.528(4)
β (°)	90.375(4)
γ (°)	112.600(4)
<i>Z</i>	2
<i>V</i> (Å ³)	2157.7(5)
Temperature (K)	100(2)
Size /mm ³	0.030 × 0.020 × 0.010
Density (g/cm ⁻³)	1.455
Measured reflections	3913
Unique reflections	2898
Parameters	586
Restraints	66
<i>R</i> _{int}	0.1378
θ range (°)	2.10-21.71
<i>R</i> ₁ , <i>wR</i> ₂	0.0810, 0.2050
<i>S</i> (GOF)	1.026
Max/min res. dens. (e/Å ³)	0.47/-0.56

$${}^a R_1 = \sum ||F_o| - |F_c|| / \sum |F_o|; {}^b wR_2 = [\sum w(F_o^2 - F_c^2)^2 / \sum w(F_o^2)^2]^{1/2}; {}^c S = [\sum w(F_o^2 - F_c^2)^2 / (N_{\text{ref}} - N_{\text{par}})]^{1/2}.$$

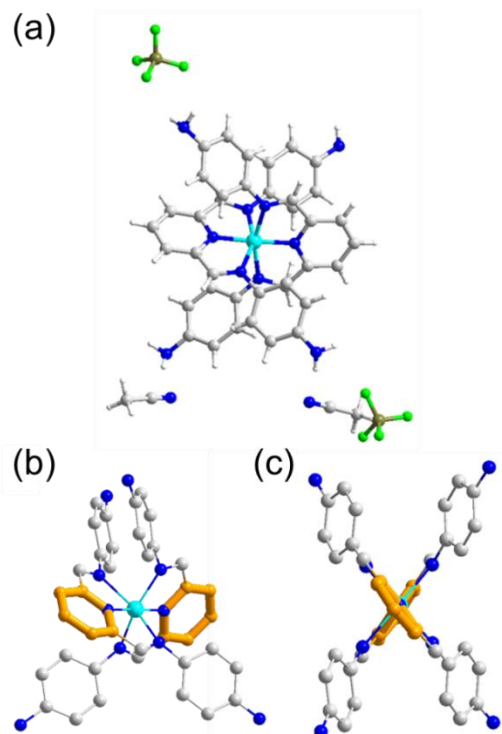


Figure A5.1. Single crystal structure of $\text{Co}(\text{NH}_2\text{-DIP})_2(\text{BF}_4)_2$ (a). The torsion angle between the pyridine rings (highlighted in orange) in $\text{Co}(\text{NH}_2\text{-DIP})_2(\text{BF}_4)_2$ is 80° , rendering the complex a more ideal tetrahedral (b) and directing the angle between the polyimine chains (c)

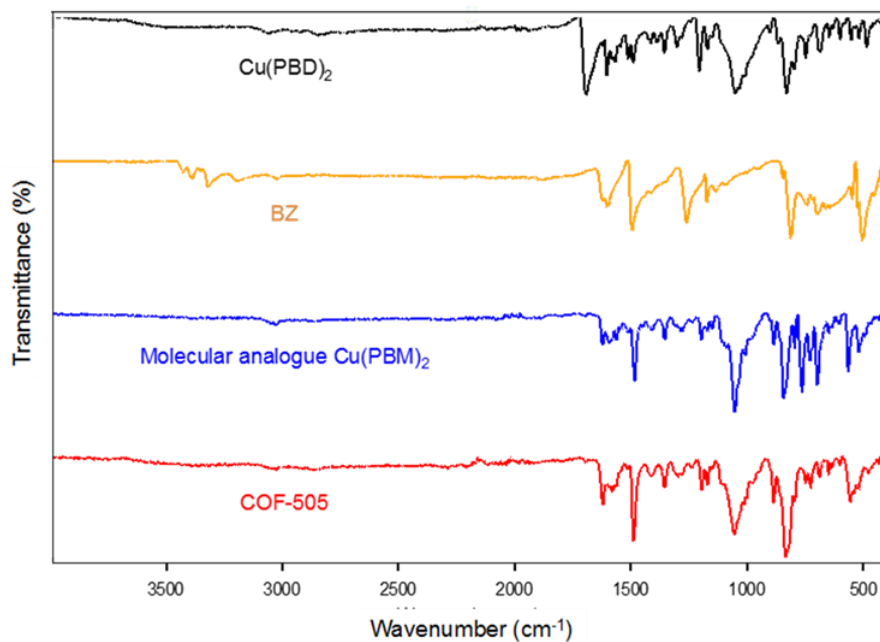


Figure A5.2. FT-IR spectra for the starting materials, molecular analogue, and activated sample of COF-505.

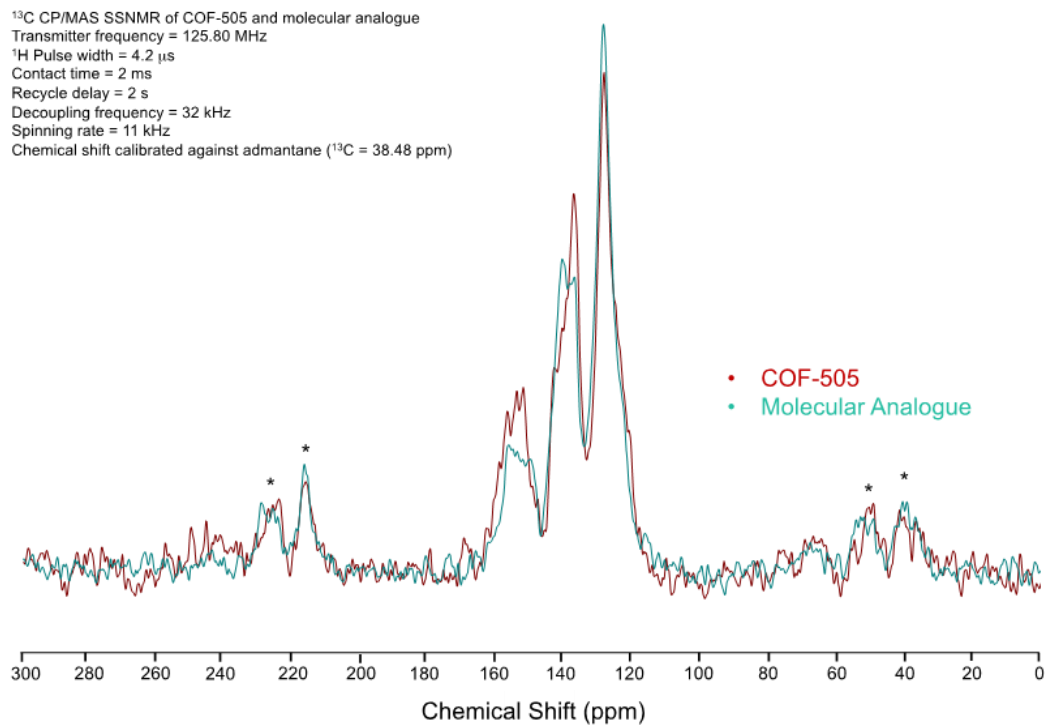


Figure A5.3. Solid-state ¹³C CP/MAS NMR spectrum of COF-505 and its molecular analogue.

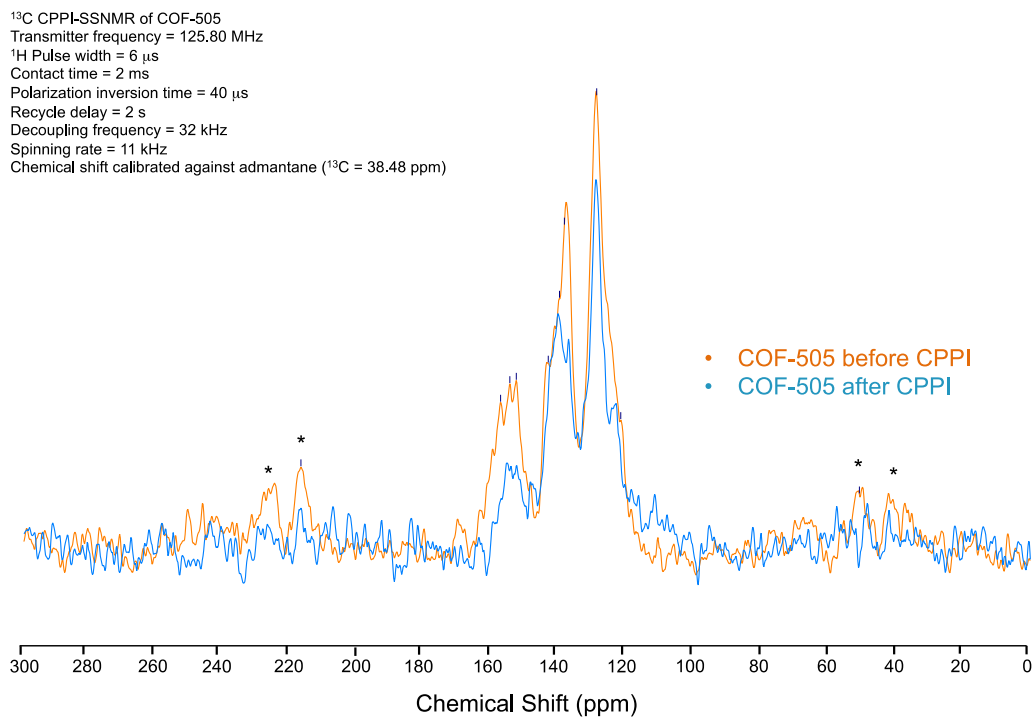


Figure A5.4. Solid-state ¹³C NMR spectrum of COF-505 before and after CPPI technique.

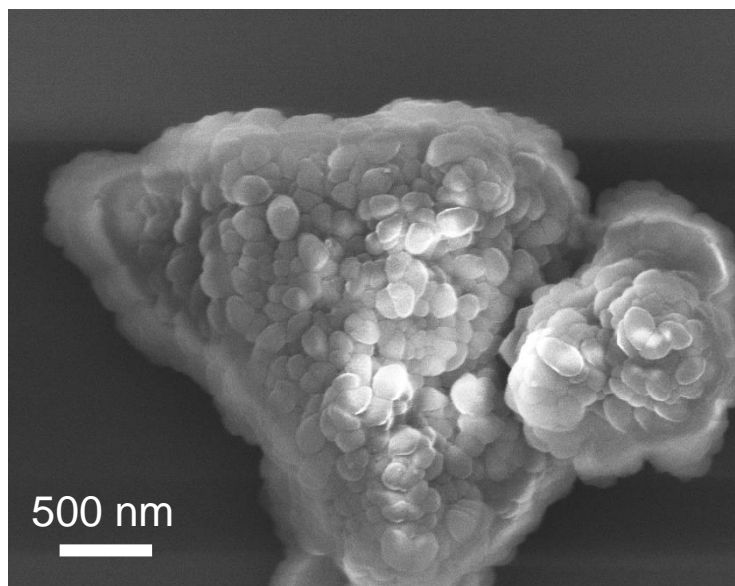


Figure A5.5 SEM image of the demetalated material, which shows similar morphology to COF-505.

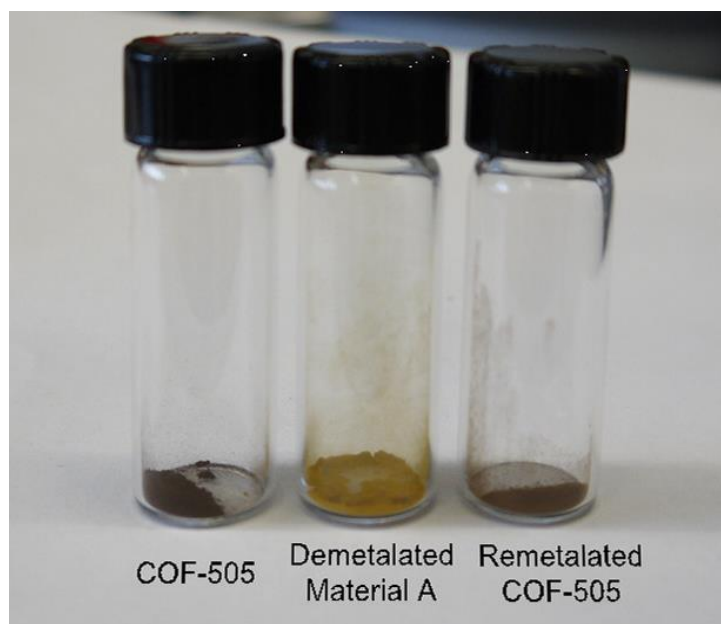


Figure A5.6. Powder of COF-505 (left), demetalated material A (middle), and remetalled COF-505 (right). The sample changed color from dark brown to yellow as it was demetalated and after remetallation, the dark color was recovered.

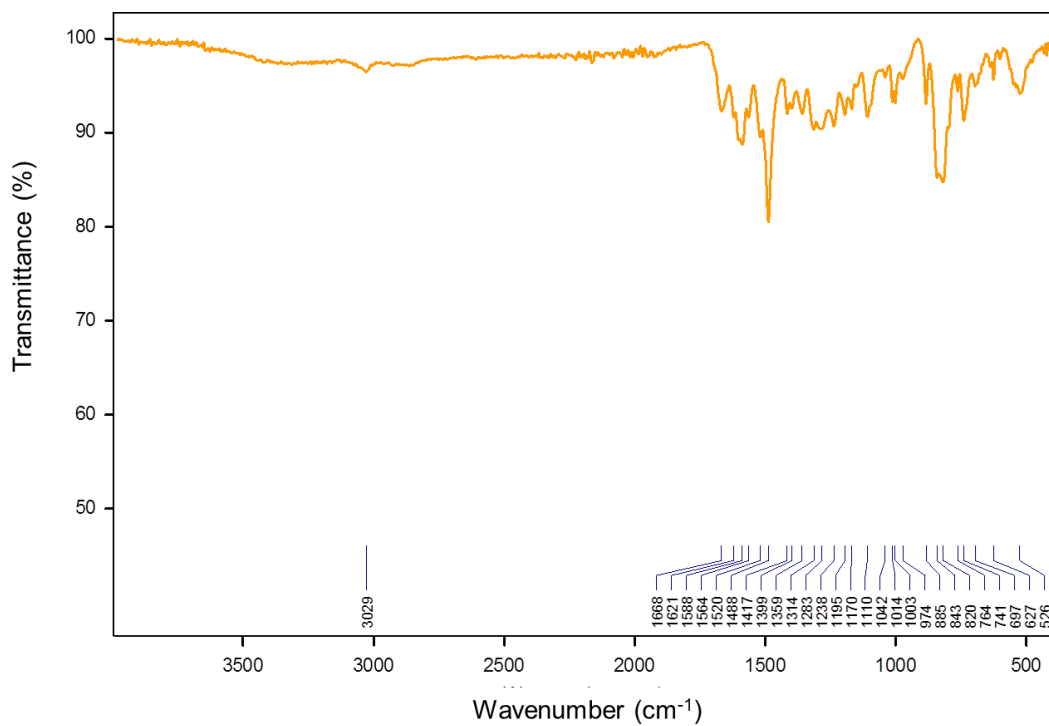


Figure A5.7. FT-IR spectrum of the demetalated material.

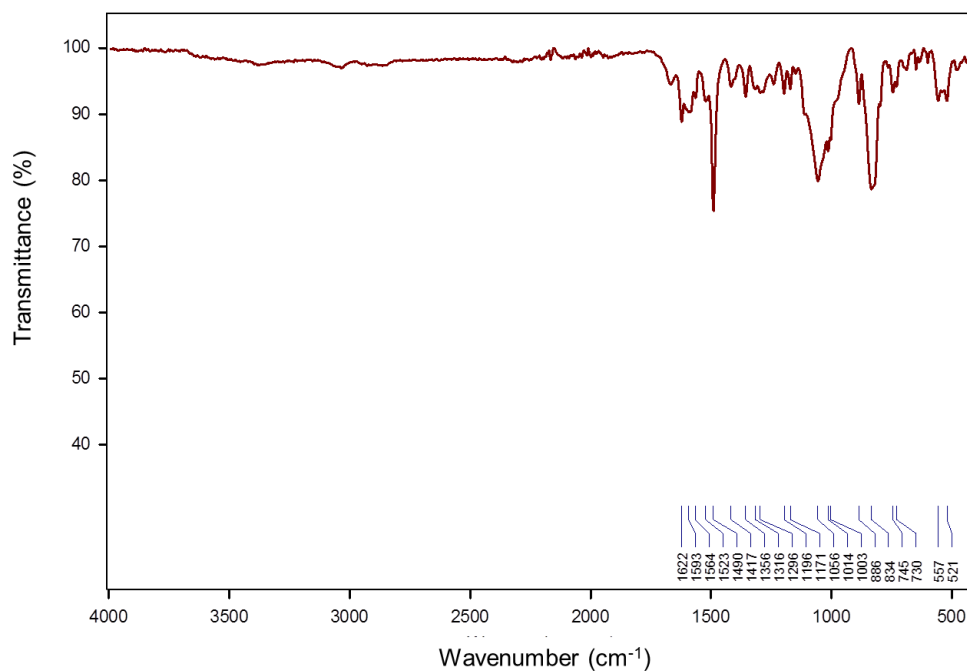


Figure A5.8. FT-IR spectrum of recovered COF-505 after remetalation.

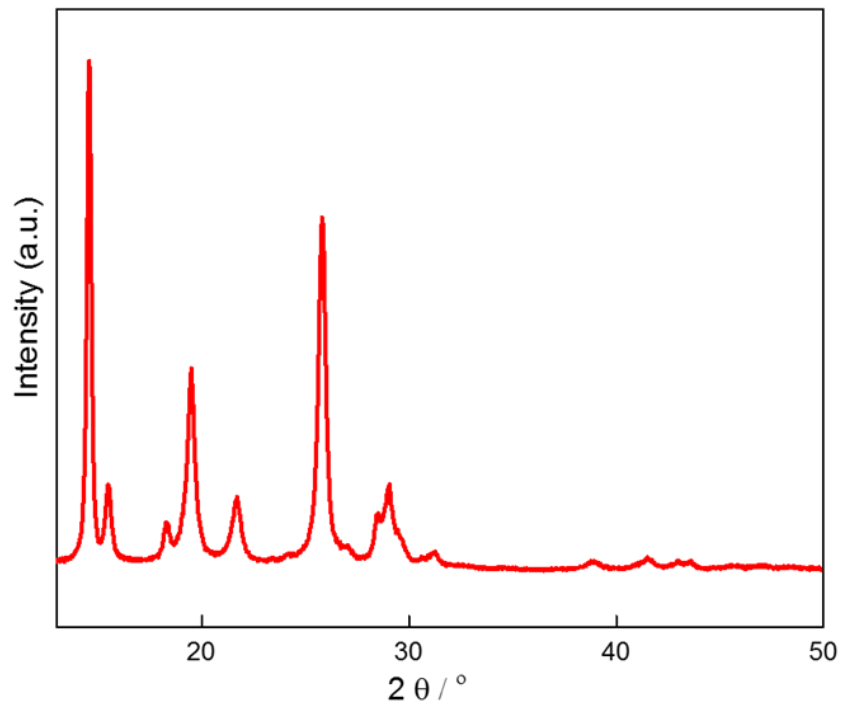


Figure A5.9. The powder X-ray diffraction pattern of crystalline polyimine with same chemical composition as the organic threads in COF-112

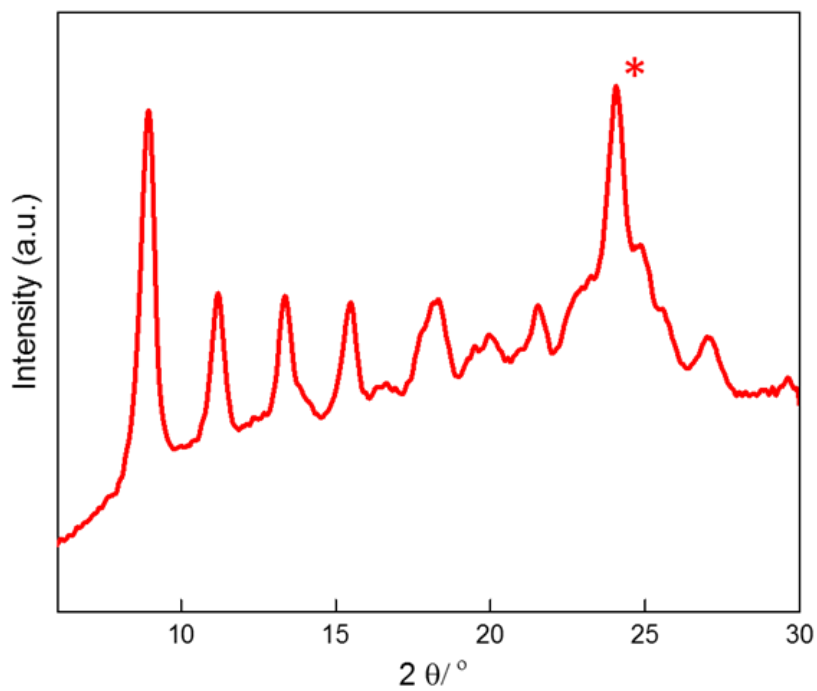


Figure A5.10. The powder X-ray pattern of the COF synthesis with Br-PCBA. * marks the Bragg diffraction peak not observed for COF-112

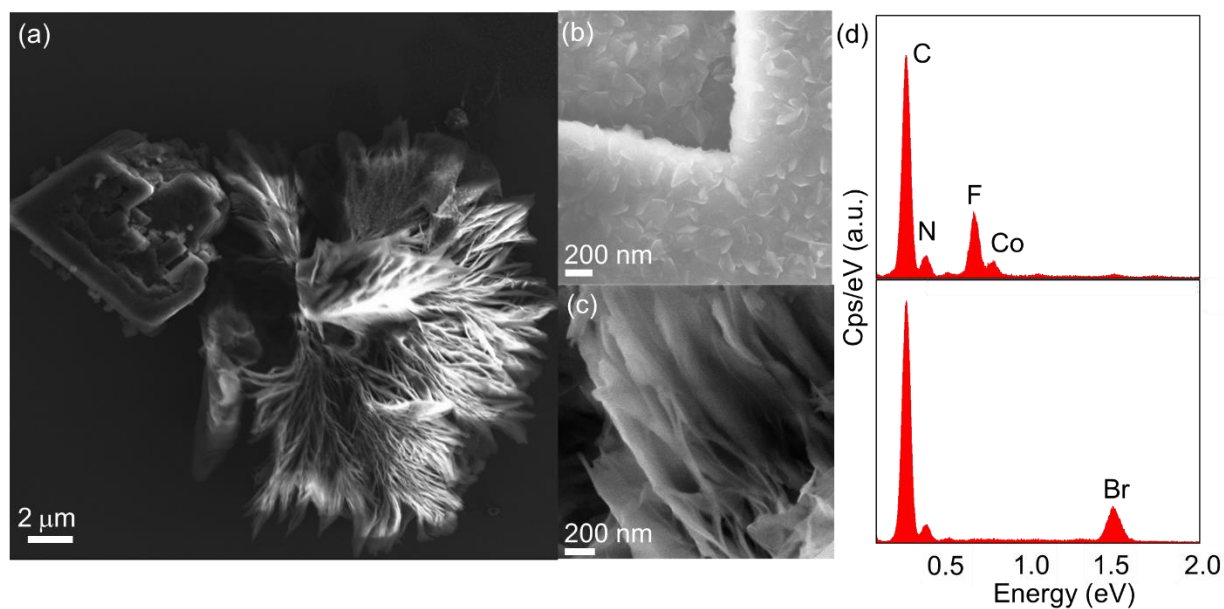


Figure A5.11. The SEM and energy dispersive X-ray spectroscopy (EDS) study of the mixture produced in reacting $\text{Co}(\text{NH}_2\text{-DIP})_2(\text{BF}_4)_2$ and Br-PCBA. It can be clearly seen that two phases are present (a), where the COF-112 forms crystalline aggregates (b) and the Br-polyimine forms fiber-like structures (c). The EDS spectrum taken on the two phases (d) shows the COF-112 particles (d, upper panel) do not incorporate Br and the Br-polyimine (d, lower panel) does not have cobalt.

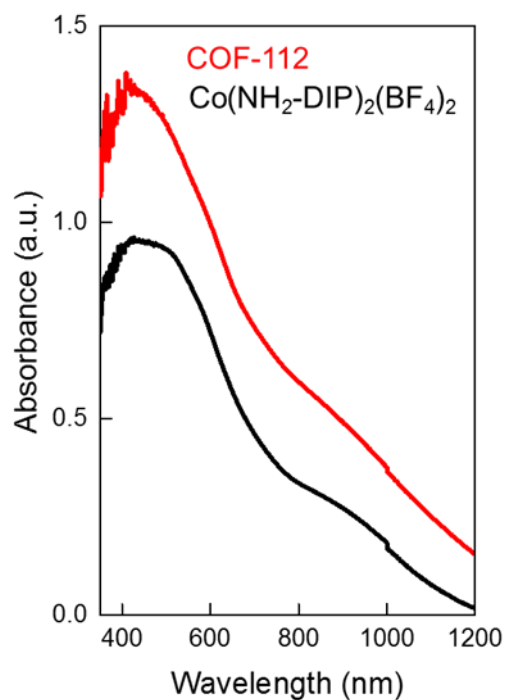


Figure A5.12. The UV-Vis spectra of COF-112 and $\text{Co}(\text{NH}_2\text{-DIP})_2(\text{BF}_4)_2$, showing almost identical absorption due to ligand to metal charge transfer.

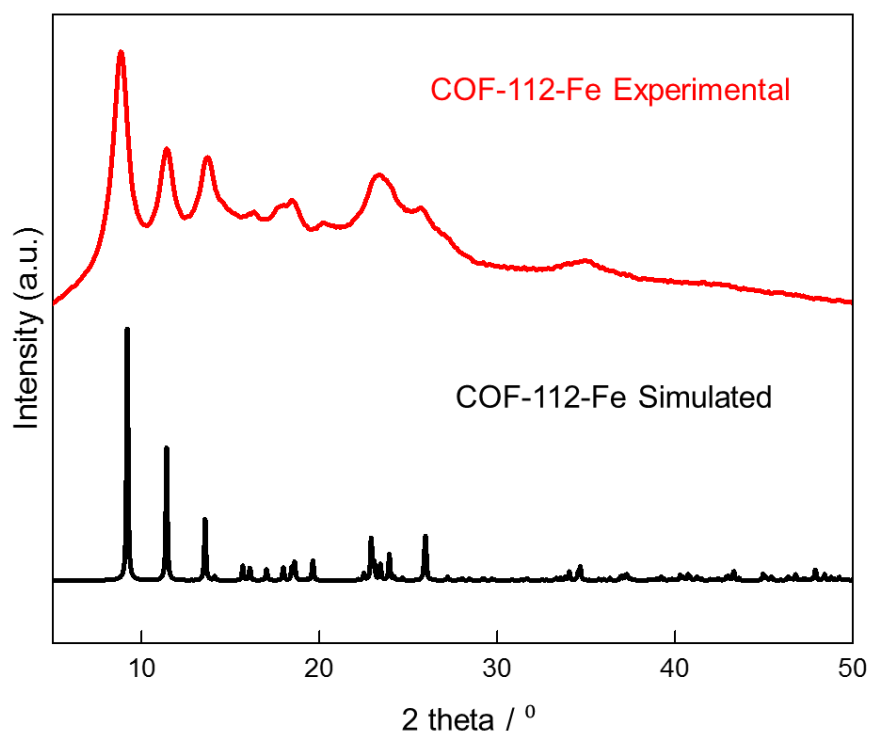


Figure A5.13. The powder X-ray diffraction pattern of COF-112-Fe.

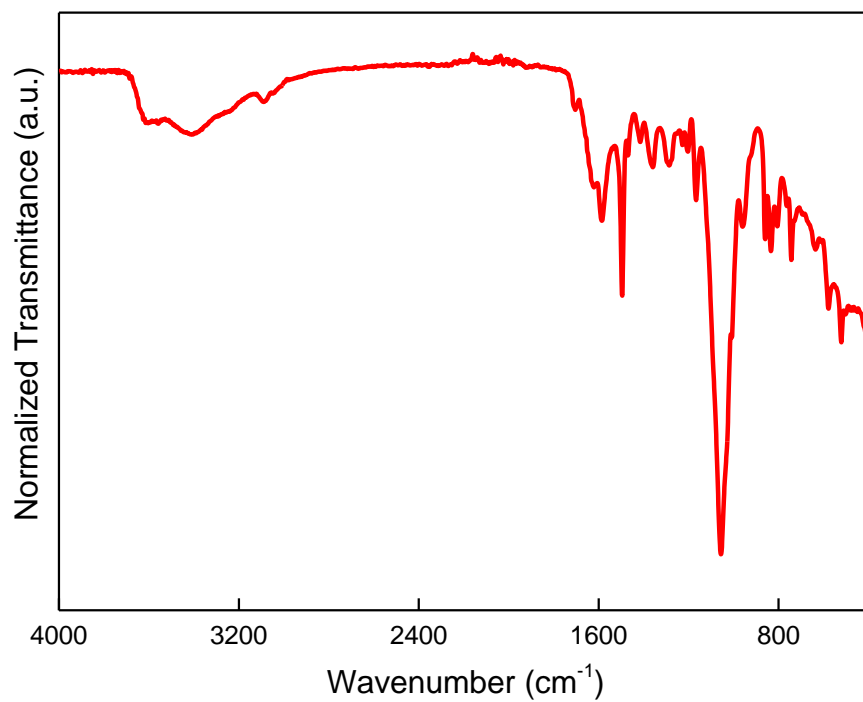


Figure A5.14. Infrared spectrum of COF-112-Fe.

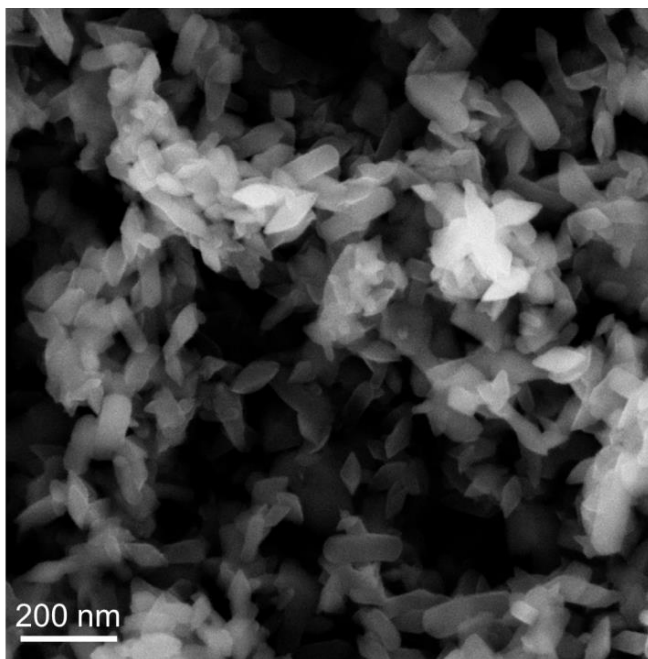


Figure A5.15. SEM image of COF-112-Fe.

Chapter 6. Synthesis of Covalent Organic Frameworks as Monodisperse Nanocrystals and Oriented Thin Films

Section 6.1 Introduction

The development of reticular chemistry has hinged upon our ability to crystallize the products of linking molecular building blocks through strong bonds into extended porous structures. In the original synthesis of metal-organic frameworks (MOFs), the key discovery for obtaining them as crystals was the control of deprotonation of the acid organic linkers and in turn the rate of reaction with metal ions.¹ The fact that the starting point of the reaction is a homogeneous solution mixture has allowed modulation of the nucleation and crystal growth using many different synthetic methods,²⁻⁶ and this has led to the vast expansion of MOFs.⁷⁻⁸ In contrast, the synthesis of the newly emerging covalent organic frameworks (COFs) generally starts with heterogeneous amorphous solids resulting from the linking of the organic building blocks.⁹ These solids are annealed by heating to potentially obtain microcrystalline materials; an aspect that leads to lack of control in making COFs and severely limits the possibilities for controlling their nucleation as being practiced in MOFs. Here, we report, a synthetic route for making COFs that starts with a homogeneous mixture of the building units, demonstrate its utility for imine-based COFs, and show how it has led to: (a) size and shape controlled, monodisperse nanocrystals of LZU-1,¹⁰ TFPB-PDA COF,¹¹ and Por-COF,¹² and (b) facile preparation of oriented thin films of LZU-1. We believe this homogeneous synthetic route will vastly expand our ability to access crystalline COFs.

In conventional imine COF synthesis, amine and aldehyde building blocks usually form amorphous polyimine precipitates upon addition of solvent mixture and aqueous acetic acid catalyst, which gradually turn into aggregates of microscopic COF crystallites after heated in sealed Pyrex tubes for days.¹³⁻¹⁴ The imine COFs thus obtained typically have morphology resembling the initial polyimine precipitates, as the COF nucleation and growth are intrinsically heterogeneous and insensitive to the addition of modulators. In this process, crystallization relies on the reversible imine condensation reaction to correct defects in the polyimine precipitate, which would not be successful when substantial structural difference is present between the desired COF and polyimine precipitate. These limitations are addressed in this study by the utilization of *tert*-butyloxycarbonyl (Boc) group protected amine as the starting reagent to synthesize COFs homogeneously, which can be gradually deprotected *in situ* with trifluoroacetic acid and build up crystalline COFs. The gradual release of amine by *in situ* deprotection slows down the imine condensation reactions and facilitates COF crystallization. This synthetic route thus enables imine based COFs to be synthesized homogeneously without involving any amorphous insoluble intermediates. We demonstrate the power of this synthetic approach by synthesizing imine COFs as monodisperse nanocrystals and thin films.

Section 6.2 Experimental Section

Section 6.2.1 Methods and Materials

Chemicals. *p*-phenylenediamine (PDA, purity $\geq 99\%$), poly(vinylpyrrolidinone) (PVP, $M_w = 10,000$, and $M_w = 360,000$), ethanol (anhydrous, purity $\geq 99.5\%$), and triethylamine (TEA, purity $\geq 99.5\%$) were obtained from Sigma-Aldrich. 1,3,5-Triformylbenzene (TFBZ, purity $\geq 98\%$), 4-(*tert*-butoxycarbonylamino)-aniline (NBPDA, purity $\geq 97\%$), acetone (anhydrous, purity $\geq 99.8\%$), isopropanol (anhydrous, purity $\geq 99.8\%$) were obtained from Acros Organics. 2,6-Pyridinedicarboxaldehyde (PCBA, purity $\geq 98\%$) was obtained from TCI. Toluene (anhydrous purity $\geq 99.8\%$), acetonitrile (purity $\geq 99.8\%$), glacial acetic acid (purity 100%) and trifluoroacetic acid (TFA, purity $\geq 99.7\%$) were obtained from EMD Millipore Chemicals. All starting materials, reagents and solvents were used without further purification.

Analytical Techniques. Gas adsorption experiments (up to 760 Torr) were carried out on a Quantachrome AUTOSORB-1 automatic volumetric instrument. Ultrahigh-purity-grade N_2 and He gases were used in all adsorption measurements. The N_2 (77 K) isotherms were measured using a liquid nitrogen bath (77 K). The backbone density of the COF-112 was measured by pycnometry on a Quantachrome-UPYC 1200e V5.04 instrument using He gas. Powder X-ray diffraction (PXRD) patterns were recorded using a Rigaku Miniflex 600 (Bragg-Brentano geometry, Cu K_α radiation $\lambda = 1.54 \text{ \AA}$) diffractometer. Solution 1H NMR spectra were acquired on a Bruker AVB-400 and AV-600 NMR spectrometer. Elemental microanalyses (EA) were performed in the Microanalytical Laboratory of the College of Chemistry at UC Berkeley, using a Perkin Elmer 2400 Series II CHNS elemental analyzer. The amount of Co, Fe and B in COF-112 was analyzed by ICP–AES spectroscopy with Optima 7000 DV (PerkinElmer) instrument. Attenuated total reflectance (ATR) FTIR spectra of neat samples were performed on a Bruker ALPHA Platinum ATR-FTIR Spectrometer equipped with a single reflection diamond ATR module. Scanning electron microscope (SEM) images were recorded on a Zeiss Gemini Ultra-55 analytical scanning electron microscope with accelerating voltage of 5 kV. High-resolution transmission electron microscopy (HRTEM) images were taken with a field emission JEM-2010F instrument equipped with a CEOS C_s corrector operated at 120kV. Optical refractive index was measured using ellipsometer (Gaertner Scientific Corporation). Single crystal X-ray diffraction data was collected using synchrotron radiation on beamline 11.3.1 at the Advanced Light Source (ALS) at Lawrence Berkeley National Lab (LBNL), equipped with a Bruker Photon 100 CMOS area detector using synchrotron radiation (16 keV). Samples were mounted on MiTeGen[®] kapton loops and placed in a 100 K nitrogen cold stream. Grazing-Incidence Wide-Angle X-ray Scattering (GIWAXS) patterns were acquired with a Pilatus 2 M (Dectris) instrument on beamline 7.3.3 at the ALS ($\lambda = 1.24 \text{ \AA}$). The incidence angle was held at 0.120° to optimize signal collection. Silver behenate was used for calibration. The Nika package for IGOR Pro was used to reduce the acquired 1D raw data to a 2D format.

Section 6.2.2 Synthesis of COF Nanocrystals and Thin Films

Synthesis of LZU-1 Nanocrystals. TFBZ (5 mg, 0.03 mmol), NBPDA (10 mg, 0.05 mmol) and PVP ($M_w = 360,000$, 20 mg) were dissolved in 2 mL ethanol and 0.24 mL TFA. The solution was transferred to a 10 mL glass microwave vessel and heated to $120^\circ C$ for 30 minutes. The reddish dispersion obtained was diluted with ethanol to 8 mL and centrifuged at 8000 rpm for 5

minutes. The red solid collected was dispersed into 8 mL ethanol and 0.5 mL TEA to give a yellow suspension. The color change indicated the protonated imine in the nanocrystals were deprotonated by the amine base. The solution was centrifuged again at 8000 rpm to collect the nanocrystals and the supernatant was decanted. The yellow solid collected can be then redispersed in polar solvents such as ethanol, methanol and *N,N*-dimethylformamide. For larger nanocrystals with size of 500 nm, 10 mg PVP ($M_w = 360,000$) instead of 20 mg PVP ($M_w = 360,000$) was used in the same synthetic procedure. For nanocrystals with size of 112 nm, the growth solution was prepared to have TFBZ (5 mg, 0.03 mmol), NBPDA (10 mg, 0.05 mmol) and 40 mg PVP ($M_w = 10,000$) dissolved in 1 mL ethanol and 0.12 mL TFA. For hexagonal shaped nanocrystals, a toluene/ethanol = 1:9 mixture was used instead of pure ethanol as the solvent.

Synthesis of Por-COF and TFPB-PDA COF nanocrystals. The synthesis of Por-COF nanocrystals was carried out similarly to LZU-1, where 8.5 mg of 4,4',4'',4'''-(porphyrin-5,10,15,20-tetrayl)tetrabenzaldehyde, 5 mg NBPDA and 15 mg PVP ($M_w = 360,000$) were dissolved in 0.3 mL toluene, 0.7 mL ethanol, 60 μ l TFA and 10 μ l water and heated under microwave irradiation at 120° C for 30 minutes. The synthesized nanocrystals are washed in a similar manner to the LZU-1 nanocrystal.

The synthesis of TFPB-PDA COF nanocrystals was carried out at the same condition as COF-366, where 5 mg TFPB, 5 mg NBPDA, and 15 mg PVP ($M_w = 360,000$) were dissolved in 0.3 mL toluene, 0.7 mL ethanol, 60 μ l TFA and 10 μ l water and heated under microwave irradiation at 120° C for 30 minutes. The synthesized nanocrystals are washed in a similar manner to the LZU-1 nanocrystals.

Synthesis of LZU-1 COF Thin Film. The growth of LZU-1 thin film was realized by suspending the substrate into a heated growth solution at a constant temperature of 100 °C with reaction time varied between 1.5 to 6 h depending on the desired thicknesses. The growth solution was prepared by dissolving TFBZ (5 mg, 0.03 mmol) and NBPDA (10 mg, 0.05 mmol) in a solvent mixture of 2.25 mL toluene, 0.75 mL dioxane and 0.6 mL TFA. The as-prepared thin films were immediately washed with dioxane/TEA mixture and ethanol and dried under a stream of nitrogen.

Synthesis and characterization of mixed matrix membrane based on LZU-1 nanocrystal. The mixed matrix membrane was produced as follows, 100 mg LZU-1 nanocrystal and 50 mg PVDF ($M_w = 27500$) was dispersed in 4 mL DMF to form a uniform solution, which was then evaporated at 100 °C to give free standing membrane. The membrane consists of LZU-1 nanocrystals encapsulated in PVDF fibers. The membrane retains moderate porosity.

Section 6.3 Result and Discussion

Section 6.3.1 Synthesis and Characterization of Monodisperse Nanocrystals

In the homogenized imine COF synthesis, nuclei form from clear solution and grow directly into crystalline frameworks, which opens up opportunities for COF nucleation and growth control. Specifically, a ‘burst of nucleation’ induced by rapid heating combined with modulator regulated growth would give monodisperse nanocrystals, while under mild heating the nucleation barrier would facilitate the selective growth of COFs on substrates. We would first demonstrate this nucleation and growth control on a prototype imine COF, LZU-1, before generalization to other ones. It is worth noting that the slow in situ deprotection of amines would facilitate crystallization and enable unprecedented facile growth of crystalline imine COFs that are only known in keto-enamine COF synthesis,¹⁵⁻¹⁸ which would add to the merit of homogenized imine COF synthesis.

Monodisperse LZU-1 nanocrystals were synthesized by reacting NBPDA and TFBZ under microwave irradiation with PVP as the capping agent. In a typical synthesis, NBPDA and TFBZ were dissolved in 2 mL ethanol with 10 mg/mL PVP ($M_w = 360,000$) and 240 μ L TFA, which was heated at 120 °C for 30 min to give a red suspension with protonated LZU-1 nanocrystals (Appendix, Figure A6.1 and 6.2).¹⁹ This suspension rapidly turned yellow upon deprotonation by washing with an ethanol/triethylamine mixture. We believe the protonation of the imine COF renders the COF nanocrystals polar during crystal growth and allows PVP to bind and passivate their surface and regulate growth in alcoholic solution.

The size and morphology of the LZU-1 nanocrystals were characterized by SEM, which revealed their spherical morphology and average size of 245 ± 25 nm (Figure 6.1a and b). The size of these nanocrystals can be tuned by the concentration of PVP, where 5 mg/mL PVP gave 500 ± 52 nm COF particles (Figure 6.1c and d) and 40 mg/mL PVP gave crystals of 112 ± 11 nm (Figure 6.1e and f). The high crystallinity of these particles was confirmed by PXRD (Figure 6.2a). These particles were highly dispersible in ethanol and could remain colloidally stable for weeks (Figure 6.2b). High resolution TEM images further characterized the composition and crystallinity of the nanocrystals, where the 2.2 nm hexagonal pore of the LZU-1 nanocrystal can be clearly observed as well as the one-dimensional channels (Figure 6.2c and d).

Moreover, the morphology of COF nanocrystals can be tuned by solvent composition, where the addition of toluene into the ethanol growth solution yielded a hexagonal morphology. This hexagonal shape also supports the homogeneous nature of the crystal growth process and the high crystallinity of these nanocrystals (Figure 6.3).

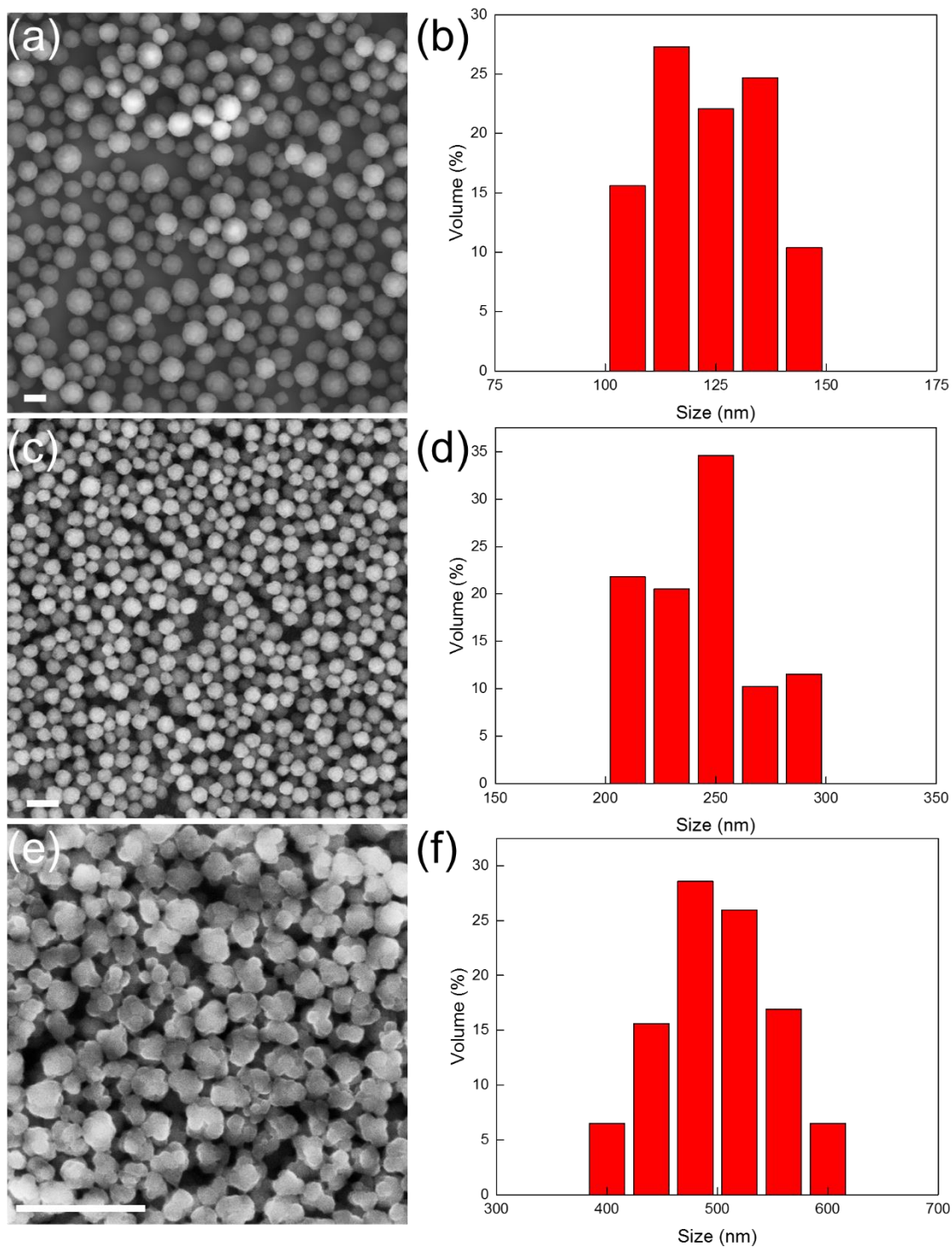


Figure 6.1. SEM and size distribution of LZU-1 nanocrystals. The size of monodisperse LZU-1 nanocrystals can be tuned from 500 ± 52 nm (a and b), 245 ± 25 nm (c and d) to 112 ± 11 nm (e and f) by tuning the concentration of PVP. From size distribution, it is clear that these particles are monodisperse (b, d and f).

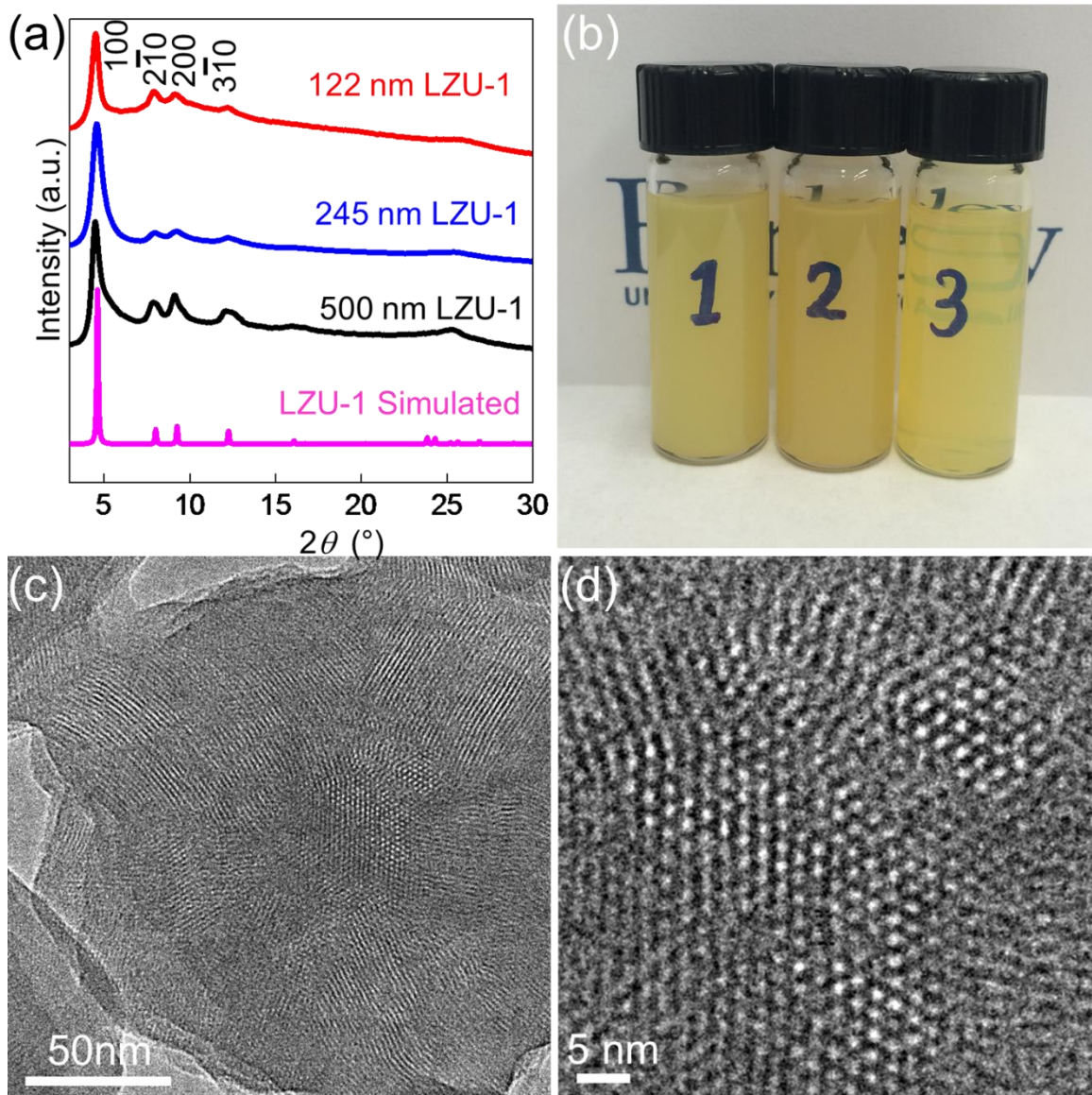


Figure 6.2. XRD and TEM study of LZU-1 nanocrystals. Powder X-ray diffraction shows high crystallinity of LZU nanocrystals with different sizes (a), which are dispersible in ethanol for weeks (b). High resolution TEM reveals LZU-1 nanocrystals consist of several crystalline domains, as both one-dimensional channels (2.2 nm wide, perpendicular to electron beam) and hexagonal pores (2.2 nm diameter, parallel to electron beam) can be observed in one particle (c), which is shown in higher magnification (d).

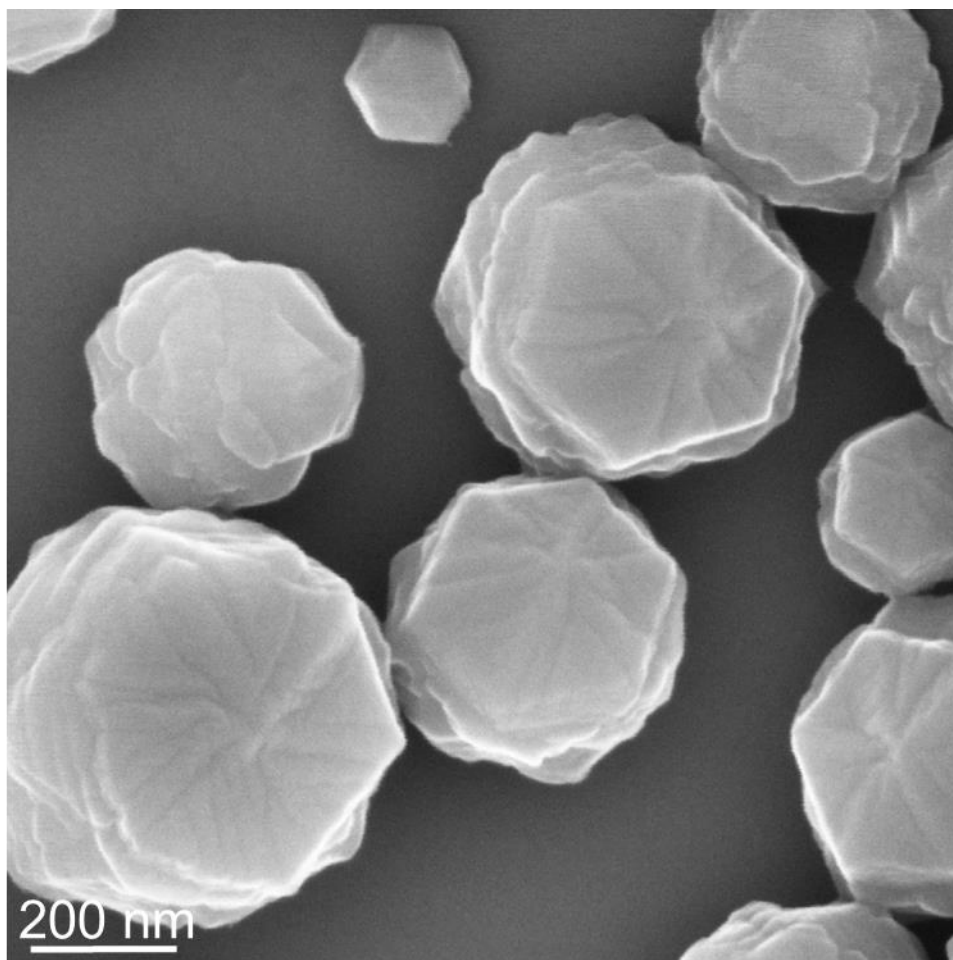


Figure 6.3. Hexagonal LZU-1 nanocrystals obtained using toluene/ethanol mixture solvents.

The optimal nanocrystal morphology can be obtained by ‘matching’ the PVP molecular weight with the desired particle size (essentially determined by PVP concentration). For small nanocrystals, if large molecular weight PVP is used (Figure 6.4a and b, $M_w = 360,000$ PVP and 40 mg/mL), one particle would usually have several small crystallites and thus have irregular star-like morphology. Similarly, for large nanocrystals, when small molecular weight PVP was used, aggregation of particles can be observed and particles would be polydisperse (Figure 6.4 c and d, $M_w = 10,000$ PVP and 5 mg/mL). The effect of toluene in this synthesis is also complex. With 1 mL toluene and ethanol mixture, a toluene fraction beyond 0.6 mL would give aggregated COFs as the solution is not polar enough to dissolve PVP and disperse the polar nanocrystals; a toluene fraction between 0.6 and 0.3 mL usually gives a clear solution or very low COF yield, and toluene behaves as an inhibitor of COF growth; a toluene fraction below 0.3 mL yields morphologically-tuned COF nanocrystals. The synthesis is insensitive to the amount of TFA added, but very sensitive to addition of water, which drastically decreases the COF yield.

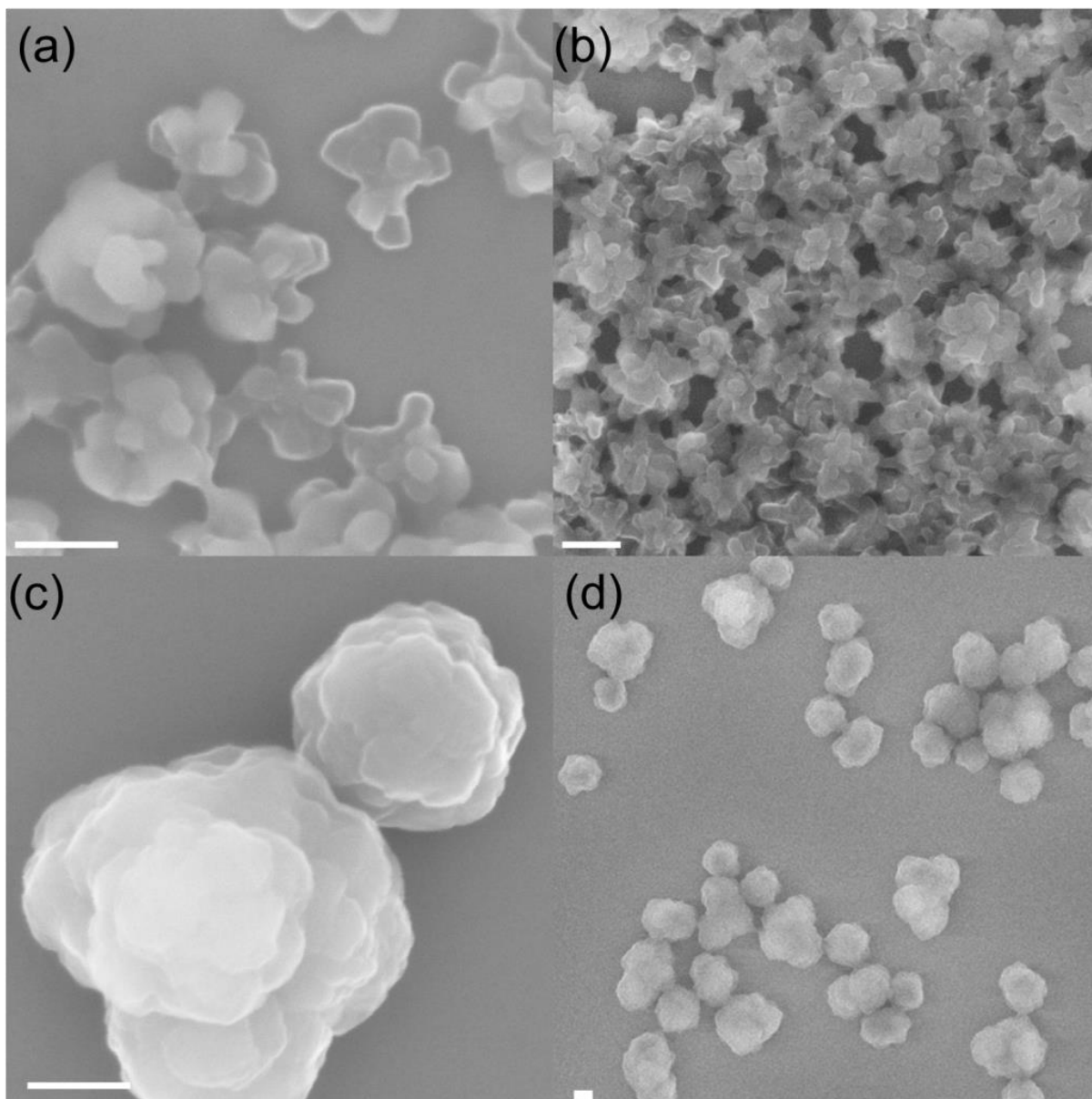


Figure 6.4. Poly-dispersed LZU-1 nanocrystals with 'mis-matched' PVP molecular weight and particle size. scale bar 200 nm.

The LZU-1 nanocrystals thus prepared display a high surface area of 729 m²/g, which is more than 1.5 times that of the original report (457 m²/g) (Figure 6.5). This synthetic method to produce COF nanocrystals is highly generalizable where two different COFs, TFPB-PDA and Por-COF were synthesized as nanocrystals with this method (Figure 6.6).

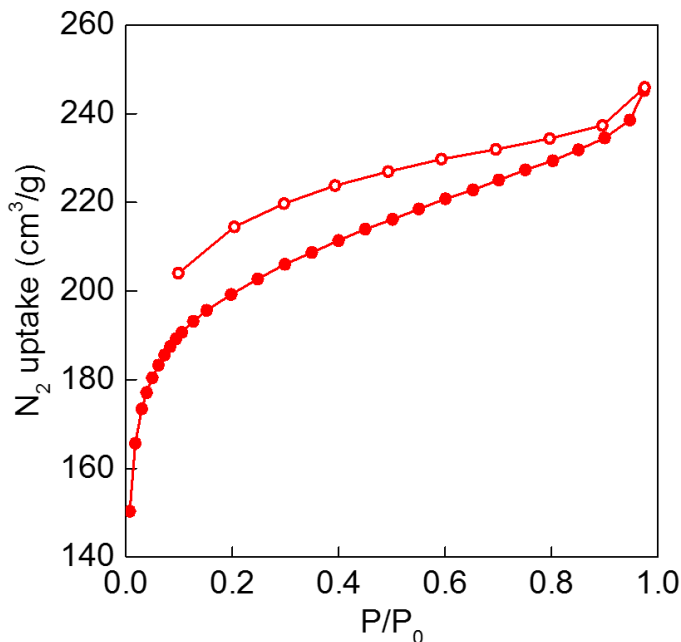
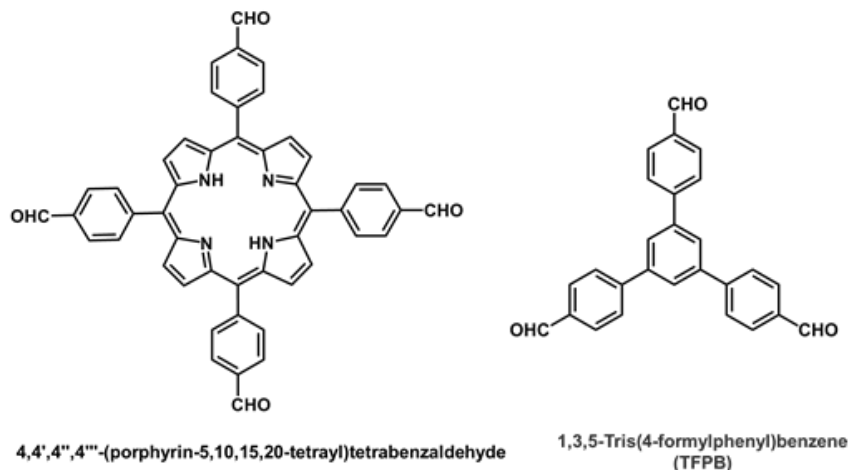


Figure 6.5. N₂ uptake of 245 nm LZU-1 nanocrystals (adsorption and desorption represented by filled and empty sphere, respectively).

It is worth noting that with these aldehyde linkers that have large molecular weight than TFBZ, COF nanocrystals can nucleate with lower concentration than LZU-1. However, these aldehydes, having lower reactivity than TFBZ, would sometimes give crystalline impurities, which could presumably be oligomers of protonated polyimines. This can be avoided with the addition of small amount of water to the reaction mixture, as in the reaction conditions provided above.

Scheme 6.1. Aldehyde building block of the Por-COF and TFPB-PDA COF.



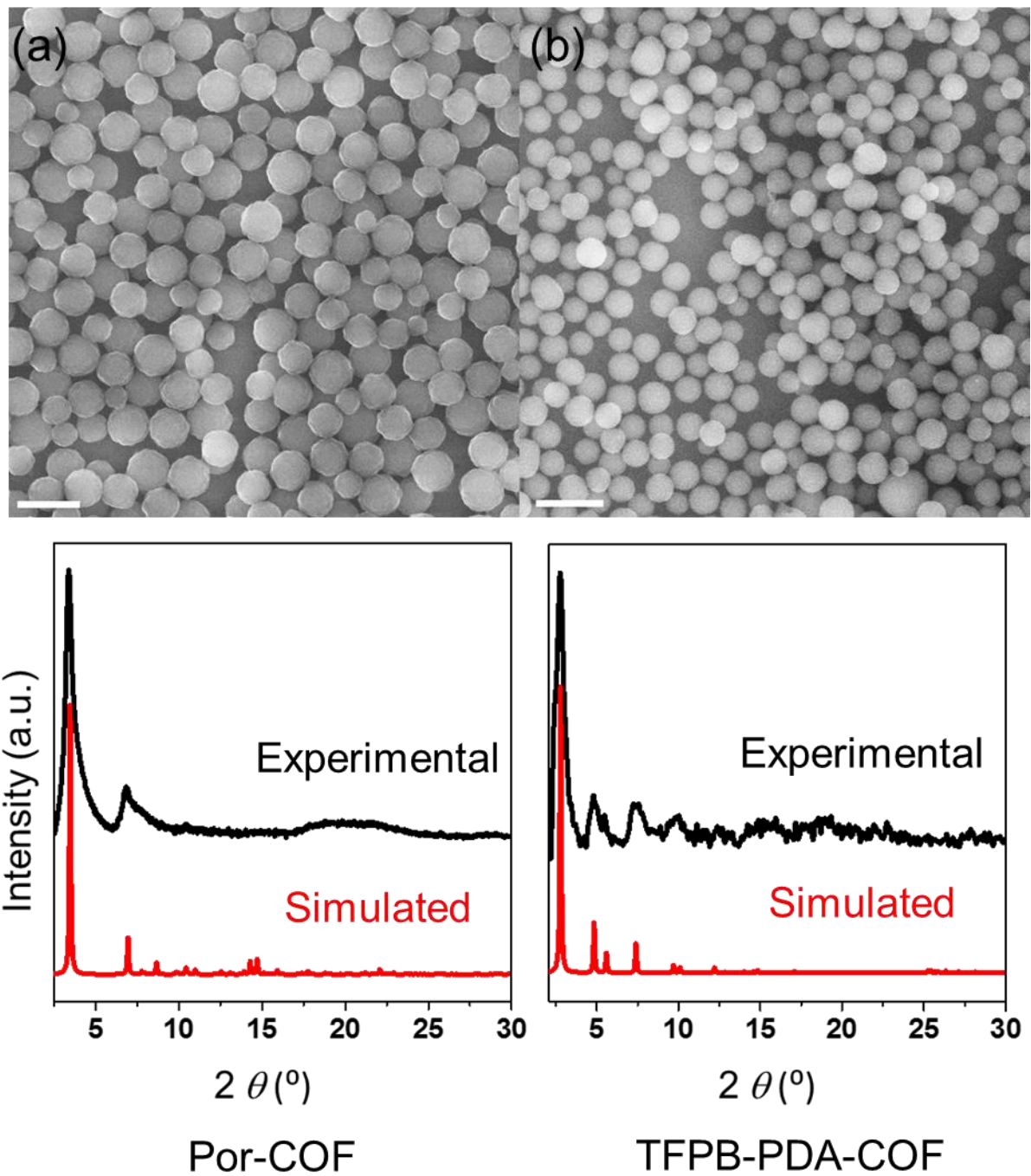


Figure 6.6. SEM images and PXRD of Por-COF and TFPB-PDA-COF nanocrystals (scale bar 1 μm).

The microwave heating not only gives homogeneous rapid heating necessary for burst of nucleation, but also allows for large scale COF preparation. With 15 mL solvent in one microwave vessel, hundred-milligram scale of COF could be produced in half an hour, compared to sealing several Pyrex glass tubes and heating for days in the conventional methods. The utilization of the Boc-protected amine in a homogeneous synthetic route also broadens the range of conditions of COF synthesis, where solvents (*i.e.* alcohols) considered undesirable in conventional synthesis can now be used to give crystalline products. We believe these features will profoundly advance the application and fabrication of imine COFs. For a proof-of-concept example, the monodisperse and porous COF nanocrystals were used as well-defined processable building blocks in preparation of COF based mixed matrix membrane, where PVDF and LZU-1 nanocrystals were both dissolved in DMF and then casted into free standing thin films with a surface area of 242 m²/g (Figure 6.7). With COFs nanocrystals below 200 nm, as their size was below the wavelength of light, the membrane became transparent.

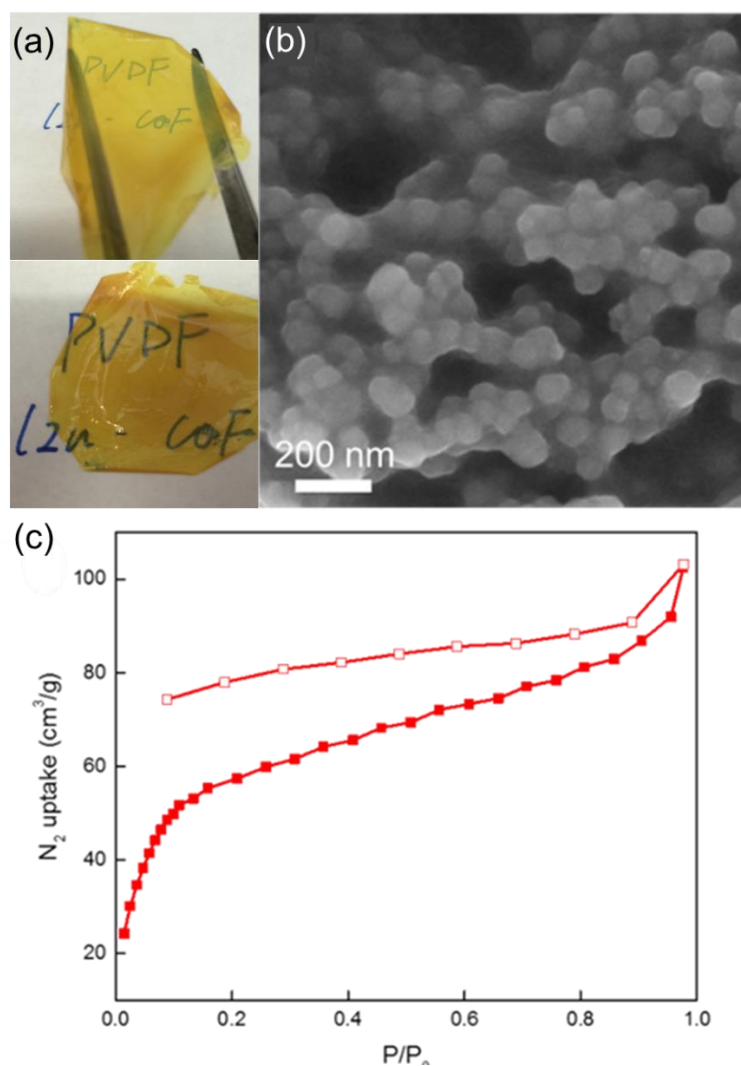


Figure 6.7. Mixed matrix membrane of LZU-1 nanocrystals. (a) The membrane can be free standing and transparent. (b) The film is consisted of LZU nanocrystal coated by PVDF. (c) The film shows accessible surface area of 241 m²/g.

Section 6.3.2 Synthesis and Characterization of Oriented Thin Films

The homogeneous synthesis of imine COFs also allows for the fabrication of imine COFs into high quality thin films. This can be demonstrated by synthesizing LZU-1 thin films on silicon substrates in hydrophobic aromatic solutions. As the protonated COF nanocrystals form homogeneously, the nucleation barrier would favor COF nucleation on the polar oxides, which would facilitate the selective growth of COF thin film on the substrates. The growth of imine COF thin film was realized by heating the substrate at 100 °C in the growth solution, where NBPDA and TFBZ were dissolved in a solvent mixture of toluene, dioxane and TFA. A uniform film was formed after 2 hours on the silicon substrate and the wall of the vial. The thin film morphology of the COF can be clearly observed by SEM at the edge of the substrate where the film was wrapped (Figure 6.8). Higher magnification SEM on the wrapped film revealed that it was composed of the small crystallites with similar orientation (Figure 6.9a). The thickness of the film was measured by cross-section SEM to be 190 nm, which can be tuned empirically by changing the reaction time and concentration of the growth solution (Figure 6.9b and A6.5). The crystallinity and orientation of the film were characterized by GIWAXS measurements, which revealed the 2D plane of the LZU-1 COF being flat on the substrate with its [001] direction perpendicular to the substrate (Figure 6.9c). The high quality polyimine film enabled us to measure its optical property by ellipsometry for the first time. Surprisingly, the highly porous material had high refractive index of 1.83 at 632.8 nm wavelength. This is higher than most polymer materials and indicates the high level of in-plane conjugation in the COF. The high film quality and well-defined optical property give rise to interesting chemical sensitive optical properties that indicates the porosity of these COF thin films (Figure 6.10). The homogeneous COF growth enabled by protected amine building blocks gives unprecedented high quality crystalline, oriented, porous COF thin films that would advance the impact of COF chemistry in optical and electronic applications.

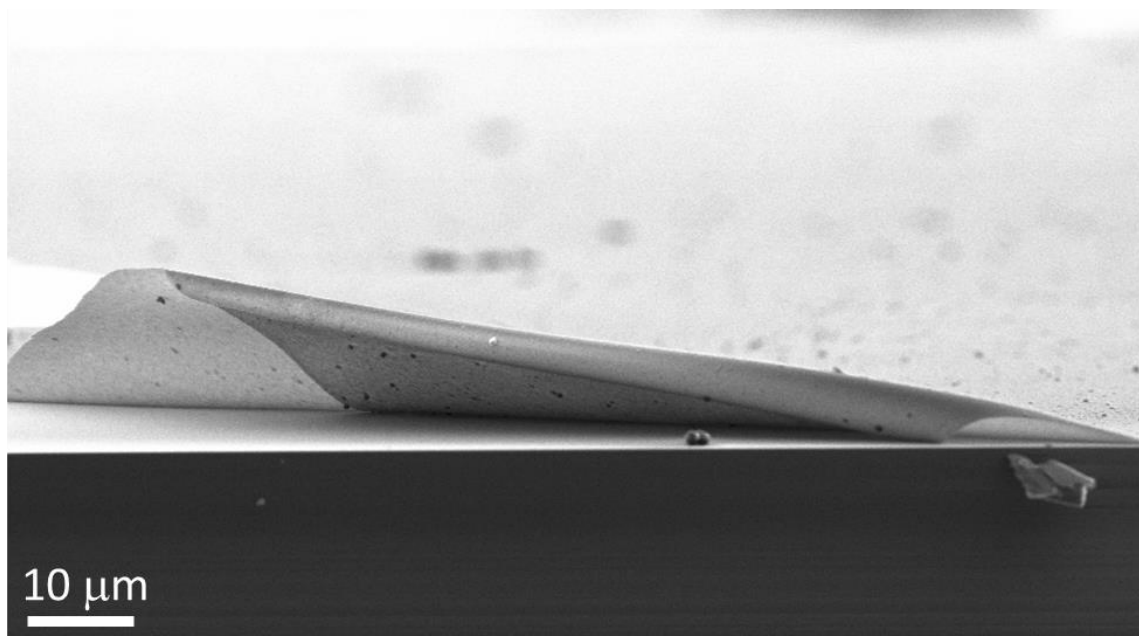


Figure 6.8. SEM image of LZU-1 thin film. The image shows the partially detached corner of the film confirms the thin film nature of the COF.

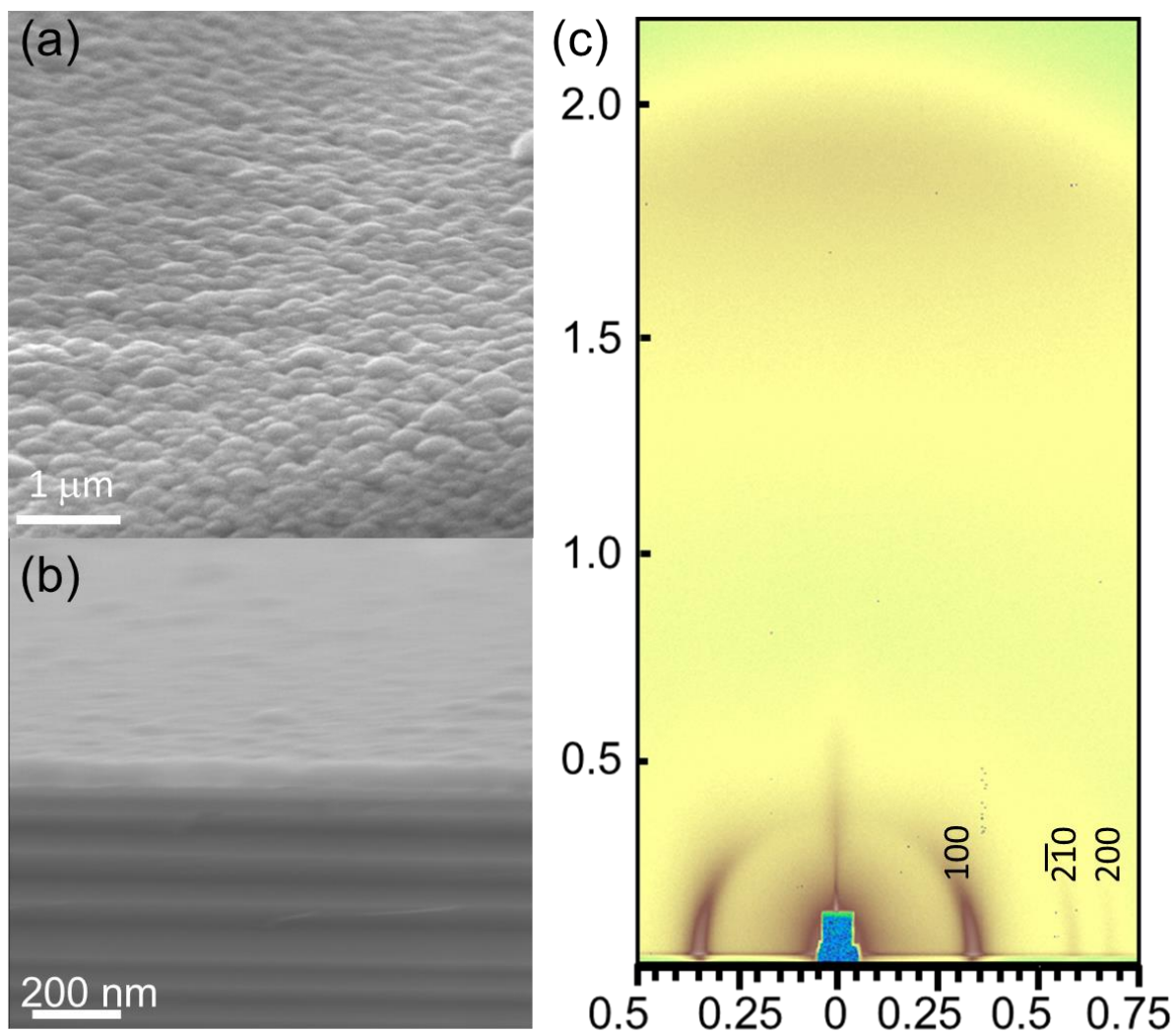


Figure 6.9. The uniformity, orientation, and crystallinity of LZU-1 COF thin film. The thin film was highly uniform (a) and composed of small crystallites with similar orientation. The thickness of the film was determined to be 190 nm by cross-sectional SEM (b) and its crystallinity and orientation confirmed by GIWAXS pattern (c).

When the COF thin films are exposed to organic vapor, its color changes due to the change of overall refractive index by gas adsorption. This color change is highly reversible, as the vapor is removed, the color change is reversed. This phenomenon indicates the accessible porosity of the film and can be best demonstrated by putting the thin film into vials with organic vapor with different vapor pressure and observe where the film changes its color with respect to the liquid level.

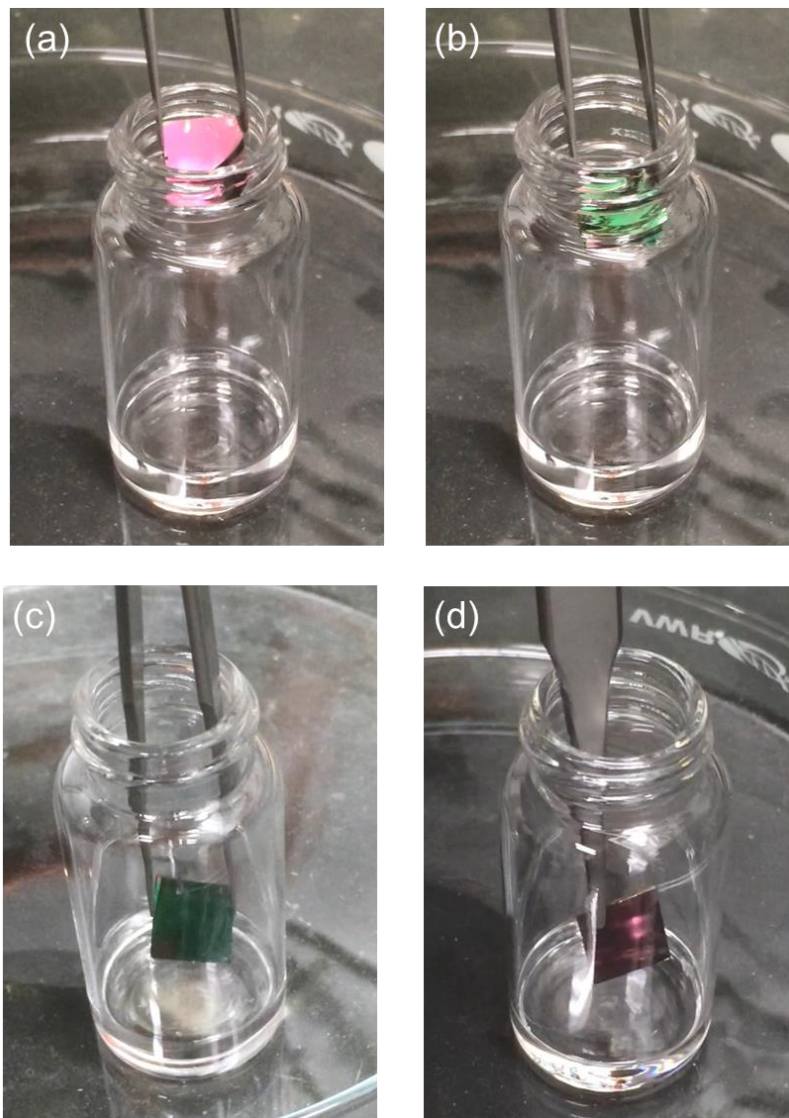


Figure 6.10. Gas adsorption triggered color change in LZU-1 thin film. The film was pink before exposure (a), and turned green after exposed to acetone (b) and methanol (c). As acetone has higher vapor pressure, the film turned green at the top of the vial, while for methanol the film only turned green after being closer to the liquid level. When ethylene glycol (d) was used, the film kept its original color due to the low vapor pressure of the liquid.

Section 6.4 Conclusion

In this chapter, we developed a synthetic approach to homogenize the COF synthesis which involves using protected amine building blocks as the starting material. This synthetic approach avoids formation of polyimine intermediates and allows COF crystallites to grow directly from clear solution. The homogeneous COF growth process can be tuned by modulators to afford monodisperse COF nanocrystals. The COF nucleation can be controlled to selectively grow thin film on substrates with high crystallinity and well-defined orientation.

The essence of developing homogeneous COF synthesis is synchronizing the COF nucleation and crystallization, which enabled the control of both nucleation and growth of COFs. The fact that the COF crystals are protonated and polar further facilitate their growth control, since surfactant like PVP can passivate their surface. The nucleation barrier in the homogeneous COF synthesis enables film growth without precipitation from the solution. In summary, in this synthetic approach, the COFs can be grown in similar manner as inorganic material, which will significantly advance their fabrication in nano-size regime and integration in mesoscopic constructs.

Section 6.5 Reference

- (1) Jiang, J.; Zhao, Y.; Yaghi, O. M. *J. Am. Chem. Soc.* **2016**, 138, 3255-3265.
- (2) Umemura, A.; Diring, S.; Furukawa, S.; Uehara, H.; Tsuruoka, T.; Kitagawa, S. *J. Am. Chem. Soc.* **2011**, 133, 15506-15513.
- (3) Kuo, C.-H.; Tang, Y.; Chou, L.-Y.; Sneed, B. T.; Brodsky, C. N.; Zhao, Z.; Tsung, C.-K. *J. Am. Chem. Soc.* **2012**, 134, 14345-14348.
- (4) Lausund, K. B.; Nilsen, O. *Nat. Commun.* **2016**, 7, 13578.
- (5) Zhao, Y.; Kornienko, N.; Liu, Z.; Zhu, C.; Asahina, S.; Kuo, T.-R.; Bao, W.; Xie, C.; Hexemer, A.; Terasaki, O.; Yang, P.; Yaghi, O. M. *J. Am. Chem. Soc.* **2015**, 137, 2199-2202.
- (6) Cavka, J. H.; Jakobsen, S.; Olsbye, U.; Guillou, N.; Lamberti, C.; Bordiga, S.; Lillerud, K. P. *J. Am. Chem. Soc.* **2008**, 130, 13850-13851.
- (7) (a) Furukawa, H.; Cordova, K. E.; O'Keeffe, M.; Yaghi, O. M., *Science* **2013**, 341, 1230444.
- (8) Rungtaweevoranit, B.; Zhao, Y.; Choi, K. M.; Yaghi, O. M., *Nano Res.* **2016**, 9, 47-58.
- (9) Smith, B. J.; Overholts, A. C.; Hwang, N.; Dichtel, W. R. *Chem. Commun.* **2016**, 52, 3690-3693.
- (10) Ding, S.-Y.; Gao, J.; Wang, Q.; Zhang, Y.; Song, W.-G.; Su, C.-Y.; Wang, W. *J. Am. Chem. Soc.* 2011, 133, 19816-19822.
- (11) Peng, Y.; Wong, W. K.; Hu, Z.; Cheng, Y.; Yuan, D.; Khan, S. A.; Zhao, D. *Chem. Mater.* **2016**, 28, 5095-5101.
- (12) Liao, H.; Wang, H.; Ding, H.; Meng, X.; Xu, H.; Wang, B.; Ai, X.; Wang, C. *J. Mater. Chem. A.* **2016**, 4, 7416-7421.

- (13) Uribe-Romo, F. J.; Hunt, J. R.; Furukawa, H.; Klöck, C.; O’Keeffe, M.; Yaghi, O. M. *J. Am. Chem. Soc.* 2009, 131, 4570-4571.
- (14) Xu, H.; Gao, J.; Jiang, D. *Nat. Chem.* 2015, 7, 905-912.
- (15) Li, Y.; Yang, C.-X.; Yan, X.-P. *Chem. Commun.* 2017, 53, 2511-2514.
- (16) Kandambeth, S.; Mallick, A.; Lukose, B.; Mane, M. V.; Heine, T.; Banerjee, R. *J. Am. Chem. Soc.* 2012, 134, 19524-19527.
- (17) Chong, J. H.; Sauer, M.; Patrick, B. O.; MacLachlan, M. J. *Org. Lett.* 2003, 5, 3823-3826.
- (18) Wei, H.; Chai, S.; Hu, N.; Yang, Z.; Wei, L.; Wang, L. *Chem. Commun.* 2015, 51, 12178-12181.
- (19) Popp, N.; Homburg, T.; Stock, N.; Senker, J., Porous imine-based networks with protonated imine linkages for carbon dioxide separation from mixtures with nitrogen and methane. *J. Mater. Chem. A.* 2015, 3, 18492-18504.

Section 6.6 Appendix

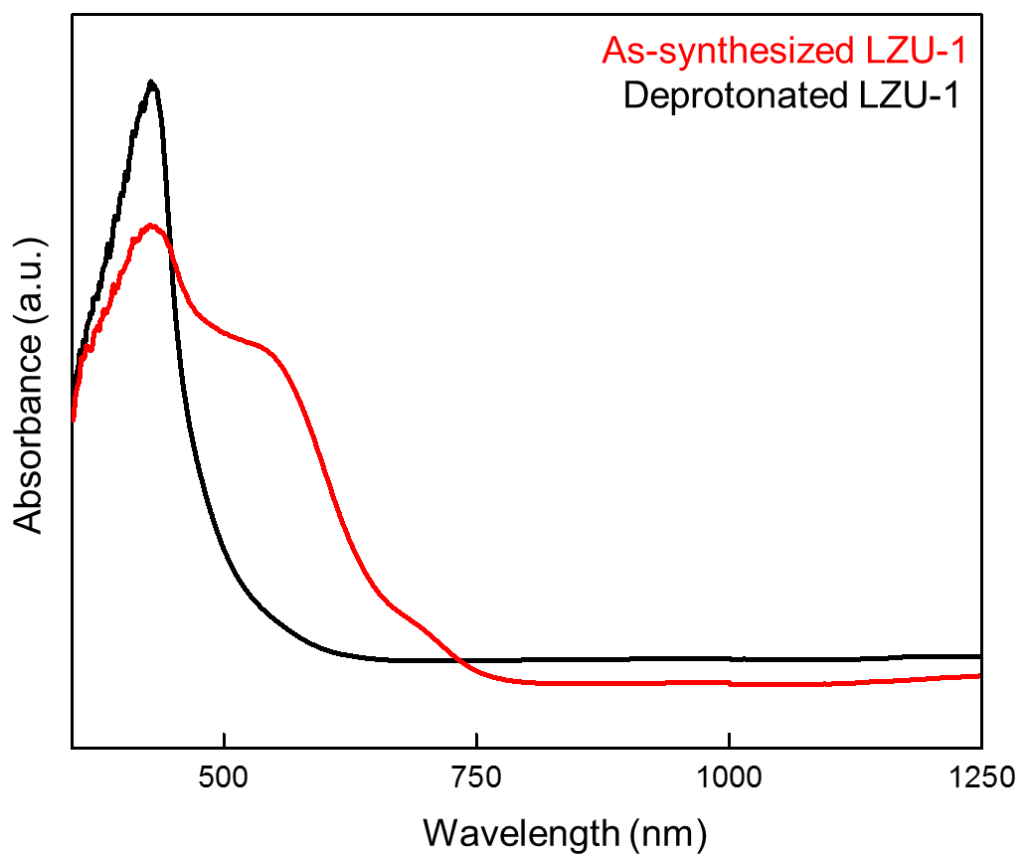


Figure A6.1. UV-Vis spectra of as-synthesized (protonated) and washed (deprotonated) LZU-1 nanocrystals.

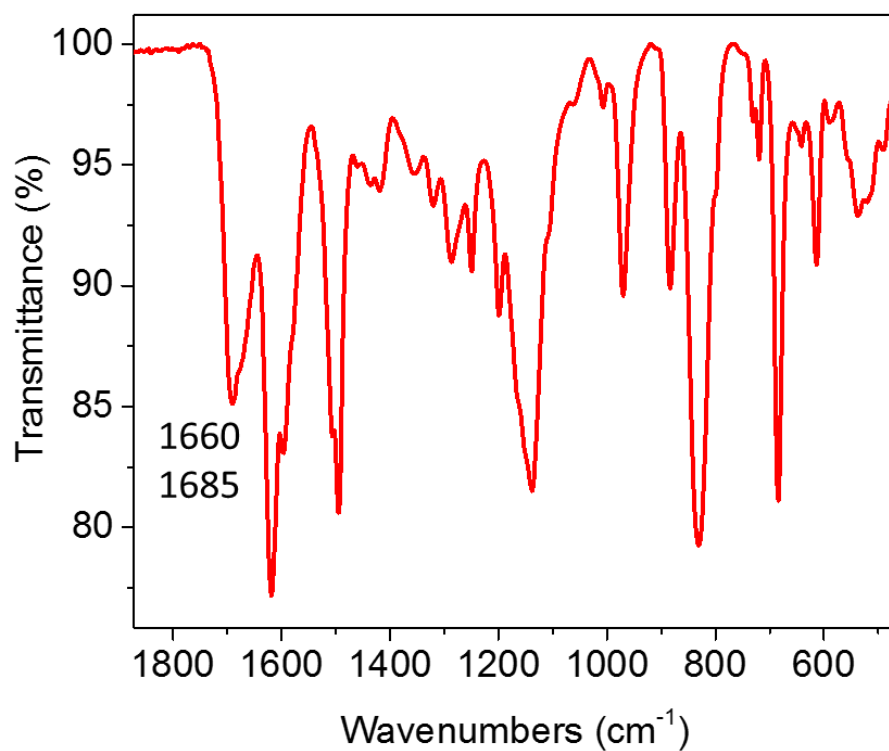
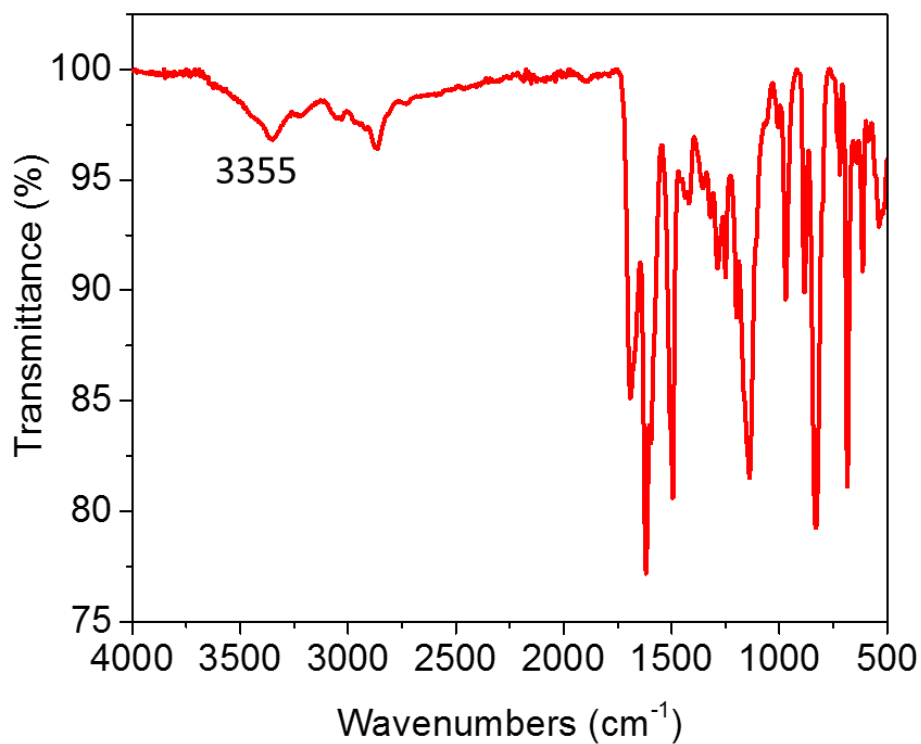


Figure A6.2. Infrared spectra of as-synthesized LZU-1 nanocrystals. 3355 cm⁻¹ vibration is attributed to N-H stretch and the 1660 cm⁻¹ shoulder is attributed to C=NH⁺ (the 1685 cm⁻¹ mode is attributed to C=O in PVP).

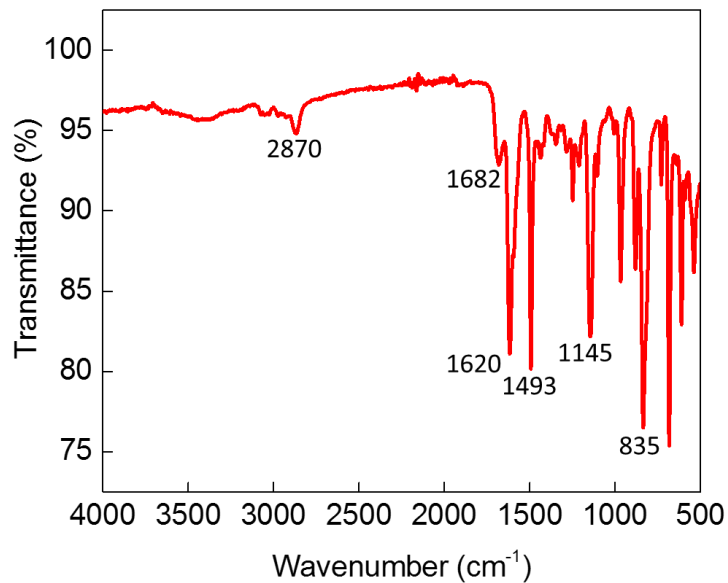


Figure A6.3. Infrared spectrum of LZU-1 nanocrystal. 1682 cm^{-1} and 2987 cm^{-1} are attributed to C=O and CH_2 -group in PVP. Other vibrational modes are consistent with the original report.

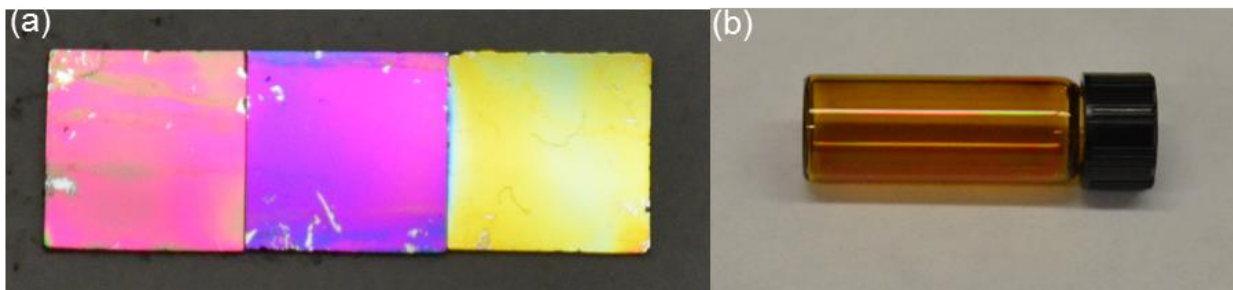


Figure A6.4. LZU-1 films of different thickness on silicon (a) and coating on glass vial (b).

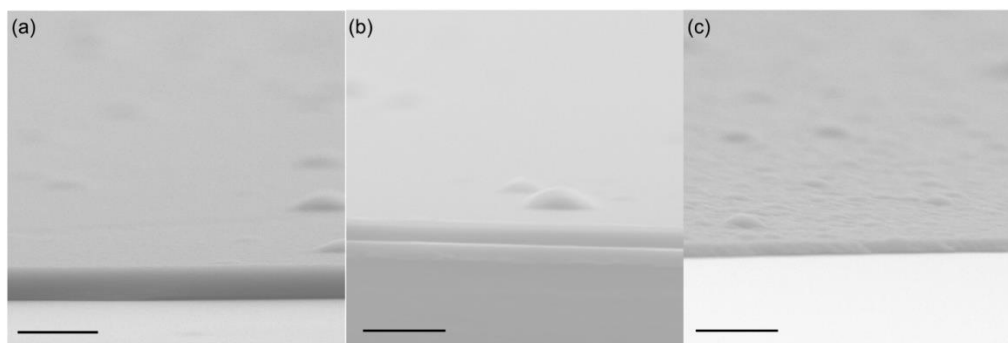


Figure A6.5. Cross-section SEM of the thin films in Figure S25. Film thickness are 400 nm, 260 nm, and 190 nm respectively in a, b and c (for the pink, purple and yellow color film). This thickness control was achieved empirically by tuning growth time and grow solution concentration. Scale bar is one micron.